Final Scientific Report

DOE Award:
DE-AI05-070R23278-001-000

Recipient:
National Institute of Standards and Technology

Phase Equilibria Relationships of High-T_c Superconductors

Principal Investigator: Winnie Wong-Ng

NIST Team member: Lawrence P. Cook

NIST Collaborators:
Igor Levin, Joseph Ritter, Mark Vaudin, Peter Schenck, Qing Huang, Ralph Klein
Guangyao Liu, Julia Suh, Zhi Yang, Mario Loung, Shailee Dawanji, Christopher Lucas

Accomplishments Summary

As an integral part of a DOE R&D program (1987-2007), we have determined phase equilibria data and phase diagrams for the three generations of superconductor materials: 1st generation, (Bi,Pb)-Sr-Ca- Cu-O systems (*e.g J. Mater. Res.,* ***15*** *(2) 296-305, 2000); J. Am. Ceram. Soc.* ***81****(7), 1829,1998*); 2nd generation, Ba-R-Cu-O systems (R=lanthanides and yttrium) (*e.g Physica C,* ***439****(2) 93-100, 2006*); and 3rd generation, MgB_2 systems (e.g. *IEEE Trans. Appl. Superconductivity,* ***15*** *[2], pp. 3227- 3229 (2005*). During the course of this work, we developed extensive collaborations with several DOE laboratories. Our studies involved bulk materials, single crystals (*e.g. Phys. Rev. B* ***41****, 4220, 1990*) and thin films (*e.g. Appl. Phys. Lett,* ***88*** *102507, 2006; Appl. Phys. Lett.* ***90****,102508, 2007*). In addition, we also studied the interactions (phase equilibria and kinetics) of superconductor phases with buffer layers and substrates of the coated conductors (*e.g. J. Solid State Chem.,* ***470****(5-6) 345-351, 2010*).

Various experimental challenges were successfully dealt with, including atmospheric contamination, substrate reaction, gas- phase interactions, and the complexity of multiphase products. Results were used to guide materials processing for optimal onset T_c, critical current density, high-field behavior, mechanical properties, and cost/performance ratio, including the development of novel flux-pinning techniques.

In addition, we have studied the theory and phenomena of phase transformation of the high T_c $BaR_2Cu_3O_{6+x}$ phases; the explanation of the trend of melting temperature of $BaR_2Cu_3O_{6+x}$ as a function of the size of the ionic radius of R; phase formation studies of the (Pb,Bi):Sr:Ca:Cu (2212 and 2223) oxide phases.

This work resulted in a number of awards and more than 150 publications. In the course of the project we were awarded the highest rating three times during the required annual DOE peer reviews. We were also given the Department of Commerce bronze awards in 2002 and in 2008.

The list of publications as a result of the partial support of the DOE program is summarized in the following pages. Fifteen selected papers are attached.

List of publications:

Journal papers:	104
Proceeding papers:	39
Book chapters:	3
Books edited	8
Total	154

104. W. Wong-Ng, Y. Zhi, J. A. Kaduk, L. P. Cook, S. Diwanji, and C. Lucas, "Interactions of $Ba_2YCu_3O_{6+x}$ with $SrTiO_3$ Substrate," undergoing NIST review, submitted to Physica C (2010).
103. G. Liu, W. Wong-Ng, J. A. Kaduk, and L.P. Cook, "Interactions of $Ba_2YCu_3O_{6+y}$ with Substrate Layer $LaMnO_3$ in Coated Conductors", Physica C, **470** (5-6) 341-351 (2010).
102. G. Liu, W. Wong-Ng, Z. Yang, J.A. Kaduk, and L.P. Cook, "Phase Equilibria of the Ba-Sm-Y-Cu-O System for Coated Conductor Applications" in press, J. Solid State Chem. (2010).
101. W. Wong-Ng, M. Otani, Z. Yang, I. Levin, P. Schenck, G. Liu, M. Green, L.P. Cook, R. Feenstra, W. Zheng, and M. Rupich, Combinatorial Studies of the Ba-Y-Cu-O Films for Coated Conductor Applications, Appl. Phys. Lett., **94** 171910 (2008).
100. W. Wong-Ng, Z. Yang, Y.F. Hu, Q. Huang, N. Lowhorn, M. Otani, J.A. Kaduk, M. Green, and Q. Li, "Thermoelectric and structural characterization of $Ba_2Ho(Cu_{3-x}Co_x)O_{6+x}$,"J. Appl. Phy. **105** (6) 63706, (2009).
99. W. Wong-Ng, Z. Yang, J. A. Kaduk, L.P. Cook, and M. Paranthaman, "Interactions of $Ba_2YCu_3O_{6+y}$ with Substrate Layer Gd_3NbO_7 in Coated Conductors", J. Solid State Chem. **470**(5-6) 345-351 (2010).
98. G. Liu, Q. Huang, J. Kaduk, Z. Yang, C. Lucas, and W. Wong-Ng, "X-ray and Neutron Powder Diffraction Studies of $Ba(Nd_xY_{2-x})CuO_5$,", J. Solid State Chem. **181** 3236(2008); doi:10.1016/j.jssc.2008.08.002.
97. W. Wong-Ng, I. Levin, J. Ritter, L.P. Cook, G. Liu, M. Otani, M. Vaudin, C. Lucas, S. P. Diwanji, "Phase Relations in Ba-(Nd,Eu,Gd)-Cu-O Coated Conductor Films," J. Mater. Res. **23** 2067 (2008).
96. H. Su, D. Welch, W. Wong-Ng, L.P. Cook and Z. Yang, "Manifestation of Anisotropy in Melting Systematics of $RBa_2Cu_3O_{7-\delta}$ (R= lanthanides)," Appl. Phys. Lett. **91** 172510 (2007).
95. L. P. Cook, W. Wong-Ng, P. Schenck, Z. Yang, I. Levin, and J. Frank, "Kinetics Studies of the Interfacial Reactions of the $Ba_2YCu_3O_{6+x}$ Superconductor with CeO_2 Buffer Systems," J. Electronic Mater. **36**(10), 1293-1298 (2007) DOI:10.1007/s11664-007-0244-3.
94. W. Wong-Ng, Z. Yang, L.P. Cook, J. Frank, M. Loung, and Q. Huang, "Phase Equilibria of BaO-R_2O_3-CuO_z Systems (R=Y and Lanthanides) under CO_2-free Conditions," J. Electronic Materials, **36**(10), 1279-1287 (2007) DOI:10.1007/s11664-007-0244-0.
93. W. Wong-Ng, I. Levin, M. Otani, M. D. Vaudin, L. P. Cook, J. Cline, R. Feenstra, and T. Holesinger, "Phase Relations in the Ba-Y-Cu-O Films on $SrTiO_3$ for the "*Ex Situ* BaF_2" Process," Appl. Phys. Lett. **90**, 102508 (2007).
92. W. Wong-Ng, Z. Yang, and L.P. Cook, "Subsolidus Phase Relationships of the BaO-R_2O_3-CuO_z (R=Tm and Yb) Systems Under Carbonate-Free Conditions at p_{O2} = 100 Pa, and T=810 °C, J. Alloys and Compounds, doi:10.1016/j.jallcom.2006.07.083 (2006).
91. W. Wong-Ng, L.P. Cook, Haibin Su, M. Vaudin, C.K. Chiang, D. Welch, E.R. Fuller, Jr, Z. Yang and L.H. Bennett, "Phase Transformations in the High T_C Superconducting Compounds, $Ba_2RCu_3O_{6+z}$ (R=Nd, Sm, Gd, Y, Ho, and Er)," J. Res. Natl. Inst. Stand. Technol., **111** (No. 1) 41 (2006).
90. W. Wong-Ng, Z. Yang, L.P. Cook, J. Suh, and M. Loung., "Subsolidus Phase Relationships of the BaO-R_2O_3-CuO_z (R=Eu, Dy, and Ho) Systems under Carbonate-Free Conditions at T = 810 °C and p_{O2} = 100 Pa, Physica C, **439**(2) 93-100 (2006).
89. Z. Yang, W. Wong-Ng, J.A. Kaduk, Q.Z. Huang and L.P. Cook, "X-ray and Neutron Powder Diffraction Studies of $(Ba_{1-x}Sr_x)Y_2CuO_5$", Powd. Diffr., **21**(3) 200-209 (2006).
88. W. Wong-Ng, I. Levin, L.P. Cook, and R. Feenstra, Nature of the Transient BaF_2-Related Phases in the

"BaF_2" Processing of $Ba_2YCu_3O_{7-x}$ Superconductors, Appl. Phys. Lett, **88** 102507 (2006).
87. W. Wong-Ng, T. Haugan, R.A. Young, J.A. Kaduk, C. Lind, Z. Yang, M.H. Jang, and M. Luong, Crystal Chemistry and Crystallography of the SrR_2CuO_5 (R=lanthanides) Phases, J. Solid State Chem., **179**(5) 1588-1595 (2006).
86. M.-H. Jang and W. Wong-Ng, "Transport AC Losses of Ag-Sheathed Bi-2223 Tapes with Different Twist-Pitch using Electrical Methods," Supercond. Sci. Technol. **19** 72-78 (2006).
85. W. Wong-Ng, Z. Yang, L.P. Cook, Q. Huang, and J. Frank, Chemical Interaction Between $Ba_2YCu_3O_{6+x}$ and CeO_2 at p_{O2} = 100 Pa, Solid States Sci, **7** 1333-1343 (2005).
84. W. Wong-Ng, L.P. Cook, J. Suh, I. Levin, and R. Feenstra, "Melting Investigation in the System BaF_2-BaO-Y_2O_3-CuO_x-H_2O," Supercond. Sci.and Technol., **18** 442-453 (2005).
83. L.P. Cook, W. Wong-Ng and R. Feenstra, $Ba(OH)_2$ Equilibria in the System Ba-O-H-F with Applications to the Formation of $Ba_2YCu_3O_{6+x}$ from BaF_2-Precursors, J. Res. Natl. Inst. Stand. Technol., **110,** pp. 115-126 (2005).
82. I. Levin, Q.Z. Huang, L.P. Cook, and W. Wong-Ng, Non-Quenchable Chemical Order-Disorder Phase Transition in Yttrium Oxyfluoride YOF, Eur. J. Inorg. Chem, 87-91 (2005).
81. L. P. Cook, R. Klein, W. Wong-Ng, Q. Huang, R. A. Ribeiro, P.C. Canfield, "Thermodynamics of MgB_2, by Calorimetry and Knudsen Thermogravimetry," IEEE Transaction on Applied Superconductivity, **15** [2], pp. 3227-3229 (2005).
80. T. J. Haugan, P. N. Barnes, T. A. Campbell, J. M. Evans, J. W. Kell, L. B. Brunke, J. P. Murphy, C.P. C. P. Varanasi, I. Maartense, W. Wong-Ng, and L. P. Cook, Addition of Alternate Phase Nanoparticle Dispersions to Enhance Flux Pinning of Y-Ba-Cu-O Thin Films, IEEE Transaction on Applied Superconductivity, **15** [2], pp. 3770-3773 (2005).
79. W. Wong-Ng, L.P. Cook, J. Suh, and J. Kaduk, "BaO-R_2O_3-CuO_x (R = Gd and Er) Subsolidus Equilibria Under Carbonate-Free Conditions at pO_2 = 100 Pa," Solid State Sciences, **6** 1211(2004).
78. W. Wong-Ng, I. Levin, R. Feenstra, L.P. Cook, and M. Vaudin, Phase Evolution of $Ba_2YCu_3O_{6+x}$ Films during the BaF_2 Process, Supercond. Sci. and Tech., **17** S548 (2004).
77. W. Wong-Ng, L.P. Cook, J. Suh, R. Feenstra, T. Haugan, and P. Barnes, "Phase Equlibria of Ba-R-Cu-O for Coated-conductor Applications (R=lanthanides and Y)," Physica C, **408-410** 20-22 (2004).
76. H. Su, D.O Welch, and W. Wong-Ng, "Strain Effects on Point Defects and Chain-Oxygen Order-Disorder Transition in 123 Cuprate Compunds", Phy. Rev B, **70** 054517 (2004).
75. W. Wong-Ng, L.P. Cook, J. Suh and J.A. Kudak, " Phase relationships in the BaO-Sm_2O_3-CuO_x system under 100Pa O_2, **"** Physica C, **405** 47-58 (2004).
74. W. Wong-Ng, L.P. Cook, J. Suh, R. Coutts, J. Stalick, I. Levin , and Q. Huang, "BaO-Nd_2O_3-CuO_x Subsolidus Equilibria Under Carbonate-Free Conditions at pO_2 = 100 Pa and at pO_2 = 21 kPa," J. Solid State Chem, **173** 476-488 (2003).
73. W. Wong-Ng, L. Swartzendruber J.A. Kaduk and L.H. Bennett, Magnetic and structural properties of the "Brown Phase" solid solution $Ba(Nd_{2-x}La_x)CuO_5$, Physica C, **390** 213-220 (2003).
72. W. Wong-Ng, W.Y. Ching, Yong-Nian Xu, J. A. Kaduk, I. Shirotani, and L. Swartzendruber "The Structure and Electronic Properties of the Orthorhombic MoRuP Superconductor Prepared at High Pressure," Phy. Rev. B, **14** 144523-1 to 144523-9 (2003).
71. T. Haugan, W. Wong-Ng, L.P. Cook, M.D. Vaudin, L. Swartzendruber, and P. Barnes, "Partial Melt processing of Solid –Solution $Bi_2SrCaCu_2O_{8+x}$ Thick film Conductors with nanophase Al_2O_3 Additions, J. Mater Res. Soc., **18**(5) 1054-1066 (2003).
70. W. Wong-Ng, I., Levin, M. Vaudin, R. Feenstra, L.P. Cook, and J.P. Cline,"High Temperature X-ray Diffractometer Study of Phase Evolution in $Ba_2YCu_3O_{6+x}$ Films Using the "BaF_2" Conversion Process, Advances in X-ray Diffraction, **46** 257-263 (2002).
69. R. Klein, L.P. Cook, and W. Wong-Ng, "Enthalpies of Formation of the Strontium Plumbates $SrPbO_3$ and Sr_2PbO_4 from Solution Calorimetry and Knudsen Effusion Thermogravimetry," J. Chemical Thermodynamics, **34** 2083-2092 (2002).
68. W.Y. Ching, Y.N. Xu, L. Ouyang and W. Wong-Ng "Comparative Study of the Electronic

Structure of Ternary Superconductors MoRuP and ZrRuP in the Orthorhombic and Hexagonal Phases, " J. Appl Phys., **93** (10) 8209-8211 (2003).

67. W. Wong-Ng, J. Suh and L.P. Cook, "Subsolidus Phase Relationships of the $BaO-Y_2O_3-CuO_x$ System Under Carbonate-Free Conditions at p_{O2} = 100 Pa and at p_{O2}= 21 kPa," Physica C, **377** 107-113 (2002).
66. W. Wong-Ng, J.A. Kaduk, and J. Dillingham, "Crystal Structures and Reference Diffraction patterns of $BaSrR_4O_8$," Powd. Diffr. **17** (No.3) 202 (2002).
65. J. Dillingham, W. Wong-Ng, I. Levin, "Phase Equilibria of the $SrO-Yb_2O_3-CuO_x$ System", Int. J. Inorg. Mater., **3** 569 (2001).
64. W. Wong-Ng, Q. Huang, I. Levin, J.A. Kaduk, J. Dillingham, T. Haugan, J. Suh, and L.P Cook, "Crystal Chemistry and Phase Equilibria of Selected $SrO-R_2O_3-CuO_x$ and Related Systems, R= Lanthanides and yttrium," Int. J. Inorg. Mater., **3** 1283 (2001).
63. Haugan, T., Wong-Ng, W., Cook, L.P., Brow, H.J., Swartzendruber, L., Shaw, T.J., "Flux pinning of $Bi_2Sr_2CaCu_2O_{8+x}$/Ag superconductors utilizing $(Sr,Ca)_{14}Cu_{24}O_{41}$, nanophase Al_2O_3 and Au particles", Physica C **335** (1-4) 129-133 (2000).
62. Wong-Ng, W., Cook, L.P., Greenwood, W., Kearsley, A., "Effect of Ag on the Primary Phase Field of High T_c (Bi,Pb)-2223 Superconductor", J. Mater. Res., **15** (2) 296-305 (2000).
61. Wong-Ng, W., Dillingham, J., and Cook, L.P., "Phase Equilibria of the $SrO-Ho_2O_3-CuO_x$ System", J. Solid State Chem., **149** 333-337 (2000).
60. W. Wong-Ng, J.A. Kaduk, Q. Huang, R.S. Roth, "Crystal Structure of Monoclinic Perovskite $Sr_{3.94}Ca_{1.31}Bi_{2.7}O_{12}$", Powd. Diffr., **15**(4) 227 (2000).
59. W. Wong-Ng, L.P. Cook, A. Kearsley, and A. Roosen, Role of melting equilibria in the Processing of high T_c Superconductors in the BSCCO system, Physica C **335** (1-4) 120-124 (2000).
58. W. Wong-Ng, J. P. Cline, L. P. Cook, and W. Greenwood**,** X-ray characterization of Compounds in the SrO-PbO system, Adv. X-Ray Anal., **42** 355-365 (2000).
57. W. Wong-Ng, M. Melamud, and L. Bennett, Local environments of three forms of $Ba_2YCu_3O_{6+x}$, Physica C **322** 177 (1999).
56. W. Wong-Ng, L.P. Cook, W. Greenwood, A. Kearsley, and C. Lawrence, Primary phase field of the Pb-doped 2223 high T_c superconductor in the (Bi,Pb)-Sr-Ca-Cu-O system, J. Res. Natl. Inst. Stand. Technol., **104** 277 (1999).
55. W. Wong-Ng, L.P. Cook, and W. Greenwood, Effect of P_{O2} and Ag on the phase formation of the Pb-2223 superconductor, J. Mater. Res. **14**(5) 1695 (1998).
54. W. Wong-Ng and L.P. Cook, Liquidus diagram of the Ba-Y-Cu-O system in the vicinity of the $Ba_2YCu_3O_{6+x}$ phase field, J. Res. Natl. Inst. Stand. Technol. **103**, 379 (1998).
53. W. Wong-Ng and L.P. Cook, Melting equilibria of the Bi-Sr-Ca-Cu-O (BSCCO) system in air. I. The primary crystallization phase field of the 2212 phase and the effect of Ag addition, J. Am. Ceram. Soc. **81**(7), 1829 (1998).
52. C. Park, W. Wong-Ng, L.P. Cook, R.L. Snyder, P.V.P.S.S. Sastry, and A.R. West, Melting investigation of $Bi_2Sr_{1.9}Ca_{2.1}Cu_3O_{10+x}$ by high temperature x-ray diffraction and quenching, Physica C **304**, 265 (1998).
51. W. Wong-Ng, J. Kaduk and W. Greenwood, Crystal structure and x-ray diffraction patterns for solid solution of $Sr_{4-x}Ca_xPb_2O_8$ (x=1,2,3), Powder Diffr. **13** (4), 232 (1998).
50. W. Wong- Ng, B. Toby and W. Greenwood, Crystallographic studies of BaR_2ZnO_5 (R=La, Nd, Dy, Ho, and Y), Powder Diffr. **13** (3), 144 (1998).
49. W. Wong-Ng, L.P. Cook, and W. Greenwood, Melting of $Sr_{14}Cu_{24}O_{41}$ at oxygen pressures of 0.0075, 0.021, and 0.1 MPa, Physcia C **299**, 9 (1998).
48. W. Wong-Ng, L.P. Cook, F. Jiang, W. Greenwood, U. Balachandran, and M. Lanagan, Subsolidus phase equilibria of the high T_c Pb-2223 superconductor in the (Bi,Pb)-Sr-Ca-Cu-O system, J. Mater. Res. **12** (11) 2855 (1997).
47. B.W. Lee, L.P. Cook, P.K. Schenck, W. Wong-Ng, C.K. Chiang, P.S. Brody, and K.W. Bennett, Processing and characterization of composition-modified $PbTiO_3$ thin films prepared by pulsed laser deposition, J. Mater. Res. **12** (2), 509 (1997).

46. W. Wong-Ng, E.J. Gonzalez, G.J, Piermarini, C. Wolters, and J. Schwartz, X-ray diffraction study of high T_c materials under high pressures, Adv. X-Ray Anal. (CD-ROM format), **40** (1996).
45. H.M. Seyoum, M. Melamud, W. Wong-Ng, L.H. Bennett, L.J. Swartzendruber, L.P. Cook and H.J. Brown, Effect of barium cuprate on high temperature superconductors, J. Appl. Phys. **81** (8), 4244 (1997).
44. E.J. Gonzalez, W. Wong-Ng, G.J. Piermarini, C. Wolters, and J. Schwartz, X-ray diffraction study of $HgBa_2CuO_{4+}$ at high pressures, Powd. Diff., **11**(1) 9 (1997).
43. W. Wong-Ng, R.S. Roth, and C.J. Rawn, Preparation and structural investigation of $Bi_{16}(Sr,Ca)_{14}O_{38}$, J. Am. Ceram. Soc. **80** (2), 324 (1997).
42. W. Wong-Ng, L.P. Cook, and F. Jiang, X-ray characterization of phase equilibria of the Raveau phase and 2212 phases in the Bi-Sr-Ca-Cu-O system, Adv. X-Ray Anal., **39**, 731 (1997).
41. W. Wong-Ng, L.P. Cook, W. Greenwood, and F Jiang, Subsolidus and melting relationship of the PbO_x-CaO-CuO system in air, Physica C **279**, 31 (1997).
40. W. Wong-Ng, F. Jiang, and L. P. Cook, Subsolidus and melting study of the Bi_2O_3-PbO_x-CuO system in air, J. Appl. Supercond. **4** (9), 385 (1996).
39. W. Wong-Ng, L.P. Cook, and F. Jiang, Phase relationships of the Pb-Sr-Ca-O system in air, Physica C **272**, 87 (1996).
38. W. Wong-Ng, R. L. Snyder, C. Park, E. Antipov, and W. F. McClune, The ICDD/PDF superconductor miniFile (SC), Powder Diffr. **12** (1), 13 (1996).
37. W. Wong-Ng and L.P. Cook, Cation non-stoichiometry of the $BaCuO_{2+x}$ phase, Physica C **273** (1&2) 135 (1996).
36. W. Wong-Ng, G. Piermarini, and M. Gallas, X-ray diffraction study of $BaLu_2CuO_5$ and $BaNd_2CuO_5$ at high pressures, Powder Diffr. **11**(4), 305 (1996).
35. L.P. Cook, W. Wong-Ng, and M. Paranthaman, Melting and vaporization of the 1223 phase in the system (Tl-Pb-Ba-Sr-Ca-Cu-O), J. Res. Natl. Instit. Stand. Technol. **5**, 675 (1996).
34. W. Wong-Ng, F. Jiang, and G.J. McCarthy, Powder x-ray diffraction characterization of $Bi_{14}(Sr,Ca)_{12}O_{33}$ solid solution, Powder Diffr. **11**, 268 (1996).
33. W. Wong-Ng, R.S. Cava, J.J. Krajewski, and W.F. Peck, Jr., X-ray diffraction pattern of $LuNi_2B_2C$ and YNi_2B_2C, Powder Diffr. **11** (2), 88 (1996).
32. W. Wong-Ng, G. Piermarini, and M. Gallas, X-ray diffraction study of $BaNd_2CuO_5$ under high pressure, Adv. X-Ray Anal. **38**, 741 (1995).
31. M.D. Hill, J.E. Blendell, C.K. Chiang, L.H. Bennett, J.J. Ritter, L. Chacon, J.F. Kelly, and W. Wong-Ng, Effect of Sm_2BaCuO_5 on the properties of sintered (Bulk) $YBa_2Cu_3O_{6+x}$, Physica C **251**, 361 (1995).
30. W. Wong-Ng, L. P. Cook, Eutectic melting study in the system BaO- Y_2O_3-CuO_x in air, J. Am. Ceram. Soc. **77** (7), 1883 (1994).
29. W. Wong-Ng and R. S. Roth, Single crystal structural investigation of BaO_2, Physica **C 233**, 97 (1994).
28. W. Wong-Ng and S.W. Freiman, High T_c superconducting Bi-Sr-Ca-Cu-O glass ceramics - A review, App. Supercond. **2** (3/4), 163 (1994).
27. W. Wong-Ng and L.P. Cook, A review of the crystallography and crystal chemistry of compounds in the BaO-CuO_x systems, Powder Diffr. **9** (4), 280 (1994).
26. H.M. Seyoum, A.M. Ritano, L.H. Bennett, and W. Wong-Ng, Reentrant superconductivity in a multiphase Tl-Ca-Ba-Cu-O system, Phys. Lett. A **190**, 483 (1994).
25. W. Wong-Ng, Structures and x-ray patterns of compounds in the Sr-Nd-Cu-O system, Powder Diffr. **10** (1), 56 (1994).
24. I. N. Sora, W. Wong-Ng, R. S. Roth, C. J. Rawn, and B. P. Burton, X-ray and neutron diffraction study of $CaBi_2O_4$, J. Solid State Chem. **109,** 251 (1994).
23. W. Wong-Ng, L.P. Cook, B. Paretzkin, M.D. Hill, and J.K. Stalick, Crystal chemistry and phase equilibrium studies of the BaO-$\frac{1}{2}R_2O_3$-CuO_x systems in air, VI. R = Neodymium, J. Am. Ceram. Soc. **97** (9), 2354 (1994).
22. W. Wong-Ng, C.K. Chiang, S.W. Freiman, L.P. Cook, and M.D. Hill, Phase formation of high T_c superconducting phases in the Bi-Pb-Sr-Ca-Cu oxides, Ceram. Bull. 1261 (1992).

21. W. Wong-Ng, The ICDD/PDF coverage of the high T_c superconductor and related compounds in the A-R-Cu-O systems (A=Ba, Sr and Ca, and R=lanthanides and Y), Powder Diffr. **7** (3), 125 (1992).
20. W. Wong-Ng and L. P. Cook, Oxidation/reduction melting reactions in the system BaO-Y_2O_3- CuO_x. II. Powder X-ray Analysis, Adv. X-Ray Anal. **35**, 633 (1992).
19. M.D. Hill, W. Wong-Ng, C.K. Chiang, E.R. Fuller, Jr., B. Paretzkin, J.E. Blendell, E. Lagergren and R. Kacker, Effect of composition on superconducting properties in the system Ba-Y-Gd-O, J. Am. Ceram. Soc. **75** (9), 2390 (1992).
18. E. Etz, T. Schroeder and W. Wong-Ng, Microbeam characterization of impurity phases in ceramic and thin film samples of the Y-Ba-Cu-O high-T_c superconductors, Microbeam Analy. 113 (1991).
17. R. Kacker, E. Lagergren, M. Hill, W. Wong-Ng, C.K. Chiang, and E. Fuller, An efficient experiment to study superconducting ceramics, Commun. Statist. - Theory Meth. **20** (2), 441 (1991).
16. W. Wong-Ng and B. Paretzkin, Crystal chemistry and phase equilibria studies of the BaO-R_2O_3- CuO systems. II. X-ray characterization and standard patterns of BaR_2O_4, R=lanthanides, Powder Diffr. **6** (4), 187 (1991).
15. E.S. Etz, T.D. Schroeder, and W. Wong-Ng, Raman and fluorescence spectra observed in laser microprobe measurements of several compositions in the Ln-Ba-Cu-O system, Microbeam Anal. 243 (1990).
14. H.M. Seyoum, J.M. Habib, L.H. Bennett, W. Wong-Ng, A.J. Shapiro, and L.J. Swartzendruber, Superconducting properties of $Bi_{2-x-y}Pb_xSn_ySr_2Ca_2Cu_3O_z$, Supercond. Sci.Technol. **3**, 616 (1990).
13. J. Stalick and W. Wong-Ng, Neutron diffraction study of the "Brown Phase" $BaNd_2CuO_5$, Mater. Lett. **9** (10), 401 (1990).
12. W. Wong-Ng, L.P. Cook and B. Paretzkin, Crystal chemistry and phase equilibria studies of the BaO-R_2O_3-CuO systems, Adv. in X-Ray Anal. 453 (1990).
11. W. Wong-Ng, B. Paretzkin, and E. Fuller, Jr., Crystal chemistry and phase equilibria studies of the BaO-R_2O_3-CuO systems. IV. Subsolidus phase relationships near the CuO-rich regions, J. Solid State Chem. **84**, 117 (1990).
10. W. Wong-Ng, C.K. Chiang, L.P. Cook, and B. Paretzkin, Crystal chemistry and phase equilibria studies of the BaO-R_2O_3-CuO systems. III. X-ray powder characterization of $Ba_3R_3Cu_6O_{14+x}$, Powder Diffr. **5** (1) 1 (1990).
9. W. Wong-Ng, D. Kaiser, F. Gayle, F. Fronzcek and S.F. Watkins, X-ray crystallographic studies of a thermomechanically detwinned single crystal of $Ba_2YCu_3O_{6+x}$, Phys. Rev. B **41**, 4220 (1990).
8. C.K. Chiang, S.W. Frieman, W. Wong-Ng, L.P. Cook, R.D. Shull, and A.J. Shapiro, Preparation of Bi-Pb-Sr-Ca-Cu-O superconducting composites using glass technology, Physica C **162-164**, 901 (1989).
7. W. Wong-Ng, M.A. Kuchinski, H.F. McMurdie, and B. Paretzkin, Crystal chemistry and phase equilibrium studies of BaO-1/2R_2O_3-CuO. X-ray powder characterization of BaR_2CuO_5 and related compounds, Powder Diffr. **4** (1), 2 (1989).
6. E.S. Etz, W. Wong-Ng, J.E. Blendell, and C.K. Chiang, Micro-Raman spectroscopy of high-T_c superconductors in the Y-Ba-Cu-O system, Microbeam Anal. 187 (1988).
5. R.S. Roth, C.J. Rawn, J.D. Whitler, C.K. Chiang, and W. Wong-Ng, Phase equilibria and crystal chemistry in the quaternary system Ba-Sr-Y-Cu-O in Air, J. Am. Ceram. Soc. **72** (3), 395 (1988).
4. Y.M. Zhang, W. Wong-Ng, C.R. Hubbard, B. Morrison, and S.W. Freiman, X-ray powder diffraction profile studies on $Ba_2YCu_3O_{7.0}$ and $Ba_2YCu_3O_{6.8}$, Physica C **152**, 103 (1988).
3. W. Wong-Ng, L.P. Cook, C.K. Chiang, L. Swartzendruber, L.H. Bennett, J.E. Blendell, and D. Minor, Structural phase transition study of $Ba_2YCu_3O_{6+x}$ in Air, J. Mater. Res. **3** (5), 832 (1988).
2. W. Wong-Ng, R.S. Roth, F. Beech, and K.L. Davis, X-ray study of the BaO-Y_2O_3-CuO_x system, Adv. X-Ray Anal. **31**, 359 (1988).
1. W. Wong-Ng, K. Davis, and R.S. Roth, X-ray characterization of 2BaO:CuO, J. Am. Ceram. Soc. **71**(2), C64 (1988).

(2) Proceeding Papers

39. W. Wong-Ng, L.P. Cook, P. Schenck, I. Levin, Z. Yang, Q. Huang, and J. Frank, "Chemical

Interactions and Reaction Kinetics of the $Ba_2YCu_3O_{6+x}$ /CeO_2 System," Proceedings of the PACRIM meeting, sponsored by ACerS, Maui, Hawaii, September, 2005; Ceramic Transactions **191** 83-98 (2006).

38. W. Wong-Ng, I. Levin, R. Feenstra, M. Vaudin, and L.P. Cook, "Phase Formation and Texture of $Ba_2YCu_3O_{6+x}$ Films Using the "BaF_2 Converison Process" Proceedings of symposium *Epitaxial Growth of Functional Oxides*, Electrochemical Society/American Ceramic Society Annual meeting, October 12-17, 2003, Orlando, FL; published by The Electrochemical Society, 2005. ISBN: 1-56677-452-7.
37. W. Wong-Ng, L.P. Cook and J. Suh, "Phase Relations in the Ba-R-Cu-O (R = Nd, Sm, Eu, Gd, Ho, Y, and Er) Systems Prepared Under Atmospherically-Controlled Conditions", *Proceedings of Frontiers in Superconducting Materials-New Materials and Applications*, Materials Research Society annual meeting, Dec. 1-5, 2003, Boston, MA, Materials Research Society, EE8.27 (2003).
36. W. Wong-Ng, L.P. Cook, I. Levin, M. Vaudin, J. Suh, and R. Feenstra, Coated Conductors: Phase Relations in the Ba-Y-Cu-F-O-H System, *Proceedings of Frontiers in Superconducting Materials-New Materials and Applications*, Materials Research Society annual meeting, Dec. 1-5, 2003, Boston, MA, Materials Research Society, EE2.9 (2003).
35. W. Wong-Ng, L.P. Cook, and J. Suh, Phase Relation in the BaO-R_2O_3-CuO_x SYSTEMS, *High Temperature Superconductor Processing, Ceramics Transaction*, 13. R. Meng, A. Goyal, W. Wong-Ng, *Fabrication of Long-Length & Bulk HTS Conductors*, Ceramic Transactions, **149**, the 105th annual meeting of the American Ceramic Society (ACerS), April 27-30, 2003, Nashsville, TN, pp. 163.
34. T. J. Haugan, J. M. Evans, J. C. Tolliver, I. Maartense, P. N. Barnes, W. Wong-Ng, L.P. Cook, and R. Shull, "Flux Pinning and Properties of Solid Solution $(Y,Nd)_{1+x}Ba_{2-x}Cu_3O_{7-\delta}$ Superconductors processed in Air and Partial Oxygen Atmospheres", *Fabrication of Long-Length & Bulk HTS Conductors*, Ceramic Transactions, **149**, R. Meng, A. Goyal, W. Wong-Ng, eds., the 105th annual meeting of the American Ceramic Society (ACerS), April 27-30, 2003, Nashsville, TN, pp. 151 (2004).
33. Mi-Hye Jang, W.Wong-Ng, R. Shull, L.P.Cook, and DeaSik Suh "Flux Loss measurements of Ag-sheathed Bi-2223 Tapes**,"** American Ceramic Society, Nashville, TN (2003). *Fabrication of Long-Length & Bulk HTS Conductors*, Ceramic Transactions, **149**, R. Meng, A. Goyal, W. Wong-Ng, eds., the 105th annual meeting of the American Ceramic Society (ACerS), April 27-30, 2003, Nashsville, TN, pp. 83 (2004).
32. W. Wong-Ng, L.P. Cook and J. Suh, "Melting Equilibria of the BaF_2-CuO_x System" ed. by A. Goyal et. at. Transaction Volume **140**, *High Temperature Superconductor Processing*, Electronics Division Focus Session at the 2002 ACerS annual meeting, St. Louis, MO, April 29 to May 1, 2002, pp. 385-397 (2003).
31. T.J. Haugan, M.E. Fowler, J.C. Tolliver, P.N. Barnes, W. Wong-Ng, and L.P. Cook, " Flux pinning and properties of solid-solution $(Y,Nd)_{1+x}Ba_{2-x}Cu_3O_{7-z}$ superconductors, ed. by A. Goyal et. at. Transaction Volume **140**, *High Temperature Superconductor Processing*, Electronics Division Focus Session at the 2002 ACerS annual meeting, St. Louis, MO, April 29 to May 1, 2002, pp. 299-308 (2003).
30. W. Wong-Ng ,L.P. Cook, J. Suh, I. Levin, M. Vaudin, R. Feenstra, and J.P. Cline, Phase Relationships and Phase Formation in the System BaF_2-BaO-Y_2O_3-CuO_x-H_2O, Proceeding Vol. **689**, Paranthaman et al eds, *Materials for High-Temperature Superconductor Technologies*, Materials Research SocietyAnnual Meeting, Boston, MA, published by MRS, Warrendale, PA, pp. 337 (2002).
29. T. Haugan, W. Wong-Ng, L.P. Cook, R.G. Geyer, H.J. Brown, L. Swartzendruber, and J. Kaduk, "Development of Low Cost $(Sr,Ca)_3Al_2O_6$ Dielectrics for $Bi_2Sr_2CaCu_2O_{8+\delta}$ Applications," IEEE Transactions on *Applied Superconductivity*, Part III, **11** (No. 1) pp. 3305 (2001).
28. L.P. Cook, W. Wong-Ng, and J. Suh, "DTA/TGA study of eutectic melting in the system BaF_2-BaO-Y_2O_3-CuO_x-H_2O", MRS Proceeding, **659**, Eds. B. Balachandran, H.C. Freyhardt, T. Izumi, and D.C. Larbalestier, *High-Temperature Superconductors-Crystal Chemistry, Processing and Properties*, II 4.8, (2001).
27. Cook, L.P., and Wong-Ng, W., "Phase equilibria of Ag with (Bi,Pb)-Sr-Ca-Cu-O (BSCCO) oxides and with Pb-2223 under various oxygen pressures", *Pervoskite Oxides for Electronic Energy Conversion and Energy Efficiency Applications, Ceramic Transactions* **104**, Eds. W. Wong-Ng, T. Holesinger, G.N. Riley and R. Guo, Published by ACerS, Westerville, OH 43086, pp. 87-95 (2000).

26. Haugan, T., Wong-Ng, W., Cook, L.P., Swartzendruber, L., Brown, H.J., Shaw, D.T., "Flux-Pinning of $Bi_2Sr_2CaCu_2O_{8+x}$ and $Sr_2CaAl_2O_6$ Defects", *Pervoskite Oxides for Electronic Energy Conversion and Energy Efficiency Applications*, Ceramic Transactions **104**, Eds. W. Wong-Ng, T. Holesinger, G.N. Riley and R. Guo, Published by ACerS, Westerville, OH 43086, pp. 163-175 (2000).
25. Wong-Ng, W., Cook, L.P., "Melting Equilibria of the 2223 ([Bi,Pb]-Sr-Ca-Cu) High T_c Superconductor in Oxygen", *Pervoskite Oxides for Electronic Energy Conversion and Energy Efficiency Applications*, Ceramic Transactions **104**, Eds. W. Wong-Ng, T. Holesinger, G.N. Riley and R. Guo, Published by ACerS, Westerville, OH 43086, pp. 97-106 (2000).
24. W. Wong-Ng, L.P. Cook, A. Kearsley, G. Lawrence, and W. Greenwood, Phase equilibria of the (Bi,Pb)-Sr-Ca-Cu-O system pertaining to the 2212 and 2223 phases, in *High Temperature Superconductors and Novel Inorganic Materials Engineering* (MSU HTSC-V), Proceedings of the NATO sponsored international workshop, Van Tendeloo et al., eds., Kluwer Academic Publisher, Netherlands (1999), p. 63.
23. W. Wong-Ng, L.P. Cook, W. Greenwood, U. Balachandran, and M. Lanagan, Preliminary melting data on the Pb-2223 ((Bi:Pb)-Sr-Ca-Cu) phase under 7.5 % O_2, in Ceramics Transaction, Vol. **84**, *Impact of Recent Advances in Synthesis and Processing of Ceramic Superconductors***,** W. Wong-Ng, U. Balachandran and A.S. Bhalla, eds., Am. Ceram. Soc., Westerville, OH (1998), p. 71.
22. L.P. Cook and W. Wong-Ng, Pb-distribution in a five-phase (Bi,Pb)-Sr-Ca-Cu-O assemblage, in Ceramics Transaction, **84**, *Impact of Recent Advances in Synthesis and Processing of Ceramic Superconductors***,** W. Wong-Ng, U. Balachandran and A.S. Bhalla, eds., Am. Ceram. Soc., Westerville, OH (1998), p.55.
21. L. P. Cook and W. Wong-Ng, Primary crystallization volume of BSCCO 2212: applications to crystal growth and melt processing, in Ceramics Transaction, **84**, *Impact of Recent Advances in Synthesis and Processing of Ceramic Superconductors***,** W. Wong-Ng, U. Balachandran and A.S. Bhalla, eds., Am. Ceram. Soc., Westerville, OH (1998), p. 41.
20. W. Wong-Ng, L.P. Cook, F. Jiang, P.V.P.S.S. Sastry, and A.R. West, Selected phase equilibria in the Bi-Sr-Ca-Cu-O system, in *High Temperature Superconductors: Synthesis, Processing and Large Scale Applications*, U. Balachandran, P.J. McGinn, and J.S. Abell, eds., The Minerals, Metals, and Materials Soc., Warrendale, PA (1996), p. 123.
19. W. Wong-Ng and L.P. Cook, Phase equilibrium studies of high T_c superconductor cuprates, in AIChE Symp. Series 287, Vol. **88**, *Superconducting Engineering*, T.O. Mensah, ed., Am. Instit. Chem. Eng., New York (1992), p. 11.
18. N. Gokcen, W. Wong-Ng, and L. H. Bennett, Effects of oxygen on yttrium- and bismuth-type superconductors, in *High Temperature Superconducting Compounds, III. Processing and Microstructure Property Relationship*, S.H. Whang, A. Das Gupta, and E. Collings, eds., TMS-AIME, (1991), p. 419.
17. L. P. Cook, W. Wong-Ng, C. K. Chiang, and L. H. Bennett, Stoichiometric variations in the 2122 (Tl:Ca:Ba:Cu Oxide) high T_c Phase, in Ceramic Transaction, Vol. **18**, *Superconductivity in Ceramic Superconductors II*, K.M. Nair, U. Balachandran, Y-M. Chiang, and A. Bhalla, eds., Am. Ceram. Soc., Westerville, OH (1991), p. 65.
16. W. Wong-Ng and L.P. Cook, Oxidation/reduction melting equilibria in the system BaO-½Y_2O_3- CuO_x. I. Methods, in Ceramic Transaction, Vol. **18**, *Superconductivity in Ceramic Superconductors II*, K.M. Nair, U. Balachandran, Y-M. Chiang, and A. Bhalla, eds., Am. Ceram. Soc., Westerville, OH (1991), p. 73.
15. L.P. Cook, W. Wong-Ng, L. Bennett, and L. Swartzendruber, Phase equilibria in the system Tl-Ca- Ba-Cu-O.I. Stability of the 2122 phase under conditions of oxygen annealing, in *High-Temperature Superconductors: Fundamental Properties and Novel Materials Processing*, Vol. **169,** D. Christen, J. Narayan, and L. Schneemeyer, eds., Mater. Res. Soc., Pittsburgh, PA (1990), p. 137.
14. W. Wong-Ng, C.K. Chiang, S.W. Freiman, and L.P. Cook, X-ray characterization of the crystallization process of high-T_c superconducting oxides in the Sr-Bi-Pb-Ca-Cu-O system, in *High-Temperature Superconductors: Fundamental Properties and Novel Materials Processing*, Vol. **169,** D. Christen, J. Narayan, and L. Schneemeyer, eds., Mater. Res. Soc., Pittsburgh, PA (1990), p. 123.

13. W. Wong-Ng, L.P. Cook, B. Paretzkin, and M.D. Hill, Crystal chemistry and phase equilibrium studies of the $BaO(BaCO_3)$-R_2O_3-CuO systems. V. Melting relations in $Ba_2(Y,Nd,Eu)Cu_3O_{6+x,}$ in *High-Temperature Superconductors: Fundamental Properties and Novel Materials Processing*, Vol. **169,** D. Christen, J. Narayan, and L. Schneemeyer, eds., Mater. Res. Soc., Pittsburgh, PA (1990), p. 81.
12. B.L. Kaiser, F.W. Gayle, L.J. Swartzendruber, W. Wong-Ng, S.F. Watkins, and F.R. Fronczek, Structural and magnetic properties of untwinned $YBa_2Cu_3O_{6+x}$ single crystals, in *High-Temperature Superconductors: Fundamental Properties and Novel Materials Processing*, Vol. **169,** D. Christen, J. Narayan, and L. Schneemeyer, eds., Mater. Res. Soc., Pittsburgh, PA (1990), p. 793.
11. C.K. Chiang, W. Wong-Ng, L.P. Cook, S.W. Freiman, N.M. Huang, M. Vaudin, M.D. Hill, R.D. Shull, A.J. Shapiro, L.J. Swartzendruber, and L.H. Bennett, Processing Bi-Pb-Sr-Ca-Cu-O superconductors from the amorphous state, in *Advances in Materials Science and Application of High Temperature Superconductors*, L.H. Bennett, Y. Flom, and K. Moorjam, eds., Goddard Space Flight Center, Greenbelt, MD (1990), p. 127.
10. W. Wong-Ng, C.K. Chiang, S.W. Freiman, and L.P. Cook, Phase formation in the Pb-doped Bi-Sr-Ca-Cu-O glass ceramics, in Ceramics Transaction, Vol. **13**, K.M. Nair et al., eds., First International Ceramic Science and Technology Congress, Anaheim, California, Oct., Amer. Ceram. Soc., Westerville, OH (1989), p. 115.
9. L.P. Cook, W. Wong-Ng, C.K. Chiang, L. Bennett, and L. Swartzendruber, Effects of synthesis conditions on the formation of the 2122 (Tl:Ca:Ba:Cu) high T_c phase, in Ceramics Transaction, Vol. **13**, K.M. Nair et al., eds., First International Ceramic Science and Technology Congress, Anaheim, CA, Oct., Am. Ceram. Soc., Westerville, OH (1989), p. 329.
8. J.E. Blendell, W. Wong-Ng, C.K. Chiang, R.D. Shull, and E.R. Fuller, Jr., Phase composition and superconducting properties of the high T_c ceramic materials $Ba_{2-z}R_{1+z}Cu_3O_{6+x}$, in *High Temperature Superconducting Compounds: Processing & Related Properties*, S.H. Whang and A. DasGupta, eds., The Minerals, Metals & Mater. Soc., Warrendale, PA (1989), p. 193.
7. W. Wong-Ng, L.P. Cook, C.K. Chiang, M.D. Vaudin, D.L. Kaiser, F. Beech, L.J. Swartzen-Druber, L.J. Bennett, and E.R. Fuller, Jr., Structural phase transition studies of $Ba_2RCu_3O_{6+x}$ in air, in *High Temperature Superconducting Compounds: Processing & Related Properties*, S.H. Whang and A. DasGupta, eds., The Minerals, Metals & Mater. Soc., Warrendale, PA (1989), p. 553.
6. W. Wong-Ng, L.P. Cook, C.K. Chiang, L. Swartzendruber, and L.H. Bennett, Structural phase transition of $Ba_2RCu_3O_{6+x}$ high T_c superconducting materials, in Adv. Ceram. Mater., *Ceramic Superconductor II*, ed., M.F., Yan, Amer. Ceram. Soc., Westerville, OH (1988), p. 27.
4. L. P. Cook, C.K. Chaing, and W. Wong-Ng, Thermal analysis of $Ba_2YCu_3O_{7-x}$ at 700-1000 °C in air, in Adv. Ceram. Mater., Vol. **2**(3B), *Ceramic Superconductors*, W. J. Smothers, ed., Am. Ceram. Soc., Westerville, OH (1987), p. 656.
3. W. Wong-Ng, L.P. Cook, C.K. Chiang, L.H. Bennett, and L. Swartzendruber, X-ray studies of helium-quenched $Ba_2YCu_3O_{7-x}$, in Adv. Ceram. Mater., Vol. **2**(3B), *Ceramic Superconductors*, W. J. Smothers, ed., Am. Ceram. Soc., Westerville, OH (1987), p. 624.
2. S. Block, G. Pieramini, R. Munro, and W. Wong-Ng, The bulk modulus and Young's modulus of the superconductor $Ba_2Cu_3YO_7$, in Adv. Ceram. Mater., Vol. **2**(3B), *Ceramic Superconductors*, W. J. Smothers, ed., Am. Ceram. Soc., Westerville, OH (1987), p. 601.
1. W. Wong-Ng, R.S. Roth, L.J. Swartzendruber, L.H. Bennett, C.K. Chiang, F. Beech, and C.R. Hubbard, X-ray powder characterization of $Ba_2YCu_3O_{7-x}$, in Adv. Ceram. Mater., Vol. **2**(3B), *Ceramic Superconductors*, W. J. Smothers, ed., Am. Ceram. Soc., Westerville, OH (1987), p. 565.

(3) Book Chapters

3. W. Wong-Ng, Phase Diagrams of High Temperature Superconductors, Handbook of Superconductivity**,** C. Poole, ed., Academic Press, pp. 625-685, 2001.
2. W. Wong-Ng, Crystal Structures and Crystal Chemistry of Bi-Containing Compounds in the Bi-Sr-Ca-Cu-O System, *in* Studies of High Temperature Superconductors (Advances in Research and Applications), Vol. **25,** Chemistry and Related Aspects of High Temperature Superconductors, A. Narlikar, ed., Nova Science Publishers Inc., Commack, NY (1997), pp. 95-133.
1. W. Wong-Ng and S.W. Freiman, Superconducting Phase Formation in Bi(Pb)-Sr-Ca-Ca-Cu-O Glasses: A Review, in Superconducting Glass-Ceramics in Bi-Sr-Ca-Cu-O: Fabrication and its Application, Y. Abe, ed., World Scientific Publishing Co., Ltd., Singapore (1997), pp. 1-15.

(4) Books/Proceedings (as Co-editor)

8. M. Paranthaman, V. Selvamanickam,, K. Matsumoto, L. Gianna, W. Zhang, A. Goyal, and W. Wong-Ng, High Temperature Superconductor Wires and Tapes (Special issue of Journal of Electronic Materials **36**(10), 2007; MS&T 2006 Proceedings, Oct 15-19, 2006, Duke Energy Center, Cincinnati, OH
7. L.P. Cook, S. Mukhopadhyay, O. Leonte, D. Misra, W. Wong-Ng, and K. Sundaram, editors, Interfaces in Electronic Materials (Proceedings Volume) PV 2003-31, Electrochem. Soc., Pennington, NJ, 334pp (2006)
6. L.P. Cook, S. I. Tanaka, W. Wong-Ng, and R. Schwartz, "Interfaces in Heterogeneous Ceramic Systems," Ceramic Transactions **169**, the 106th annual meeting of the American Ceramic Society (ACerS), April 18-21, 2004, Indianapolis, IN. (2005).
5. W. Wong-Ng, A. Goyal, R. Huo, and A. Bhalla, Synthesis, *Properties, and Crystal Chemistry of Perovskite-Based Materials*, Ceramic Transactions **169**, the 106th annual meeting of the American Ceramic Society (ACerS), April 18-21, 2004, Indianapolis, IN. (2005).
4. C.L. Claeys, W. Wong-Ng, and K.M. Nair, Proceedings of Electrochemical Society/American Ceramic Society Annual meeting on *Low Temperature Electronics and Low-temperature Cofired Ceramics Based Electronic Devices*, October 12-17, 2003, Orlando, FL.
3. A. Goyal, Y. Kuo, O. Leonte, and W. Wong-Ng, *Epitaxial Growth of Functional Oxides*, Electrochemical Society/American Ceramic Society Annual meeting, October 12-17, 2003, Orlando, FL, published by The Electrochemical Society, 2005. ISBN: 1-56677-452-7.
2. R. Meng, A. Goyal, W. Wong-Ng, *Fabrication of Long-Length & Bulk HTS Conductors*, Ceramic Transactions, 149, the 105th annual meeting of the American Ceramic Society (ACerS), April 27-30, 2003, Nashsville, TN.
1. A. Goyal, W. Wong-Ng, M. Murakami, and J. Driscoll, *High Temperature Superconductor Processing*, Ceramics Transaction, **140**, American Ceramic Society, Westerville, OH (2003). (American Ceramic Society annual meeting, St. Louis, MO, April 29 – May 1, 2002).

A phase relation study of Ba–Y–Cu–O coated-conductor films using the combinatorial approach

W. Wong-Ng,[1,a)] M. Otani,[1] I. Levin,[1] P. Schenck,[1] Z. Yang,[1] G. Liu,[1] L. P. Cook,[1] R. Feenstra,[2] W. Zhang,[3] and M. W. Rupich[3]
[1]*Ceramics Division, Materials Science and Engineering Laboratory, National Institute of Standards and Technology, Gaithersburg, Maryland 20899, USA*
[2]*Materials Science and Technology Division, Oak Ridge National Laboratory, Oak Ridge, Tennessee 37831, USA*
[3]*American Superconductor Corporation, Westborough, Massachusetts 01581, USA*

(Received 28 December 2008; accepted 16 March 2009; published online 30 April 2009)

Phase relationships in bulk and thin film Ba–Y–Cu–O high-T_c superconductor system were determined at processing conditions relevant for industrial production of coated conductors. Our results demonstrated that the absence of BaY_2CuO_5 (which has a critical effect on flux pinning) at 735 °C—a typical temperature employed in production of coated conductors—in thin films processed *in situ* from the BaF_2 precursor is caused by the sluggish reaction kinetics rather than by the presence of fluorine in the system. Thermodynamic calculations combined with annealing experiments confirmed that BaY_2CuO_5 is thermodynamically stable but forms at temperatures higher than 735 °C. © *2009 American Institute of Physics*. [DOI: 10.1063/1.3127222]

Since the discovery of high-T_c superconducting oxides in 1986,[1] extensive research has led to a variety of prototype applications. In particular, the low-cost second generation high-T_c wire and tape (coated conductor) technology[2–5] is promising for large-scale commercialization of superconductors. The coated-conductor materials are based on $Ba_2YCu_3O_{6+x}$ (Y-213) and its lanthanide variants, $Ba_2RCu_3O_{6+x}$ (R-213, R=lanthanides).[6,7] Major techniques for processing biaxially textured templates include the rolling-assisted biaxially textured substrate (so-called RABiTS)[2,3] and ion-beam-assisted deposition[4,5] methods. The BaF_2 *ex situ* process is among the leading candidates for producing long-length tapes with high performance.[8–11] Information on phase relationships in the Ba–Y–Cu–O system is critical for manufacturing of coated conductors, particularly for flux pinning applications.

Previously, we used *in situ* high-temperature x-ray diffraction (HTXRD)[11,12] to establish phase relations in high-T_c superconductor Ba–Y–Cu–O and Ba-R-Cu–O films grown on $SrTiO_3$ via the "*ex situ* BaF_2" process (e-beam evaporation and spin coating techniques).[11,12] Phase assemblages for both $BaO–Y_2O_3–CuO_x$ and $BaO\text{-}R_2O_3–CuO_x$ systems in thin films at typical processing conditions (T=735 to 750 °C, $p_{O_2} \approx 100$ Pa) were found to be different from those reported for the bulk at 810 °C and $p_{O_2} \approx 100$ Pa. The "brown-phase" structure $BaNd_2CuO_5$[13] readily formed in thin films, whereas the "green phases" BaY_2CuO_5, $BaGd_2CuO_5$, and $Ba(Nd_{1/3}Eu_{1/3}Gd_{1/3})_2CuO_5$[14] have never been observed. In the absence of the green phase, the stability field of $Ba_2YCu_3O_{6+x}$ in thin films expands considerably compared to the bulk system, yielding tie-lines $Ba_2YCu_3O_{6+x}–Y_2O_3$ and $Ba_2YCu_3O_{6+x}–Y_2Cu_2O_5$. Similarly, in thin films a tie-line is found between $Ba_2GdCu_3O_{6+x}$ and Gd_2O_3 in the BaO-poor region of the Ba–Gd–Cu–O diagram, whereas this tie-line is absent in the bulk.[14] These stability considerations are important and could affect the type of pinning centers present in thin films relative to bulk.[15]

The factors that could contribute to the observed differences in thin film and bulk phase equilibria include presence of fluorine (due to the nature of the BaF_2 process), different processing conditions, strain, interfacial reactions, and texture. In the present study, we used compositional spreads (combinatorial libraries) deposited on rolling-assisted biaxially textured substrates (RABiTS) and polycrystalline $SrTiO_3$ (on Si substrates) to identify the principal factors that control phase assemblages in thin films. RABiTS consisted of the metal-alloy substrate (from 50 to 75 μm) followed by layers of Y_2O_3 (≈75 nm), yttrium-stabilized ZrO_2 (≈75 nm), and CeO_2 (≈75 nm). $SrTiO_3$-coated substrates were prepared by depositing layer of polycrystalline $SrTiO_3$ (≈0.5 μm) on commercial 3 in. Si substrates.[16] Compositional spreads were prepared by pulsed laser deposition (PLD) using a KrF excimer laser (wavelength of 248 nm) and ceramic Y_2O_3, CuO, and $BaCuO_2$ as targets. $BaCuO_2$ was prepared from a stoichiometric mixture of $BaCO_3$ and CuO using conventional solid-state synthesis at temperatures between 850 and 950 °C in air with intermediate grindings. The CuO target was prepared by sintering CuO powder in air at 1000 °C for 5 days. A single deposition cycle involved sequential laser ablation of the three targets, while the substrate was rotated by 120° between the ablations. This process was repeated hundreds of times to achieve thicknesses of ≈200 nm.[17] The deposition was conducted at two substrate temperatures of 550 and 700 °C (the maximum temperature attainable in our deposition system).

Phase assemblages were determined using XRD in a Bruker D8 diffractometer[18] equipped with a submillimeter beam capability, an *XYZ* translation stage, and an area detector. This instrument enables high-throughput, spatially resolved characterization of combinatorial libraries. The resulted phases on the PLD-fabricated compositional spreads were corroborated by *in situ* HTXRD studies of a phase formation sequence in the BaF_2-based films[9] (prepared by

a)Electronic mail: winnie.wong-ng@nist.gov.

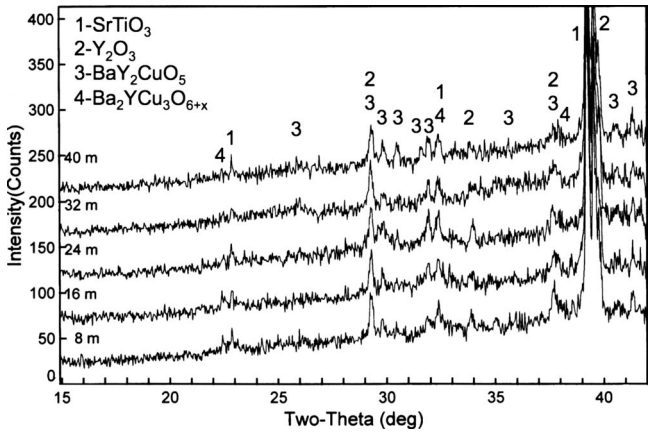

FIG. 1. HTXRD patterns of a "BaF_2" film with nominal composition of Ba:Y:Cu≈1:2:1 (green phase) as a function of time at 800 °C. It is seen that the green phase does not form at around 735 °C but begins to form at a higher temperature of 800 °C.

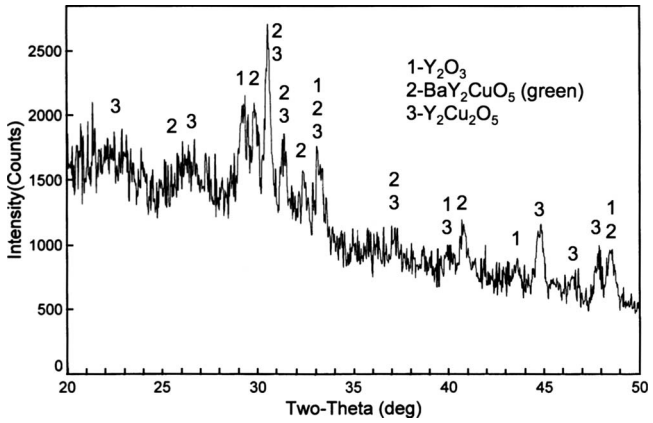

FIG. 3. XRD pattern of a typical PLD composition spread combinatorial film prepared using targets of $BaCuO_2$, Y_2O_3, and CuO on $SrTiO_3$ as a substrate (experiment at PLD≈700 °C).

e-beam evaporation) with the nominal Ba:Y:Cu ratios of 1:2:1. These studies were conducted in a θ-θ Siemens D5000 x-ray diffractometer[18] equipped with a high-temperature furnace, a position sensitive detector, and a gas flow system that enables emulation of the BaF_2-based *ex situ* processing of coated conductors. The details of the HTXRD experiments were described in our previous papers.[11,12]

A series of diffraction patterns recorded *in situ* during the conversion reaction from the BaF_2–Cu–Y films in the temperature range between 100 and 820 °C confirmed the formation of the barium oxyfluoride phase $Ba(F_{2-2x}\square_x)O_x$ (□ represents anions vacancies),[11] along with CuO, Y_2O_3, and $Ba_2YCu_3O_{6+x}$ at $T<800$ °C (Fig. 1). However, at 800 °C, the green phase crystallized and continued to grow at the expense of Y_2O_3 and CuO; concurrently, a decrease in the amount of $Ba_2YCu_3O_{6+x}$ was observed. Thus, temperatures significantly higher than those used in the conventional BaF_2-conversion processing are required to induce formation of the green phase.

Experiments conducted on the fluorine-free combinatorial libraries deposited on different substrates further proved that formation of the green phase is controlled by the reaction kinetics rather than by the presence of fluorine or other factors specific to thin films (e.g., strain, texture, etc.). In particular, XRD data on the combinatorial PLD films deposited on $SrTiO_3$ at low temperature (550 °C) displayed no sign of the green phase and instead suggested the existence of tie-lines between $Ba_2YCu_3O_{6+x}$, Y_2O_3, $Y_2Cu_2O_5$, $BaCuO_2$, and CuO, as was observed in the BaF_2-based films processed at 735 °C. Figure 2 presents a typical XRD pattern from this film, which reveals a coexistence of $Ba_2YCu_3O_{6+x}$, Y_2O_3, and $Y_2Cu_2O_5$. In contrast, XRD patterns for the film deposited at high temperature (700 °C) reveal the green phase (because of the interactions between the energetic laser plum and the sample surface, the deposition temperatures are known to correspond to higher conventional furnace temperatures). The phase regions BaY_2CuO_5–CuO_x–$Ba_2YCu_3O_{6+x}$, BaY_2CuO_5–$Y_2Cu_2O_5$–Y_2O_3 (Fig. 3), and BaY_2CuO_5–$Y_2Cu_2O_5$–CuO_x deduced from the XRD analysis of the 700 °C film match those observed in the bulk. Similar results were obtained for the films deposited on RABiTS. Figure 4 illustrates an XRD pattern from the compositional library deposited at 700 °C on RABiTS. Tie-lines between BaY_2CuO_5, CuO_x, and $Ba_2YCu_3O_{6+x}$ are verified.

A thermodynamic stability of the green phase BaY_2CuO_5 relative to the compositionally equivalent two-phase mixture of Y_2O_3 and $BaCuO_2$ can be calculated from the data by Azad *et al.*[19] according to the reaction $Y_2O_3+BaCuO_2 \rightarrow BaY_2CuO_5$ with $\Delta G(\text{kJ})=-9.1-0.0268\ T$. These estimates yield $\Delta G=-17.1$ kJ and $\Delta G=-39.2$ kJ for

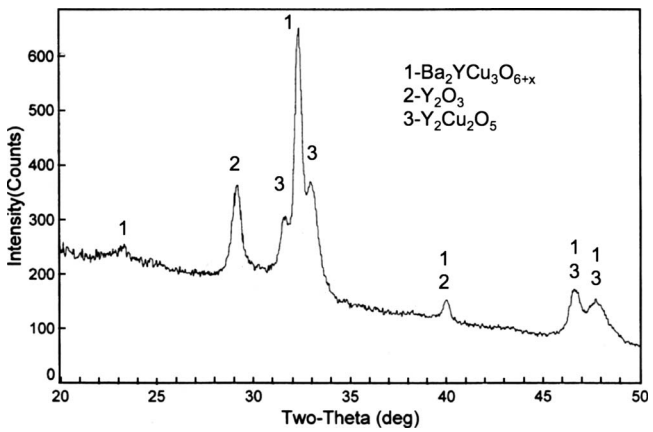

FIG. 2. XRD pattern of a typical PLD composition spread combinatorial film prepared using targets of $BaCuO_{2+x}$, Y_2O_3, and CuO on $SrTiO_3$ as a substrate (experiment at PLD≈550 °C).

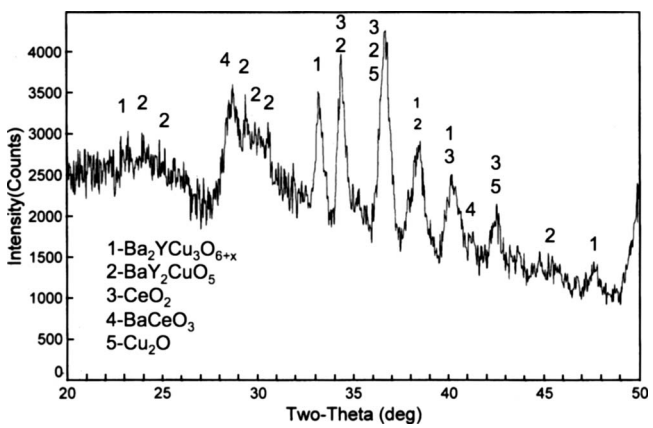

FIG. 4. XRD patterns of a typical PLD composition spread combinatorial film prepared using the targets of $BaCuO_2$, Y_2O_3, and CuO on RABiTS (experiment at PLD≈700 °C).

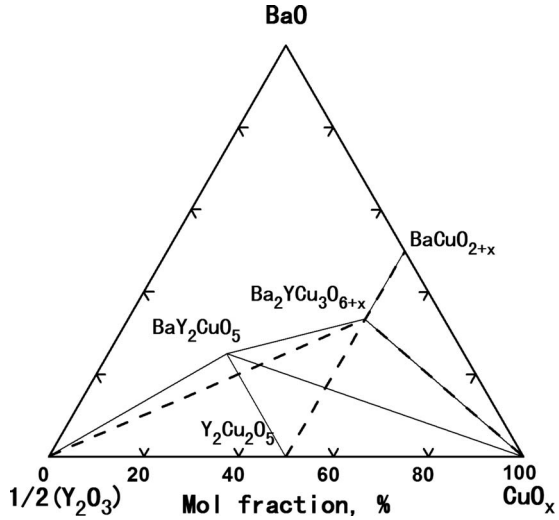

FIG. 5. Phase relationships constructed based on results from the combinatorial synthesis approach ($BaCuO_2$, Y_2O_3, and CuO as targets on substrates $SrTiO_3$ and RABiTS), HTXRD experiments on a BaF_2 film with nominal composition of Ba:Y:Cu≈1:2:1, XRD studies of the BaY_2CuO_5 bulk sample, and our previous work[20]; dotted lines ($T<800$ °C, $p_{O_2}\approx 100$ Pa) and solid lines [$T\approx 800$ to 850 °C ($p_{O_2}\approx 100$ Pa)].

298 and 1123 K, respectively. Thus, BaY_2CuO_5 is thermodynamically stable in the temperature range typically used for solid-state processing. We annealed a pressed pellet containing a mixture $Y_2O_3+BaCuO_2$ at 735 °C ($p_{O_2}\approx 100$ Pa) for 2 days with intermediate grinding; however, no reaction was observed under these conditions. Yet, further annealing at 800 °C induced partial reaction accompanied by formation of BaY_2CuO_5. Subsequent annealing at 735 °C for 3 days (with one intermediate grinding) produced no changes in the fraction of BaY_2CuO_5. These experiments along with the thermodynamic calculations suggest that the absence of BaY_2CuO_5 in the films heated at $T\leq 735$ °C could be caused by the sluggish kinetics of the reaction $Y_2O_3+BaCuO_2 \rightarrow BaY_2CuO_5$ rather than by thermodynamic reasons.

Application of the second-phase precipitation method for flux pinning in coated conductors requires accurate knowledge of the nature of phases that are compatible with $Ba_2YCu_3O_{6+x}$ under relevant processing conditions. Figure 5 summarizes phase relationships for the Ba–Y–Cu–O system as deduced from the present combinatorial experiments on compositional spreads, *in situ* XRD experiments on BaF_2-based films, XRD studies of the BaY_2CuO_5 bulk sample, and our previous work.[20] In this diagram, dotted tie-lines refer to $T<800$ °C ($p_{O_2}\approx 100$ Pa), whereas solid lines correspond to the temperature range between 800 and 850 °C ($p_{O_2}\approx 100$ Pa). Clearly, a processing temperature appears to be the most critical parameter that controls formation of the Ba–Y–Cu–O phases exhibiting flux pinning properties in both thin films and bulk materials. Therefore, for the BaF_2 process, our research suggests that temperatures above 800 °C ($p_{O_2}\approx 100$ Pa) are necessary for the formation of BaY_2CuO_5 flux pinning centers. This correlates well with the studies concerning the temperature effect on the flux pinning structures (for example, planer and columnar defects[21] and stacking fault density[22]) in $Ba_2YCu_3O_{6+x}$.

This work was partially supported by the U.S. Department of Energy.

[1] J. G. Bednorz and K. A. Müller, Z. Phys. B: Condens. Matter **64**, 189 (1986).
[2] M. W. Rupich, W. Zhang, X. Li, T. Kodenkandath, D. T. Verebelyi, U. Schoop, C. Thieme, M. Teplitsky, J. Lynch, N. Nguyen, E. Siegal, J. Scudiere, V. Maroni, K. Venkataraman, D. Miller, and T. G. Holesinger, Physica C **412–414**, 877 (2004).
[3] A. Goyal, P. Paranthaman, and U. Schoop, MRS Bull. **29**, 552 (2004).
[4] P. N. Arendt, S. R. Foltyn, L. Civale, R. F. DePaula, P. C. Dowden, J. R. Groves, T. G. Holesinger, Q. X. Jia, S. Kreiskott, L. Stan, I. Usov, H. Wang, and J. Y. Coulter, Physica C **412–414**, 795 (2004).
[5] S. R. Foltyn, E. J. Peterson, J. Y. Coulter, P. N. Arendt, Q. X. Jia, P. C. Dowden, M. P. Maley, X. D. Wu, and D. E. Peterson, J. Mater. Res. **12**, 2941 (1997).
[6] T. Goto, E. Sato, K. Watanabe, G. Nishijima, Y. Matsui, T. Nagai, and C. Tsuruta, Physica C **425**, 166 (2005).
[7] A. Hu, M. R. Koblischka, X. Yao, H. Zhou, M. Winter, U. Hartmann, and M. Murakami, Supercond. Sci. Technol. **19**, S580 (2006).
[8] S. W. Chan, B. G. Bagley, L. H. Greene, M. Giroud, W. L. Feldmann, K. R. Jenkin II, and B. J. Wilkins, Appl. Phys. Lett. **53**, 1443 (1988).
[9] R. Feenstra, T. B. Lindemer, J. D. Budai, and M. D. Galloway, J. Appl. Phys. **69**, 6569 (1991).
[10] P. C. McIntyre, M. J. Cima, and A. Roshko, J. Appl. Phys. **77**, 5263 (1995).
[11] W. Wong-Ng, I. Levin, M. Otani, M. D. Vaudin, L. P. Cook, J. Cline, R. Feenstra, and T. Holesinger, Appl. Phys. Lett. **90**, 102508 (2007).
[12] W. Wong-Ng, I. Levin, J. Ritter, L. P. Cook, G. Liu, M. Otani, M. Vaudin, C. Lucas, S. P. Diwanji, and R. Feenstra, J. Mater. Res. **23**, 2067 (2008).
[13] J. Stalick and W. Wong-Ng, Mater. Lett. **9**, 401 (1990).
[14] W. Wong-Ng, M. A. Kuchinski, H. F. McMurdie, and B. Paretzkin, Powder Diffr. **4**, 2 (1989).
[15] A. O. Ijaduola, J. R. Thompson, R. Feenstra, D. K. Christen, A. A. Capud, and X. Song, Phys. Rev. B **73**, 134502 (2006).
[16] P. K. Schenck, D. L. Kaiser, and A. V. Davydov, Appl. Surf. Sci. **223**, 200 (2004).
[17] H. M. Christen, S. D. Silliman, and K. S. Hanshavardhan, Rev. Sci. Instrum. **72**, 2673 (2001).
[18] Certain commercial equipment, instruments, or materials are identified in this paper to foster understanding. Such identification does not imply recommendation or endorsement by the National Institute of Standards and Technology, nor does it imply that the materials or equipment identified are necessarily the best available for the purpose.
[19] A. M. Azad, O. M. Sreedharan, and K. T. Jacob, J. Mater. Sci. **26**, 3374 (1991).
[20] W. Wong-Ng, L. P. Cook, and J. Suh, Physica C **377**, 107 (2002).
[21] D. M. Feldmann, O. Ugurlu, B. Maiorov, L. Stan, T. G. Holesinger, L. Civate, S. R. Foltyn, and Q. X. Jia, Appl. Phys. Lett. **91**, 162501 (2007).
[22] J. Wang, J. H. Kwon, J. Yoon, H. Wang, J. J. Haugan, F. J. Baca, N. A. Pierce, and P. N. Barnes, Appl. Phys. Lett. **92**, 082507 (2008).

Phase evolution in Ba–(Nd,Eu,Gd)–Cu–O-coated conductor films

W. Wong-Ng,[a] I. Levin, J. Ritter, L.P. Cook, G. Liu, M. Otani, and M. Vaudin
Materials Science and Engineering Laboratory, National Institutes of Standards and Technology, Gaithersburg, Maryland 20899

C. Lucas and S.P. Diwanji
Chemistry Department, University of Maryland, College Park, Maryland 20742

R. Feenstra
Materials Science & Engineering Laboratory, Oak Ridge National Laboratory, Oak Ridge, Tennessee 37831

(Received 20 November 2007; accepted 24 January 2008)

Phases that are in equilibrium with BaR_2CuO_{6+x} (R = lanthanides and Y), such as the "green-phase" and "brown-phase" structural variants of BaR_2CuO_5 in bulk samples, are attractive choices for flux-pinning for coated conductor applications because of the guaranteed chemical stability. In films, high-temperature x-ray diffraction studies of $Ba_2RCu_3O_{6+x}$ superconductor deposited on $SrTiO_3$ substrate using the trifluoroacetate solution method demonstrate that while $BaNd_2CuO_5$ ("brown-phase" structure) develops at 735 °C and 100 Pa p_{O2}, neither $BaGd_2CuO_5$ nor $Ba(Nd_{1/3}Eu_{1/3}Gd_{1/3})_2CuO_5$ (both green-phase structure) form at these conditions. As a result, $Ba_2(Nd_{1/3}Eu_{1/3}Gd_{1/3})Cu_3O_{6+x}$ in thin films is in equilibrium with the brown-phase, and $Ba_2GdCu_3O_{6+x}$ is in equilibrium with Gd_2O_3 in the Ba–Gd–Cu–O system, in contrast to the bulk systems. Different phase relationships in the vicinity of the $Ba_2RCu_3O_{6+x}$ phase imply different phases are available for flux-pinning applications. These differences will need to be considered carefully in designing optimized superconducting coated conductors.

I. INTRODUCTION

Coated-conductor technology for fabrication of second-generation superconductor wire/tape holds significant promise for the superconductor industry, partly because of a lower production cost. The key feature of the coated-conductor process is the deposition of biaxially textured superconducting films onto metallic substrates (usually Ni or Ni-alloy). Currently the principal techniques for preparing coated conductor templates are the rolling-assisted biaxially textured substrate technique (RABiTS)[1–3] and the ion-beam-assisted deposition technique (IBAD).[4,5] Extensive global research activities using these two techniques are continuing, with the goal of facilitating the entry of second-generation wire/tape technology into the market place to meet the high demand for improved electrical power distribution.

The principal high-T_c superconductors used for coated conductor technology are in the $Ba_2RCu_3O_{6+x}$ series (R = lanthanides and Y). Although the main focus of research in the past has been on the Y-containing system, in recent years, much research work has also been conducted in lanthanide-substituted $Ba_2RCu_3O_{6+x}$ (R-213) systems, in both bulk materials and films.[6–9] Extensive phase equilibria data are available for the bulk Ba–R–Cu–O systems under atmospheric-controlled conditions[10–15]; however, little information is available for the phase evolution and relationships in the Ba–R–Cu–O films. In our previous study,[16] we found that the phase relationships of the $Ba_2YCu_3O_{6+x}$ superconductor phase are different in the bulk and in the film form. For example, the green-phase, BaY_2CuO_5, which is commonly used for flux pinning purposes to improve the superconducting properties, is absent in the film. As flux pinning investigation of high-T_c materials is an important area for coated conductor processing, the goal of this paper is to describe the phase evolution and phase relationships of $Ba_2(Nd_{1/3}Eu_{1/3}Gd_{1/3})Cu_3O_{6+x}$ and the related $BaNd_2CuO_5$ and $BaGd_2CuO_5$ thin films based on high-temperature x-ray diffraction (HTXRD) data. The $Ba_2(Nd_{1/3}Eu_{1/3}Gd_{1/3})Cu_3O_{6+z}$ system was chosen because of its promising J_c properties.[6]

II. EXPERIMENTAL

Films of $Ba_2(Nd_{1/3}Eu_{1/3}Gd_{1/3})Cu_3O_{6+x}$, $BaNd_2CuO_5$, and $BaGd_2CuO_5$ were prepared by the spin coating

[a]Address all correspondence to this author.
e-mail: winnie.wong-ng@nist.gov
DOI: 10.1557/JMR.2008.0273

technique.[17] To prepare the spin-coating solution, Ba- and Cu-acetate were first dissolved in distilled water, followed by the addition of trifluoroacetic acid. The lanthanide oxides were dissolved in a trifluoroacetic acid/water solution, which was mixed subsequently with the Ba–Cu solution. The total solution volume was reduced by heating and stirring. For spin-coating application, it was determined that a final volume resulting in a solution with a viscosity similar to that of a syrup was nearly ideal. A commercial, programmable spin coater with a vacuum chuck substrate holder was used to prepare the films. A $SrTiO_3$ substrate, approximately 10 × 10 × 0.5 mm in size, was mounted on the vacuum chuck, flooded with a viscous solution prepared as described above, and accelerated at 400–3400 rpm. A preliminary heat treatment designed to remove organics from the precursor film while minimizing Cu loss was completed in 100% O_2 using a thermogravimetric analyzer (25–190 °C at 1 °C/min; 190–300 °C at 0.1 °C/min). Gravimetric estimates using density data suggested film thickness on the order of 500 nm.

To compare phase relations in the Ba–(Nd,Eu,Gd)–Cu–O films with the corresponding bulk materials, we determined whether bulk samples of $Ba_2(Nd_{1/3}Eu_{1/3}Gd_{1/3})Cu_3O_{6+x}$ and the phases in close compositional proximity, $Ba(Nd_{1/3}Eu_{1/3}Gd_{1/3})_2CuO_5$, $Ba(Nd_{1/3}Eu_{1/3}Gd_{1/3})_2O_4$, and $(Nd_{1/3}Eu_{1/3}Gd_{1/3})_2CuO_4$, formed single-phase materials. These bulk samples were prepared using conventional solid-state synthesis. Stoichiometric amounts of $BaCO_3$, Nd_2O_3, Gd_2O_3, Eu_2O_3, and CuO were mixed, palletized, and annealed at 850 °C overnight. Further annealing was conducted between 930 and 950 °C for about two weeks with intermediate grindings.

HTXRD was used to study phase evolution and phase relations of the $Ba_2(Nd_{1/3}Eu_{1/3}Gd_{1/3})Cu_3O_{6+x}$, $BaNd_2CuO_5$, and $BaGd_2CuO_5$ films. A θ-θ geometry Siemens D5000 x-ray diffractometer (Germany), equipped with a high-temperature stage and a position sensitive detector (PSD), was modified by adding a gas flow apparatus. This apparatus included a series of bubblers containing NaCl-saturated water at room temperature and an oxygen analyzer. Helium gas containing ≈1000 μl/l (or ppm) O_2 by volume was flowed through the bubblers and passed directly over the sample in the enclosed furnace chamber. Cu K_α radiation was used for the x-ray analysis. The x-ray patterns were recorded continuously for ~10 min each. The three films were ramped from room temperature to 735 °C in ~150 min.

III. RESULTS AND DISCUSSION

The $Ba(Nd_{1/3}Eu_{1/3}Gd_{1/3})_2CuO_5$, $Ba(Nd_{1/3}Eu_{1/3}Gd_{1/3})_2O_4$, $(Nd_{1/3}Eu_{1/3}Gd_{1/3})_2CuO_4$, and $Ba_2(Nd_{1/3}Eu_{1/3}Gd_{1/3})Cu_3O_{6+x}$ bulk samples were all found to be single phase and were isostructural with $BaEu_2CuO_5$, $BaNd_2O_4$,[10] Nd_2CuO_4,[10] and $Ba_2NdCu_3O_{6+x}$ ("brown-phase," R-121), respectively. BaR_2CuO_5 phases crystallize with two distinct structure types,[18] depending on the ionic size of the R-cation: (i) a tetragonal *P4/mbm* brown-phase (R = La and Nd) and (ii) an orthorhombic *Pbnm* green-phase (R = Sm, Eu, Gd, Dy, Ho, Y, Er, Tm, Yb). Figure 1 displays the x-ray diffraction (XRD) pattern for the bulk $Ba(Nd_{1/3}Eu_{1/3}Gd_{1/3})_2CuO_5$,which evidently exhibits a green-phase structure presumably because the R sites in this compound are predominantly occupied by Eu and Gd, which promote formation of the green-phase.

A sequence of HTXRD patterns (not shown) of $Ba_2(Nd_{1/3}Eu_{1/3}Gd_{1/3})Cu_3O_{6+x}$ as a function of temperature indicated formation of CuO, the $Ba(F_{2-2x}\square_x)O_x$ superstructure phase[19] (□ represents a vacant site), and the $Ba_2(Nd_{1/3}Eu_{1/3}Gd_{1/3})Cu_3O_{6+x}$ phase, as temperature increased from 25 to 735 °C. XRD patterns recorded as a function of time at 735 °C are shown in Fig. 2. We observed the disappearance of $Ba(F_{2-2x}\square_x)O_x$ and CuO after about 120 min, and the gradual growth of $Ba_2(Nd_{1/3}Eu_{1/3}Gd_{1/3})Cu_3O_{6+x}$, $BaCuO_{2+x}$, and the brown-phase BaR_2CuO_5. These XRD patterns also indicate that the $Ba_2(Nd_{1/3}Eu_{1/3}Gd_{1/3})Cu_3O_{6+x}$ is somewhat Cu-deficient [due to Cu loss during the trifluoroacetate (TFA) annealing stage]. The green-phase solid solution, $Ba(Nd_{1/3}Eu_{1/3}Gd_{1/3})_2CuO_5$, which was found to be stable in the bulk form, was absent in the film; instead, formation of the brown-phase, BaR_2CuO_5, was observed. This result agrees with the absence of the green-phase BaY_2CuO_5 in the thin films of $BaO–Y_2O_3–CuO$ system, as reported previously.[16] In the thin-film version of the $BaO–Y_2O_3–CuO$ system, the Y-213 phase is in equilibrium with Y_2O_3, $Y_2Cu_2O_5$, and CuO_x instead of the green-phase, BaY_2CuO_5.

The HTXRD patterns of the $BaNd_2CuO_5$ (Nd-121) film (brown-phase) are shown in Fig. 3. At 700 °C, formation of both the barium oxyfluoride-type phase,

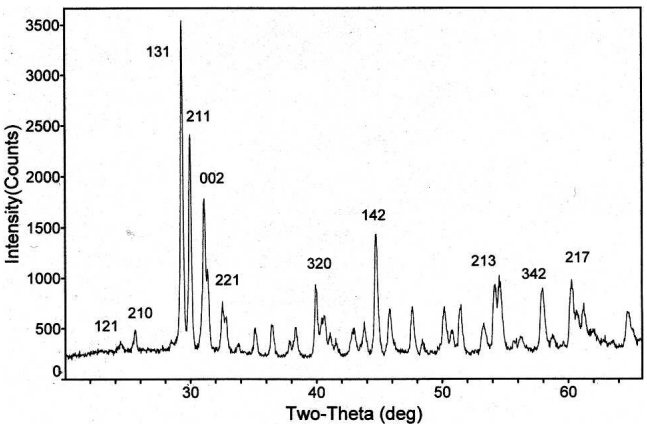

FIG. 1. X-ray diffraction pattern for a bulk single phase of $Ba(Nd_{1/3}Eu_{1/3}Gd_{1/3})_2CuO_5$; Miller indices are shown for selected diffraction peaks.

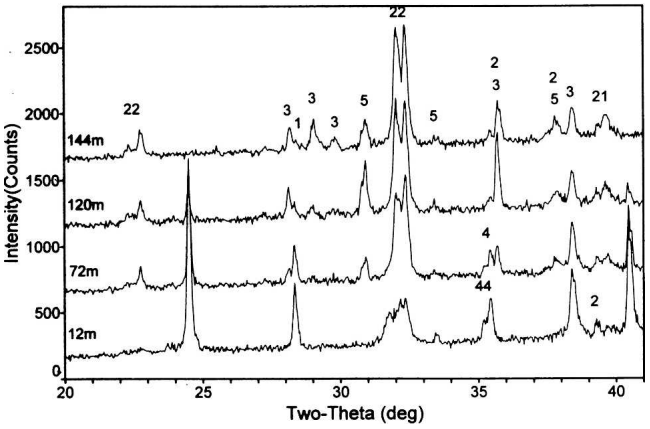

FIG. 2. High-temperature XRD patterns of the nominal (Cu-deficient) $Ba_2(Nd_{1/3}Eu_{1/3}Gd_{1/3})Cu_3O_{6+x}$ composition taken as a function of time (minutes) at 735 °C. Phases that produce diffraction peaks are indicated by numbers: (1) $Ba(F_{2-2x-x})O_x$ superstructure, (2) $Ba_2(Nd_{1/3}Eu_{1/3}Gd_{1/3})Cu_3O_{6+x}$, (3) $BaCuO_2$, (4) CuO, and (5) brown-phase BaR_2CuO_5. The absence of the green-phase $Ba(Nd_{1/3}Eu_{1/3}Gd_{1/3})_2CuO_5$ is illustrated.

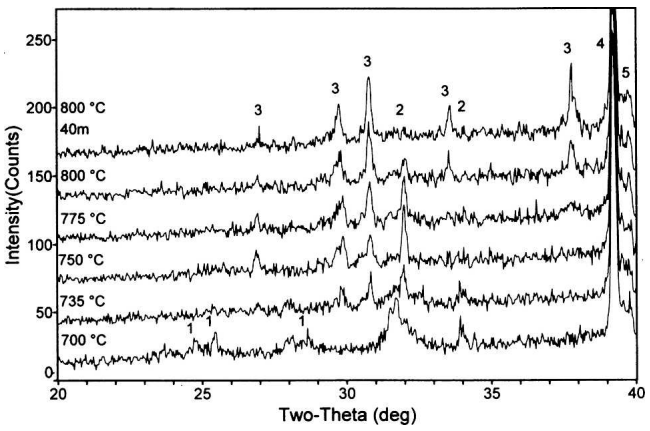

FIG. 3. High-temperature XRD patterns of a $BaNd_2CuO_5$ film (tetragonal, *P4/mbm*) heat-treated as a function of temperature. Phases that produce diffraction peaks are indicated by numbers: (1) $Ba(F_{2-2x-x})O_x$ superstructure, (2) Nd_2CuO_4, (3) BaR_2CuO_5 (brown-phase), (4) Pt, and (5) $SrTiO_3$.

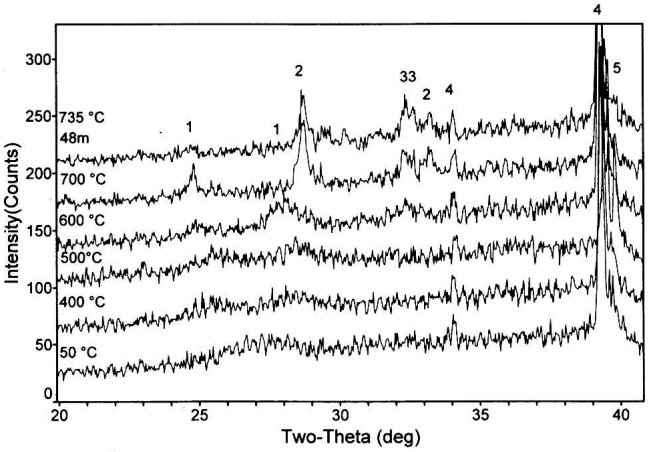

FIG. 4. High-temperature XRD patterns for a $BaGd_2CuO_5$ (orthorhombic, *Pbnm*) film as a function of temperature up to 735 °C. Phases that produce diffraction peaks are indicated by numbers: (1) $Ba(F_{2-2x-x})O_x$ superstructure, (2) Gd_2O_3, (3) $Ba_2GdCu_3O_{6+x}$, (4) Pt, and (5) $SrTiO_3$.

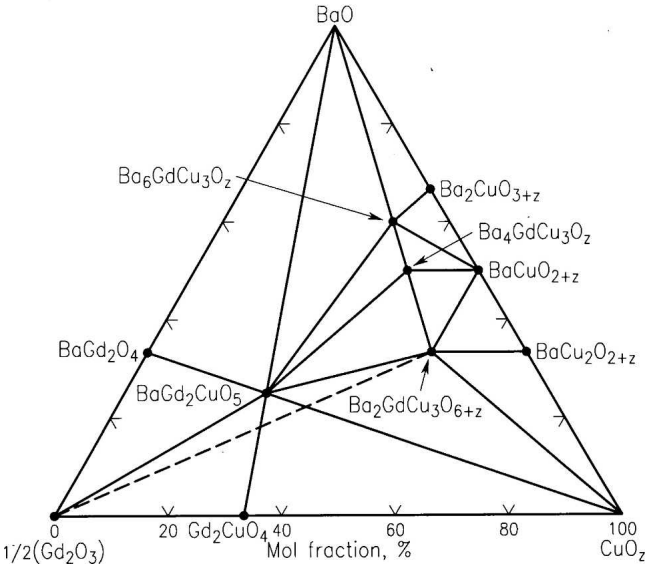

FIG. 5. Phase relations of the BaO-poor portion of the BaO–½Gd_2O_3–CuO_z region in films (dotted line) with equivalent data for the bulk equilibrium system[13] (solid lines). A tie-line is found between $BaGd_2CuO_5$ and Gd_2O_3 in films.

$Ba(F_{2-2x}\square_x)O_x$, and Nd_2CuO_4 is observed. At 735 °C, the brown-phase, $BaNd_2CuO_5$, started to form and persisted throughout a prolonged annealing at this temperature. Clearly, the brown- phase is stable in the thin film form under the present processing conditions, and it is compatible with the Nd-213 superconductor solid solution, $Ba_{2-z}Nd_{1+z}Cu_3O_{6+x}$.

Figure 4 shows a sequence of high-temperature XRD patterns for the green-phase composition $BaGd_2CuO_5$ (Gd-121) as a function of temperature up to 735 °C. This series of patterns reveals the presence of $Ba(F_{2-2x}\square_x)O_x$ at a relatively lower temperature followed by the formation of Gd_2O_3 and $Ba_2GdCu_3O_{6+x}$. The XRD pattern that was recorded after a 48 min exposure to 735 °C reveals no sign of the green-phase, $BaGd_2CuO_5$. Figure 5 illustrates different phase relations for the BaO-poor region of the BaO–½Gd_2O_3–CuO_z diagram in the film as compared to the bulk equilibrium diagram.[13] A tie-line is found between the $BaGd_2CuO_5$ and Gd_2O_3 in the films. Thus we demonstrated that the green-phase $BaGd_2CuO_5$ does not form in the Gd-121 thin films deposited on $SrTiO_3$ using a spin-coating technique and annealed at 735 °C and 100 Pa p_{O2}.

These findings are relevant to Ba–R–Cu–O-coated conductor research for the following reasons. Phases that are in equilibrium with the R-213 phase are attractive choices for flux-pinning because of the guaranteed

chemical stability. Therefore, as an alternative to the widespread use of the green-phase as a flux-pinning agent, one can propose the use of R_2O_3 or $R_2Cu_2O_5$ phases as flux-pinning agents in the BaO-poor region for systems with R = Sm, Eu, Gd, Dy, Ho, Er, Tm, Yb, and Lu. In the systems with larger R-cations, the R-213 is compatible with BaR_2CuO_5 (brown-phase), and therefore R_2CuO_4 and CuO are the possible candidates for flux-pinning applications. In general, phases in the BaO-rich region are sensitive to the presence of moisture and CO_2 and are therefore difficult to handle.

There are various possible reasons for different phase relationships in thin film and bulk materials, including strain, texturing, interactions between film and substrate, and kinetic factors that are determined by the substrate, film thickness, and the processing conditions. In the BaF_2 ex situ process, the difference in phase relations could also be due to the presence of fluorine. We plan to further investigate the causes of these differences by analyzing phase formation in fluoride-free Ba–Y–Cu–O films on $SrTiO_3$ using a high-throughput combinatorial approach.[20] These experiments will determine the effect of fluorine on phase assemblages.

IV. SUMMARY

Since information on phase evolution and phase relations can facilitate the development of processing blueprints, our results are important for research and development on Ba–R–Cu–O-coated conductors. Phases that are in equilibrium with the $Ba_2RCu_3O_{6+x}$ superconductors are candidates for flux-pinning agents for improving superconducting properties, and it is important to understand phase relationships in the vicinity of the $Ba_2RCu_3O_{6+x}$ phase. We found that contrary to the bulk systems, the green-phases, $BaGd_2CuO_5$ and $Ba(Nd,Eu,Gd)_2CuO_5$, do not form in the Gd-121 and (Nd,Eu,Gd)-121 thin films that were deposited on $SrTiO_3$ substrates and annealed at 735 °C and 100 Pa p_{O2}. Different phase relationships in the vicinity of the $Ba_2RCu_3O_{6+x}$ phase imply different phases available for flux-pinning applications in bulk versus thin-film form. These differences will need to be considered carefully in designing optimized superconducting coated conductors.

To determine the effects of the presence of fluorine and different processing conditions, we plan to continue studies of phase relations in the Ba–R–Cu–O films using a combinatorial library approach. The complex phase compatibilities in the CuO-deficient region of the diagram will also be addressed in future work.

ACKNOWLEDGMENTS

This work has been partially supported by the Office of Electricity Delivery and Energy Reliability of the United States Department of Energy. The authors are also grateful to Dr. Amit Goyal and Dr. Mariappan Paranthaman of Oak Ridge National Laboratory for their valuable discussions. Mr. Nil Swanson is thanked for his graphic assistance.

Certain commercial equipment, instruments, or materials are identified in this paper to foster understanding. Such identification does not imply recommendation or endorsement by the National Institute of Standards and Technology, nor does it imply that the materials or equipment identified are necessarily the best available for the purpose.

REFERENCES

1. M.W. Rupich, W. Zhang, X. Li, T. Kodenkandath, D.T. Verebelyi, U. Schoop, C. Thieme, M. Teplitsky, J. Lynch, N. Nguyen, E. Siegal, J. Scudiere, V. Maroni, K. Venkataraman, D. Miller, and T.G. Holesinger: Progress on MOD/RABiTS^{TM} 2G HTS wire. *Physica C* **412–414,** 877 (2004).
2. A. Goyal, D.P. Norton, J.D. Budai, M. Paranthaman, E.D. Specht, D.M. Kroeger, D.K. Christen, Q. He, B. Saffian, F.A. List, D.F. Lee, P.M. Martin, C.E. Klabunde, E. Hartfield, and V.K. Sikka: High critical current density superconducting tapes by epitaxial deposition of $YBa_2Cu_3O_x$ thick films on biaxially textured metals. *Appl. Phys. Lett.* **69,** 1795 (1996).
3. A. Goyal, U. Schoop, and P. Paranthaman: The RABiTS Approach: Using rolling-assisted biaxially textured substrates for high-performance YBCO superconductors. *MRS Bull.* **29**(8), 552 (2004).
4. P.N. Arendt, S.R. Foltyn, L. Civale, R.F. DePaula, P.C. Dowden, J.R. Groves, T.G. Holesinger, Q.X. Jia, S. Kreiskott, L. Stan, I. Usov, H. Wang, and J.Y. Coulter: High critical current YBCO coated conductors based on IBAD MgO. *Physica C* **412–414,** 795 (2004).
5. S.R. Foltyn, E.J. Peterson, J.Y. Coulter, P.N. Arendt, Q.X. Jia, P.C. Dowden, M.P. Maley, X.D. Wu, and D.E. Peterson: Influence of deposition rate on the properties of thick $YBa_2Cu_3O_{7-d}$ films produced by pulsed laser deposition. *J. Mater. Res.* **12,** 2941 (1997).
6. M. Muralidhar, N. Sakai, N. Chikumoto, M. Jirsa, T. Machi, M. Nishiyama, Y. Wu, and M. Murakami: New type of vortex pinning structure effective at very high magnetic fields. *Phys. Rev. Lett.* **89**(23), 237001 (2002).
7. T. Goto, E. Sato, K. Watanabe, G. Nishijima, Y. Matsui, T. Nagai, and C. Tsuruta: High critical-current density and ultra high-voltage TEM study of filamentary 0.1 at.% Zr-doped $(Nd_{0.33}Eu_{0.33}Gd_{0.33})Ba_2Cu_3O_x$ superconductors. *Physica C* **425,** 166 (2005).
8. A. Hu, M.R. Koblischka, X. Yao, H. Zhou, M. Winter, U. Hartmann, and M. Murakami: Recent progress on compositional nanostripes of $REBa_2Cu_3O_{7-x}$ (RE = Sm,Eu,Ge) superconductors. *Supercond. Sci. Technol.* **19,** S580 (2006).
9. C. Cai, G. Holzapfel, J. Hänisch, L. Fernández, and L. Schlutz: High critical current density and its field dependence in mixed rare earth $(Nd,Eu,Gd)Ba_2Cu_3O_{7-\delta}$ thin films. *App. Phys. Lett.* **84,** 377 (2004).
10. W. Wong-Ng, L.P. Cook, and J. Suh: Subsolidus phase relationships of the $BaO–Y_2O_3–CuO_x$ system under carbonate-free conditions at p_{O2} = 100 Pa and at p_{O2} = 21 kPa. *Physica C* **377,** 107 (2002).
11. W. Wong-Ng, L.P. Cook, J. Suh, R. Coutts, J.K. Stalick, I. Levin,

and Q. Huang: $BaO–Nd_2O_3–CuO_x$ subsolidus equilibria under carbonate-free conditions at $pO_2 = 100$ Pa and at $pO_2 = 21$ kPa. *J. Solid State Chem.* **173,** 476 (2003).
12. W. Wong-Ng, L.P. Cook, J. Suh, and J.A. Kaduk: Phase relationships in the $BaO–Sm_2O_3–CuO_x$ system under 100 Pa O_2. *Physcia C* **405,** 47 (2004).
13. W. Wong-Ng, L.P. Cook, and J. Suh: $BaO–R_2O_3–CuO_x$ (R = Gd and Er) subsolidus equilibria under carbonate-free conditions at $pO_2 = 100$ Pa. *Solid State Sci.* **6,** 1211 (2004).
14. W. Wong-Ng, Z. Yang, L.P. Cook, J. Frank, and M. Loung: Subsolidus phase relationships of the $BaO–R_2O_3–CuO_z$ (R = Eu, Dy, and Ho) systems under carbonate-free conditions at $T = 810$ °C and $p_{O2} = 100$ Pa. *Physica C* **439,** 93 (2006).
15. W. Wong-Ng, Z. Yang, and L.P. Cook: Subsolidus phase relationships of the $BaO–R_2O_3–CuO_z$ (R = Tm and Yb) systems under carbonate-free conditions at $p_{O2} = 100$ Pa, and $T = 750$ °C and 810 °C. *J. Alloys Compd.* **437,** 58 (2007).
16. W. Wong-Ng, I. Levin, M. Otani, M.D. Vaudin, L.P. Cook, J. Cline, R. Feenstra, and T. Holesinger: Phase relations in the Ba–Y–Cu–O films on $SrTiO_3$ for the ex situ BaF_2 process. *Appl. Phys. Lett.* **90,** 102508 (2007).
17. M. Yoshizumi, I. Seleznev, and M.J. Cima: Reactions of oxyfluoride precursors for the preparation of barium yttrium cuprate films. *Physica C* **403,** 191 (2004).
18. W. Wong-Ng, M.A. Kuchinski, H.F. McMurdie, and B. Paretzkin: Crystal chemistry and phase equilibrium studies of $BaO–1/2R_2O_3–CuO$. X-ray powder characterization of BaR_2CuO_5 and related compounds. *Powder Diffr.* **4,** 2 (1989).
19. W. Wong-Ng, I. Levin, L.P. Cook, and R. Feenstra: Nature of the transient BaF_2-related phases in the "BaF_2" processing of $Ba_2YCu_3O_{7-x}$ superconductors. *Appl. Phys. Lett.* **88,** 102507 (2006).
20. H.M. Christen, S.D. Silliman, and K.S. Harchavardhan: Continuous compositional-spread technique based on pulsed-laser deposition and applied to the growth of epitaxial films. *Rev. Sci. Instrum.* **72,** 2673 (2001).

Manifestation of anisotropy in melting systematics of RBa$_2$Cu$_3$O$_{7-\delta}$ (R=lanthanides)

H. B. Su[a)]
Division of Materials Science, Nanyang Technological University, 50 Nanyang Avenue, 639798 Singapore, Singapore

D. O. Welch[b)]
Department of Condensed Matter Physics and Materials Science, Brookhaven National Laboratory, Upton, New York 11973, USA

W. Wong-Ng,[c)] L. P. Cook, and Z. Yang
Ceramics Division, National Institute of Standards and Technology, Gaithersburg, Maryland 20899, USA

(Received 27 May 2007; accepted 25 September 2007; published online 24 October 2007)

The conventional isotropic Debye temperature fails to account for the trend of melting temperatures for the high T_c superconductors, RBa$_2$Cu$_3$O$_{7-\delta}$ (R-123), as a function of the ionic radius of R^{3+}. We overcame this problem by calculating Debye temperatures using mean sound velocity along the c axis that features an anisotropic layered structure. Using the "improved" Debye temperature, the trend of derived melting temperatures based on the "Lindemann law" matches well with experimental data. This trend is also confirmed by comparing theoretical and experimental Raman active modes corresponding to the Cu–O (plane copper and apical oxygen) and Ba–O (in-plane) bonds in R-123 series. © *2007 American Institute of Physics*. [DOI: 10.1063/1.2799242]

In recent years, there has been a growing interest in both bulk and multilayer RBa$_2$Cu$_3$O$_{7-\delta}$ (R-123, R=yttrium and lanthanides) cuprate superconductors,[1,2] particularly in coated-conductor applications.[3–6] To improve the properties and application range of R-123, prior knowledge of the phase stability of these compounds based on phase diagrams, including melting temperatures, is required. Understanding melting is important for both materials processing and for thermodynamic modeling. Osamura and Zhang[7] have systematically studied the change in melting temperature of R-123 superconductors (processed using "artificial air") as a function of the size r of R ions. Although a monotonic trend of melting temperature with r for the R-123 family has been experimentally observed, a detailed understanding of this trend at the atomic scale is not available due to the complexity of the structure of R-123. Poirier[8] found a correlation between the melting temperature and the Debye temperature for 15 compounds with the simple ABO_3 perovskite-type structure. This correlation stimulated us to carry out a systematic study of the dependence of melting temperature of R-123 on the ionic radius of R^{3+} or $r(R^{3+})$ based on the "Lindemann law."[9]

To confirm the melting trend with ionic size, as well as the variation of melting temperature of selected R-123 samples of interest under different atmospheric conditions, we prepared five R-123 samples (R=Nd, Sm, Gd, Y, and Er) using the solid-state technique. Stoichiometric amounts of $BaCO_3$, R_2O_3, and CuO were well mixed, and heat treated at 850 °C overnight. Subsequent heat treatments were conducted in air at 950 °C for 5 days with intermittent grindings. For the melting studies, two series of experiments were carried out using differential thermal/thermogravimetric analysis (DTA/TGA). Calibration of the system was completed using the α/β quartz transition (571 °C) and the melting points of NaCl and Au (801 and 1064 °C, respectively). In the first series, samples were annealed in oxygen to constant mass at 500 °C followed by slow cooling in oxygen to room temperature in order to ensure the maximum oxygen content of 7 in RBa$_2$Cu$_3$O$_{7-\delta}$.[10] Then DTA/TGA experiments were conducted in oxygen at 10 °C/min up to 1300 °C. In the second series of experiments, samples were also annealed in oxygen to constant mass at 500 °C followed by slow cooling, however the DTA/TGA experiments were conducted in purified air. We found that while the absolute values of the melting temperatures of these series of samples differ from each other, the general trends agreed well with each other, namely, the larger the size of R^{3+}, the higher the melting temperature. The difference in melting temperature for a given member of the series is due to the fact that melting temperature is higher under a higher oxygen partial pressure. These two sets of melting data are tabulated in Table I.

From thermodynamic considerations, the melting conditions of a compound can be obtained by equating temperatures, pressures, and Gibbs free energies of both solid and liquid phases. The traditional difficulty of such a thermodynamic melting theory arises from the complex relationship

TABLE I. Experimental melting temperatures of Ba$_2R$Cu$_3$O$_{7-x}$ measured under 0.1 MPa O_2 (or 100% O_2) and purified air. $r(R)^{3+}$ is the ionic radius (Å) of R^{3+} taken from Shannon by assuming a VIII-coordination environment (Refs. 13 and 14).

		Melting temperature	
R	$r(R)^{3+}$	0.1 MPa O_2 (or 100% O_2) °C (K)	purified air °C (K)
Sm	1.079	1097.0(1370.16)	1075.5(1348.66)
Eu	1.066	1089.6(1362.76)	1067.3(1340.46)
Gd	1.053	1069.7(1342.86)	1049.1(1322.26)
Y	1.019	1039.8(1312.96)	1021.0(1294.16)

[a)]Electronic mail: hbsu@ntu.edu.sg
[b)]Electronic mail: dwelch@bnl.gov
[c)]Electronic mail: winnie.wong-ng@nist.gov

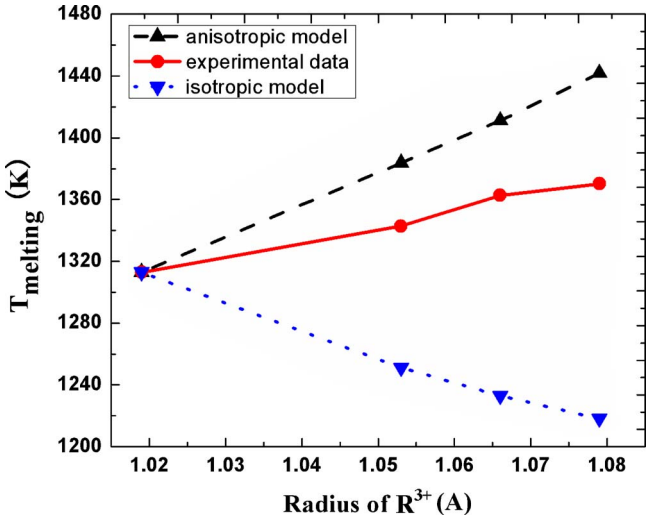

FIG. 1. (Color online) Calculated and experimental melting temperatures of $R\mathrm{Ba_2Cu_3O_7}$ as a function of $r(R^{3+})$ (Ref. 13 and 14). Solid circular symbols, linked by a solid read line, stand for experimental melting data under 0.1 MPa $p\mathrm{O_2}$ (100% $\mathrm{O_2}$). The data represented by down triangles, linked by a dot blue line, are calculated using the Debye temperatures by isotropic approximation. The data represented by up triangles, linked by a dash black line, are computed by selecting sound waves propagate along c axis.

between the free energy of the liquid phase and the interatomic forces. It is often necessary, especially for complex compounds, to resort to simple and conceptual methods, such as the Lindemann law.[9,11] The Lindemann theory assumes that at certain temperature the amplitude of vibration of solids is so large that the energy of the solid phase rises significantly. This temperature is the melting temperature of the solid. In 1950s, Gilvarry gave a firmer microscopic basis to the Lindemann law.[9] Instead of assuming that melting occurs when neighboring spheres collide, he stated that the root mean square amplitude of atomic vibrations at fusion r_m is a critical fraction of the distance of separation of nearest neighbor atoms. By substituting the root mean square amplitude of atomic vibration into Debye's approximation, we obtained the formula of melting temperature as

$$T_m = 0.0032 f^2 M V^{2/3} \Theta^2, \tag{1}$$

where M is the mean atomic mass of a solid, V is the mean atomic volume, f is the Gilvarry critical ratio, which is about 0.11 for perovskite oxides,[8] and Θ_D is the Debye temperature. If we simply proceed in this fashion using the Θ_D computed by an *isotropic* approximation, the calculated trend of melting temperature disagrees with the trend of measured data (Fig. 1). In order to explain the experimental results, it is necessary to examine carefully the structure of R-123 (see Fig. 1 in Ref. 20) and the elastic constants associated with the structure. There exists a notable anisotropic feature in this structure, namely, the elastic constants $[C_{33},(C_{44},C_{55})]$ are 50% smaller than $[(C_{11},C_{22}),C_{66}]$.[12] In fact, this layered structure can be approximated better by an anisotropic hexagonal model rather than the isotropic one. Note that the sound velocities are much smaller if the sound wave propagates along the c axis of the structure. If we calculate the Debye temperature by the mean sound velocity along the c axis, we can obtain better insight about melting since the vibrations along the c axis have larger amplitudes than those along the a and b axes. Hence, we first approximated the R-123 structure by a hexagonal one, then we computed the

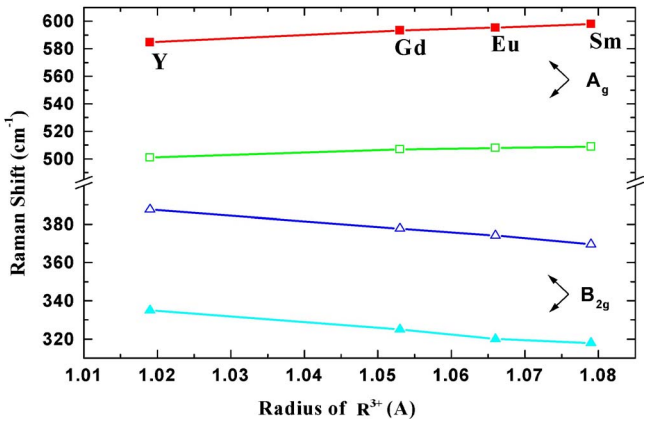

FIG. 2. (Color online) Raman Spectrum of $R\mathrm{Ba_2Cu_3O_7}$ as a function of radius of R^{3+}. Solid points stand for the calculated data; open ones for experimental data.[15] Squares are for A_g mode and triangles for B_{2g} mode.

sound velocities using a longitudinal/transverse wave along the c axis by

$$v_p = \sqrt{\frac{C_{33}}{\rho}},$$

$$v_s = \sqrt{\frac{C_{44}+C_{55}}{2\rho}}, \tag{2}$$

where ρ is the density. The mean sound velocity v_m can be computed by $3^{1/3}[(1/v_p^3)+(2/v_s^3)]^{-1/3}$. The Debye temperature is then given by

$$\Theta_D = \frac{h}{k_B}\left(\frac{3N_A}{4\pi V}\right)^{1/3} v_m, \tag{3}$$

where h is Planck's constant, k_B is the Boltzmann constant, N_A is Avogadro's number, and V is the molar volume. By using the melting temperature of Y-123 as a reference (scaling factor), the melting temperatures of the remaining R-123 were computed. Since the key feature, when comparing theoretical and experimental data, is strikingly similar for experimental data under both 100% $\mathrm{O_2}$ and purified air, we plotted only the computed data in Fig. 2 along with the current experimental melting data under 100% $\mathrm{O_2}$. The trend of the calculated melting temperatures agreed well with that of the experimental ones, although our calculated data were somewhat overestimated when compared with the experimental ones.

The trend of melting temperature dependence on $r(R^{3+})$ was corroborated by the calculations of selected Raman-active modes in $R\mathrm{Ba_2Cu_3O_7}$. We assessed the accuracy of our calculations by comparing the calculated and experimental A_g and B_{2g} Raman-active modes. The detailed calculation procedure of Raman modes was elaborated in Ref. 12. The A_g mode was assigned as the apical stretching mode due to the Cu–O bond (d_1) (planar copper and apical oxygen along the c axis). The B_{2g} mode is a result of an in-plane Ba–O stretching vibration. The frequency of the A_g mode [584^{calc} (503^{expt}) $\mathrm{cm^{-1}}$ for Y-123] and the B_{2g} mode [335^{calc} (388^{expt}) $\mathrm{cm^{-1}}$ for Y-123] were plotted, respectively, against $r(R^{+3})$ in R-123 (Refs. 13 and 14) in Fig. 2. The experimental data were taken from the work by Rosen *et al.*[15] The frequency of the Ag mode increases linearly with increasing $r(R^{+3})$ by approximately $2.28\%^{\mathrm{calc}}$ ($1.60\%^{\mathrm{calc}}$) from Y-123 to

Sm-123. At a first glance, this result appears to be inconsistent with the assignment of this mode to the apical oxygen bridging stretch vibration since the dimension of the unit cell in the c direction increases with increasing ionic radii. This expansion might be expected to lead to increasing bond lengths and decreasing force constants and therefore vibrational frequencies. However, neutron diffraction data show that despite the c axis increases, the Cu–O (d_2) (chain-copper and apical-oxygen) distances remain approximately constant[16] while the d_1 bond length decreases as the $r(R^{3+})$ increases.[13,14,16] Therefore the d_1 bond presumably controls the apical oxygen stretch frequency. The nice agreement between calculated and experimental d_1 bond lengths versus the $r(R^{3+})$ is shown in Ref. 12. On the other hand, the B_{2g} stretching mode [335^{calc} (388^{expt}) cm^{-1} for Y-123] decreases in frequency with increasing ionic radius. This change is substantial and corresponds to an approximately $4.64\%^{\text{calc}}$ ($-5.07\%^{\text{expt}}$) shift in the vibrational frequency. This shift is consistent with the identification of this mode as an in-plane Ba–O stretching vibration, since structural data indicate that the in-plane Ba–O bond lengths increase with the ionic radius of the rare earth.[12]

The sources of strain can be either host-lattice-nonconserved or host-lattice-conserved defects. One typical example for the former type is the strain field generated at R-123 grain boundaries, which strongly determines the segregation of calcium, consequently, affects passivating of disorder at the boundary.[17] Our work clearly demonstrates that the latter case, internal lattice strain, which occurs to accommodate the different ionic radii, has significant anisotropic effects on the trend of melting temperatures. As the ionic size of R increases, the distance of the Ba–O block between the barium layers becomes shorter along the c axis due to the shortening of the d_1 bond length. Due to the complexity of R-123 structure, one surprising consequence is that the corresponding *increase* of the separation between adjacent CuO_2 layers results in the remarkable reduction in the coherent interlayer single-particle hopping strength.[18] These results reveal the importance of the electronic origin of the rare-earth ionic anisotropic effect on T_c in this family.[19] In this study, this shortening in d_1 distance will increase the elastic constants $[C_{33},(C_{44},C_{55})]$ such that the melting temperature rises up with increasing ionic size of R. From previous studies,[20,21] it was found that while the formation energy of Schottky defects, which provides an unambiguous measure of the average cohesive strength (volumetric strain), is proportional to $B\Omega$ (where B is the bulk modulus and Ω is the mean volume per atom) for elemental and binary crystals; this relationship is violated in the R-123 series. In other words, the smaller the Schottky defect formation energy is, the lower is the melting temperature of simple elemental and binary crystals. Despite the fact that the Schottky defect formation energy of Sm-123 is smaller than that of Y-123, Sm-123 has the higher melting temperature, indicating that it is the internal strain due to the inhomogeneous changes of the bond distances within the unit cell for R-123 rather than the volumetric strain that controls the melting temperature of R-123. This intriguing finding is consistent with the melting systematics viewed from dislocation-mediated melting model, where the melting temperature is proportional to $B\Omega$ directly. The internal strains arising from the complex R-123 structure have significant anisotropic effects on the melting of these compounds. The dependence of melting temperatures on $r(R^{3+})$ that we report herein also provides a useful guide to estimate as well as to manipulate melting temperatures of $R\text{Ba}_2\text{Cu}_3\text{O}_{7-\delta}$ and of mixed lanthanide systems, $(R,R')\text{Ba}_2\text{Cu}_3\text{O}_{7-\delta}$.

Work at NTU is supported in part by COE-SUG grant (No. M58070001) and A*STAR SERC grant (No. 0521170032). The work at NIST was partially supported by the U.S. Department of Energy (DOE). The work at Brookhaven National Laboratory was performed under the auspices of the Division of Materials Sciences, Office of Science, U.S. Department of Energy under Contract No. DE-AC-02-98CH10886.

[1] A. Hu, M. Murakami, and H. Zhou, Appl. Phys. Lett. **83**, 1788 (2003).
[2] A. Hu, N. Sakai, and M. Murakami, Appl. Phys. Lett. **78**, 2539 (2001).
[3] A. P. Malozemoff, W. Carter, S. Flexhler, L. Fritzemeier, Q. Li, L. Masur, D. Parker, R. Parrella, E. Pedtburg, G. N. Riley, M. Rupich, J. Scudiere, and W. Zhang, IEEE Trans. Appl. Supercond. **9**, 2469 (1999).
[4] A. P. Malozemoff, S. Annavarapu, L. Fritzemeier, Q. Li, V. Prunier, M. Rupich, C. Thieme, W. Zhang, A. Goyal, M. Paranthaman, and D. F. Lee, Supercond. Sci. Technol. **13**, 473 (2000).
[5] A. Goyal, D. F. Lee, F. A. List, E. D. Specht, R. Feenstra, M. Paranthaman, X. Cui, S. W. Lu, P. M. Martin, D. M. Kroeger, D. K. Christen, B. W. Kang, D. P. Norton, C. Park, D. T. Verebelyi, J. R. Thompson, R. K. Williams, T. Aytug, and C. Cantoni, Physica C **357**, 903 (2001).
[6] T. Aytug, A. Goyal, N. Rutter, M. Paranthaman, J. R. Thompson, H. Y. Zhai, and D. K. Christen, J. Mater. Res. **18**, 872 (2003).
[7] K. Osamura and W. Zhang, Z. Metallkd. **84**, 522 (1993).
[8] J. P. Poirier, Phys. Earth Planet. Inter. **54**, 364 (1989).
[9] J. J. Gilvarry, Phys. Rev. **102**, 308 (1956).
[10] W. Wong-Ng, R. S. Roth, L. J. Swartzendruber, L. H. Bennett, C. K. Chiang, F. Beech, and C. R. Hubbard, *Ceramic Superconductors*, Advaced Ceramic Materials Vol. 2, edited by W. J. Smothers (American Ceramic Society, Westerville, OH, 1987), p. 565.
[11] J. P. Poirier, *Introduction to the Physics of the Earth's Interior* (Cambridge University Press, Cambridge, 1991).
[12] H. B. Su, Ph.D. thesis, State University of New York at Stony Brook, 2002.
[13] R. D. Shannon and C. T. Prewitt, Acta Crystallogr., Sect. B: Struct. Crystallogr. Cryst. Chem. **26**, 1046 (1970).
[14] R. D. Shannon, Acta Crystallogr., Sect. A: Cryst. Phys., Diffr., Theor. Gen. Crystallogr. **32**, 751 (1976).
[15] H. J. Rosen, R. M. Macfarlane, E. M. Engler, V. Y. Lee, and R. D. Jacowitz, Phys. Rev. B **38**, 2460 (1988).
[16] M. Guillaume, P. Allenspach, W. Henggeler, J. Mesot, B. Roessli, U. Staub, P. Fischer, A. Furrer, and V. Trounov, J. Phys.: Condens. Matter **6**, 7963 (1994).
[17] H. B. Su and D. O. Welch, Supercond. Sci. Technol. **18**, 24 (2005).
[18] E. Pavarini, I. Dasgupta, T. Saha-Dasgupta, O. Jepsen, and O. K. Andersen, Phys. Rev. Lett. **87**, 047003 (2001).
[19] X. J. Chen and H. B. Su, Phys. Rev. B **71**, 094512 (2005).
[20] H. B. Su, D. O. Welch, and W. Wong-Ng, Phys. Rev. B **70**, 054517 (2004).
[21] P. Varorsos and W. Ludwig, Phys. Rev. B **18**, 2683 (1978).

Journal of ELECTRONIC MATERIALS, Vol. 36, No. 10, 2007
DOI: 10.1007/s11664-007-0224-3

Special Issue Paper

Kinetic Studies of the Interfacial Reaction of the $Ba_2YCu_3O_{6+x}$ Superconductor with a CeO_2 Buffer

L.P. COOK,[1,3,4] W. WONG-NG,[1] P. SCHENCK,[1] Z. YANG,[1,2] I. LEVIN,[1] and J. FRANK[1,3]

1.—Ceramics Division, Materials Science and Engineering Laboratory, National Institute of Standards and Technology, Gaithersburg, MD 20899, USA. 2.—Yunnan Normal University, Kunming 650092, P. R. China. 3.—Northern Illinois University, DeKalb, IL 60115, USA. 4.—e-mail: lawrence.cook@nist.gov

Interfacial reactions between the $Ba_2YCu_3O_{6+x}$ superconductor and the CeO_2 buffer layers employed in coated conductors have been modeled experimentally by investigating the kinetics of the reaction between $Ba_2YCu_3O_{6+x}$ films and CeO_2 substrates. At 810°C, the $Ba_2YCu_3O_{6+x}$-CeO_2 join within the BaO-Y_2O_3-CeO_2-CuO_x quaternary system is nonbinary, thereby establishing the phase diagram topology that governs the $Ba_2YCu_3O_{6+x}$/CeO_2 reaction. At a mole ratio of $Ba_2YCu_3O_{6+x}$:CeO_2 of 40:60, a phase boundary was found to separate two four-phase regions. On the $Ba_2YCu_3O_{6+x}$-rich side of the join, the four-phase region consists of $Ba_2YCu_3O_{6+x}$, $Ba(Ce_{1-z}Y_z)O_{3-x}$, BaY_2CuO_5, and CuO_x; on the CeO_2 rich side, the four phases were determined to be $Ba(Ce_{1-z}Y_z)O_{3-x}$, BaY_2CuO_5, CuO_x and CeO_2. The $Ba_2YCu_3O_{6+x}$/CeO_2 reaction is limited by solid-state diffusion, and the reaction kinetics obey the parabolic rule, $x = Kt^{1/2}$, where x = thickness of the reaction layer, t = time, and K = a constant related to the rate constant; K was determined to be 1.6×10^{-3} $\mu m/s^{1/2}$ at 790°C and 4.7×10^{-3} $\mu m/s^{1/2}$ at 830°C. The activation energy for the reaction was determined to be $E_{act} = 2.67 \times 10^5$ J/mol using the Arrhenius equation.

Key words: Coated conductor, kinetics of interfacial reactions, $Ba_2YCu_3O_{6+x}$-CeO_2 system, activation energy

INTRODUCTION

With increased demand for electrical power, energy shortages and electricity outages have become common global problems. Consequently, there are pressing needs for improvements in electrical distribution grids and for more efficient utilization of energy resources. High-temperature superconductors have demonstrated potential for meeting these needs,[1] leading to an accelerated effort within the high-T_c community on research and development of coated conductors for wire and tape applications.[2–8] These coated conductors are based on $Ba_2YCu_3O_x$ (Y-213) and $Ba_2RCu_3O_x$ (R = lanthanides) as the principal superconductors. They can be deposited on flexible metallic tapes using various deposition techniques, and the resulting materials show excellent current-carrying capability.

State-of-the-art substrates and buffer layers form the basis for coated conductor fabrication. The two promising technologies for producing biaxially textured buffers or substrates are commonly known as ion-beam-assisted deposition (IBAD),[2,3] developed at Los Alamos National Laboratory, and rolling assisted biaxially textured substrate (RABiTS),[4–8] developed at Oak Ridge National Laboratory. Typically, the architecture of a RABiTS film includes a number of buffer layers of different materials deposited on the biaxially textured metallic substrate. These layers are the seed layer, barrier layer, and lower cap layer beneath the superconductor layer, and an overlayer on top.[9] The seed layer

(Received February 24, 2007; accepted May 17, 2007; published online September 21, 2007)

provides a thin epitaxial layer to protect the substrate from oxidation during deposition of the barrier layer. The barrier layer is a thick epitaxial layer to provide a physical/chemical barrier to substrate oxidation and substrate reaction with the superconductor layer. The lower cap layer provides additional protection for the superconductor film from chemical reaction, and also provides a texture for crystallographic alignment. The overlayer on top of the superconductor, typically Ag, helps provide thermal and electrical stability. Examples of lower cap layer materials include CeO_2, $LaMnO_3$, $SrTiO_3$, Gd_3NbO_7, and $SrRuO_3$. The two most extensively used materials have been CeO_2 and $SrTiO_3$.

Despite many benefits of the use of buffer layers, including the promotion of epitaxial growth of $Ba_2YCu_3O_{6+x}$, there may be unavoidable reactions at the interfaces between layers. Understanding of interfacial reactions of Y-213 phase with the buffer layers will provide information about how to avoid and/or control the formation of secondary phases. Phase equilibrium data will also allow better interpretation of the results of transmission electron microscopy (TEM) analysis of coated conductor interfaces.

This paper summarizes the equilibrium data for the multi-component systems representing the interaction of $Ba_2YCu_3O_{6+x}$ with CeO_2,[10] and describes a kinetic study of phases formed at the Y-213/CeO_2 interface.[11] The kinetic studies reported herein were completed by depositing the Y-213 superconductor on polished CeO_2 pellets using pulsed laser deposition (PLD). X-ray diffraction and TEM were used for characterization of phase formation and to determine the thickness of the product layer.

EXPERIMENTAL*

Kinetic studies were conducted by depositing the $Ba_2YCu_3O_{6+x}$ superconductor on highly polished polycrystalline CeO_2 pellets (obtained from Alfa Aesar, 99.9 wt.%, metals basis) using pulsed laser deposition (PLD) at NIST.

Preparation of the Y-213 Target

The target Y-213 for PLD was prepared by the reactive sintering technique using a mixture of the two binary phases $BaCuO_2$ and $Y_2Cu_2O_5$. These compounds were prepared by heating a mixture of BaO, and CuO, and Y_2O_3 and CuO, respectively, under purified air (CO_2- and H_2O-scrubbed). The BaO starting material was produced from $BaCO_3$ (99.99 mass%, metals basis) by vacuum calcination in a vertical tube furnace. The following heating schedule was used to produce high-purity BaO: room temperature to 1300°C in 20 h; isothermal at 1300°C for 10 h; 1300°C to room temperature in 20 h. Compositions for production of $BaCuO_2$ and $Y_2Cu_2O_5$ were weighed out, well mixed, and calcined in an atmospherically controlled high temperature furnace first at 850°C, followed by repeated calcinations at 930°C with intermediate grindings, for about two weeks. After single-phase materials of $BaCuO_2$ and $Y_2Cu_2O_5$ were successfully synthesized (as evidenced by powder X-ray diffraction), a mixture of the two phases was prepared to give a Ba:Y:Cu stoichiometry of 2:1:3, pelletized, and then placed inside the atmospherically controlled furnace at 950°C for three days. The X-ray diffraction pattern of the resulting well-sintered pellet indicated the material to be a single-phase Y-213.

Pulsed Laser Deposition

Y-213 was deposited using the NIST PLD system, which is based on an excimer laser (λ = 248 nm). The laser energy and frequency were 100 mJ, and 10 Hz, respectively, yielding a deposition rate of ≈11.5 nm/min. The background oxygen pressure in the chamber during deposition was 6.7 Pa. The resulting Y-213 film thicknesses were approximately 570 nm.

Kinetic Studies

To study the reaction kinetics, preliminary experiments to obtain the appropriate temperature range for heat treatments in air were carried out on four of the seven films prepared by PLD. Heat treatments were subsequently conducted on the other three films in air at 790°C, 810°C, and 830°C. For each film, successive heat treatments were in general planned so as to approximately double the cumulative time. X-ray diffraction was used to obtain intensities of selected reflections of these samples. The intensity values are assumed to be proportional to the amount of a particular phase, or the thickness of the reaction layer. Transmission electron microscopy (TEM) studies were carried out to obtain the microstructure, including identification of phases and thickness of the reaction layer. Cross-sectional samples for TEM were prepared by mechanical polishing and dimpling followed by ion-thinning in a GATAN PIPS system at ambient temperature until perforation. From these observations, a kinetic model describing the progress of reaction could be determined using the Arrhenius equation.[12]

RESULTS AND DISCUSSION

Summary of Phase equilibria between $Ba_2YCu_3O_{6+x}$ and CeO_2

Figure 1 illustrates the phase equilibria along the $Ba_2YCu_3O_{6+x}$-CeO_2 join in the context of the

*Certain trade names and company products are mentioned in the text or identified in illustrations in order to adequately specify the experimental procedures and equipment used. In no case does such identification imply recommendation or endorsement by the National Institute of Standards and Technology (NIST).

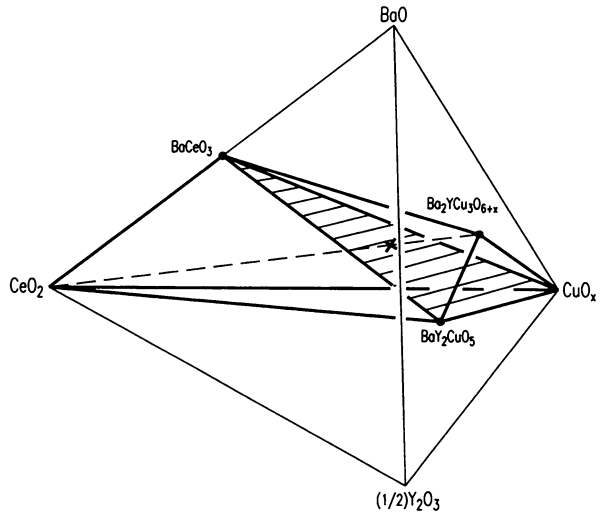

Fig. 1. The BaO-Y_2O_3-CuO_x-CeO_2 tetrahedron showing the two subvolumes $Ba_2YCu_3O_{6+x}$-Ba(Ce,Y)O_{3-x}-BaY_2CuO_5-CuO_x and $BaCeO_3$-BaY_2CuO_5-Cu_2O-CeO_2, within which the compositions of the $Ba_2YCu_3O_{6+x}$-CeO_2 join lie. "$BaCeO_3$" is a solid solution with the formula Ba$(Ce_{1-z}Y_z)O_{3-x}$. The "x" indicates the intersection of the $Ba_2YCu_3O_{6+x}$-CeO_2 join with the $BaCeO_3$-BaY_2CuO_5-CuO_x plane.

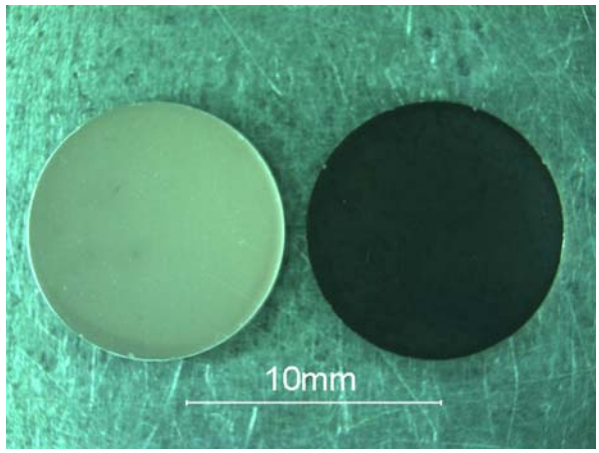

Fig. 2. Optical images of uncoated CeO_2 (left) and $Ba_2YCu_3O_{6+x}$/CeO_2 (right).

BaO-½Y_2O_3-CuO_x-CeO_2 framework. It is seen clearly that two tetrahedral volumes (four-phase regions) corresponding to $Ba_2YCu_3O_{6+x}$-$BaCeO_3$-BaY_2CuO_5-CuO_x and $BaCeO_3$-BaY_2CuO_5-CuO_x-CeO_2 are mutually consistent and do not overlap. These two tetrahedra share a common plane defined by BaY_2CuO_5 (commonly referred to as the green phase), CuO_x, and $BaCeO_3$. In other words, as a (CeO_2)-(Y-213) composition vector passes through the two tetrahedra, only three phases are observed at equilibrium at the plane forming the boundary between the two tetrahedra. This phase boundary exists at a of $Ba_2YCu_3O_{6+x}$:CeO_2 mole ratio of 40:60. On the $Ba_2YCu_3O_{6+x}$-rich side, the four phases possible as a result of equilibrium chemical interaction were found to be $Ba_2YCu_3O_{6+x}$, $BaCeO_3$, BaY_2CuO_5, and CuO_x; whereas on the CeO_2-rich side, the four phases were $BaCeO_3$, BaY_2CuO_5, CeO_2, and CuO_x. CuO_x designates either CuO (air) or Cu_2O (p_{O_2} = 100 Pa), depending on the oxygen partial pressure; for our kinetic experiments in air, CuO was observed, in agreement with calculated CuO/Cu_2O equilibria.[13]

Cerium is known to possess various oxidation states (+2, +3, and +4), and CeO_{2-x} undergoes a complex oxidation/reduction chemistry leading to other phases under different oxygen partial pressures. However, under the conditions of the present study, CeO_2 was the only stable form of cerium oxide. The $BaCeO_3$ phase is a solid solution and is more appropriately written as Ba$(Ce_{1-z}Y_z)O_{3-x}$. This solid solution is the only new multicomponent phase found in the system. The range of Ba$(Ce_{1-z}Y_z)O_{3-x}$ was determined to be rather small, namely, $0 \le z \le 0.13$.[10] We have studied the structure of a solid solution member of Ba$(Ce_{1-z}Y_z)O_{3-x}$ using neutron diffraction.[10] The structure of Ba$(Ce_{0.94}Y_{0.06})O_{2.84}$ was found to be of the perovskite type. Y was found to substitute for the Ce site with an occupancy of 0.06(2), giving rise to the unit cell content of $Ba_4(Ce_{3.76}Y_{0.24})O_{11.36}$, or the chemical formula of Ba$(Ce_{0.94}Y_{0.06})O_{2.84}$, with Z = 4, (space group of *Pmcn*, a = 8.7817(4) Å, b = 6.2360(4) Å, and c = 6.2190(3) Å, V = 340.57 Å^3, and a density of 6.236 g/cm^3).

Kinetic Study of $Ba_2YCu_3O_{6+x}$/CeO_2

Figure 2 shows optical images of two substrates, CeO_2 (uncoated) and CeO_2 coated with $Ba_2YCu_3O_{6+x}$ using PLD. The substrates, prepared by finely polishing densely sintered CeO_2 pellets, had optically smooth surfaces, as evidenced from high-magnification reflected light microscopy.

Figures 3 and 4 show the X-ray patterns of samples heat-treated at 810°C and 830°C as a function of the annealing time. The decrease in intensity of the 031 reflection of the $Ba_2YCu_3O_{6+x}$ phase is accompanied by an increase in reflection intensities for the phases Ba$(Ce_{1-z}Y_z)O_{3-x}$ (reflection 213), and BaY_2CuO_5 (reflection 131). A similar trend was observed for the 790°C experiments. The changes in intensity of the peaks as a function of time are interpreted as due to the progressive formation of Ba$(Ce_{1-z}Y_z)O_{3-x}$ and the green phase, by reaction of $Ba_2YCu_3O_{6+x}$ with CeO_2.

In many solid-state reactions there is a well-defined interface between reacting phases.[14] The overall process involves: (1) transport of material to the interface, (2) reaction at the interface to produce a new product phase, and (3) for some situations, transport of reaction products away from the interface. The two general classes of heterogeneous reactions are those controlled by transport rate, and those controlled by phase-boundary reaction rate.

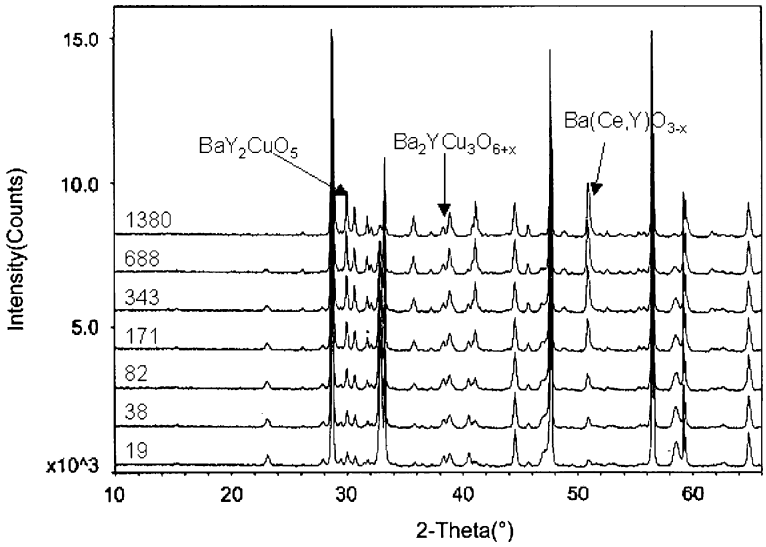

Fig. 3. Sequential X-ray diffraction patterns of a $Ba_2YCu_3O_{6+x}/CeO_2$ pellet heat-treated at 810°C for increasing cumulative time (minutes).

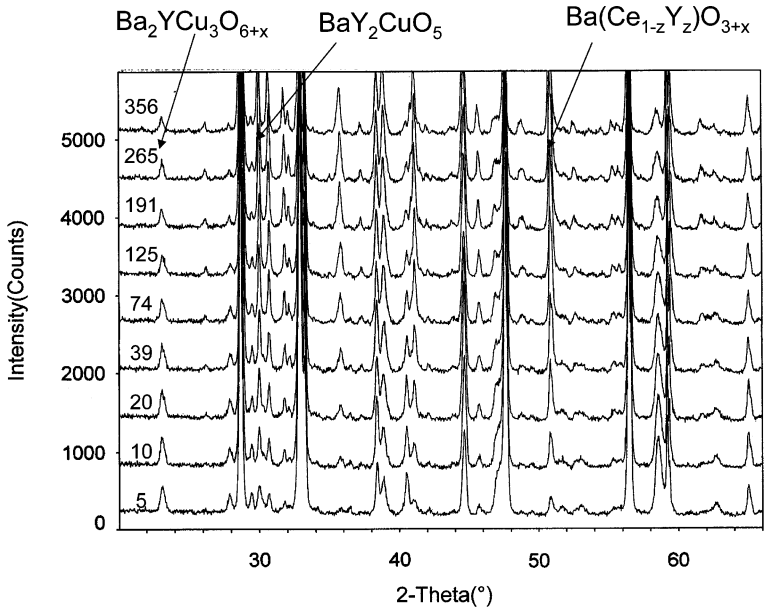

Fig. 4. Sequential X-ray diffraction patterns of a $Ba_2YCu_3O_{6+x}/CeO_2$ pellet heat-treated at 830°C for increasing cumulative time (minutes).

For a reaction in which a compound is formed as a planar reaction layer and the rate of product formation is controlled by diffusion through the product layer, then a parabolic rate law, $x = Kt^{1/2}$, is observed, where x = thickness of the reaction layer, t = time, and K = a constant related to reaction rate.

Under the present conditions, parabolic rate behavior was observed at all three temperatures studied. Plots of X-ray diffraction peak intensity versus $t^{1/2}$ for the experiments at 810°C are shown in Fig. 5. For the product phases $Ba(Ce_{1-z}Y_z)O_{3-x}$ and BaY_2CuO_5, the intensity curves are rather similar. The curves show a linear increase to the longest reaction times, after which further increases in intensity are dramatically less. For the Y-213 reactant phase, intensities showed a concomitant linear decrease with increasing reaction time. The intensity versus $t^{1/2}$ plots for the product phases of the experiments at 790°C and at 830°C are similar to those at 810°C.

When one compares the phase formation of $Ba(Ce_{1-z}Y_z)O_{3-x}$ at the three temperatures (Fig. 6), different rates are clearly evident. For example, at the highest temperature of 830°C, the formation of $Ba(Ce_{1-z}Y_z)O_{3-x}$ exhibits the fastest kinetics, as expected. At this temperature, the formation of $Ba(Ce_{1-z}Y_z)O_{3-x}$ was complete after about 180 min. At 810°C the corresponding time to completion was

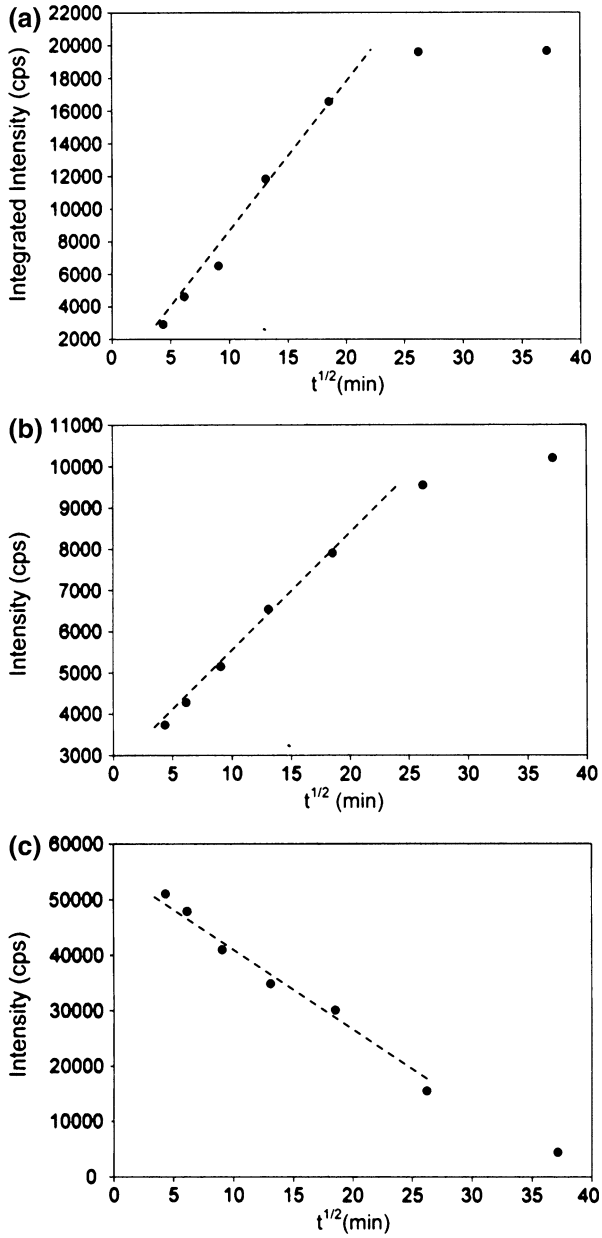

Fig. 5. Plots of integrated intensity versus cumulative (time, minutes)$^{1/2}$ (a) $Ba(Ce_{1-z}Y_z)O_{3-x}$, (reflection 213), (b) BaY_2CuO_5 (reflection 131), and (c) $Ba_2YCu_3O_{6+x}$ (reflection 031) for samples heat-treated at 810°C. cps: counts per second.

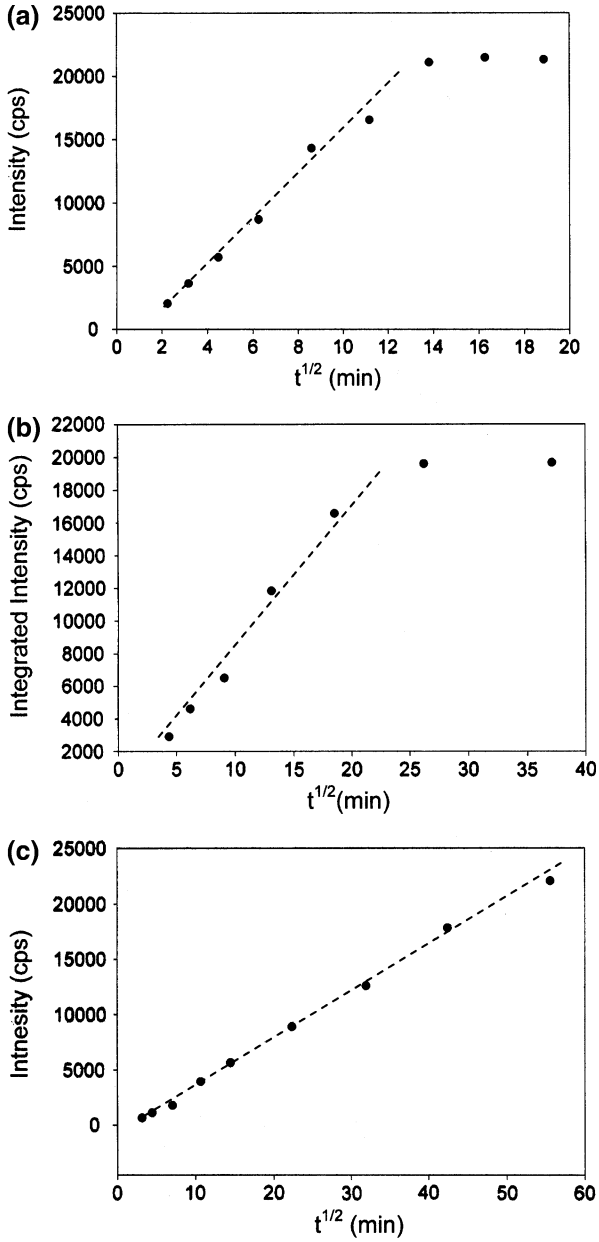

Fig. 6. Plots of integrated intensity versus cumulative (time, minutes)$^{1/2}$ of $Ba(Ce_{1-z}Y_z)O_{3-x}$ (reflection 213) at three different temperatures: (a) 830°C, (b) 810°C, and (c) 790°C. cps: counts per second.

530 min. At 790°C, the reaction was continuing, even after 3600 minutes.

A bright-field TEM image of a cross-section of a sample heat-treated at 830°C for 123 minutes is shown in Fig. 7. Electron energy-loss spectroscopy/energy-dispersive spectroscopy (EELS/EDS) measurements in TEM confirmed existence of a monophasic reaction layer about 0.4 μm thick, comprised of $Ba(Ce_{1-z}Y_z)O_{3-x}$. A mixture of Y-213, green phase, and CuO was observed in the immediate vicinity of $Ba(Ce_{1-z}Y_z)O_{3-x}$, whereas the outer part of the film consisted primarily of unreacted Y-213. Using a thickness of 0.40 μm, the parabolic equation gives a value of 4.7×10^{-3} $\mu m/s^{1/2}$ for K at 830°C.

The activation energy for the reaction was determined using the Arrhenius equation:[12]

$$K_1/K_2 = \left[Ae^{(-E_{act}/RT_1)} \Big/ Ae^{(-E_{act}/RT_2)}\right] \quad (1)$$

where K_1 and K_2 = constants relating to the reaction rate at temperatures T_1 and T_2 (Kelvin), respectively; A = an empirical pre-exponential factor, E_{act} = activation energy, and R = gas constant. K_1 and K_2 were obtained from the parabolic law $x = Kt^{1/2}$, as

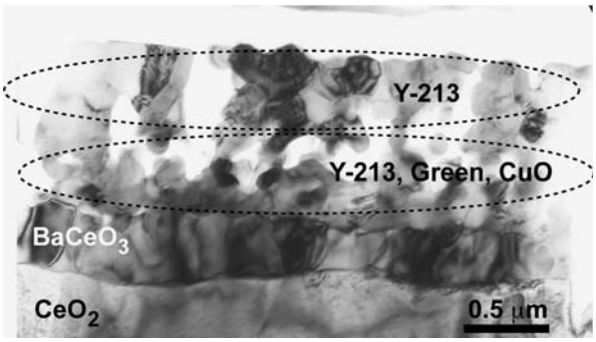

Fig. 7. Bright-field TEM image of a cross-section of a sample heat-treated at 830°C for 123 minutes.

discussed above. From the experiments at 790°C (1063 K) and 830°C (1103 K), K_1 = 0.0016 μm/s$^{1/2}$ and K_2 = 0.0047 μm/s$^{1/2}$, and

$$E_{act} = 2.67 \times 10^5 \text{ J/mol}$$

The standard uncertainty (type B) for the above activation energy is $\pm 0.23 \times 10^5$ J/mol. The activation energy is similar in magnitude to activation energies reported for reactions between other multicomponent ceramic oxides.[15,16]

The fact that a monophasic product layer of $Ba(Ce_{1-z}Y_z)O_{3-x}$ was formed adjacent to the CeO_2 suggests that the reaction occurred primarily by diffusion of Ba into the CeO_2. This process left behind products of green phase and CuO, as indicated by Fig. 7.

Since the present study was completed using polycrystalline substrates, it gives an average reaction rate summed over all crystallographic orientations. The data presented here provide a first approximation to the actual reaction rates expected for highly textured CeO_2 cap layers with the overlying superconductor. A parallel study using epitaxial CeO_2 is underway.

SUMMARY

We have studied the kinetics of reaction of the $Ba_2YCu_3O_{6+x}$ superconductor phase with CeO_2, one of the most promising buffer layers for coated conductor architecture. The reaction involves two four-phase fields and the reaction products are $Ba(Ce_{1-z}Y_z)O_{3-x}$, BaY_2CuO_5, and CuO. We followed the kinetics of reaction by monitoring the product phases $Ba(Ce_{1-z}Y_z)O_{3-x}$ and BaY_2CuO_5 as a function of time and temperature. The reaction kinetics obey a simple parabolic rate law, characteristic of diffusion-limited processes. The activation energy for the reaction between $Ba_2YCu_3O_{6+x}$ and CeO_2 has been estimated using the Arrhenius equation to be 2.67×10^5 J/mol. Studies of interfacial reactions of $Ba_2YCu_3O_{6+x}$ with other important substrate materials for coated conductor applications, such as $SrTiO_3$ and Gd_3NbO_7, are planned.

ACKNOWLEDGEMENTS

This project was partially supported by the U.S. Department of Energy. Nils Swanson of NIST is thanked for his graphical assistance. We are grateful to Edward Nie of Severna Park High School, Maryland, for his help with substrate preparation and some of the early exploratory experiments. We also acknowledge valuable discussions with our colleagues, Drs. A. Goyal, M. Paranthaman, and R. Feenstra from Oak Ridge National laboratory, and Dr. T. Holesinger from Los Alamos National Laboratory.

REFERENCES

1. US Department of Energy high temperature superconductivity program; for details, visit web site http://www.eere.energy.gov/EE/power_superconductivity.html
2. S.R. Foltyn, E.J. Peterson, J.Y. Coulter, P.N. Arendt, Q.X. Jia, P.C. Dowden, M.P. Maley, X.D. Wu, and D.E Peterson, *J. Mater. Res.* 12, 2941 (1997).
3. M.R.H. Bauer Semerad Kinder, *IEEE Trans. Appl. Supercond.* 9(2), 1502 (1999).
4. A.P. Malozemoff, S. Annavarapu, L. Fritzemeier, Q. Li, V. Prunier, M. Rupich, C. Thieme, W. Zhang, A. Goyal, M. Paranthaman, and D.F. Lee, *Supercond. Sci. Technol.* 13(5), 473 (2002).
5. M. Paranthaman, C. Park, X Cui, A. Goyal, D.F. Lee, P.M. Martin, T.G. Chirayil, D.T. Verebelyi, D.P. Norton, D.K. Christen, and D.M. Kroeger, *J. Mater. Res.* 15(12), 2647 (2000).
6. A. Goyal, D.F. Lee, F.A. List, E.D. Specht, R. Feenstra, M. Paranthaman, X. Cui, S.W. Lu, P.M. Martin, D.M. Kroeger, D.K. Christen, B.W. Kang, D.P. Norton, C. Park, D.T. Verebelyi, J.R. Thompson, R.K. Williams, T. Aytug, and C. Cantoni, *Physica C* 357, 903 (2001).
7. T. Aytug, A. Goyal, N. Rutter, M. Paranthaman, J.R. Thompson, H.Y. Zhai, and D.K. Christen, *J. Mater. Res.* 18(4), 872 (2003).
8. M.W. Rupich, W. Zhang, X. Li, T. Kodenkandath, D.T. Verebelyi, U. Schoop, C. Thieme, M. Teplitsky, J. Lynch, N. Nguyen, E. Siegal, J. Scudiere, V. Maroni, K. Venkataraman, D. Miller, and T.G. Holesinger, *Physica C* 412–414, 877 (2004).
9. M. Rupich, American Superconductor Corporation, private communication (2000).
10. W. Wong-Ng, Z. Yang, L.P. Cook, Q. Huang, J.A.1 Kaduk, and J. Frank, *Solid State Sci.* 7, 1333 (2005).
11. W. Wong-Ng, L.P. Cook, P. Schenck, I. Levin, Z. Yang, Q. Huang and J. Frank (Proceedings of the PACRIM meeting, sponsored by ACerS, Maui, Hawaii, September, 2005) *Ceramic Trans.* 191, 83 (2006).
12. K.J. Laidler, *Chemical Kinetics,* 3rd ed. (Benjamin-Cummings, 1997).
13. M.W. Chase Jr., *NIST-JANAF Thermochemical Tables,* 4th ed. *J. Phys. Chem. Ref. Data*, Monograph No. 9 (1998).
14. W.D. Kingery, H.K. Bowen, and D.R. Uhlmann, *Introduction to Ceramics*, 2nd ed. (New York, USA: Wiley, 1976), pp 381–447.
15. J.-T. Shiue and T.-T. Fang, *J. Mater. Res.* 18(11), 2594 (2003).
16. J. Xu, X.H. Zhu, and Z.V. Meng, *IEEE Trans. Comp. Pack. Technol.* 22(1), 11 (1999).

Journal of ELECTRONIC MATERIALS, Vol. 36, No. 10, 2007
DOI: 10.1007/s11664-007-0227-0

Phase Equilibria of $BaO\text{-}R_2O_3\text{-}CuO_z$ Systems (R = Y and Lanthanides) under CO_2-free Conditions

W. WONG-NG,[1,5] Z. YANG,[1,2] L.P COOK,[1] J. FRANK,[1] M. LOUNG,[3] and Q. HUANG[4]

1.—Ceramics Division, National Institute of Standards and Technology, Gaithersburg, MD 20899, USA. 2.—Chemistry Department, Yunnan Normal University, Kunming 650092, P. R. China. 3.—Chemistry Department, University of Maryland, College Park, MD 20742, USA. 4.—Center for Neutron Research, National Institute of Standards and Technology, Gaithersburg, MD 20899, USA. 5.—e-mail: winnie.wong-ng@nist.gov

For applications ranging from phase equilibria to the processing of second-generation high T_c superconductor-coated-conductors, phase diagrams constructed under carbonate-free conditions are needed. Subsolidus phase equilibria of $BaO\text{-}R_2O_3\text{-}CuO_z$ (R = Ho) have been investigated at $p_{O_2} = 100$ Pa (810°C), 21 kPa (875°C) and 0.1 MPa (850 and 930°C) by applying controlled atmosphere methods to minimize the presence of carbonate and CO_2 and H_2O contamination. Under carbonate-free conditions, most of these phase diagrams are different from those reported in the literature. In this paper, we also review and compare the phase diagrams of ten $BaO\text{-}R_2O_3\text{-}CuO_z$ systems (R = Nd, Sm, Eu, Gd, Dy, Y, Ho, Er, Tm and Yb) that were previously determined in this laboratory under $p_{O_2} = 100$ Pa. Among these diagrams, a distinct trend of phase formation and tie-line relationships is observed.

Key words: Superconductors, phase equilibria, $BaO\text{-}R_2O_3\text{-}CuO_z$ (R = lanthanides and Y), second generation coated conductors, carbonate-free conditions

INTRODUCTION

Phase diagrams are considered blueprints for improving processing of second-generation coated-conductors.[1–5] Currently this state-of-the-art conductor technology holds the most promise for commercial electric utility and high magnetic field applications. Second-generation superconductors are based on epitaxial films of $Ba_2RCu_3O_{6+z}$ (R = lanthanides) and $Ba_2YCu_3O_{6+z}$ materials[6–8] separated from the underlying flexible, textured metallic conductor by one or more layers of epitaxial oxide buffer. The two most promising technologies for preparing coated metallic substrates suitable for deposition of high T_c superconductors are known as the rolling-assisted biaxially textured substrate method (RABiTS)[1–3] and the ion beam-assisted deposition method (IBAD).[4,5]

It is essential to have a database for the phase diagrams of the entire $BaO\text{-}R_2O_3\text{-}CuO_z$ series as a guide for superconductor processing using the RABiTS and IBAD technologies. The goal of the present paper is twofold. The first goal is to summarize and compare the phase diagrams of the ten $BaO\text{-}R_2O_3\text{-}CuO_z$ systems (R = Nd, Sm, Eu, Gd, Dy, Y, Ho, Er, Tm and Yb) that were previously prepared in our laboratory under carbonate-free conditions (T = 810°C, $p_{O_2} = 100$ Pa).[9–14] This set of experimental conditions was chosen to match the processing conditions of the IBAD and RABiTS films. Although various phase diagrams of the $BaO\text{-}R_2O_3\text{-}CuO_z$ systems are available in literature,[7,15–22] the majority of these diagrams were prepared using $BaCO_3$ as one of the starting reagents, undoubtedly because of the difficulty in handling BaO. Those few studies that reported using BaO were not carried out entirely under atmospherically controlled conditions. The second goal of our work is to study the effect of different temperatures and oxygen partial pressures on the $BaO\text{-}R_2O_3\text{-}CuO_z$ phase equilibria under carbonate-free conditions. For this purpose, we have chosen to

(Received February 7, 2007; accepted April 3, 2007; published online September 21, 2007)

concentrate on the BaO-Ho_2O_3-CuO system at $p_{O_2} = 100$ Pa (810°C), $p_{O_2} = 21$ kPa (purified air, 875°C), and at $p_{O_2} = 0.1$ MPa (850 and 930°C).

The crystal chemistry and crystal structure of most of the compounds of the BaO-R_2O_3-CuO_z systems have been reported extensively elsewhere and will not be discussed in detail here, except for the selected few which are relatively new phases.

EXPERIMENTAL*

The experimental details for the BaO-R_2O_3-CuO_z systems at $p_{O_2} = 100$ Pa (0.1% O_2 volume fraction in Ar, 810°C) have been discussed previously.[9–14] The experimental procedure for the study of the BaO-Ho_2O_3-CuO_z system under purified air (p_{O_2} = 21 kPa, or 21% O_2 by volume fraction in Ar, 875°C) and 0.1 MPa p_{O_2} (100% O_2 by volume fraction at 850 and 930°C) is given below.

Preparation of BaO

BaO starting material was produced from $BaCO_3$ (99.99% purity, metals basis) by vacuum calcination in a specially designed vertical tube furnace. An MgO crucible containing ≈15 g of $BaCO_3$ was suspended in the hot zone of the furnace, and the furnace was evacuated to a pressure of ≈1.33 Pa or less by a high capacity mechanical pump. The following heating schedule was used: room temperature to 1300°C in 20 h; isothermal at 1300°C for 10 h; 1300°C to room temperature in 20 h. During the vacuum calcination the pressure typically increased to ≈200 μm Hg as CO_2 was evolved, and then rapidly returned to ≈10 μm Hg or less as the decomposition of the $BaCO_3$ was completed. After cooling, the BaO was lowered through an interlock into a transfer vessel. It was then transported to an Ar-filled glovebox equipped with a recirculating purifier, which continually removed atmospheric contaminants from the Ar to $<10^{-4}$% (1 ppm) by volume.

Sample Preparation

All sample weighings, homogenizations and pellet pressings were performed inside a glove-box. Pelletized samples were placed inside individual MgO crucibles for annealing in a horizontal box-type controlled-atmosphere furnace. Transfer from the glove-box to the box furnace and *vice versa* was achieved via a second transfer vessel and an interlock system attached to the furnace. Samples were prepared using the solid state sintering method (Table I). Stoichiometric amounts of BaO, Ho_2O_3 (99.99% purity, metals basis), and CuO (99.99% purity, metals basis) were mixed and pressed into pellets, and annealed in an atmospherically controlled box furnace. During the annealings, the oxygen pressure of Ar/O_2 mixtures was controlled using a mass flow meter and monitored at both the inlet and outlet of the furnace using a zirconia oxygen sensor. Samples were annealed at 875°C for the experiments at $p_{O_2} = 21$ kPa (at 875°C) and at $p_{O_2} = 0.1$ MPa (at 850 and at 930°C). Intermediate grindings and pelletizations took place until no further changes were detected in the powder X-ray diffraction patterns. Samples were processed for about 2 weeks each.

X-ray Powder Diffraction

X-ray powder diffraction was used to identify the BaO-Ho_2O_3-CuO_z phases synthesized and to confirm phase purity. Specimens were loaded into a hermetically sealed cell[23] inside an Ar-filled glove box. Data were collected using a computer-controlled automated diffractometer equipped with a theta-compensation slit; CuK_α radiation was used at 45 kV and 40 mA. The radiation was detected by a scintillation counter and a solid-state amplifier. A Siemens diffraction software package and reference X-ray diffraction patterns of the ICDD Powder Diffraction File (PDF)[24] were used for phase identification.

RESULTS AND DISCUSSION

Phase Diagrams of the Ba-Ho-Cu-O System as a Function of Oxygen Partial Pressure

The phase diagram of the BaO-Ho_2O_3-CuO_z system that was prepared at 100 Pa p_{O_2} was reported earlier,[13] and is shown in Fig. 1a for comparison purpose. The three phase diagrams of the BaO-Ho_2O_3-CuO_z systems prepared under purified air (875°C) and 0.1 MPa p_{O_2} (at 850 and 930°C) are shown in Fig. 1b–d.

BaO-CuO_z

A review of the crystal chemistry and crystallography of the phases in the BaO-CuO_z system was given by Wong-Ng and Cook.[25] In the present study, we have observed a total of two binary compounds: Ba_2CuO_{3+z} and $BaCuO_{2+z}$,[26–29] whereas under $p_{O_2} = 100$ Pa, the $BaCu_2O_{2+z}$ phase (Fig. 1) is also observed. The Ba_2CuO_{3+z} phase is atmospherically sensitive and cannot be prepared in the presence of moisture and carbonate; this phase has not been reported in several previous studies of the BaO-CuO_z binary. The oxygen content of the $BaCuO_{2+z}$ series has been reported to vary between 2.0 and 2.5. Three structure types of $BaCuO_{2+z}$ are known, with $0 < z < 0.12$, $0.29 < z < 0.36$, and $z = 0.5$. The most commonly recognized structure is cubic, with $0 < z < 0.12$. Phase compositions with z greater than 0.12 have been reported by Petricek et al. [30] We found no evidence for the existence of the $Ba_2Cu_3O_{5+z}$ or $Ba_3Cu_5O_{8+z}$ phases[25] under the current conditions. The Ba_3CuO_4 phase, reported by Frase

*Certain trade names and company products are mentioned in the text or identified in illustrations in order to adequately specify the experimental procedure and equipment used. In no case does such identification imply recommendation or endorsement by National Institute of Standards and Technology.

Table I. Compositions (Mole Fraction, %) of Samples Prepared for Studies in the BaO-Ho_2O_3-CuO_z System at p_{O_2} = 21 kPa (T = 875°C), 0.1 MPa (T = 850°C and 930°C)

#	Ba	Ho	Cu	#	Ba	Ho	Cu
1	60	10	30	2	50	17	33
3	65	17.5	17.5	4	70	5	25
5	58	3	39	6	54	8	38
7	52	12	36	8	40	40	20
9	49	11	40	10	40	20	40
11	35	60	5	12	20	70	10
13	25	25	50	14	40	5	55
15	25	5	70	16	10	35	55
17	10	65	25	18	50	25	25
19	45	10	45	20	35	53	12
21	42	14	44	22	45	45	10
23	58	11	31	24	45	15	40

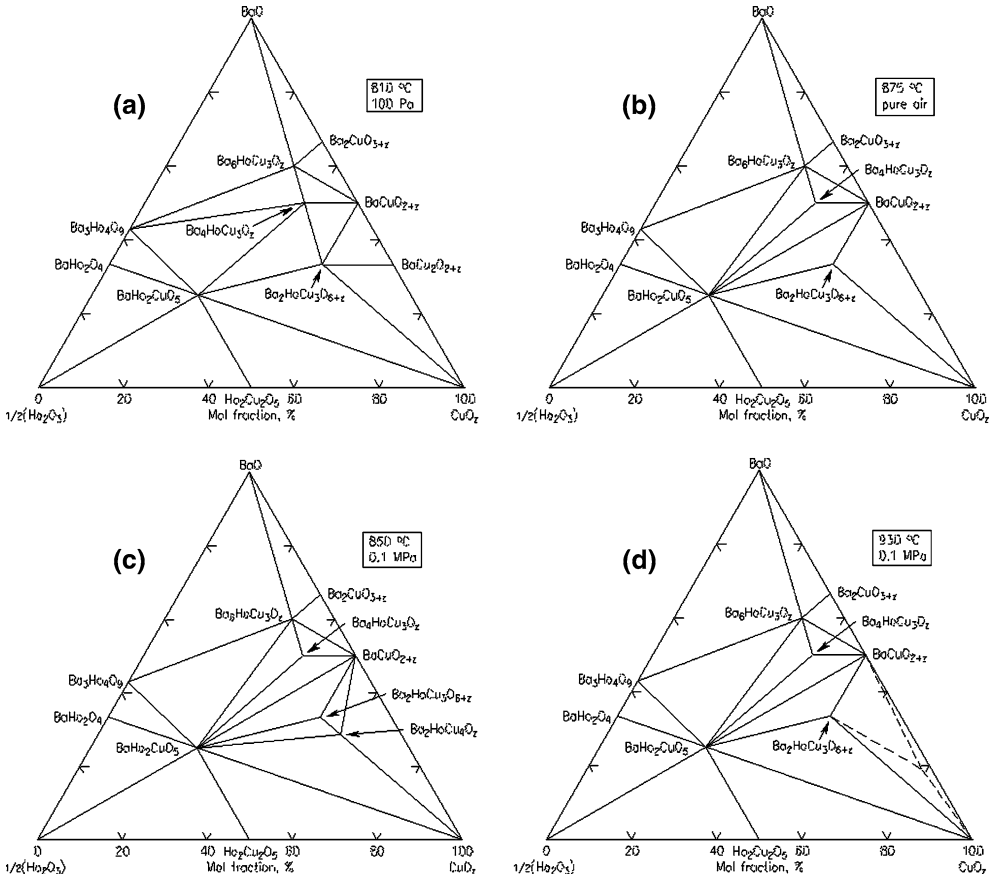

Fig. 1. Phase diagrams of the BaO-Ho_2O_3-CuO_z system prepared at (a) p_{O_2}=100 Pa (T = 810°C),[13] (b) 21 kPa (T = 875°C), (c) 0.1 MPa (T = 850°C), and (d) 0.1 MPa (T = 930°C). Eutectic melting of the system takes place at 925°C (p_{O_2} = 0.1 MPa) in the region bounded by $Ba_2HoCu_3O_{6+z}$, CuO_z and $BaCuO_{2+z}$.

and Clarke[31] and Abbattista et al.[32,33] to be stable only under extremely reduced conditions, was not detected in the present study.

BaO-Ho_2O_3

$Ba_3Ho_4O_9$ and $BaHo_2O_4$ were the only two phases formed under the three processing conditions investigated in this study. $BaHo_2O_4$ was reported to crystallize in the orthorhombic *Pnam* system, which is isostructural with other BaR_2O_4 phases.[34,35] There was a controversy about the definitive structure of $Ba_3R_4O_9$. Kovba et al.,[36] Spitsyn[37] and Wong-Ng et al.[38] reported the symmetry of the structure to be *Rm*; however, according to Müeller-Buschbaum

and Scheikowski,[39] Müller-Buschbaum and Schvandt,[40] and Krueger and Mueller-Buschbaum,[41,42] $Ba_3R_4O_9$ is trigonal with an *R3* space group (a = 6.098 Å, c = 25.136 Å; Z = 3[39]). The *R3* structure of $Ba_3R_4O_9$ consists of corner-shared planar HoO_6 octahedra and HoO_6 trigonal prisms connected as a Kagomè-network. The Ba sites have a (6 + 3) coordination.[39,40] The Ba-rich $Ba_4HoR_2O_7$ and $Ba_2Ho_2O_5$ phases were found to be absent in the BaO-Ho_2O_3 system. These two phases, which are in fact the oxycarbonates $Ba_2Ho_2O_5 \cdot CO_2$ and $Ba_4Ho_2O_7 \cdot 2CO_2$ respectively,[43] are present when $BaCO_3$ is used as a starting material, and dissociate according to the following reactions:

$$3Ba_2Ho_2O_5 \cdot CO_2 \rightarrow 2BaHo_2O_4 + Ba_4Ho_2O_7 \cdot 2CO_2 + CO_2$$

$$2Ba_4Ho_2O_7 \cdot 2CO_2 \rightarrow Ba_3Ho_4O_9 + 5BaO + 4CO_2$$

As carbonate appears to be essential for their formation, it is logical that they were not observed under the conditions of our experiments.

Ho_2O_3-CuO_z

In the binary Ho_2O_3-CuO_z diagrams, only the $Ho_2Cu_2O_5$ phase was observed under all three processing oxygen partial pressures.[13] The reported Ho_2CuO_4 phase was prepared using the aqueous solution route via high pressure processing[44] and is not stable under current conditions. Similarly, the reported reduced phase of the $RCuO_2$ structure type[45] was not found.

BaO-Ho_2O_3-CuO_z

A total of four ternary oxides ($Ba_2HoCu_3O_{6+z}$ (213), $Ba_4HoCu_3O_z$ (413), $Ba_6HoCu_3O_z$ (613), and the 'green phase' $BaHo_2CuO_5$ (121)) were found in the BaO-Ho_2O_3-CuO_z system. The occurrence of the compounds $Ba_4HoCu_3O_z$ and $Ba_6HoCu_3O_z$ in the BaO-rich part of the diagram is similar to that of the BaO-Y_2O_3-CuO_z[11] system. The structure of $Ba_4HoCu_3O_z$ was reported to be of the cubic oxygen-defect perovskite type (a = 8.08236(5) Å when prepared in oxygen).[46] The orthorhombic $Ba_6HoCu_3O_z$ phase is of the $SrTi_2O_4$-type (layered perovskite structure).[47] The $BaHo_2CuO_5$ "green phase" is isostructural with BaY_2CuO_5.[48–50] Similar to $Ba_2YCu_3O_{6+z}$, the $Ba_2HoCu_3O_{6+z}$ phase is a stoichiometric compound with respect to the cation content.

There is a significant difference in tie-line connections under different processing conditions. These differences mainly occur in two regions. The first one is bounded by $BaHo_2CuO_5$, $Ba_2HoCu_3O_{6+z}$, $BaCuO_{2+z}$, and $Ba_4HoCu_3O_z$, and the second one by $Ba_4HoCu_3O_z$, $BaHo_2CuO_5$, $Ba_3Ho_4O_9$ and $Ba_6HoCu_3O_z$. It was reported previously that under 100 Pa p_{O_2}, the tie-line in the first region occurs between $Ba_2HoCu_3O_{6+z}$ and $Ba_4HoCu_3O_z$, and in the second region it is between $Ba_3Ho_4O_9$ and $Ba_4HoCu_3O_z$. However, under the oxygen-rich conditions, namely under purified air as well as under 0.1 MPa p_{O_2}, the tie-lines in both regions are between $BaHo_2CuO_5$ and $BaCuO_{2+z}$ in the first region, and between $BaHo_2CuO_5$ and $Ba_6HoCu_3O_z$ in the second region, respectively. It is apparent that both oxygen partial pressure and the ionic size of R have a significant influence in the tie-line relationships.

Under 0.1 MPa p_{O_2} at 850°C, we observed an additional $Ba_2HoCu_4O_{8+z}$ (214) phase in the CuO-rich region. The 80 K $Ba_2YCu_4O_{8+z}$ phase[51] was first observed as an intergrowth in $Ba_2YCu_3O_{6+z}$ and forms a planar defect in which a second CuO layer is introduced between BaO layers, thereby increasing the Y–Y distance from 11.7 to 13.6 Å. Because the positions of Cu in the Cu-O layers differ by $a/2$ along the a-axis, c is doubled to about 27.2 Å.

Eutectic melting of the BaO-Ho_2O_3-CuO_z system under 0.1 MPa p_{O_2} takes place at around 925°C according to

$$Ba_2HoCu_3O_{6+z} + BaCuO_2 + CuO_z \rightarrow L \text{ (Liquid)}$$

At about 930°C, $Ba_2HoCu_3O_{6+z}$ is relatively more stable than the $Ba_2HoCu_4O_{8+z}$ phase. $Ba_2HoCu_4O_{8+z}$ decomposes according to

$$Ba_2HoCu_4O_{8+z} \rightarrow Ba_2HoCu_3O_{6+z} + CuO_z + O_2 \uparrow$$

The Trend of the BaO-R_2O_3-CuO_z Diagrams (R = Nd, Sm, Eu, Gd, Dy, Ho, Y, Er, Tm and Yb) as a Function of the Ionic Size of R^{3+} Under 100 kPa p_{O_2}

The ternary phase compatibility diagrams of the BaO-R_2O_3-CuO_z systems, where R = Nd, Sm, Eu, Gd, Dy, Ho, Y, Er, Tm and Yb, are shown in Fig. 2a–j.[9–14] For ease of comparison, the diagram for R=Ho (Fig. 1a) is repeated here as Fig. 2f. Since exact tie-line connections would require detailed lattice parameter determinations, the tie-lines connecting the solid solution series in this report are schematic only. Proceeding from the Nd-system, which has the largest ionic size of R in the current series, towards the Tm system with a smaller ionic size, a general trend in phase formation, solid solution formation, and phase relations is found to be correlated with the ionic size of R. Several features of the progressive changes in the appearance of these ternary diagrams will be discussed below. In brief, these features are the following: (1) the Nd-system has the largest number of ternary compounds and solid solution series; this number decreases as the ionic size of R decreases; (2) the superconductor phases, $Ba_2RCu_3O_{6+z}$, for the first half of the lanthanide elements, i.e., R = Nd, Sm, and Eu, which are relatively larger in the ionic size of R, exhibit a solid solution of $Ba_{2-x}R_{1+x}Cu_3O_{6+z}$, with a range of formation which decreases as the ionic size of R decreases; this solid solution region

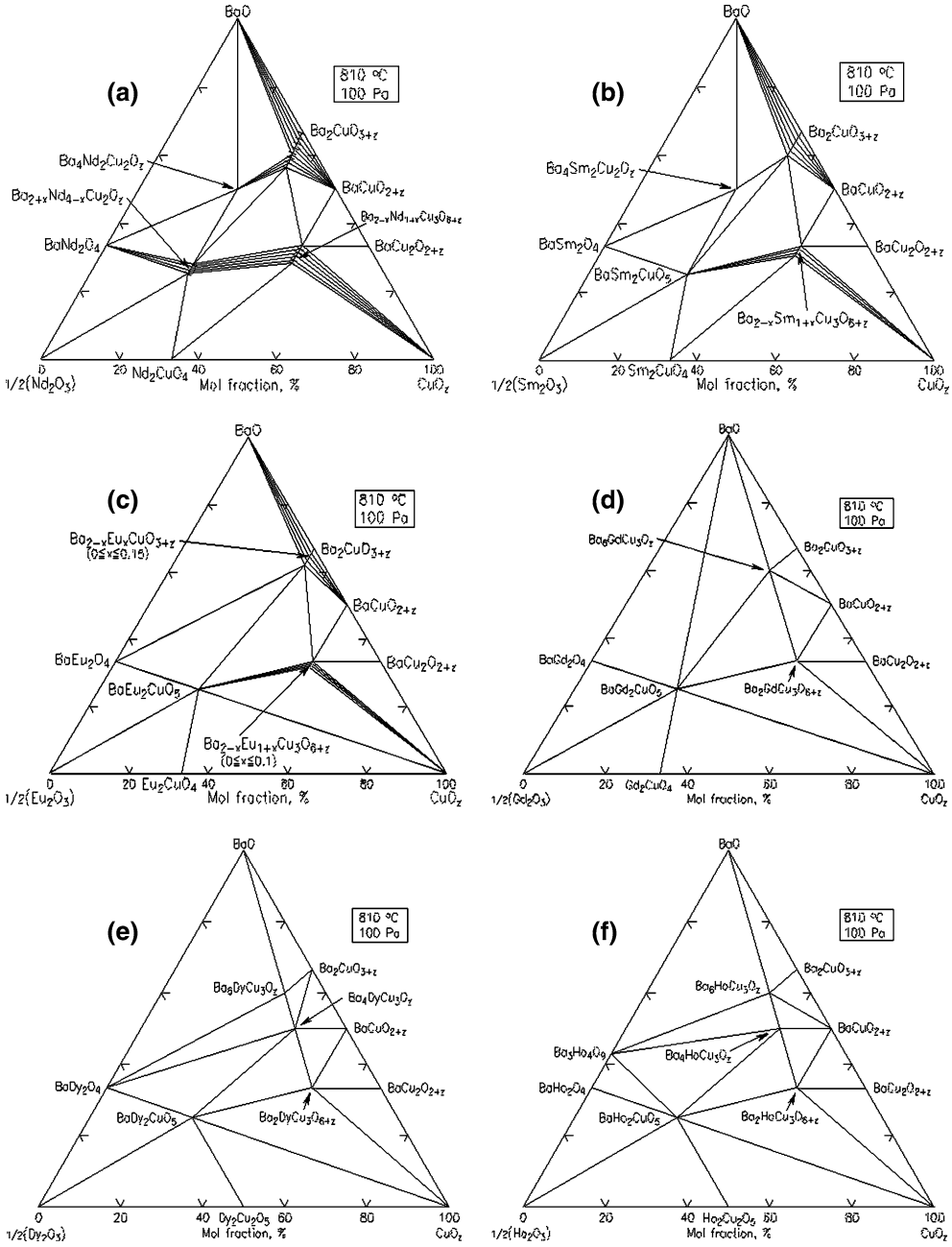

Fig. 2. Phase diagram of the BaO-R_2O_3-CuO_z systems prepared at $p_{O_2} = 100$ Pa ($T = 810$°C): (a) R = Nd, (b) R = Sm, (c) R = Eu, (d) R = Gd, (e) R = Dy, (f) R = Ho, (g) R = Y, (h) R = Er, (i) R = Tm, and (j) R = Yb.[9–14]

terminates at Gd and beyond, where the superconductor phase assumes a point cation stoichiometry; (3) a trend is observed regarding the tie-line connections between BaR_2CuO_5, CuO, $Ba_{2-x}R_{1+x}Cu_3O_{6+z}$, and the binary phases R_2CuO_4, or $R_2Cu_2O_5$. The binary phase R_2CuO_4 is replaced by $R_2Cu_2O_5$ after the tie-line connection changes.

Phase Formation

(1) BaO-R_2O_3

Under 100 Pa p_{O_2}, two phases (BaR_2O_4 and $Ba_3R_4O_9$) were successfully prepared in the BaO-R_2O_3 system. Depending on the ionic size of R, there is a trend in formation of these two phases. The BaR_2O_4 phase forms in the systems with relatively larger R (Nd, Sm, Eu, Gd, Dy, Ho, Y, and Er), while $Ba_3R_4O_9$ forms in the relatively smaller R systems (Ho, Y, Er, Tm, Yb and Lu).

(2) R_2O_3-CuO_z

While all the R_2O_3-CuO_z systems contain only one binary compound, there exist two distinctive compositions. Binary compounds of 2:1 composition with general formula R_2CuO_4 can be prepared with the

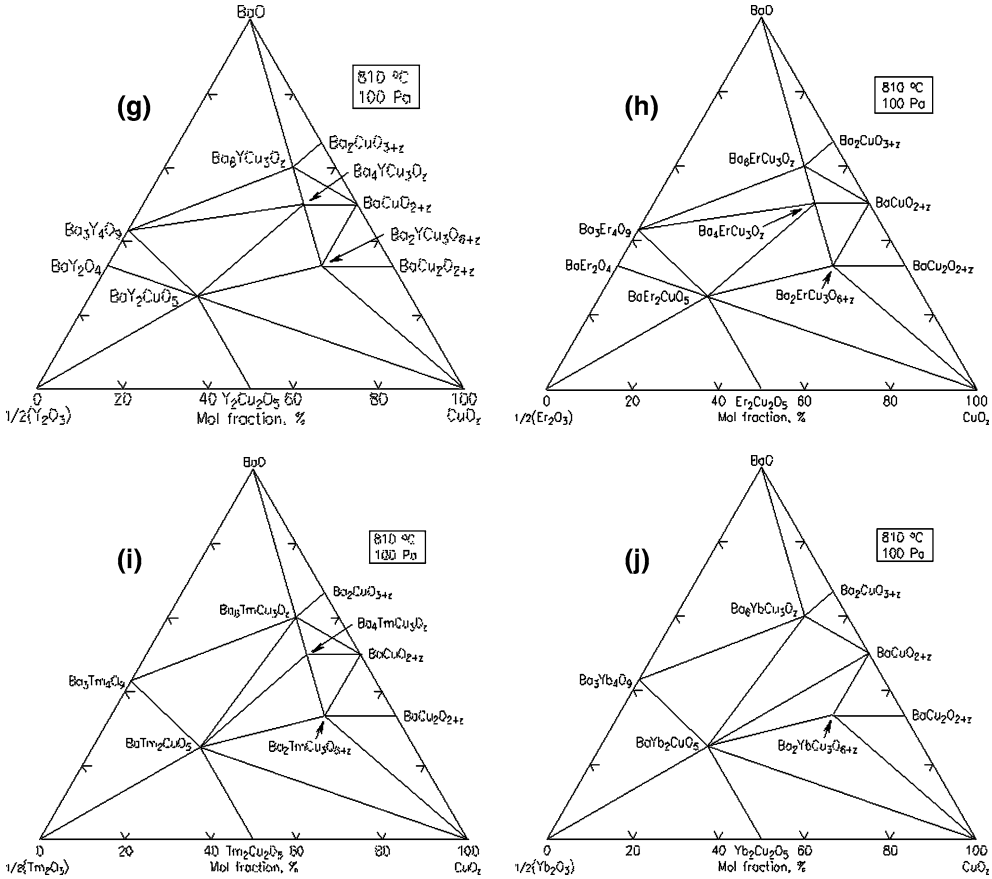

Fig. 2. Continued.

lighter and larger ionic size of R, for example with R = Nd, Sm, Eu and Gd, whereas oxides in the second half of the lanthanide series tend to form a R_2O_3:2CuO binary compound $R_2Cu_2O_5$ (R = Dy, Ho, Y, Er, Tm, Yb, and Lu). Not all R_2CuO_4 phases in the lanthanide series are isostructural. For example, while Nd_2CuO_4, Sm_2CuO_4, Eu_2CuO_4, and Gd_2CuO_4 are tetragonal with space $I4/mmm$,[52] La_2CuO_4 is orthorhombic with space group *Cmca* and has distorted K_2NiF_4-type structure.[53] Structure determination of $R_2Cu_2O_5$ have been controversial in the past 25 years. The structure and X-ray diffraction patterns of seven $R_2Cu_2O_5$ compounds were later re-examined by Lambert and Eysel in 1981 and 1982;[54] they were found to be isostructural and have the $Ho_2Cu_2O_5$-type structure with space group $Pna2_1$.[13]

(3) BaO-R_2O_3-CuO_z system

$Ba_{2-x}R_{1\pm x}Cu_3O_{6\pm z}$

The high T_c superconductor solid solution, $Ba_{2-x}R_{1+x}Cu_3O_{6+z}$, is of technological importance because one can tailor the superconductor and melting properties by varying the content of x. The members of this solid solution (R = Nd, Sm, and Eu), exhibit different solid solution extent. The tendency of the solid solution formation is particularly great for the Nd-analog because of the close match of the ionic size of Nd^{3+} and Ba^{2+}.[55] As a result, the formation of $Ba_2NdCu_3O_{6+z}$ is rather difficult to control and single-phase material is difficult to prepare. The range of solid solution is smaller as the oxygen partial pressure decreases. The extent of x in $Ba_{2-x}R_{1+x}Cu_3O_{6+z}$ encompasses a range of $0 \le x \le 0.3$ for Nd, $0 \le x \le 0.2$ for Sm, and $0 \le x \le 0.1$ for Eu. The $Ba_2GdCu_3O_{6+z}$ phase does not form solid solution at p_{O_2}<100 Pa, whereas when the sample is prepared in air, a narrow solid solution region of $0 \le x \le 0.1$ can be obtained.[7]

$Ba_{2-x}R_xCuO_{3\pm z}$

When R is relatively large, the Ba-rich Ba_2CuO_{3+z} phase can form solid solution, with R (R = Nd, Sm, and Gd) substituting at the Ba site, giving rise to $Ba_{2-x}R_xCuO_{3+z}$. The value of x was found to be $0 \le x \le 0.3$ for Nd; $0 \le x \le 0.2$ for Sm; and $0 \le x \le 0.15$ for Eu. This solid solution is only stable in an essentially carbonate-free system. According to Abbattista et al.,[56] $Ba_{2-x}Nd_xCuO_{3+z}$ undergoes a phase transition at 740°C, with the high-temperature form being tetragonal with a K_2NiF_4-type structure, and the low-temperature form being orthorhombic with a structure derived from that of Sr_2CuO_3. We found that the $Ba_{2-x}R_xCuO_{3+z}$ samples (prepared under

100 Pa p_{O_2}) can be indexed as orthorhombic, *Immm*. The lattice parameters of the orthorhombic $Ba_{2-x}Sm_xCuO_{3+z}$ phases were found to be: a = 12.995(6) Å, b = 4.096(2) Å, c = 3.904(2) Å, and V (volume) = 207.77 (13) Å^3 for Ba_2CuO_{3+z} (x = 0); a = 12.890(21) Å, b = 4.035(6) Å, c = 3.880(5) Å, and V = 201.8(3) Å^3 for $(Ba_{1.9}Sm_{0.1})CuO_{3+z}$ (x = 0.1); and a = 12.797 (32) Å, b = 4.048(10) Å, c = 3.843(11) Å, and V = 199.1(6) Å^3 for $(Ba_{1.8}Sm_{0.2})CuO_{3+z}$ (x = 0.2). Substitution of the smaller Sm^{3+} into the larger Ba^{2+} site causes the contraction of the unit cell.

BaR_2CuO_5

The commonly known "green phase", or the BaR_2CuO_5 (121) phase, can be prepared for R = Sm, Eu, Gd, Dy, Y, Ho, Er, Tm and Yb. Among the oxides with a stable R^{3+} valence state, there is a size range of R for which this phase forms. However, this phase does not form with lanthanides of larger ionic size. For example, the formation of green phases for R = Nd^{3+} does not take place. The material formed in this case is brown and is found to have a completely different crystal structure from that of the "green phase". While all green phase materials are orthorhombic with space group *Pbnm*, the "brown phase" tends to form a solid solution with formula $Ba_{2+2x}Nd_{4-2x}Cu_{2-x}O_{10-2x}$ ($0.0 \le x \le 0.1$), and with a tetragonal space group *P4/mbm*. The framework of the Nd "brown phase" is principally built from edge- and face-sharing RO_{10} and RO_8 polyhedra. These octahedra and decahedra provide large enough space to accommodate the Nd^{3+} ions. On the other hand, in the green phase structure, each lanthanide ion is surrounded by seven oxygen neighbors. The framework can be considered as being built from distorted monocapped trigonal prisms, RO_7, which share one triangular face forming R_2O_{11} blocks. There is an apparent upper size limit, bounded by Sm, beyond which stability of the monocapped trigonal prism, RO_7, is unattainable.

$Ba_4R_2Cu_2O_{9-z}$

Within the $BaO\text{-}R_2O_3\text{-}CuO_x$ systems, the $Ba_4R_2Cu_2O_{9-z}$ phase only exists in those with relatively large R^{3+}, namely, R = Nd and Sm. The $Ba_4Nd_2Cu_2O_{9-z}$ structure is tetragonal with a space group of $P\bar{4}n2$ (a = 11.9505(8) Å and c = 3.8556(2) Å by neutron diffraction).[10] This semiconductor phase is one of the first cuprate phases reported which possesses the unusual 1-dimensional chains of CuO_5 units. The (001) projection of the $Ba_4R_2Cu_2O_{9-z}$ structure is shown in Fig. 3a, and the one-dimensional chains of CuO_5 are shown in Fig. 3b. These distorted and isolated CuO_5 units form corner-shared infinite chains running parallel to the c-axis. The CuO_5 chains are connected via Ba^{2+} and R^{3+} cations, which themselves adopt distorted monocapped trigonal prismatic configurations (RO_7 and BaO_7). Octagonal tunnels are found throughout the

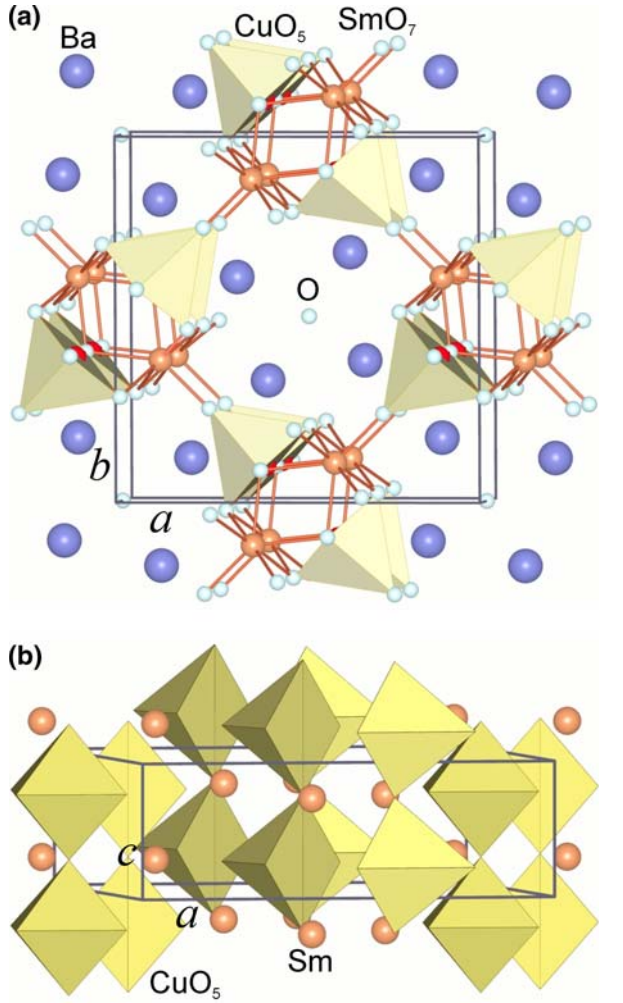

Fig. 3. (a) Crystal structure of the $Ba_4R_2Cu_2O_9$ phase showing the (001) projection; (b) Crystal structure of the $Ba_4R_2Cu_2O_9$ phase showing the one-dimensional corner-sharing chains of CuO_5 square-pyramids along the c-axis.[10]

structure. The R^{3+} environment in $Ba_4R_2Cu_2O_{9-z}$ is rather different from that of the "brown phase" $BaNd_2CuO_5$ in which the Nd has an eightfold coordination,[34] but is similar to that of the "green phase" $BaSm_2CuO_5$.[10] The structure of $Ba_4Sm_2Cu_2O_{9-z}$ was, however, found to be orthorhombic with a space group *Pnn2* (a subgroup of $P\bar{4}n2$).[10] The lattice parameters determined using powder X-ray diffraction are a = 11.9718(7) Å, b = 11.8884(7) Å, c = 3.8465 (2) Å, and V = 547.47 Å^3.

$Ba_6RCu_3O_z$ and $Ba_4RCu_3O_z$

There are two additional ternary oxide phases in the BaO-rich region of the $BaO\text{-}R_2O_3\text{-}CuO_z$ systems, namely, the $Ba_6RCu_3O_z$ (613) and $Ba_4GdCu_3O_z$ (413) phases. The $Ba_6GdCu_3O_z$ phase exists in the systems with relatively smaller R, namely, Gd, Dy, Ho, Y, Er, Tm, and Yb. The structure of the 613 phase was reported by Zhang and Osamura[47] to be perovskite-related and is tetragonal with the space

group $I4/mmm$ (a = 4.074(4) Å and c = 21.696 Å for the Gd-analog when prepared in air). $Ba_6ErCu_3O_z$ was reported to be orthorhombic and with the $SrTi_2O_4$-type structure (layered perovskite).[47] The difference of these two structures lies in the distribution of oxygen atoms on the (R,Cu)-O layers. The $Ba_4RCu_3O_z$ (413) phase can be prepared under 100 Pa p_{O_2} in the systems with R = Dy, Ho, Y, Er, and Tm. The structure of 413 was reported to be of the cubic oxygen-defect perovskite type (a = 8.08236(5) Å) for $Ba_4ErCu_3O_z$ when prepared in oxygen[46]).

Tie-line Relationships

In general, the tie-lines determined in the CuO- and R_2O_3-rich part of the BaO-R_2O_3-CuO_x phase diagrams are in agreement with most literature reported diagrams, whether prepared using $BaCO_3$, BaO_2, BaO, or $Ba(NO_3)_2$. However, the region of the diagrams near the BaO corner is substantially different.

The tie-line distribution appears to be the most complicated in the Nd- and the Sm-systems where three solid solution series were determined. The solid solution range is the greatest in the Nd-system, as revealed in the width of the tie-line bundles. Since the Eu-system does not have the $Ba_4R_2Cu_2O_{9-z}$ phase, the tie-line relations are not totally the same as those in the Nd and Sm systems. The tie-line relations in the Dy, Ho, Y, Er, and Tm systems are rather similar, despite the fact that the Dy and Tm systems only have one $Ba_3R_4O_9$ binary phase instead of two. In all these systems except for the Yb system, the tie-line relations involving the four phases, $Ba_2RCu_3O_{6+z}$, BaR_2CuO_5, $BaCuO_{2+z}$, and $Ba_4RCu_3O_z$, are rather similar, and are different from the literature data. The $Ba_2RCu_3O_{6+z}$ phase is found to be compatible with the $Ba_4RCu_3O_z$ phase, whereas the literature reports indicated a tie-line between $BaCuO_{2+z}$ and BaR_2CuO_5.[11,16–22]

In the Yb-system; however, a tie-line was found between $BaYb_2CuO_5$ and $BaCuO_{2+z}$, instead. It appears that the presence of CO_2 and the ionic size of the R cation both affect the tie-line relationships.

IMPLICATIONS FOR PROCESSING OF $Ba_2RCu_3O_{6+z}$ SUPERCONDUCTORS

For applications of phase equilibria to coated conductor processing, phase diagrams constructed under carbonate-free conditions should be employed. From examination of the BaO-R_2O_3-CuO_z diagrams included in this paper, there is a significant difference in the tie-line distributions occurring under carbonate-free conditions, relative to those occurring in the phase diagrams based on $BaCO_3$-derived starting materials. Under carbonate-free conditions at p_{O_2} = 100 Pa, the tie-line $Ba_2RCu_3O_{6+z}$(barium-rich phase) replaces the $BaCuO_{2+z}$-BaR_2CuO_5 tie-line in a majority of our BaO-R_2O_3-CuO_z diagrams; here the (barium-rich phase) refers to the $Ba_{2-x}R_xCuO_{3+z}$ solid solution in the R = Nd, Sm, and Eu systems, to the $Ba_6RCu_3O_z$ phase in the Gd-system, and to the $Ba_4RCu_3O_z$ phase in the R = Dy, Ho, Y, Er, and Tm systems. The net effect of this tie-line change is to expand the field of stability of R-213 toward the BaO-rich corner of the phase diagram. However, it is questionable as to whether this expansion is an advantage for the R-213 processing. The barium-rich phases are known to be atmospherically more sensitive than BaR_2CuO_5. As a result of the difference in the tie-line relationships, these atmospherically unstable phases can coexist with R-213, and their presence in R-213 materials could be deleterious. It may be important during the RABiTS and IBAD processes to avoid BaO-rich phases.

SUMMARY AND CONCLUSION

We have investigated the phase relationships of the BaO-Ho_2O_3-CuO_z system at p_{O_2} = 100 Pa (810°C), 21 kPa (875°C), and 0.1 MPa (850 and 930°C) under CO_2-free conditions. We have also reviewed and compared ten BaO-R_2O_3-CuO_z systems prepared at p_{O_2} = 100 Pa (810°C). We found that the oxygen partial pressure, ionic size of R^{3+}, and the presence of CO_2 affect the phase formation and the tie-line relationships. There are significant differences in the tie-line distributions occurring under carbonate-free conditions relative to those occurring in the phase diagrams based on $BaCO_3$-derived starting materials. For applications ranging from phase equilibria to coated conductor processing, phase diagrams constructed under carbonate-free conditions should be employed.

Since phase diagrams of the BaO-R_2O_3-CuO_z (R = lanthanides) systems are important for second-generation coated-conductor development, systematic studies of diagrams of the remaining lanthanide analogs (i.e., R = La, and Lu) under atmospherically controlled conditions are further needed to augment the data presently available.

ACKNOWLEDGEMENTS

The United States Department of Energy is acknowledged for partial financial support of this project. Mr. Nils Swanson and Dr. Peter Schenck of NIST are thanked for their assistance with the phase diagram graphics.

REFERENCES

1. A. Goyal, D.P. Norton, J.D. Budai, M. Paranthaman, E.D. Specht, D.M. Kroeger, D.K. Christen, Q. He, B. Saffian, F.A. List, D.F. Lee, P.M. Martin, C.E. Klabunde, E. Hartfield, and V.K. Sikka, *Appl. Phys. Lett.* 69(12), 1795 (1996).
2. M.W. Rupich, W. Zhang, X. Li, T. Kodenkandath, D.T. Verebelyi, U. Schoop, C. Thieme, M. Teplitsky, J. Lynch, N. Nguyen, E. Siegal, J. Scudiere, V. Maroni, K. Venkataraman, D. Miller, and T.G. Holesinger, *Physica C.* 412–414, 877 (2004).
3. X. Li, M.W. Rupich, W. Zhang, N. Nguyen, T. Kodenkandath, U. Schoop, D.T. Verebelyi, C. Thieme, M. Jowett, P.N. Arendt, S.R. Foltyn, T.G. Holesinger, T. Aytug, D.K.

Christen, and M.P. Paranthaman, *Physica C.* 390, 249 (2003).
4. S.R. Foltyn, P. Tiwari, R.C. Dye, M.Q. Le, and X.D. Wu, *Appl. Phys. Lett.* 63(13), 1848 (1993).
5. M. Bauer, R. Semerad, and H. Kinder, *IEEE Trans. Appl. Supercond.* 9(2), 1502 (1999).
6. J.L. MacManus-Driscoll, *Advanced Materials VCH* Verlagsgesellschaft, (May 1997) 9(6), 456 (1997).
7. W. Wong-Ng, B. Paretzkin, and E.R. Fuller Jr., *J. Solid State Chem.* 85(1), 117 (1990).
8. J.E. Ullman, R.W. McCallum, and J.D. Verhoeven, *J. Mater. Res.* 4(4), 752 (1989).
9. W. Wong-Ng, L.P. Cook, J. Suh, R. Coutts, J.K. Stalick, I. Levin, and Q. Huang, *J. Solid State Chem.* 173(2), 476 (2003).
10. W. Wong-Ng, L.P. Cook, J. Suh, and J.A. Kaduk, *Physcia C.* 405, 47 (2004).
11. W. Wong-Ng, L.P. Cook, and J. Suh, *Physica C.* 377, 107 (2002).
12. W. Wong-Ng, L.P. Cook, and J. Suh, *Solid State Sci.* 6(1–2), 1211 (2004).
13. W. Wong-Ng, Z. Yang, L.P. Cook, J. Frank, and M. Loung, *Physica C.* 439, 93 (2006).
14. W. Wong-Ng, Z. Yang, and L.P. Cook, *J. Alloys Comp* doi:10.1016/j.jallcom.2006.07.083 (2006).
15. W. Przybylo and K. Fitzner, *Mater. Res. Bull.* 30(11), 1413 (1995).
16. S.A. Hodorowicz, A. Lasocha, W. Lasocha, and H.A. Eick, *J. Solid State Chem.* 75(2), 270 (1988).
17. C.N. Pieczulewski, J.E. McAdams, and T.O. Mason, *J. Am. Ceram. Soc.* 73(10), 3088 (1990).
18. E. Hodorowicz, S.A. Hodorowicz, and H.A. Eick, *J. Solid State Chem.* 84, 401 (1991).
19. H. Ishizuka, Y. Idemoto, and K. Fueki, *Physica C.* 195(1–2), 145 (1992).
20. E. Hodorowicz, S.A. Hodorowicz, C. Raymond, and H.A. Eick, *J. Solid State Chem.* 98(1), 187 (1992).
21. Y.L. Zhang, J.K. Liang, X.R. Chen, G.H. Rao, H.B. Liu, Y.M. Ni, D.N. Zheng, and S.S. Xie, *J. Less Comm. Metals.* 146, 121 (1989).
22. K. Osamura and W. Zhang, *Z. Metallkd.* 84(8), 522 (1993).
23. J.J. Ritter, *Powd. Diff.* 3(1), 30 (1988).
24. PDF, Powder Diffraction File (Newtown Square, PA: International Centre for Diffraction Data (ICDD), 1941–2007).
25. W. Wong and L.P. Cook, *Powd. Diffr.* 9(4), 280 (1994).
26. W. Wong, K.L. Davis, and R.S. Roth, *J. Amer. Ceram. Soc.* 71(2), C64 (1988).
27. J.L. Luce and A.M. Stacy, *Chem. Mater.* 9(7), 1508 (1997).
28. D.M. Deleeuw, H.A. Mutsaers, C. Langereis, H.C.A. Smoorenburg, and P.J. Rommers, *Physica C.* 152, 39 (1988).
29. J. Thompson, J.D. FitzGerald, R.L. Withers, P.J. Barlow, and J.S. Anderson, *Mater. Res. Bull.* 24, 505 (1989).
30. S. Petricek, N. Bukovec, and P. Bukovec, *J. Solid State Chem.* 99, 58 (1992).
31. K.G. Frase and D.R. Clarke, *Adv. Ceram Mater.* 2(3B), 295 (1987).
32. F. Abbattista, M. Vallino, and D. Mazza, *Mater. Chem. Phys.* 21, 521 (1989).
33. F. Abbattista, M. Vallino, D. Mazza, M.L. Borlera, and C. Brisi, *Mater. Chem. Phys.* 20(2), 191 (1988).
34. J. Stalick and W. Wong-Ng, *Mater. Lett.* 9(10), 401 (1990).
35. W. Wong-Ng and B. Paretzkin, Set 42–1495, Powder Diffraction File (Newtown Square, PA: International Centre for Diffraction Data (ICDD), 1993).
36. L.M. Kovba, L.N. Lykova, and E.V. Antipov, *Russ. J. Inorg. Chem.* 28, 409 (1983).
37. K. Spitsyn, *Dokl. Chem.* 180, 516 (1968).
38. W. Wong-Ng, H.F. McMurdie, B. Paretzkin, Y. Zheng, C.R. Hubbard, A.L. Dragoo, and J.M. Stewart, *Powd. Diffr.* 3, 47 (1988).
39. H. Müeller-Buschbaum and M. Scheikowski, *Z. Anorg. Allg. Chem.* 591(12), 181 (1990).
40. H. Müeller-Buschbaum and O. Schrandt, *J. Alloys Comp.* 191(1), 151 (1993).
41. J. Krueger and H. Müeller-Buschbaum, *Z. Anorg. Allg. Chem.* 512(5), 59 (1984).
42. J. Krueger and H. Müeller-Buschbaum, *Rev. Chim. Miner.* 20(4–5), 456 (1983).
43. R.S. Roth, C.J. Rawn, F. Beech, J.D. Whitler, J.O. *Anderson, in Ceramic Superconductors II*, ed. M.F. Yan (American Ceramic Society, Westerville, OH), pp. 13–26.
44. H. Okada, M. Takano, and Y. Takeda, *Physica C.* 166, 111 (1990).
45. T. Ishiguro, N. Ishizawa, N. Mizutani, and M. Kato, *J. Solid State Chem.* 49, 232 (1983).
46. Y. Zhu, E.J. Peterson, P.S. Baldonado, J.Y. Coulter, D.E. Peterson, and F.M. Mueller, *J Alloys Compd.* 281, 137 (1998).
47. W. Zhang and K. Osamura, *Physica C.* 174, 126 (1991).
48. W. Wong-Ng, M.A. Kuchinski, H.F. McMurdie, and B. Paretzkin, *Powd. Diff.* 4, 2 (1989).
49. R.M. Hazen, L.W. Finger, R.I. Angel, C.T. Prewitt, N.K. Ross, H.L. Mao, C.G. Hadidiacos, P.H. Hov, R.L. Meng, and C.W. Chu, *Phys. Rev. B.* 35(13), 7238 (1987).
50. S.F. Watkins, F.R. Fronczek, K.S. Wheelock, R.G. Goodrich, W.O. Hamilton, and W.W. Johnson, *Acta Cryst.* C44, 3 (1988).
51. D.E. Morris, J.H. Nickel, J.Y.T. Wei, N.G. Asmar, J.S. Scott, U.M. Scheven, C.T. Hultgren, A.G. Markelz, J.E. Post, P.J. Heaney, D.R. Veblen, and R.M. Hazen, *Phys. Rev. B.* 39(10), 7347 (1989).
52. H.k. Müeller-Buschbaum and W. Well-Schlager, *Z. Anorg. Allg. Chem.* 414, 76 (1975).
53. B. Grande, H.k. Müeller-Buschbaum, and M. Schweizer, *Z. Anorg. Allg. Chem.* 428, 120 (1977).
54. E. Lambert and W. Eysel, JCPDS Grant-in-Aid Report for Powder Diffraction File, Set 33–455, 33–456, 33–458, 33–511, and 33–507 (1981) and 34–385, 34–386 and 34–387 (1982).
55. R.D. Shannon, *Acta Crystallogr.* A32, 751 (1976).
56. F. Abbattista, D. Mazza, and M. Vallino, *Eur. J. Solid State Inorg. Chem.* 28, 649 (1991).

Volume 111, Number 1, January-February 2006
Journal of Research of the National Institute of Standards and Technology

[J. Res. Natl. Inst. Stand. Technol. **111**, 41-55 (2006)]

Phase Transformations in the High-T_c Superconducting Compounds, $Ba_2RCu_3O_{7-\delta}$ (R = Nd, Sm, Gd, Y, Ho, *and* Er)

Volume 111 Number 1 January-February 2006

W. Wong-Ng and L. P. Cook
National Institute of Standards and Technology, Gaithersburg, MD 20899-0001

H. B. Su
Beckman Institute, California Institute of Technology, Pasadena, CA 91125

M. D. Vaudin and C. K. Chiang
National Institute of Standards and Technology, Gaithersburg, MD 20899-0001

D. R. Welch
Department of Materials Science, Brookhaven National Laboratory, Upton, NY 11973

and

E. R. Fuller, Jr, Z. Yang, and L. H. Bennett
National Institute of Standards and Technology, Gaithersburg, MD 20899-0001

The phase transformation between the orthorhombic and tetragonal structures of six high-T_c superconductors, $Ba_2RCu_3O_{7-\delta}$, where R = Nd, Sm, Gd, Y, Ho, and Er, and $\delta = 0$ to 1, has been investigated using techniques of x-ray diffraction, differential thermal analysis/thermogravimetric analysis (DTA/TGA) and electron diffraction. The transformation from the oxygen-rich orthorhombic phase to the oxygen-deficient tetragonal phase involves two orthorhombic phases. A superlattice cell caused by oxygen ordering, with $a' = 2a$, was observed for materials with smaller ionic radius (Y, Ho, and Er). For the larger lanthanide samples (Nd, Sm, and Gd), the $a' = 2a$ type superlattice cell was not observed.

The structural phase transition temperatures, oxygen stoichiometry and characteristics of the T_c plateaus appear to correlate with the ionic radius, which varies based on the number of f electrons. Lanthanide elements with a smaller ionic radius stabilize the orthorhombic phase to higher temperatures and lower oxygen content. Also, the superconducting temperature is less sensitive to the oxygen content for materials with smaller ionic radius. The trend of dependence of the phase transformation temperature on ionic radius across the lanthanide series can be explained using a quasi-chemical approximation (QCA) whereby the strain effect plays an important role on the order-disorder transition due to the effect of oxygen content on the CuO chain sites.

Key words: ac magnetic susceptibility; orthorhombic/tetra-gonal transformation; oxygen ordering; phase transformation of $Ba_2RCu_3O_{7-\delta}$ (R=lanthanides); strain effect on phase transition; transition temperature.

Accepted: January 3, 2006

Available online: http://www.nist.gov/jres

1. Introduction

Recent advances in coated conductor science and engineering have brought commercial high-T_c superconductor technology closer to reality [1]. It is now likely that many potential large-scale industrial applications will soon be realized. Three state-of-the-art technologies for producing textured coated conductors show promise: Ion Beam Assisted Deposition (IBAD) [2-5], Rolling Assisted Bi-axially Textured Substrate (RABiTS) deposition [6-11], and Inclined Substrate Deposition (ISD) technique [12,13]. Good quality textured conductors, which are based on the $Ba_2YCu_3O_{7-\delta}$ superconductor, have been successfully produced with

both film deposition and open-air solution techniques [14-22]. To further optimize the superconducting properties of long-length coated conductors for practical applications, recent research has also included the use of lanthanide-substituted variants, $Ba_2RCu_3O_{7-\delta}$ (R=lanthanides with stable 3+ oxidation state). Phase equilibrium research pertaining to $Ba_2RCu_3O_{7-\delta}$, including a thorough understanding of phase transition phenomena, is therefore important for processing.

The progressive reduction in size of the lanthanide, which is known as the lanthanide contraction, allows systematic study of the trend of crystal chemistry, solid solution formation, and phase equilibria in the systems $BaO\text{-}R_2O_3\text{-}CuO_x$ as a function of the size of lanthanide ion, R^{3+} [23-29]. Numerous investigations pertaining to the crystal chemistry, and the effect of oxygen stoichiometry on properties of $Ba_2RCu_3O_{7-\delta}$ have been reported [30-35]. The present paper is part of our continuing effort to understand the effect of lanthanide substitution on the properties and processing parameters of the high-T_c superconductors $BaR_2Cu_3O_{7-\delta}$ [23-29,36-39]. Since our preliminary reports [36-38] on the structural phase transitions of $Ba_2RCu_3O_{7-\delta}$, for R = Sm, Gd, Er, Y, and Ho, we have completed studies of the Nd series, including additional characterization of some of these materials using electron diffraction techniques. We have also improved our understanding of the phase transition in $Ba_2RCu_3O_{7-\delta}$ as related to the size of ionic radius of R^{3+} by using a quasi-chemical approximation to describe the effect of oxygen order-disorder [40].

After annealing the $Ba_2RCu_3O_{7-\delta}$ compounds at various temperatures and then rapidly quenching to liquid nitrogen temperature, we have made several observations concerning the phase transitions in these materials. Most interesting is the presence of T_c plateaus (annealing temperature ranges over which T_c remains approximately constant, even as the oxygen content changes). Examples are given of the existence of a 90 K and a 60 K T_c plateau in the Y, Ho, and Er materials [36-38,41-42]. Although there are extensive literature reports [43-49] describing the experimental observations or theoretical predictions of a single phase 60 K material in the Y system, very little information has previously been reported describing the lanthanide-substituted materials. Furthermore, most of the reported Y materials were prepared using processing routes different from our quenching methods [46-49].

2. Experimental

Since Nd_2O_3 reacts with atmospheric moisture to form $Nd(OH)_3$, the Nd_2O_3 powder was heat-treated at 600 °C overnight prior to sample preparation. A single phase master batch of $Ba_2NdCu_3O_{7-\delta}$ was prepared from a stoichiometric mixture of CuO, Nd_2O_3 and $BaCO_3$. Before firing and annealing, the powder was pressed into pellets and placed on MgO single crystals. The pellets were reground and annealed several times until the presence of a single-phase material was confirmed by x-ray powder diffraction analysis. Annealing was carried out at temperatures of 850 °C, 870 °C, and 900 °C each in air for 1 d, followed by firing in air at 940 °C for 2 d. Analysis by scanning electron microscopy and energy dispersive x-ray analysis (SEM/EDS) showed absence of substitution of magnesium in these samples.

A total of 10 barium-neodymium-copper-oxide samples were prepared for this investigation from the single-phase master batch. Batches of the other $Ba_2RCu_3O_{7-\delta}$ phases were prepared in similar fashion, using the appropriate lanthanide oxides [36-38]. To investigate the phase transitions, specimens weighing about 200 mg to 500 mg were annealed in an MgO crucible for up to 2 d in air at temperatures between 400 °C and 900 °C. The temperature was measured using a Pt/Pt10Rh thermocouple calibrated against the melting point of gold. Temperature of the Pt-wound resistance furnace used in these experiments was controlled to ± 2 °C by using a Wheatstone bridge type controller. After annealing, the samples were quenched into a liquid nitrogen-cooled copper cold well, through which liquid nitrogen-cooled helium gas was passed at a rapid rate (Fig. 1). Rapid cooling under these conditions prevented the oxygen gain that would normally occur for samples cooled in air.

Samples studied by electron microscopy are listed in Table 1, together with their processing conditions and oxygen content (all were quenched in liquid nitrogen-cooled helium). Specimens for electron microscopy were prepared by crushing small pieces of the sample material and then following one of two procedures: either the powder was dispersed in ethanol and drops of the liquid were placed on a carbon-coated copper grid, or a grid was scooped through the powder to avoid possible reactions with the alcohol. These two techniques produced samples with no detectable differences between them. Conventional electron microscopy and electron diffraction were carried out at 120 keV and 300 keV, and exposure times up to 50 s were used to record the faint superlattice diffraction spots.

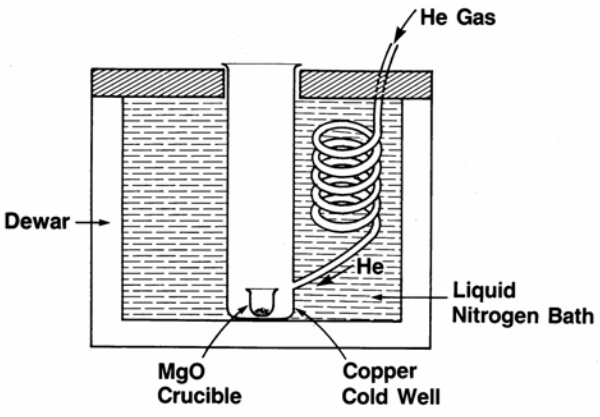

Fig. 1. An experimental setup showing a liquid nitrogen cooled copper cold well into which liquid helium was rapidly flowing through as an annealed sample that was contained in a MgO crucible was quenched.

Table 1. Samples investigated by electron diffraction techniques in the transmission electron microscope

Sample notation	Chemical formula	Annealing temperature	Time	Oxygen content $(7-\delta)$
Nd6.90	$Ba_2NdCu_3O_{7-\delta}$	620 °C	20 h	6.90
Sm6.75	$Ba_2SmCu_3O_{7-\delta}$	580 °C	40 h	6.75
Gd6.79	$Ba_2GdCu_3O_{7-\delta}$	620 °C	20 h	6.79
Y6.85	$Ba_2YCu_3O_{7-\delta}$	502 °C	36 h	6.85
Y6.63	$Ba_2YCu_3O_{7-\delta}$	635 °C	23 h	6.63
Y6.55	$Ba_2YCu_3O_{7-\delta}$	675 °C	21 h	6.55

The oxygen content of the $Ba_2RCu_3O_{7-\delta}$ compounds was determined by thermogravimetric analysis (TGA) from measurements of the weight change as a function of temperature in both air and in an oxygen atmosphere. An MgO sample holder was used for the yttrium compound and a platinum sample holder was used for the other four samples, since the temperatures of the TGA curves were below those at which any reactions with platinum were observed. The ground powder was heated from 50 °C to 850 °C at a rate of 2 °C per min to measure the change of weight, and thereby oxygen uptake and loss. The maximum observed weight was assumed to correspond to full oxygenation of seven oxygen atoms, or $Ba_2RCu_3O_7$. The weight loss at a given temperature was then used to compute the oxygen content. The correspondence between oxygen content and quenching temperatures was thus established. Due to the difficulty of applying a precise correction for the buoyancy effect, oxygen content established in this way may have an estimated relative uncertainty of ± 5 % (k=2).

Digital x-ray data were collected at room temperature on a computer-controlled powder diffractometer equipped with a focusing graphite crystal monochromator and a theta-compensating slit. Copper radiation ($CuK\alpha_1$, $\lambda = 1.5405981$ Å [50]) was employed for all studies. Two certified d-spacing standards: silicon, SRM640b [51], and fluorophlogopite, SRM675 [52] were used as internal standards for calibration [53]. Sample preparation, mounting methods and data processing followed those described by McMurdie et al. [54].

The flux exclusion of these powders was studied by using a computerized ac magnetometer. A sample powder of 10 mg to 20 mg was packed in a small, non-magnetic holder and mounted on a stage containing a calibrated silicon diode thermometer. The ac susceptibility was measured as a function of temperature from 300 K to 20 K for most samples in a Hartshorn type bridge circuit at a frequency of 1.68 kHz. The magnitude of the applied ac field was about 0.5×10^{-4} T. The relative Meissner effect was detected by observing the real part of the signal arising from the diamagnetism of the sample. We define the superconducting onset temperature, T_{CO}, as the temperature at which the ac susceptibility deviates from the near zero value of the normal state.

3. Results and Discussion

The x-ray spectra of $Ba_2RCu_3O_{7-\delta}$ (δ from 0 to 1) are, in general, similar to the yttrium analogs [24]. The progressive changes of shape and the indexing of peaks in the five main regions of the Bragg angle, 2θ, around 32º to 33º, 38º to 39º, 45º to 49º, 57º to 60º, and 68º to 70º reveal the crystallographic phase transition from orthorhombic to tetragonal for all compounds. Figure 2 illustrates the diffraction patterns of the $Ba_2NdCu_3O_{7-\delta}$ samples quenched from various temperatures at 401 °C, 545 °C, 570 °C, 578 °C and 592 °C. These diffraction patterns demonstrate a gradual reduction in orthorhombicity as evidenced, for example, by the peak shape changes for the 200 and 020 reflections at 46º to 48º 2θ and the 213 and 123 reflections at 57º to 59º 2θ.

3.1 Lattice Parameters

Using the least-squares refinement results [55], the transition from orthorhombic to tetragonal symmetry was estimated to take place between 570 °C and 578 °C. No doubling of cell parameters along either the a or b axes has been observed for $Ba_2NdCu_3O_{7-\delta}$ by x-ray powder diffraction. Based on a similar analysis, the

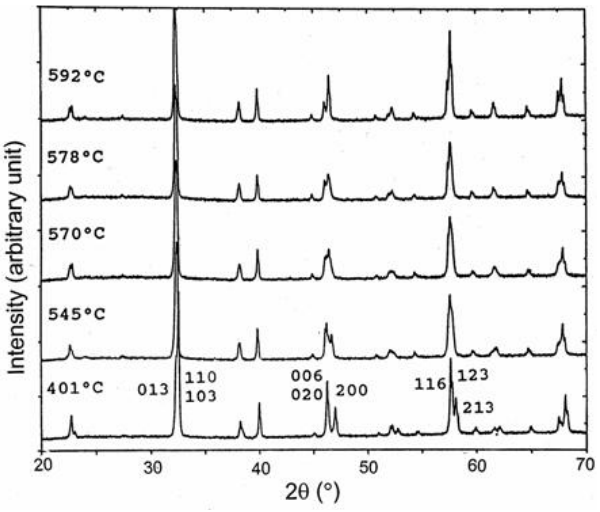

Fig. 2. X-ray diffraction patterns ($CuK\alpha_1$) from $Ba_2NdCu_3O_{7-\delta}$ samples quenched from 401 °C, 545 °C, 570 °C, 578 °C, and 592 °C, showing progressive changes of peak shapes. Selected Miller indices (hkl values) of the diffraction peaks for the sample quenched from 401 °C are indicated.

structural transition temperature for the other lanthanide analogues were found to be as follows: Sm: 625 °C to 650 °C, Gd: 650 °C to 660 °C, Y: 708 °C to 720 °C, Ho: 748 °C to 761 °C, and Er: 750 °C to 770 °C [36-39,41-49]. The tetragonal-orthorhombic structural transition temperatures are summarized in Table 2 along with ionic radii of the lanthanide ions, R^{3+} [56] and the estimated oxygen composition.

Table 2. Shannon's ionic radii [56] for R^{3+} (VIII-coordination), tetragonal orthorhombic phase transition temperature and oxygen content, ($x = 7-\delta$), for selected $Ba_2RCu_3O_{7-\delta}$

Compound	Shannon's ionic radius R^{3+} (Å) [56]	Temperature (°C)	Oxygen content
$Ba_2NdCu_3O_{7-\delta}$	1.109	570 to 578	6.82-6.84
$Ba_2SmCu_3O_{7-\delta}$	1.079	625 to 650	6.65-6.69
$Ba_2GdCu_3O_{7-\delta}$	1.053	650 to 660	6.75-6.76
$Ba_2YCu_3O_{7-\delta}$	1.019	708 to 720	6.47-6.49
$Ba_2HoCu_3O_{7-\delta}$	1.015	740 to 760	6.46-6.47
$Ba_2ErCu_3O_{7-\delta}$	1.004	750 to 770	6.38-6.41

Table 3 gives the cell parameters of $Ba_2NdCu_3O_{7-\delta}$ calculated from the x-ray patterns. Figures 3(a) to 3(f) depict the convergence of the *a* and *b* axis dimensions as the annealing temperature rises for these six compounds. While the merging curves exhibit similar shape and form, the different positions of the convergence of these curves can be related to the size of the lanthanide ion R^{3+}. The *a* and *b* axis dimensions (a_o, b_o) in the orthorhombic structure and the *a* axis dimension (a_t) in the tetragonal structure remain the largest for $Ba^2NdCu_3O_{7-\delta}$ across the entire annealed temperature range. Correspondingly, those of $Ba_2ErCu_3O_{7-\delta}$ are the smallest.

Table 3. Least-squares cell parameters for $Ba_2NdCu_3O_{7-\delta}$ as a function of quenched temperatures (°C). Number in parenthesis indicates one standard deviation from results of least-square refinements [37]

Quenched temperatures	*a*(Å)	*b*(Å)	*c*(Å)	*V*(Å^3)
401	3.8681(11)	3.9180(3)	11.762(3)	178.26(7)
464	3.8676(14)	3.9223(8)	11.779(2)	178.69(6)
501	3.8724(7)	3.9237(12)	11.781(2)	179.00(5)
556	3.882(2)	3.9180(12)	11.792(4)	179.30(9)
570	3.8870(2)	3.9115(5)	11.797(2)	179.35(8)
578	3.9034(a)		11.799(1)	179.78(3)
592	3.9029(6)		11.8103(14)	179.90(5)
697	3.9051(4)		11.8336(11)	180.46(3)
800	3.9025(3)		11.8511(12)	180.48(3)
900	3.9000(3)		11.8564(12)	180.34(3)

The variation with annealing temperature of the *c* axis cell dimension and the cell volume of these six compounds is illustrated in Fig. 4. Although these curves show, in general, the expected trend of increasing value as the temperature increases, the $Ba_2GdCu_3O_{7-\delta}$ compounds behave somewhat differently. For example, the *c*-dimension did not fall in the expected order relative to the other compounds. By analogy with the yttrium system, the elongations along the *c* axis of these compounds are considered to be due to the increased number of oxygen vacancies. At 400 °C the relative *c* axis cell dimensions of these compounds are as expected: $c_{Nd} > c_{Sm} > c_{Gd} > c_Y \sim c_{Ho} > c_{Er}$. At higher temperature the trend alters and becomes $c_{Nd} > c_{Sm} > c_{Ho} > c_Y > c_{Er} > c_{Gd}$. The volume plots in Fig. 5 illustrate the expected trends in volume expansion as the annealing temperatures increase, namely, $V_{Nd} > V_{Sm} > V_{Gd} > V_Y \sim V_{Ho} > V_{Er}$.

Figure 6 shows the first derivative of the TGA curves against temperature for the six compounds. While the weight change curves (not shown) are continuous, the first derivatives show relatively abrupt changes in slope. The temperature at which this abrupt change in temperature takes place can be considered as due to a phase transition, presumably the orthorhombic/tetragonal transition, and the trend of this behavior therefore parallels that listed in Table 2, namely, the lanthanide elements with a smaller ionic radius stabilize the orthorhombic phase to higher temperatures.

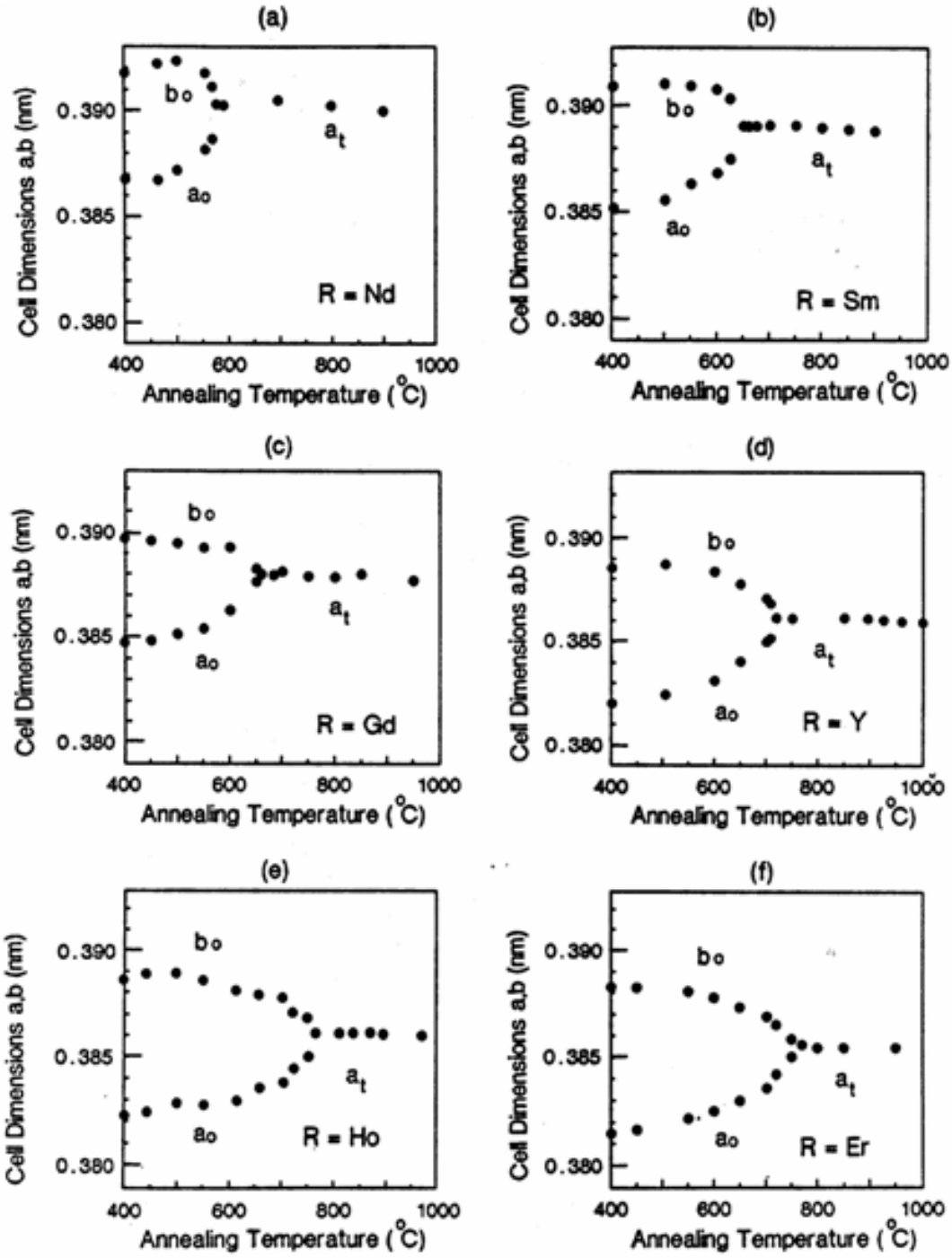

Fig. 3. Crystallographic dependence of the *a* and *b* axes of $Ba_2RCu_3O_{7-\delta}$ on the annealing temperature. Lanthanide ion R: (a) Nd (b) Sm (c) Gd (d) Y (e) Ho, and (f) Er.

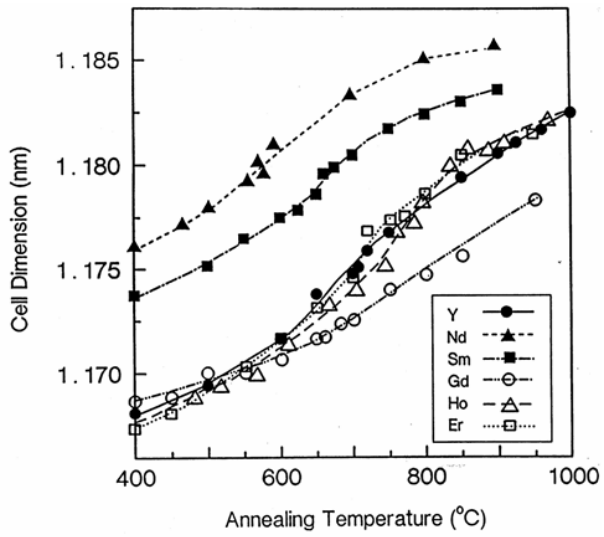

Fig. 4. The *c* axis cell parameter as a function of annealing temperature for $Ba_2RCu_3O_{7-\delta}$, with R = Nd, Sm, Gd, Y, Ho, and Er.

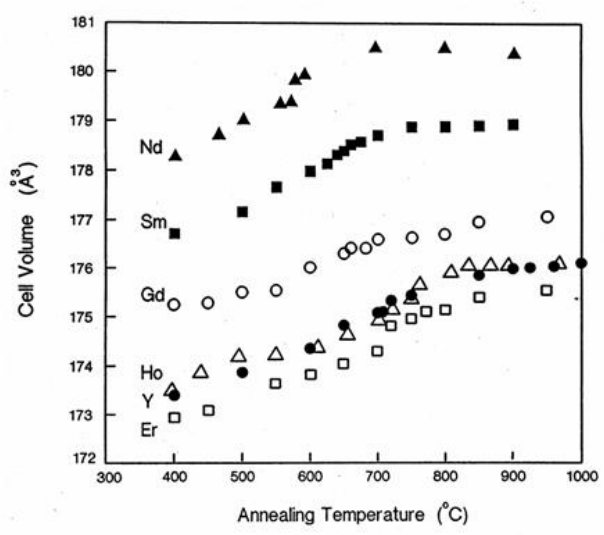

Fig. 5. Unit cell volume as a function of annealing temperature for $Ba_2RCu_3O_{7-\delta}$, with R = Nd, Sm, Gd, Y, Ho, and Er.

3.2 Chain-Oxygen Order-Disorder Transition

Figure 7 shows the structure of $Ba_2RCu_3O_{7-\delta}$ with the labeling of atoms and the oxygen sublattice site. Curve (a) of Fig. 8 shows a plot of these experimental transition temperatures as a function of the ionic radius of the R^{3+} ions. An obvious trend is observed. Lanthanide elements of smaller ionic size stabilize the orthorhombic phase to a higher temperature as well as to lower oxygen content. This trend can be understood in terms of order-disorder theory.

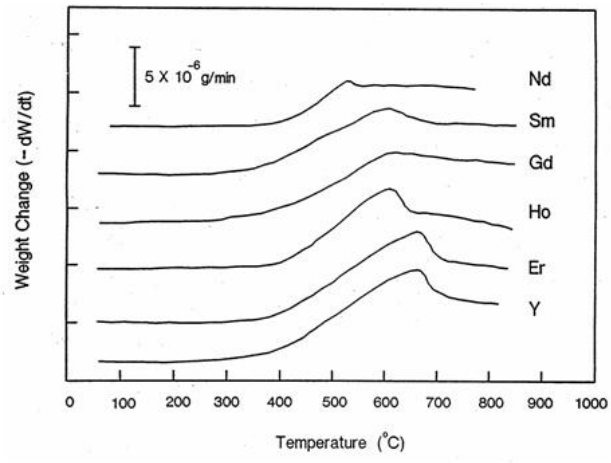

Fig. 6. Thermogravimetric analysis of $Ba_2RCu_3O_{7-\delta}$ showing the slope of the heating curve.

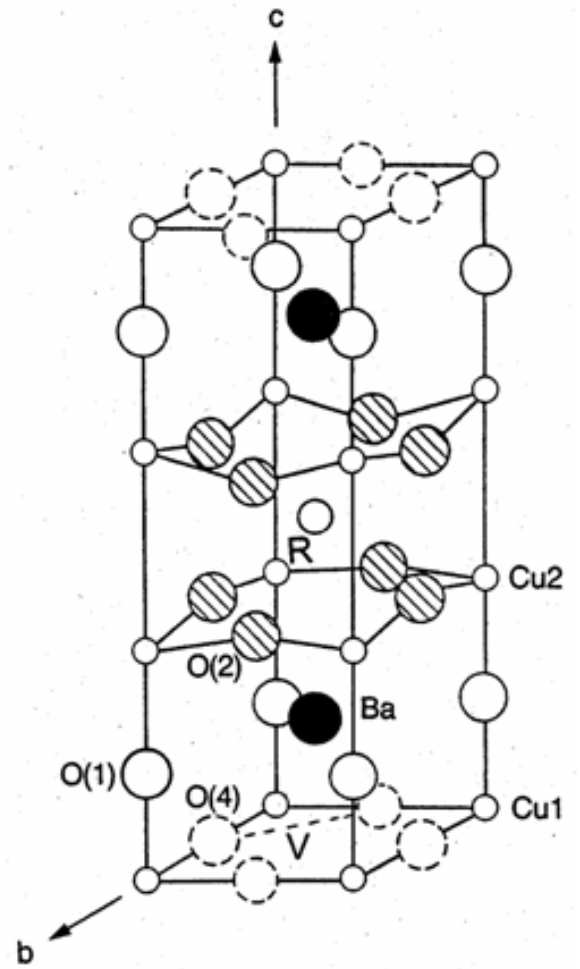

Fig. 7. Crystal structure and atom labels for $Ba_2RCu_3O_{7-\delta}$. The repulsion energy, *v*, between the oxygen atoms on two sublattice sites is represented as "*v*".

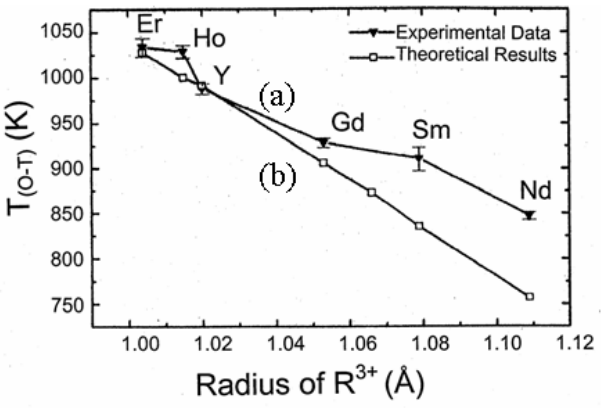

Fig. 8. Chain-oxygen order-disorder experimental (curve (a)) and theoretical (curve (b) [40]) phase transition temperatures vs. Shannon's ionic radius of R^{3+}(VIII-coordination) [55]. The theoretical data are calculated by using the transition temperature of $Ba_2YCu_3O_{7-\delta}$ as a reference.

Theoretical studies aimed at understanding the phase transformation in the $Ba_2YCu_3O_{7-\delta}$ system have been carried out extensively by Wille et al. [44], Bakker et al. [57], and Herman [58]. Recently, the similar approach has been applied by Su et al. to the lanthanide-substituted systems [40]. In brief, the formation energies of Frenkel pair defects as a function of volumetric strain for $Ba_2RCu_3O_{7-\delta}$, and for $Ba_2RCu_3O_7$ under hydrostatic pressure were calculated. These theoretical calculations show good agreement with experimental observations in that increased pressure favors ordering of the CuO chains. For example, the Frenkel pair formation energy indeed increases significantly (around –0.25 eV/0.01 volumetric strain) under compression.

Based on a quasi-chemical approach (QCA) by Bakker et al. [57], the orthorhombic/tetragonal transition temperatures for $Ba_2RCu_3O_{7-\delta}$ have been computed by scaling the effective oxygen-oxygen short-range repulsive energy in the CuO chain. At a given temperature T, a simplified relation [Eq. (1)] can be obtained to express the oxygen-oxygen repulsion energy, v, on two sublattice sites α and β, as a function of the long range parameter (S), the short range order expressed by the fraction (p) of near-neighbor pair sites occupied by oxygen-oxygen pairs, and the fractional site occupancy averaged over both sublattices (c).

$$v/kT = \ln\left(\frac{(c(1+S)-p)(c(1-S)-p)}{p(1-2c+p)}\right). \qquad (1)$$

The fraction p is equal to $N_{00}/4N$, where N is the number of sites on each of the sublattice, and N_{00} is the number of oxygen-oxygen near neighbor pairs. In Eq. (1), k is the Boltzmann constant. The long-range order parameter is defined such that the fractional site occupancy of oxygen on one of the two sublattice site β is $c(1+S)$, while that on sublattice α is $c(1–S)$. In $Ba_2YCu_3O_{7-\delta}$, c is assumed to be 0.5 when δ is zero, and $\delta = 1 - 2c$. The order-disorder transition temperature (orthorhombic to tetragonal), T_{O-T}, is therefore related to the oxygen-oxygen repulsion energy, v, on the two sublattice sites and the value of the average site occupancy c by

$$kT_{O-T} = v \ln\{16(1-c)/[1-4(1-2c)^2]\}. \qquad (2)$$

The trend of dependence of the ionic radius across the lanthanide series using the QCA is summarized in Fig. 8. The upper curve (a) represents the experimental data taken from this work while the lower one (b) represents the theoretical results using the current data (i.e., experimental phase transition temperatures) [40]. The theoretical data are calculated by using the transition temperature of $Ba_2YCu_3O_{7-\delta}$ as a reference (transition takes place at an oxygen content of 6.5). The calculated results agree with experimental data in that the larger the ionic size of R, the lower the orthorhombic/tetragonal phase transition temperature. The observable difference in these two curves is partly because the orthorhombic to tetragonal transition in the R-systems takes place at an oxygen content different from that of the reference Y-system, namely, 6.4 (Er) to 6.83 of Nd. The formation energy of Frenkel pairs is altered because of the difference of oxygen content (which affect lattice parameters and atomic positions). This formation energy of Frenkel pairs decreases as anisotropy in the *ab* plane [(*b*–*a*)/*a*] decreases.

From a simple point of view, if an assumption is made that the orthorhombic phase (absence of oxygen on the *a* axis) is favored at lower temperatures, then as the size of the lanthanide ion decreases, so does the distance between neighboring basal oxygens; the repulsion energy, v (Fig. 7), between these oxygens increases correspondingly. The transformation temperature, according to Eq. (2), is directly proportional to the repulsion energy, and is therefore higher the smaller the size of R.

3.3 T_c Dependence of Oxygen Content

Figure 9 shows a typical plot of the rationalized ac susceptibility of $Ba_2RCu_3O_{7-x}$ [31] as a function of temperature. The annealing temperatures are indicated from 400 °C to 708 °C. A bulk sample exhibiting 100 % flux exclusion would have an ac susceptibility

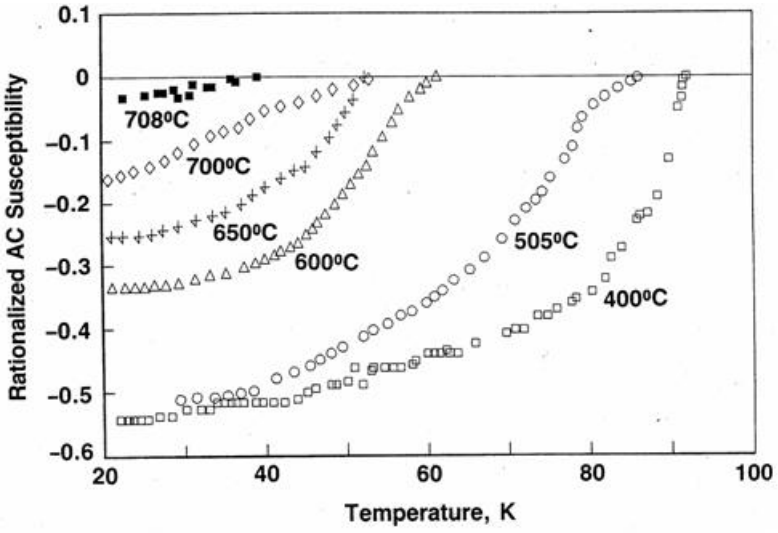

Fig. 9. A plot of the rationalized ac susceptibility as a function of temperature. The annealing temperatures are indicated. All samples were fully packed fine powders. Samples annealed at 750 °C and above did not exhibit any flux exclusion.

of –1 (dimensionless). Finnemore et al. [59] has shown that 100 % flux exclusion is not expected for fine powders of a completely superconducting material. It is thus not possible to determine exactly the fraction of the sample that is superconducting from the curves of Fig. 9. However, these curves have the approximate shape and magnitude expected for a ratio of particle diameter to superconducting penetration depth between 2 and 10 [59]. The decrease in the magnitude of the flux exclusion seen in Fig. 9 for the samples annealed at higher temperatures can be due either to a decrease in the fraction of the materials that is superconducting or to an increase in the superconducting penetration depth, or likely, to a combination of both.

Figure 10 shows plots of the superconducting temperature onset, T_{CO}, obtained from flux exclusion meas-

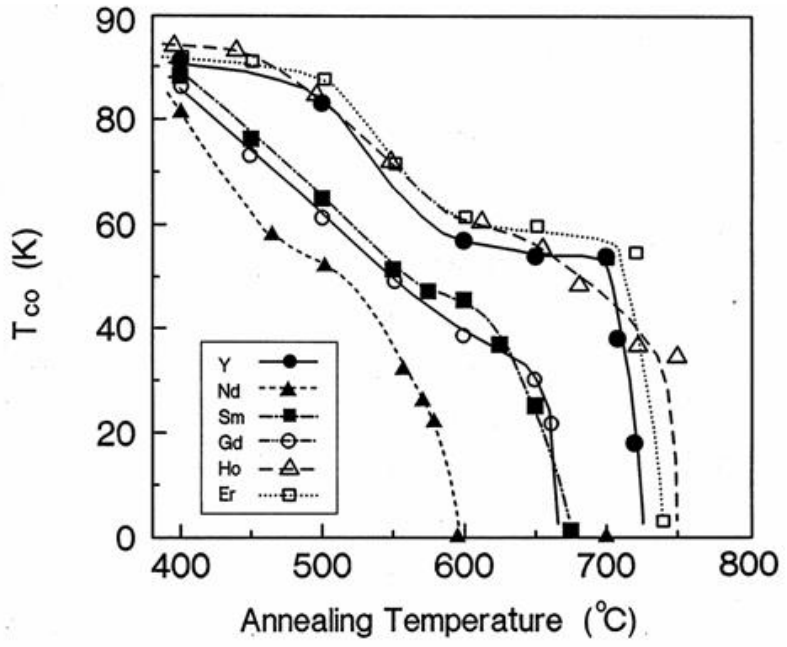

Fig. 10. Dependence of the superconducting transition temperature, as determined by ac magnetic susceptibility, on the annealing temperature in $Ba_2RCu_3O_{7-\delta}$ with R = Nd, Sm, Gd, Y, Ho, and Er.

urements as a function of the annealing temperature for all six compounds. Two apparent plateaus in T_{CO} were observed for the materials with yttrium, holmium and erbium substitution: one at 83 K to 92 K and the other at 58 K to 60 K. Narrower and somewhat lower plateaus were detected for the gadolinium, samarium and neodymium compounds. Although, in general, the orthorhombic structure is superconducting whereas the tetragonal is not, this structure correlation does not appear to be exact. For example, the tetragonal yttrium material annealed at 719 °C is superconducting, whereas the orthorhombic Er compound annealed at 750 °C is a non-superconductor. Furthermore, despite reports from literature that even in the $Ba_2YCu_3O_{7-\delta}$ system alone, one can achieve plateau features varying from broad plateaus at 60 K and 90 K to complete absence of plateaus depending on how samples were prepared [60], our samples were all prepared under similar conditions, therefore it is possible that one should be able to correlate the features of these plateaus with size of R.

Figure 11 depicts the oxygen content dependence of the transition temperatures of these six compounds as derived from thermogravitmetric analysis/differential thermal analysis (TGA/DTA) data. It is noteworthy that a correlation exists between the size of the R^{3+} ion and both the phase transition temperatures (or oxygen compositions) and T_c values for these plateaus, as is summarized in Table 4. Compounds with a smaller size lanthanide 3+ ion have a tendency to have both a wider 90 K plateau in T_c and a wider and relatively higher T_c

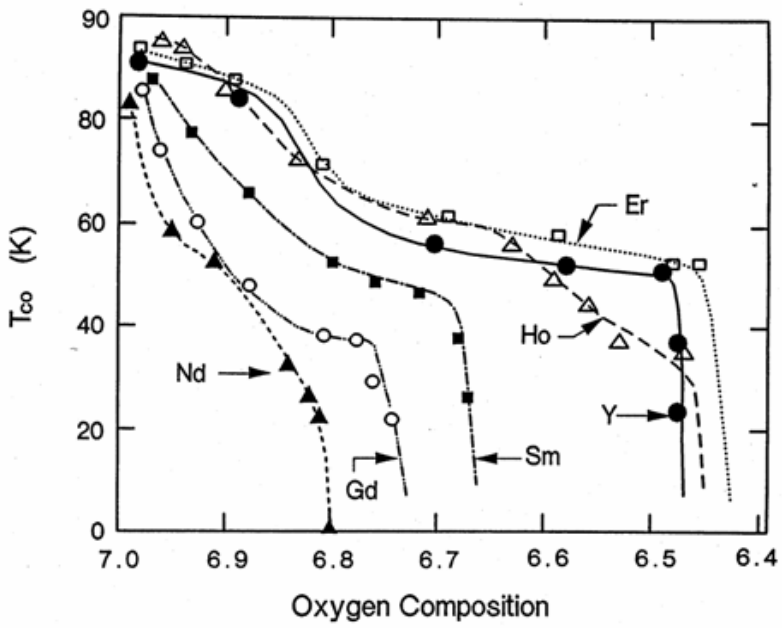

Fig. 11. Dependence of superconducting transition temperature, as determined by ac magnetic susceptibility, on the oxygen content in $Ba_2RCu_3O_{7-\delta}$, with R = Nd, Sm, Gd, Y, Ho and Er.

Table 4. Characteristics of the low temperature T_c plateaus for $Ba_2RCu_3O_{7-\delta}$ with R = Nd, Sm, Gd, Y, Ho, and Er

Lanthanide R	Approximate compositional range ($x = 7-\delta$)	Approximate anneal temperature range in air	T_c
Nd	6.83 < x < 6.88	40 °C (460 °C to 500 °C)	55 K
Sm	6.82 < x < 6.83	70 °C (550 °C to 620 °C)	52 K
Gd	6.77 < x < 6.81	70 °C (580 °C to 650 °C)	38 K
Y	6.62 < x < 6.80	100 °C (600 °C to 700 °C)	58 K
Ho	6.62 < x < 6.77	80 °C (580 °C to 660 °C)	60 K
Er	6.58 < x < 6.80	120 °C (600 °C to 720 °C)	60 K

in the 50 K to 60 K range. The Nd, Sm and Gd samples behave otherwise. They lack any obvious 90 K plateau, and they also play a narrow low T_c plateau (55 K, 52 K and 38 K, respectively). The observed trends appear to differentiate the early and later members of the lanthanide series.

3.4 Structural Features of $Ba_2RCu_3O_{7-\delta}$

The behavior of the curves of T_c versus annealing temperature (Fig. 10) and T_c versus oxygen content (Fig. 11) suggests the presence of more than one structural phase. X-ray results indicated both to be orthorhombic and they are designated here as O(A) and O(B). Other studies such as that of Cava et al. [41] have suggested that the second plateau region indicates the presence of a second orthorhombic phase. The presence of an O(B) phase in the yttrium sample has been confirmed by electron diffraction studies, which gave information about the degree to which ordering of the oxygen ions had occurred in the specimens. Diffraction patterns from the yttrium specimens (Y6.85, Y6.63, and Y6.55, as defined in Table 1) contained elongated superlattice reflections (streaks) lying along the [100] direction and centered on positions $\boldsymbol{g}$ + ½00 in reciprocal space (where $\boldsymbol{g}$ is a reciprocal lattice vector of the conventional orthorhombic structure).

A typical image of a crystallite in the yttrium specimen, Y6.55, together with a diffraction pattern from the crystallite, are shown in Fig. 12. The image, Fig. 12(a), shows an approximately regular arrangement of twins. From the diffraction pattern, Fig. 12(b), we can determine that the habit plane of the twins is (110), as expected, and that the orthorhombicity (b/a) of the material is 1.01, which agrees with the value of 1.008 obtained previously [37]. Diffuse scattering spots were also observed in the diffraction patterns, as indicated by the arrows. Despite the twinning, by a careful examination of the diffraction pattern far from the transmitted beam where the splitting of the orthorhombic matrix spots was greatest, it was possible to determine that the superlattice streaks were at $\boldsymbol{g}$ + ½00 and not $\boldsymbol{g}$ + 0½0. This corresponds to a doubling of the unit cell dimension along the a axis, suggesting that the oxygen atoms of every other CuO chain, running along the b axis, are removed. These results agree with those reported by Alario-Franco et al. [42], who observed diffuse scattering in a $Ba_2YCu_3O_{7-\delta}$, $\delta = 0.5$ sample. For the yttrium specimen, Y6.85, the streaks at ½00 were particularly faint and long, as is expected as the oxygen content increases. In all cases where superlattice streaks were observed, there was variation in both the intensity and length of the streaks between different grains from the same specimen, indicating that the oxygen content was not constant throughout the specimen and that the diffusion of oxygen through the lattice is slow at these temperatures. However, on average, the lengths of the streaks for specimens Y6.63 and Y6.55 corresponded to short range order on the 5 nm to10 nm (50 Å to100 Å) scale.

Although short range ordering was observed in the Y sample using electron diffraction, long range ordering was not observed using either electron diffraction or powder x-ray diffraction. Neutron scattering studies on a 60 K yttrium material annealed at 640 °C also showed no evidence of long range ordering. The results agreed with those of the x-ray powder diffraction and indicate the absence of any doubling of the cell parameters along either the a or b axis. The nature of supercell ordering in Y-123 $Ba_2YCu_3O_{7-\delta}$ have been studied extensively by Beyers et al [61], Zeiske et al. [62], and Ourmazd and Spence [63]. De Fontaine et al. [64] suggested that this supercell is stabilized at low temperature. It is now generally agreed that the degree of plateau behavior of $Ba_2YCu_3O_{7-\delta}$ depends on the degree to which the ordered $2a \times b \times c$ supercell is stabilized [65].

The gadolinium specimen was unique in that there was very little twinning in the crystallites studied; all the other lanthanide specimens were twinned. Diffraction patterns from the neodymium, samarium and gadolinium specimens (Nd6.90, Sm6.75 and Gd6.79) showed no evidence of superlattice formation of the type corresponding to the doubling of the unit cell dimension along the a axis. It is conceivable that the O(B) phase in compounds with smaller size R, has a doubling of the unit cell dimension along the a axis, corresponding to the absence of oxygen in every other Cu-O chain along the b axis. For the larger size R, the compositions with lower T_c plateau that we investigated correspond to those deviating significantly from the oxygen content of 6.50. We postulate that these lower T_c plateau regions of 55 K, 52 K, and 38 K in the Nd, Sm and Gd samples may result from another orthorhombic phase with a superlattice cell of the type corresponding to different oxygen vacancies. A superlattice cell other than the type with $a' = 2a$ has also been reported. For example, Alario-Franco et al. [42] reported a superlattice type in the Y compound corresponding to an oxygen content of 6.85; this superlattice can be indexed on a unit cell of $2\sqrt{2}a_c \times 2\sqrt{2}a_c \times 3a_c$, where a_c is the basic cubic perovskite cell dimension.

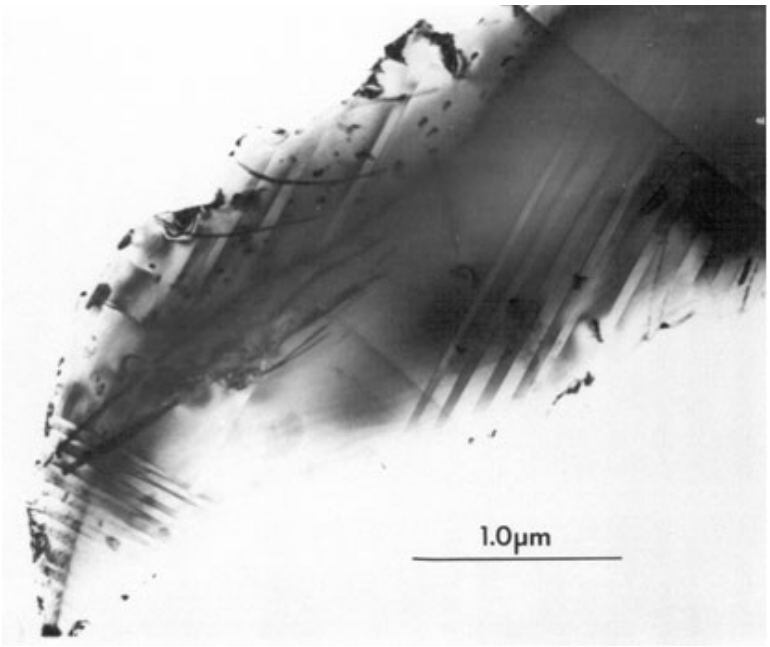

Fig. 12(a). TEM micrograph of $Ba_2YCu_3O_{7-\delta}$ grain annealed at 675 °C for 21 h showing typical twin boundary arrangement.

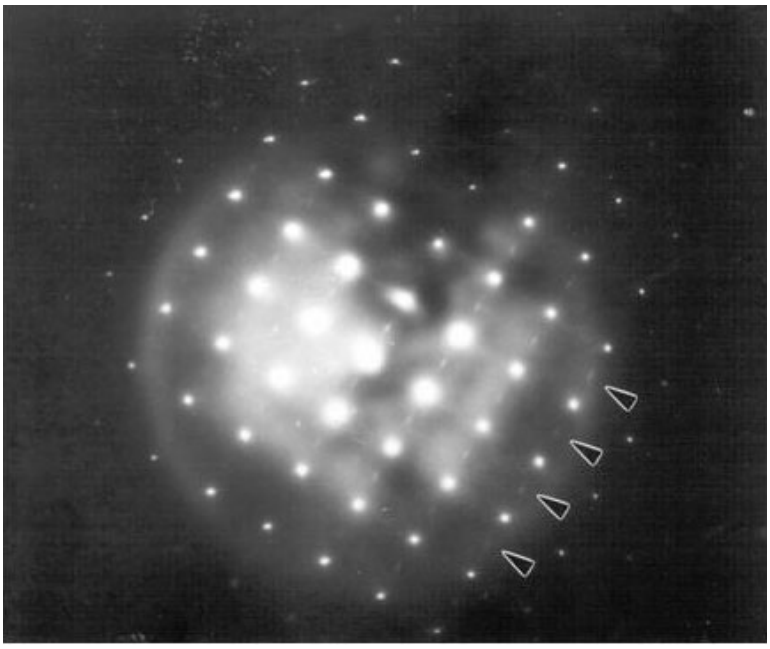

Fig. 12(b). Electron diffraction pattern from the grain shown in Fig. 12(a). The diffuse spots (indicated by arrows) correspond to a doubling of the *a* axis (a superlattice indexable with a cell of $a' \approx 2a$). Twinning is demonstrated by the splitting of the diffraction spots.

Oxygen stoichiometry is an important parameter affecting the T_c depression and the presence of T_c plateaus. The CuO chain in the basal plane and the CuO plane [66-69] can be considered as an interacting electronic unit. Tokura et al. [70] and Cava et al. [41,71] have suggested that the chains function as a charge reservoir which controls the electron density on the Cu-O planes. By applying this concept to our samples, when oxygen atoms are removed from the chains, the electrons which were bound to them are transferred to the lowest unoccupied energy level. When the total oxygen content is near 7, the T_c value of 90 K is due to the coupling of the chains and the planes. As illustrated in Fig. 13, when oxygen atoms are removed from the chains, the chain copper-bridging oxygen distance, Cu(1)-O(1), becomes shorter and the plane copper-bridging oxygen distance, Cu(2)-O(1), becomes longer, with the result that the chains and the planes become decoupled. The distance Cu(1)-O(1) first shortens gradually in the orthorhombic O(A) region, then changes rather sharply in region B [36,72]. In the tetragonal region it resumes a much smaller slope. The Cu(2)-O(1) bond elongates in a similar way in these materials. It appears that the decoupling effect of the chains and the planes takes place much more dramatically in region O(B). The observed superconductivity at the lower T_c regions of 60 K, 60 K, 58 K, 38 K, 52 K and 55 K in the Er, Ho, Y, Gd, Sm and Gd compounds, respectively, is probably due to sufficient decoupling of the chain-plane unit, and the different T_c are intrinsic

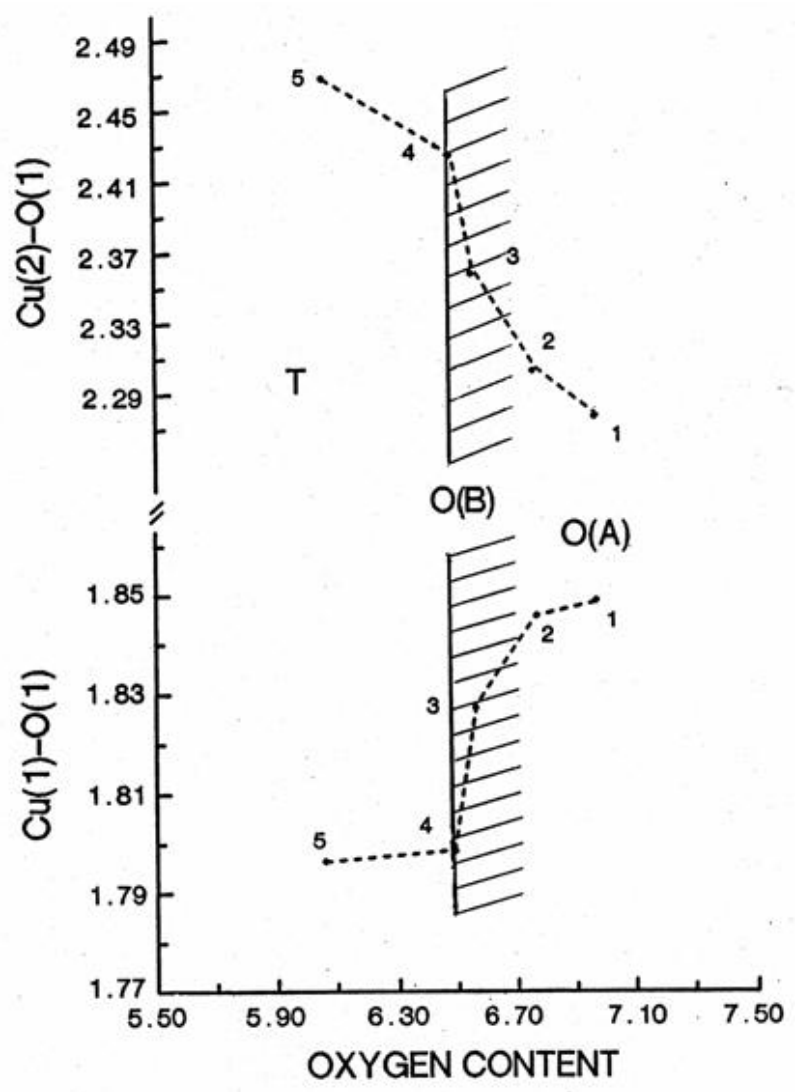

Fig. 13. Illustration of the bond lengths, Cu(1)-O(1) and Cu(2)-O(1), as a function of oxygen content in the $Ba_2YCu_3O_{7-\delta}$ samples.

values of the plane. When the capacity of the CuO chain-reservoirs to hold charge is exhausted, charge is transferred from the chains to planes, and superconductivity disappears. This charge transfer is equivalent to a decrease in the hole concentration in the planes [41,70].

4. Conclusions

The structural phase transformation that occurs in the high-T_c ceramic superconductors is of considerable importance in the processing of these materials. We have found that the temperature of this structural phase transition, its oxygen stoichiometry, and characteristics of the associated T_c plateaus follow a trend depending on the ionic radius of the lanthanide ions. Lanthanide elements with a smaller ionic size stabilize the orthorhombic phase to higher temperatures, or lower oxygen content. The superconducting temperature is less sensitive to the oxygen content for materials with smaller ionic radii.

Electron microscopy studies indicated that the O(B) phase in the Y compound has a doubling of the unit cell dimension along the *a* axis, corresponding to the absence of oxygen in every other Cu-O chain along the *b* axis. While not yet investigated, this type of superlattice can probably also be found in $Ba_2RCu_3O_{7-\delta}$ compounds with smaller size R. This is most likely short-range ordering as both the x-ray and neutron diffraction data indicate a lack of evidence for a long-range ordering of oxygen in samples quenched around the "lower" T_c plateau region. For the lanthanide samples with larger size of R (i.e., Nd, Sm, and Gd), the lower T_c plateau is postulated as corresponding to a different superlattice resulting from different oxygen stoichiometry.

Our study also illustrates the importance of strain effects on the orthorhombic/tetragonal phase transition in the $Ba_2RCu_3O_{7-\delta}$ compounds. The formation energy of Frenkel pair defects as a function of volumetric strain for $Ba_2RCu_3O_{7-\delta}$, and for $Ba_2YCu_3O_7$ under hydrostatic pressure show good agreement with experimental observations that pressure favors ordering of the CuO chains. For example, the Frenkel pair formation energy indeed increases significantly (around –0.25 eV/0.01 volumetric strain) under compression. Based on a quasi-chemical approach, the orthorhombic/tetragonal transition temperatures for $Ba_2RCu_3O_{7-\delta}$ have been computed by scaling the effective oxygen-oxygen short-range repulsive energy in the CuO chain using the Frenkel pair formation energy. The calculated results agree with experimental data in that the larger the ionic size of the lanthanide, the lower the orthorhombic/tetragonal phase transition temperature.

Acknowledgments

Thanks to Ms. R. Drew for performing the ac magnetic susceptibility measurements. We also gratefully acknowledge the financial support of the Department of Energy (DOE) for Wire/Tapes Development, and also for the portion of the research carried out at Brookhaven National Laboratory, operated by Brookhaven Science Associates, LLC under Contract No. DE-AC02-98CHI-886 with the U.S. Department of Energy. The United States Government retains, and the publisher, by accepting the article for publication, acknowledges, a world-wide license to publish or reproduce the published form of this manuscript, or allow others to do so, for United States Government purposes.

5. References

[1] M. P. Paranthaman and T. Izumi, MRS Bull. **29** (8), 533-536 (2004).
[2] Y. Iijima, K. Kakimoto, Y. Yamada, T. Izumi, T. Saitoh, and Y. Shiohara, MRS Bull. **29** (8), 564-571 (2004).
[3] R. P. Reade, P. Berdahl, R. E. Russo, and S. M. Garrison, Appl. Phys. Lett. **61** (18), 2231-2233 (1992).
[4] S. R. Foltyn, P. Tiwari, R. C. Dye, M. Q. Le, and X. D. Wu, Appl. Phys. Lett. **63** (13), 1848-1850 (1993).
[5] P. N. Arendt and S. R. Foltyn, MRS Bull. **29** (8), 543-550 (2004).
[6] A. Goyal, M. P. Paranthaman, and U. Schoop, MRS Bull. **29** (8), 552-561 (2004).
[7] A. P. Malozemoff, S. Annavarapu, L. Fritzemeier, Q. Li, V. Prunier, M. Rupich, C. Thieme, W. Zhang, A. Goyal, M. Paranthaman, and D. F. Lee, Supercond. Sci. Technol. **13** (5), 473-376 (2002).
[8] M Paranthaman, C. Park, X. Cui, A. Goyal, D. F. Lee, P. M. Martin, T. G. Chirayil, D. T. Verebelyi, D. P. Norton, D. K. Christen, and D. M. Kroeger, J. Mater. Res. **15** (12), 2647-2652 (2000).
[9] A. Goyal, D. F. Lee, F. A. List, E. D. Specht, R. Feenstra, M. Paranthaman, X. Cui, S. W. Lu, P. M. Martin, D. M. Kroeger, D. K. Christen, B. W. Kang, D. P. Norton, C. Park, D. T. Verebelyi, J. R. Thompso, R. K. Williams, T. Aytug, and C. Cantoni, Physica C **357**, 903-913 (2001).
[10] T. Aytug, A. Goyal, N. Rutter, M. Paranthaman, J. R. Thompson, H. Y. Zhai, and D. K. Christen, J. Mater. Res. **18** (4), 872-877 (2003).
[11] M. Paranthaman, A. Goyal, F. A. List, E. D. Specht, D. F. Lee, P. M. Martin, Q. He, D. K. Christen, D. P. Norton, J. D. Budai, and D. M. Kroeger, Physica C **275**, 266-272 (1997).
[12] M. Bauer, R. Semerad, and H. Kinder, IEEE Trans. Appl. Supercond. **9** (2), 1502-1505 (1999).
[13] U. Balachandran and M. P. Chudzik, U.S. Patent No. 6,361,598, March (2002).

[14] R. Feenstra, T. B. Lindemer, J. D. Budai, and M. D. Galloway, J. Appl. Phys. **69**, 6569-6585 (1991).
[15] R. Feenstra, US Patent 5,972,847 (1999).
[16] V. F. Solovyov, H. J. Wiesmann, M. Suenaga, and R. Feenstra, Physica C **309** (3-4), 269-274 (1998).
[17] L. Wu, Y. Zhu, V. F. Solovyov, H. J. Wiesmann, A. R. Moodenbaugh, R. L. Sabatini, and M. Suenaga, J. Mater. Res. **16** (10), 2869-2884 (2001).
[18] V. Selvamanickam, Y. Xie, J. Reeves, and Y. Chen, MRS Bull. **29** (8), 579-582 (2004).
[19] A. Usoskin and H. C. Freyhardt, MRS Bull. **29** (8), 583-589 (2004).
[20] M. W. Rupich, D. T. Verebelyi, W. Zhang, T. Kodenkandath, and X. Li, MRS Bull. **29** (8), 572-578 (2004).
[21] P. C. McIntyre, M. J. Cima, and A. Roshko, J. Appl. Phys. **77** (10), 5263-5272 (1995).
[22] M. Yoshizumi, I. Seleznev, and M. J. Cima, Physica C **403** (3), 191-199 (2004).
[23] W. Wong-Ng, M. A. Kuchinski, H. F. McMurdie, and B. Paretzkin, Powder Diffr. **4** (1), 2-8 (1989).
[24] W. Wong-Ng and B. Paretzkin, Powder Diffr. **6** (4), 187-192 (1991).
[25] W. Wong-Ng, C. K. Chiang, B. Paretzkin, and E. R. Fuller, Jr., Powder Diffr. **5** (1), 26-32 (1990).
[26] W. Wong-Ng, B. Paretzkin and E. R. Fuller, Jr., J. Solid State Chem. **85** (1), 117-132 (1990).
[27] W. Wong-Ng, L. P. Cook, M. D. Hill, B. Paretzkin, and E. R. Fuller, Jr., Proceedings of the 1990 MRS Symposium on High-temperature Superconductors: Fundamental Properties and Novel Materials Processing, in Boston, MA, edited by D. Christen, J. Narayan, and L. Schneemeyer, **169**, 81 (1990).
[28] W. Wong-Ng, L. P. Cook, B. Paretzkin, J. Stalick, and M. D. Hill, J. Am. Ceram. Soc. **97** (9), 2354-2362 (1994).
[29] W. Wong-Ng, B. Paretzkin, and E. R. Fuller, Jr., Adv. X-ray Anal. **33**, 453 (1989).
[30] Y. Lepage, W. R. McKinnon, J. M. Tarascon, L. H. Greene, G. W. Hull, and D. M. Hwang, Phys. Rev. B **35** (13), 7245-7248 (1987).
[31] R. S. Kwok, S.-W. Cheong, J. D. Thompson, Z. Fisk, J. L. Smith, and J. O. Willis, Physica C **152** (3), 240-246 (1988).
[32] J. M. Tarascon, P. Barboux, P. F. Miceli, L. H. Greene, and G. W. Hull, M. Eibschutz, and S. A. Sunshine, Phys. Rev. B **37** (13), 7458-7469 (1988).
[33] H. Shaked, B. W. Veal, J. Faber, Jr., R. L. Hitterman, U. Balachandran, G. Tomlins, H. Shi, L. Morss, and A. P. Paulikas, Phy. Rev. B **41** (7), 4173-4180 (1990).
[34] S. Chittipeddi, Y. Song, D. L. Cox, J. R. Gaines, J. P. Golben, and A. J. Epstein, Phy. Rev. B **37** (13), 7454-7457 (1988).
[35] Y. Le Page, T. Siegrist, S. A. Sunshine, L. F. Schneemeyer, D. W. Murphy, S. M. Zahurak, and J. V. Waszczak, Phy. Rev. B **36** (7), 3617-3621 (1987).
[36] W. Wong-Ng, L. P. Cook, C. K. Chiang, M. D. Vaudin, D. L. Kaiser, F. Beech, L. J. Swartzendruber, L. H. Bennett, and E. R. Fuller, Jr., Proceedings of the 1989 TMS Symposium on High Temperature Superconducting Compounds: Processing & Related Properties, in Las Vegas, NV, edited by S. H. Whang and A. DasGupta, eds. (1989) p. 553.
[37] W. Wong-Ng, L. P. Cook, C. K. Chiang, L. J. Swartzendruber, L. H. Bennett, J. E. Blendell, and D. Minor, J. Mater. Res. **3** (5), 832-839 (1988).
[38] W. Wong-Ng, L. P. Cook, C. K. Chiang, L. J. Swartzendruber, and L. H. Bennett, in Ceramic Superconductors II, edited by M. F. Yan, Am. Ceram. Soc., 27 (1988).
[39] J. E. Blendell, W. Wong-Ng, C. K. Chiang, R. D. Shull, and E. R. Fuller, Jr., High Temperature Superconducting Compounds: Processing & Related Properties, edited by S. H. Whang and A. DasGupta, The Mineral, Metals & Materials Society (1989) p. 193.
[40] H. B. Su, D. O. Welch, and W. Wong-Ng, Phy. Rev B **70**, 054517 (2004).
[41] R. J. Cava, B. Batlogg, C. H. Chen, E. A. Rietman, S. M. Zahurak, and D. Werder, Phys. Rev. B **36** (10), 5719-5722 (1987).
[42] M. A. Alario-Franco, C. Chaillout, J. J. Capponi, J. Chenavas, and M. Marezio, Physica C **156** (3), 455-460 (1988).
[43] D. Shi and D. W. Capone, II, Appl. Phys. Lett. **53** (2), 159-161 (1988).
[44] L. T. Wille, A. Berera, and D. de Fontaine, Phys. Rev. Lett. **60** (11), 1065-68 (1988).
[45] B. W. Veal, A. P. Paulikas, J. W. Downey, H. Claus, K. Vandervoort, G. Tomlins, H. Shi, M. Jensen, and L. Morss, Physica C **162-164**, 97-98 (1989).
[46] J. D. Jorgenson, M. A. Beno, D. G. Hinks, L. Soderholm, K. J. Volin, R. L. Hitterman, J. D. Grace, I. K. Schuller, C. U. Segre, K. Zhang, and M. S. Kleefisch, Phys. Rev. B **36** (7), 3608-3616 (1987).
[47] W. K. Kwok, G. W. Crabtree, A. Umezawa, B. W. Veal, J. D. Jorgenson, S. K. Malik, L. J. Nowicki, A. P. Paulikas, and L. Nunez, Phys. Rev. B **37**, 106-110 (1988).
[48] E. D. Specht, C. J. Sparks, A. G. Dhere, J. Brynestad, O. B. Cavin, D. M. Kroeger, and H. A. Oye, Phy. Rev. B **37** (13), 7426-7434 (1988).
[49] P. K. Gallagher, H. M. O'Bryan, S. A. Sunshine, and D. W. Murphy, Mat. Res. Bull. **22**, 995-1005 (1987).
[50] R. D. Deslattes and A. Henins, Phys. Rev. Lett. **31**, 972 (1973).
[51] C. R. Hubbard, C. Robbins, and W. Wong-Ng (1987). Standard Reference Material 640b, Silicon Powder X-ray Diffraction Standard, obtainable from the Natl. Inst. Stand. Technol., Office of Standard Reference Materials, Gaithersburg, MD 20899. Current price will be quoted on request.
[52] C. R. Hubbard (1982). Standard Reference Material 675, Fluorophlogopite Powder X-ray Diffraction Standard, To obtain, see procedure above for SRM 640b.
[53] W. Wong-Ng and C. R. Hubbard, Powd. Diff. **2** (3), 242 (1988).
[54] H. F. McMurdie, M. C. Morris, E. H. Evans, B. Paretzkin, W. Wong-Ng, and C. R. Hubbard, Powd. Diff. **1** (1), 40 (1986).
[55] D. E. Appleman and H. T. Evans, Jr., Report #PB216188, U.S. Dept of Commerce, National Technical Information Service, 5285 Port Royal Rd., Springfield, VA 22151 (1973).
[56] R. D. Shannon, Acta Cryst. A **32**, 751 (1976).
[57] H. Bakker, D. O. Welch, and O. W. Lazareth, Jr., Solid State Comm. **64** (2), 237-240 (1988).
[58] F. Herman, Novel Superconductivity, edited by S. A. Wolf and A. Vladimir, Plenum Publishing Co. 521 (1987).
[59] D. K. Finnemore, R. N. Shelton, J. R. Clem, R. W. McCallum, H. C. Ku, R. E. McCarley, S. C. Chen, P. Klavins, and V. Kogan, Phys. Rev. B **35** (10), 5319-5322 (1987).
[60] C. Namgung, J. T. S. Irvine, and A. R. West, Physica C **168**, 346-350 (1990).
[61] R. Beyers, B. T. Ahn, G. Gorman, V. Y. Lee, S. S. P. Parkin, M. L. Ramirez, K. P. Roche, J. E. Vazquez, T. M. Gür, and R. A. Haggins, Nature **340**, 619-621 (1989).
[62] T. Zeiske, R. Sonntag, D. Hohlwein, N. H. Anderson, and T. Wolf, Nature **353**, 542-544 (1991).
[63] A. Ourmazd and J. C. H. Spence, Nature **329**, 425-427 (1987).

[64] D. de Fontaine, G. Ceder, and M. Asta, J. Less-Comm Metals **164 & 165**, 108-123 (1990).
[65] R. J. Cava, A. W. Hewat, E. A. Hewat, B. Batlogg, M. Marezio, K. M. Rabe, J. J. Krajewski, W. F. Peck, Jr., and L. W. Rupp, Jr, Physica C **165** (5-6), 419-433 (1990).
[66] F. Beech, S. Miraglia, A. Santoro, and R. S. Roth, Phys. Rev. B **35** (11), 8778-8781 (1987).
[67] S. Miraglia, F. Beech, A. Santoro, D. Tran Qui, S. A. Sunshine, and D. W. Murphy, Mater. Res. Bull. **22**, 1733-1740 (1987).
[68] R. J. Cava, B. Batlogg, C. H. Chen, E. A. Rietman, S. M. Zahurak, and D. Werder, Nature **329**, 423-425 (1987).
[69] R. J. Cava, B. Batlogg, S. A. Sunshine, T. Siegrist, R. M. Fleming, K. Rabe, L. F. Schneemeyer, D. W. Murphy, R. B. van Dover, P. K. Gallagher, S. H. Glarum, S. Nakahara, R. C. Farrow, J. J. Krajewski, S. M. Zahurak, J. V. Waszczak, J. H. Marshall, P. Marsh, L. W. Rupp, Jr., W. F. Peck, and E. A. Rietman, Physica C **153-155**, 560-565 (1988).
[70] Y. Tokura, J. B. Torrance, T. C. Huang, and A. I. Nazzal, IBM Research Report, Solid State Phys. RJ 6221 (61211), (May 4, 1988).
[71] R. J. Cava, B. Batlogg, K. M. Rabe, E. A. Rietman, P. K. Gallagher, and L. W. Rupp, Jr., Physica C **156** (4), 523-527 (1988).
[72] J. D. Jorgensen, B. W. Veal, A. P. Paulikas, L. J. Nowicki, G. W. Crabtree, H. Class, and W. K. Kwok, Phy. Rev. B **41** (4), 1863-1877 (1990).

About the authors: *W. Wong Ng is a senior research staff member in the Ceramics Division of the NIST Materials Science and Engineering Laboratory and is the leader of the project "Advanced Materials for Energy Applications". Her main research areas at NIST have been phase equilibria, x-ray crystallography, and the crystal chemistry of technologically important high-temperature materials.*

L. P Cook is a research staff member in the Ceramics Division of the NIST Materials Science and Engineering Laboratory and is the leader of the project "Nanocalorimetry: Thermochemistry of Interfacial Reactions at the Nanoscale". He has worked on a variety of materials systems including high temperature superconductors, energetic materials, and materials for coal conversion technology.

H. B. Su is an Assistant Professor at School of Materials Science and Engineering, Nanyang Technological University (NTU), Singapore. His current research interest is in the area of molecular electronics.

M. D. Vaudin is in the Ceramics Division of the NIST Materials Science and Engineering Laboratory. He works on texture measurement techniques and standards, using x-ray and electron diffraction methods. He investigates texture and microtexture in bulk and thin film ceramics and metals, with particular interest in improving the accuracy and precision of the techniques used.

C. K. Chiang is a Physicist in Polymers Division of the NIST Materials Science and Engineering Laboratory. His research interest is the electrical properties of materials. Current efforts concentrate on electrical and dielectric properties of polymer thin films. Dr. Chiang is the leading author of several of the Nobel Prize papers that led to the creation of the field of conducting polymers.

D. O. Welch is a senior materials scientist in the Magnetic Materials Group, Materials Science Division of Brookhaven National Laboratory. His current research interests include theoretical materials science, crystal lattice defects and physical properties, superconducting and magnetic materials, and statistical thermodynamics and kinetics.

E. R. Fuller, Jr. is a physicist in the Ceramics Division of the NIST Materials Science and Engineering Laboratory. His research interests include metrology and fracture behavior of small-scale structures, and modeling and computer simulations of micro-mechanical and physical behavior of heterogeneous, stochastic microstructures. He is co-developer and principal alpha tester of the NIST OOF (Object Oriented Finite Element) tools for physical property simulations from material microstructures.

Zhi Yang is a guest research scientist in the Ceramics Division of the NIST Materials Science and Engineering Laboratory. His expertise is in the area of crystal chemistry and structural science of solid state materials. He has worked on a number of materials systems, including optical materials, superconductors, and dielectrics.

Lawrence H. Bennett was in the Metallurgy Division of the NIST Materials Science and Engineering Laboratory, and headed its Alloy Physics and Magnetic Materials Groups for a number of years. Since his retirement in 1996, he has been a guest scientist at NIST, and a Research Professor at George Washington University. He has performed research on magnetic materials, superconductivity, magnetooptics, and magnetic refrigeration.

The National Institute of Standards and Technology is an agency of the Technology Administration, U.S. Department of Commerce.

Available online at www.sciencedirect.com
SCIENCE DIRECT
Physica C 439 (2006) 93–100
PHYSICA C
www.elsevier.com/locate/physc

Subsolidus phase relationships of the $BaO–R_2O_3–CuO_z$ (R = Eu, Dy, and Ho) systems under carbonate-free conditions at $T = 810\ °C$ and $p_{O_2} = 100\ Pa$

W. Wong-Ng *, Z. Yang, L.P. Cook, J. Frank, M. Loung

Ceramics Division, Materials Science and Engineering Laboratory, National Institute of Standards and Technology, Gaithersburg, MD 20899, United States
Chemistry Department, University of Maryland, College Park, MD 20742, United States

Received 28 July 2005
Available online 18 April 2006

Abstract

For applications of phase equilibria to second-generation coated-conductor high-T_c superconductor processing, phase diagrams constructed under carbonate-free conditions are needed. Using a procedure for preparing carbonate-free precursors based on BaO, the phase diagrams of three $BaO–R_2O_3–CuO_z$ systems (R = Eu, Dy, and Ho) were determined at 810 °C and $p_{O_2} = 100$ Pa (0.1% O_2 by volume). The three phase diagrams are substantially different from one another. Among the three systems, Eu^{3+} has the largest ionic radius and therefore most closely matches the ionic size of Ba^{2+}. Two solid solution series, namely, $Ba_{2-x}Eu_xCuO_{3+z}$ and $Ba_{2-x}Eu_{1+x}Cu_3O_{6+z}$ were found in the $BaO–Eu_2O_3–CuO_z$ system. The $BaO–Dy_2O_3–CuO_z$ and the $BaO–Ho_2O_3–CuO_z$ systems do not contain solid solution phases. In these systems, which contain the smaller R = Dy, and Ho rare earths, the $Ba_{2-x}Eu_xCuO_{3+z}$ solid solution and Eu_2CuO_4 phases of the Eu-system are replaced by the $Ba_6RCu_3O_z$ (6 1 3) phase and the $R_2Cu_2O_5$ phase, respectively. Additionally, the $Ba_4RCu_3O_z$ (4 1 3) phase appears in systems with smaller R (Dy and Ho) but not in the Eu-system. The Ho-system contains the $Ba_3R_4O_9$ phase, as well. Consequently, the tie-line relationships are substantially different in these three systems. Among the three diagrams, the diagram for R = Ho is most similar to that of the R = Y system.

1. Introduction

Phase diagrams are considered as blueprints or roadmaps for improving the processing of superconducting materials. In particular, second-generation high-T_c superconductor tapes fabricated by deposition on flexible coated-conductors have received increased attention recently [1–5]. Currently this state-of-the-art technology holds the most promise for commercial electric utility and high magnetic field applications. Second-generation superconductors are based on epitaxial films of $BaO–R_2O_3–CuO_z$ and $BaO–Y_2O_3–CuO_z$ materials (R = lanthanides) [6–8] separated from the underlying flexible, textured metallic conductor by one or more layers of epitaxial oxide buffer. The two most promising technologies for preparing coated metallic substrates suitable for deposition of high-T_c superconductors are known as the rolling-assisted biaxially textured substrate method (RABiTS) [1,2], and the ion beam-assisted deposition method (IBAD) [3,4].

The entire family of $Ba_2RCu_3O_{6+z}$ [2 1 3] materials is of interest for the development of coated-conductor superconductors. This family of materials is important partly because a number of 2 1 3 phases have higher T_c values than the Y-analog, and also because thin films of certain of the 2 1 3 phases have better surface properties than the Y-analog [9]. It is essential to have a data base for the entire $BaO–R_2O_3–CuO_z$ series as a guide for superconductor processing using the RABiTS and IBAD technologies.

* Corresponding author. Address: Ceramics Division, Materials Science and Engineering Laboratory, National Institute of Standards and Technology, Gaithersburg, MD 20899, United States. Tel.: +1 301 975 5791; fax: +1 301 975 5334.
E-mail address: winnie.wong-ng@nist.gov (W. Wong-Ng).

0921-4534/$ - see front matter © 2006 Elsevier B.V. All rights reserved.
doi:10.1016/j.physc.2006.03.001

The phase diagrams reported previously by us for the $BaO–R_2O_3–CuO_z$ systems (R = Nd [10], Sm [11], Y [12], Gd and Er [13]) were determined under carbonate-free conditions to better match RABiTS and IBAD processing conditions. The goal of the present study is to extend our phase diagram determinations to the R = Eu, Dy, and Ho systems under similar experimental conditions ($T = 810$ °C, $p_{O_2} = 100$ Pa, BaO as a source for Ba). This particular set of experimental condition was chosen in the current and earlier studies [10–13] to match the processing condition of the IBAD and RABiTS films. Although various phase diagrams of the $BaO–Eu_2O_3–CuO_z$ [7,14–16], $BaO–Dy_2O_3–CuO_z$ [7,17,18], and $BaO–Ho_2O_3–CuO_z$ [19–21] systems are available in literature, the majority of these diagrams were prepared using $BaCO_3$ as one of the starting reagents, undoubtedly because of the difficulty in handling BaO. Those few studies which reported using BaO were not carried out entirely under atmospherically controlled conditions. In this paper, emphasis will be placed on phase formation and subsolidus phase compatibilities. The crystal chemistry and crystal structure of compounds of the $BaO–R_2O_3–CuO_z$ systems have been reported extensively elsewhere and will not be discussed in detail here. This project is part of an intensive Department of Energy research and development program focused on high-T_c wires and cables for high-impact commercial applications.

2. Experimental details[1]

2.1. Preparation of BaO

BaO was prepared in this laboratory by vacuum calcination of $BaCO_3$ (99.99% purity, metals basis) in a specially designed vertical tube furnace. An MgO crucible containing ≈15 g of $BaCO_3$ was suspended in the hot zone of the furnace, and the furnace was evacuated to a pressure of ≈10 μm Hg or less by a high capacity mechanical pump. The following heating schedule was used: room temperature to 1300 °C in 20 h; isothermal at 1300 °C for 10 h; 1300 °C to room temperature in 20 h. During vacuum calcination the pressure typically increased to ≈200 μm Hg as CO_2 was evolved, and then rapidly returned to ≈10 μm Hg or less as the decomposition of the $BaCO_3$ was completed. After cooling, the BaO was lowered through an interlock into a transfer vessel, and then transported to an Ar-filled glove-box continually purged with a recirculating purifier, which removed atmospheric contaminants from the Ar to <1 ppm by volume. X-ray powder diffraction showed only the characteristic peaks for BaO.

[1] Certain commercial equipment, instruments, or materials are identified in this paper to foster understanding. Such identification does not imply recommendation or endorsement by the National Institute of Standards and Technology, nor does it imply that the materials or equipment identified are necessarily the best available for the purpose.

2.2. Sample preparation

All sample weighings, homogenizations and pressings of pellets were performed inside the glove-box. Pelletized samples were placed inside individual MgO crucibles for annealing in a horizontal box-type controlled-atmosphere furnace. Transfer from the glove-box to the box furnace and vice versa was achieved via a second transfer vessel and an interlock system attached to the furnace.

Samples of 34, 32, and 40 compositions, for the $BaO–R_2O_3–CuO_z$ (R = Eu, Dy, and Ho) systems, respectively, were prepared using the solid state sintering method (Tables 1–3). Stoichiometric amounts of BaO, R_2O_3 (99.99% purity, metals basis), and CuO (99.99% purity, metals basis) were mixed and pressed into pellets, and annealed in an atmospherically controlled box furnace. During the annealings, the oxygen pressure of Ar/O_2 mixtures was controlled using a mass flow meter and monitored at both the inlet and outlet of the furnace using a zirconia oxygen sensor. Samples were annealed at 810 °C for the experiments at $p_{O_2} = 100$ Pa (0.1% O_2 by volume). Intermediate grindings and pelletizations took place until

Table 1
Samples prepared for studies in the $BaO–Eu_2O_3–CuO_z$ system at $T = 810$ °C and $p_{O_2} = 100$ Pa

#	Ba	Eu	Cu
1	33.33	16.67	50
2	31.67	18.33	50
3	30	20	50
4	28.33	21.67	50
5	50	25	25
6	44	20	36
7	65	15	20
8	50	40	10
9	40	40	20
10	45	27.5	27.5
11	63.33	3.33	33.33
12	60	6.67	33.33
13	56.67	10	33.33
14	53.33	13.33	33.33
15	48.75	26.25	25
16	47	8	45
17	40	20	40
18	40	5	55
19	25	5	70
20	10	70	20
21	20	70	10
22	32	11	57
23	27.5	47.5	25
24	22.5	52.5	25
25	27	33	40
26	51.25	23.75	25
27	31	30	39
28	10	40	50
29	60	10	30
30	45	23	32
31	55	5	40
32	42.86	57.14	0
33	35	15	50
34	70	3	27

Table 2
Samples prepared for studies in the $BaO–Dy_2O_3–CuO_z$ system at $T = 810$ °C and $p_{O_2} = 100$ Pa

#	Ba	Dy	Cu
1	60	10	30
2	50	17	33
3	65	17.5	17.5
4	70	5	25
5	58	3	39
6	54	8	38
7	45	15	40
8	40	40	20
9	60	35	5
10	40	20	40
11	35	60	5
12	20	70	10
13	25	25	50
14	40	5	55
15	25	5	70
16	10	35	55
17	10	65	25
18	50	25	25
19	45	10	45
20	35	53	12
21	50	40	10
22	35	20	45
23	33.33	16.67	50
24	31.67	18.33	50
25	63.33	3.34	33.33
26	33.33	66.67	0
27	50	50	0
28	66.67	33.33	0
29	42.86	57.14	0
30	10	50	40
31	50	12.5	37.5
32	0	50	50

Table 3
Samples prepared for studies in the $BaO–Ho_2O_3–CuO_z$ system at $T = 810$ °C and $p_{O_2} = 100$ Pa

#	Ba	Ho	Cu
1	50	16.67	33.33
2	31.67	18.33	50
3	30	20	50
4	50	25	25
5	44	20	36
6	65	15	20
7	50	40	10
8	40	40	20
9	45	27.5	27.5
10	63.33	3.33	33.33
11	60	6.67	33.33
12	48.75	26.25	25
13	47	8	45
14	40	20	40
15	40	5	55
16	25	5	70
17	10	70	20
18	20	70	10
19	32	11	57
20	22.5	52.5	25
21	27	33	40
22	51.25	23.75	25
23	31	30	39
24	10	40	50
25	60	10	30
26	45	23	32
27	55	5	40
28	42.86	57.14	0
29	48.75	13.75	37.5
30	47.5	15	37.5
31	46.25	16.25	37.5
32	59	11	30
33	58	12	30
34	57	13	30
35	43	11	46
36	43	16	41
37	55	13	32
38	53	9	38
39	62	12	26
40	64	7	29

no further changes were detected in the powder X-ray diffraction patterns. Samples were processed for about 3 weeks each. All X-ray patterns were obtained using a hermetic cell designed for air-sensitive materials [22].

2.3. X-ray powder diffraction

X-ray powder diffraction was used to identify the $BaO–R_2O_3–CuO_z$ phases synthesized and to confirm phase purity. Specimens were loaded into a hermetically sealed cell [22]. Samples were loaded inside an Ar-filled glove box. Data were collected using a computer-controlled automated diffractometer equipped with a theta-compensation slit; CuK_α radiation was used at 45 kV and 40 mA. The radiation was detected by a scintillation counter and a solid-state amplifier. A Siemens diffraction software package and reference X-ray diffraction patterns of the ICDD Powder Diffraction File (PDF) [23] were used for phase identification.

3. Results and discussion

Figs. 1–3 give the phase diagrams of the $BaO–Eu_2O_3–CuO_z$, $BaO–Dy_2O_3–CuO_z$, and $BaO–Ho_2O_3–CuO_z$ systems. These diagrams appear to be relatively simple, but are different from each other and also from those prepared using $BaCO_3$ [7,14–21], particularly in the Ba-rich region.

3.1. Phase equilibria of the $BaO–R_2O_3–CuO_z$ systems

All three systems have in common the $BaO–CuO_z$ binary. A review of the crystal chemistry and crystallography of the phases in the $BaO–CuO_z$ system was given by Wong-Ng and Cook [24]. In the present study, we have observed a total of three binary compounds at $p_{O_2} = 100$ Pa: the reduced phase $BaCu_2O_{2+z}$, Ba_2CuO_{3+z} [25–28] and $BaCuO_{2+z}$. The Ba_2CuO_{3+z} phase is atmospherically very sensitive, and cannot be prepared in the presence of moisture and carbonate; this phase has not been reported in several previous studies of the $BaO–CuO_z$ binary. The oxygen content of the $BaCuO_{2+z}$ series has been reported to vary between 2.0 and 2.5. Three structure types are known, with

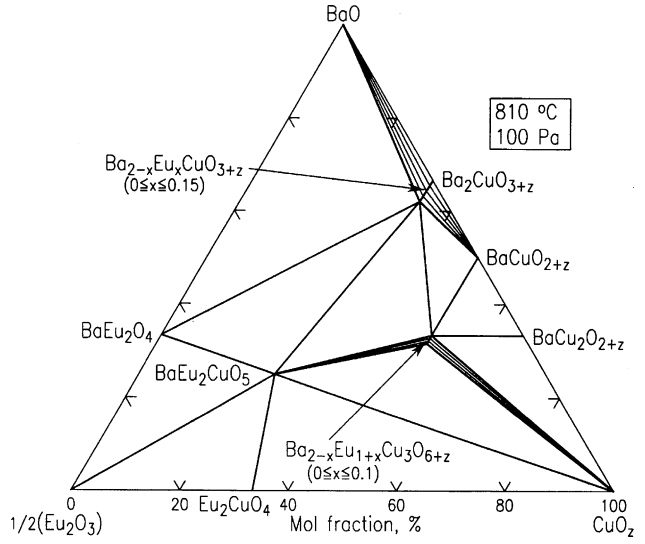

Fig. 1. Phase diagram of the BaO–1/2Eu_2O_3–CuO_z system prepared at ≈810 °C, p_{O_2} = 100 Pa, with BaO starting material.

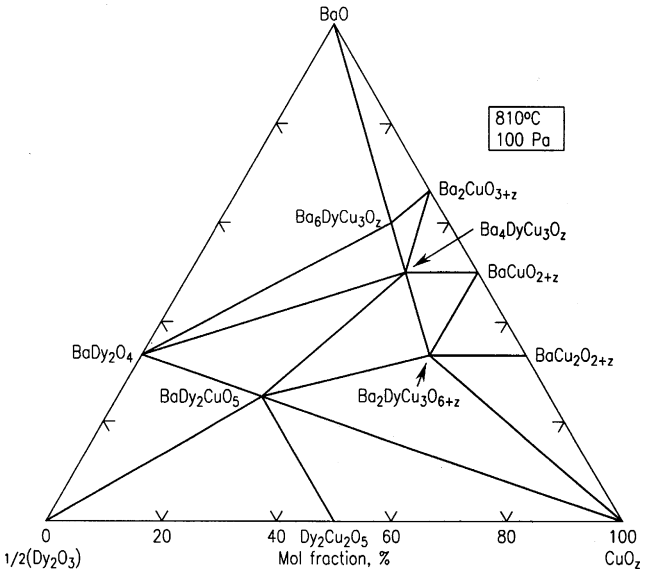

Fig. 2. Phase diagram of the BaO–1/2Dy_2O_3–CuO_z system prepared at ≈810 °C, p_{O_2} = 100 Pa, with BaO starting material.

$0 < z < 0.12$, $0.29 < z < 0.36$, and $z = 0.5$. The most commonly recognized structure is cubic, with $0 < z < 0.12$. Phase compositions with z greater than 0.12 have been reported by Petricek et al. [29]. We found no evidence for the existence of the $Ba_2Cu_3O_{5+z}$ or $Ba_3Cu_5O_{8+z}$ phases [24] under the current conditions. The Ba_3CuO_4 phase, reported by Frase and Clarke [30] and Abbattista et al. [31,32] to be stable under very reduced conditions, was not detected in the present study. In contrast to the BaO–Nd_2O_3–CuO_z [10] and the BaO–Sm_2O_3–CuO_z systems [11], as the ionic sizes of Dy and Ho [24] are rather different from that of Ba (1.42 Å (VIII-coordination for Ba^{2+}) vs. 1.027 Å for Dy^{3+}, and 1.015 Å for Ho^{3+}) [33], no solid solution of the (Ba, R)$_2CuO_{3+z}$ type was observed.

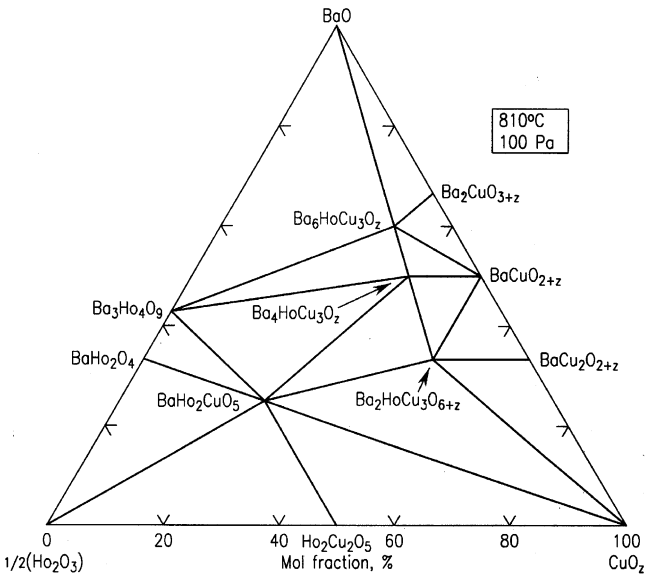

Fig. 3. Phase diagram of the BaO–1/2Ho_2O_3–CuO_z system prepared at ≈810 °C, p_{O_2} = 100 Pa, with BaO starting material.

3.1.1. *BaO–Eu_2O_3–CuO_z system*

3.1.1.1. BaO–Eu_2O_3. The $BaEu_2O_4$ phase was the only compound found in the binary BaO–Eu_2O_3 system. $BaEu_2O_4$ was reported to crystallize in the orthorhombic *Pnam* system [18,34], which is isostructural with the $BaNd_2O_4$ structure [35]. The $Ba_3R_4O_9$ type phase (rhombohedral *R*3*m*) which exists in systems with smaller R^{3+} (for example, R = Y) [12] cannot be prepared with the relatively larger Eu^{3+}. Similar to the other (R = Nd, Sm, Y, Gd, and Er) analogs, the $Ba_4R_2O_7$- and $Ba_2R_2O_5$-type phases were found to be absent. These two phases, which are actually the oxycarbonates $Ba_2R_2O_5 \cdot CO_2$ and $Ba_4R_2O_7 \cdot 2CO_2$ [36], respectively, dissociate according to the following reactions [27,32]:

$$3Ba_2R_2O_5 \cdot CO_2 \rightarrow 2BaR_2O_4 + Ba_4R_2O_7 \cdot 2CO_2 + CO_2$$

$$2Ba_4R_2O_7 \cdot 2CO_2 \rightarrow Ba_3R_4O_9 + 5BaO + 4CO_2$$

As carbonate appears to be essential for their formation, it is logical that they were not observed under the conditions of our experiments.

3.1.1.2. Eu_2O_3–CuO_z. In the Eu_2O_3–CuO_z system, Eu_2CuO_4 (tetragonal *I*4/*mmm* symmetry [37]) was confirmed to be the only compound formed. Apparently, under 100 Pa p_{O_2}, the reduced rhombohedral $RCuO_2$ phase reported by Ref. [38] is not stable. Luce and Stacy [26] reported an oxidized monoclinic phase $EuCu_2O_4$ (*I*2/*a*, $a = 5.7638(3)$ Å, $b = 9.6422(4)$ Å, $c = 5.6864(3)$ Å, $\beta = 92.350(2)°$), which was prepared from hydroxide melts. However, this phase is not expected to be stable under reducing conditions.

3.1.1.3. BaO–Eu_2O_3–CuO_z. There are a total of three phases in the ternary BaO–Eu_2O_3–CuO_x system. Among

them, two form solid solutions. These three phases are $Ba_{2-x}Eu_{1+x}Cu_3O_{6+z}$ $(0 \leqslant x \leqslant 0.1)$, $(Ba_{2-x}Eu_x)CuO_{3+z}$ $(0 \leqslant x \leqslant 0.15)$, and $BaEu_2CuO_5$. The $Ba_4R_2Cu_2O_{9-z}$ phase, which we have successfully prepared in the Nd- and Sm-systems [10,11], cannot be prepared in the Eu-system. The $Ba_6EuCu_3O_z$ (Eu-613) [39,40] and $Ba_4EuCu_3O_{8.5+z}$ (Eu-413, cubic perovskite-related) [40,41] phases, which were stable under more oxidized conditions, were found to be unstable under 100 Pa p_{O_2}. In addition, according to Osamura and Zhang [21], the perovskite-related phase, $Ba_6EuCu_3O_z$ (*I4/mmm*, $a = 4.0656(2)$ Å and $c = 21.7101(1)$ Å) [39], which exists in air, was not observed under 100 Pa p_{O_2}. Two structural types of R-613 (orthorhombic and tetragonal) were reported, depending on the distribution of oxygen atoms on the (R, Cu)–O layers in the structure. Apparently, when the size of R is small, such as for Y, the 413 phase is stable at 100 Pa p_{O_2} [12]. The 'green phase' $BaEu_2CuO_5$ (121) is isostructural to BaY_2CuO_5 [42–44], but has a different structure from that of the Nd-'brown phase', $BaNd_2CuO_5$ (Nd-121) [10]. While Nd-121 is tetragonal *I4/mmm*, Eu-121 is orthorhombic *Pbnm* [42].

3.1.2. BaO–Dy_2O_3–CuO_z system

3.1.2.1. BaO–Dy_2O_3. The $BaDy_2O_4$ phase was the only compound found in the binary BaO–Dy_2O_3 system. $BaDy_2O_4$ is isostructural with $BaEu_2O_4$ [34] and was reported to have the lattice parameters of $a = 10.4274(14)$ Å, $b = 12.1550(11)$ Å, and $c = 3.4730(6)$ Å [45]. Similar to the Eu-system, the $Ba_3R_4O_9$-type phase [46,47] cannot be prepared with the relatively larger Dy^{3+} under reduced conditions, and the $Ba_4R_2O_7$ and $Ba_2R_2O_5$ type phases [20,27,32,36] were found to be absent under carbonate-free conditions.

3.1.2.2. Dy_2O_3–CuO_z. In the Dy_2O_3–CuO_z system, a 1:1 phase $Dy_2Cu_2O_5$ was found [48]. The $Dy_2Cu_2O_5$ was determined by Garcia-Munoz and Rodriguez-Carvajal from neutron diffraction to be orthorhombic, $Pna2_1$, with $a = 10.830$ Å, $b = 3.514$ Å and $c = 12.465$ Å [48]. The R_2CuO_4 type phase usually exists when R is relatively large $(r_R^{3+} > r_{Dy}^{3+})$. The Dy_2CuO_4 phase as reported by Okada et al. [49] was prepared under high pressure. The oxygen partial pressure of 100 Pa p_{O_2} used in our experiments is presumably not low enough for the reduced $RCuO_2$ phase [38] to be stable. Luce and Stacy [26] reported a monoclinic phase $DyCu_2O_4$ (*I2/a*, $a = 5.7049(3)$ Å, $b = 9.5912(4)$ Å, $c = 5.6248(3)$ Å, $\beta = 92.448(2)°$), but it was prepared from a hydroxide melt and was not observed under the conditions of our experiments.

3.1.2.3. BaO–Dy_2O_3–CuO_z. A total of four ternary oxides ($Ba_2DyCu_3O_{6+x}$ (2:1:3), $Ba_4DyCu_3O_x$ (4:1:3), $Ba_6DyCu_3O_x$ (6:1:3), and the 'green phase' $BaDy_2CuO_5$ (1:2:1)) was found in the BaO–Dy_2O_3–CuO_x system. The $(Ba_{2-x}R_x)CuO_{3+z}$ solid solution phase, found in some analogs near the BaO corner, is absent here. Instead, compounds $Ba_4DyCu_3O_x$ and $Ba_6DyCu_3O_x$ were found. The BaO–Dy_2O_3–CuO_z phase diagram is rather similar to the BaO–Y_2O_3–CuO_z system reported by Wong-Ng et al. [12], Abbattista et al. [31], and Osmura and Zhang [21]. A number of different phases reported near the Ba-rich end are apparently a result of the use of barium carbonate [7,14–16,18–21,36].

The $Ba_2DyCu_3O_{6+x}$ phase is a cation stoichiometric compound. By contrast, a solid solution was reported in the lanthanide-containing $Ba_{2-x}R_{1+x}Cu_3O_{6+z}$ phases with relatively larger size of R (R = La, Nd, Sm, Eu, and Gd) [16], where the Shannon ionic radius of Ba (1.42 Å (VIII-coordination [34])) and R are more comparable for lighter lanthanides (1.079–1.160 Å from Sm to La, VIII-coordination). The $Ba_2DyCu_3O_{6+x}$ phase is tetragonal *P4/mmm* when quenched from 810 °C. The structure of $Ba_4DyCu_3O_{6+x}$ was reported to be of the cubic oxygen-defect perovskite type [39,50], and that of the orthorhombic $Ba_6DyCu_3O_{6+x}$ phase is of the $SrTi_2O_4$-type (layered perovskite structure) [39,41]. The structure of the BaY_2CuO_5 "green" phase, orthorhombic with space group *Pnma*, has been studied extensively [42–44].

3.1.3. BaO–Ho_2O_3–CuO_z system

3.1.3.1. BaO–Ho_2O_3. $Ba_3Ho_4O_9$ and $BaHo_2O_4$ [51] were both formed at $p_{O_2} = 100$ Pa in the BaO–Ho_2O_3 system. The structure of $BaHo_2O_4$ [51] is similar to that of $BaEu_2O_4$ [37] and $BaDy_2O_4$ [45]. There appears to be controversy about the definitive structure of $Ba_3R_4O_9$ type. For example, Kovba et al. [52], Spitsyn [53] and Wong-Ng et al. [54] reported the structure to be $R\bar{3}m$, however, according to Müller-Buschbaum and Scheikowski [55], Müller-Buschbaum and Schrandt [47], and Krueger and Müller-Buschbaum [56,57], $Ba_3R_4O_9$ is trigonal with an *R*3 space group ($a = 6.098$ Å, $c = 25.136$ Å; $Z = 3$ [55]). The *R*3 structure of $Ba_3R_4O_9$ consists of corner-shared planar HoO_6 octahedra and HoO_6 trigonal prisms connected as a Kagomè-network. The Ba's have a (6 + 3) coordination [47,55].

3.1.3.2. Ho_2O_3–CuO_z. In the binary Ho_2O_3–CuO_z diagrams, only the $Ho_2Cu_2O_5$ phase was observed at $p_{O_2} = 21$ kPa [20]. The R_2CuO_4 type phase exists only when R is relatively large $(r_R^{3+} > r_{Dy}^{3+})$. As the ionic radius of R^{3+} decreases beyond Eu^{3+} (from Dy^{3+} to Lu^{3+}), the $R_2Cu_2O_5$ type phase (orthorhombic, $Pna2_1$) was found instead [13]. The reported Ho_2CuO_4 phase has been prepared using the aqueous solution route via high pressure processing [49]. Similar to the Dy-system, the $HoCu_2O_4$ [26] was not stable under current conditions. The reduced phase of the $RCuO_2$ structure type [38] also was not found.

3.1.3.3. BaO–Ho_2O_3–CuO_z. A total of four ternary oxides ($Ba_2HoCu_3O_{6+z}$ (213), $Ba_4HoCu_3O_z$ (413), $Ba_6HoCu_3O_z$ (613), and the 'green phase' $BaHo_2CuO_5$ (121)) was found in the BaO–Ho_2O_3–CuO_z system. The occurrence of the compounds $Ba_4HoCu_3O_z$ and $Ba_6HoCu_3O_z$ in the BaO-rich part of the diagram is similar to that of the

$BaO–Y_2O_3–CuO_z$ [12] and the $BaO–Dy_2O_3–CuO_z$ systems. The structure of $Ba_4HoCu_3O_z$ was reported to be of the cubic oxygen-defect perovskite type ($a = 8.08236(5)$ Å when prepared in oxygen) [58]. The orthorhombic $Ba_6HoCu_3O_z$ phase is of the $SrTi_2O_4$-type (layered perovskite structure) [39]. The $BaHo_2CuO_5$ "green phase" is isostructural with BaY_2CuO_5 [42–44]. Similar to $Ba_2YCu_3O_{6+z}$, the $Ba_2HoCu_3O_{6+z}$ (2:1:3) phase is a stoichiometric compound with respect to the cation content.

3.2. Comparisons of phase equilibria of $BaO–R_2O_3–CuO_z$ (R = Eu, Dy, and Ho)

The phase formation of the $BaO–R_2O_3–CuO_z$ (R = Eu, Dy, and Ho) systems follows a general trend in that the larger the size of lanthanide, the more solid solutions there are present, which in general agrees with our observations in the $BaO–R_2O_3–CuO_z$ analogs, as prepared in air [16].

In the binary systems, the phase formation in the $R_2O_3–CuO_z$ and the $BaO–R_2O_3$ systems are the same for R = Eu and Dy, but different from the R = Ho system. In the Ho-system, in addition to the BaR_2O_4 phase, it also has the $Ba_3R_4O_9$ phase. While the Eu-system contains Eu_2CuO_4 (tetragonal *I4/mmm* symmetry [37]), the Dy- and Ho-systems have the $Dy_2Cu_2O_5$ and $Ho_2Cu_2O_5$ phases (orthorhombic, $Pna2_1$ symmetry [48]) instead.

The tie-line distribution in the $BaO–Eu_2O_3–CuO_z$ system, as shown in Fig. 2, is in general similar to that found in the $BaO–Sm_2O_3–CuO_z$ system [11]. Due to the greater mismatch of the Ba^{2+} and Eu^{3+} (1.42 Å vs. 1.066 Å (VIII-coordination)) as compared with the Ba^{2+} and Sm^{3+} (1.42 Å vs. 1.079 Å), while there is a single phase range of the ternary solid solutions $Ba_{2-x}Sm_{1+x}Cu_3O_{6+z}$ ($0 \leqslant x \leqslant 0.2$) in the $BaO–Sm_2O_3–CuO_z$ system, the Eu-213 phase has a smaller single phase region, with $x \leqslant 0.1$. As a result, there is only a narrow tie-line bundle connecting the Eu-213 phase to the 'green phase', $BaEu_2CuO_5$, and to the CuO_z phase. The Dy-213 and Ho-213 phases are stoichiometric compound with respect to the cation content. The Dy- and Ho-systems contain the 6 1 3 and 4 1 3 phases while the Eu-system includes the solid solution region of $(Ba, Eu)_2CuO_{3+z}$. All ternary oxides are compatible with at least four other phases. In the case of BaR_2CuO_5, six tie-lines were found to originate from it. In the BaO-rich region of the $BaO–Eu_2O_3–CuO_z$ system, tie-lines are found between $(Ba_{2-x}R_x)CuO_{3+z}$ and $BaEu_2CuO_5$, and between BaO and $(Ba_{2-x}R_x)CuO_{3+z}$. The tie-lines determined near the CuO_z and R_2O_3 regions of all these systems are in agreement with most other diagrams, whether prepared using $BaCO_3$, BaO_2, BaO, or $Ba(NO_3)_2$. However, the diagrams near the BaO region are substantially different. The tie-line relationships around the R-213 phase are also different from the literature data. For example, in the present study, the $Ba_2HoCu_3O_{6+z}$ phase is found to be compatible with the $Ba_4HoCu_3O_z$ phase. The formation of the tie-line between $Ba_2RCu_3O_{6+z}$ and $Ba_4RCu_3O_z$ was also found in our previous studies of the Nd-, Sm-, Y-, Gd-, and Er-systems [10–13]. However, most literature phase diagrams reported to date involve a tie-line between $BaCuO_{2+z}$ and BaR_2CuO_5 [59–66]. The majority of literature studies were not conducted entirely under atmospherically controlled conditions, and it is clear that the presence of CO_2 affects the tie-line relationships.

4. Summary and conclusions

We have investigated the phase relationships of the $BaO–Eu_2O_3–CuO_z$, $BaO–Dy_2O_3–CuO_z$, and the $BaO–Ho_2O_3–CuO_z$ systems at 810 °C, $p_{O_2} = 100$ Pa. Sample preparation and handling were accomplished using a glove box filled with argon and an atmospherically controlled furnace and apparatus. Among the three systems, only the Eu-system has two solid solution series, namely $Ba_{2-x}Eu_{1+x}Cu_3O_{6+z}$ ($0 \leqslant x \leqslant 0.1$) and $(Ba_{2-x}Eu_x)CuO_{3+z}$ ($0 \leqslant x \leqslant 0.15$). Similar to the Nd-, Sm-, Gd-, Y-, and Er-systems that we have reported previously [10–13], the presence of CO_2 affects the tie-line relationships. For example, the tie-line relationships among the phases, BaR_2CuO_5, $Ba_2RCu_3O_{6+z}$, $BaCuO_{2+z}$, $Ba_4RCu_3O_z$ and $Ba_6RCu_3O_z$ are different from the literature data. Most literature phase diagrams reported to date involve a tie-line between $BaCuO_{2+z}$ and BaR_2CuO_5. A comparison of the three systems indicates that due to the absence of the $Ba_3R_4O_9$ phase in the Eu- and Dy-systems, the formation of R_2CuO_4 type phase instead of $R_2Cu_2O_5$ phases in the Eu-analog, and the absence of R-413 and R-613 phases in the Eu-system, the tie-line relations are different in the three systems.

For applications of phase equilibria to coated conductor processing, phase diagrams constructed under carbonate-free conditions should be employed. From examination of Figs. 1–3, there are significant differences in the tie-line distributions occurring under carbonate-free conditions, relative to those occurring in the phase diagrams based on $BaCO_3$-derived starting materials. Under carbonate-free conditions at a p_{O_2} of 100 Pa, the $Ba_2EuCu_3O_{6+z}–Ba_6EuCu_3O_z$ tie line replaces a $BaCuO_{2+z}–BaEu_2CuO_5$ tie line in the $BaO–Eu_2O_3–CuO_z$ system; the $Ba_2DyCu_3O_{6+z}–Ba_6DyCu_3O_z$ tie line replaces a $BaCuO_{2+z}–BaDy_2CuO_5$ tie line in the $BaO–Dy_2O_3–CuO_z$ system; and the $Ba_2HoCu_3O_{6+z}–Ba_6HoCu_3O_z$ tie line replaces a $BaCuO_{2+z}–BaHo_2CuO_5$ tie line in the $BaO–Ho_2O_3–CuO_z$ system. The net effect of the difference in the tie-line relationships is to expand the field of stability of the Eu-213, Dy213, and Ho-213 superconductors toward the BaO-rich corner of the phase diagram. For example, the $Ba_4HoCu_3O_z$ phase can coexist with Ho-213. Because $Ba_4RCu_3O_z$ is atmospherically more sensitive than BaR_2CuO_5, its presence in R-213 materials could be deleterious. It may be important during the RABiTS and IBAD processes to avoid bulk compositions in this region.

Phase diagrams of the $BaO–R_2O_3–CuO_z$ (R = lanthanides) systems are important for second-generation coated-conductor development: systematic studies of diagrams of other analogs (i.e., R = La, Pr, Tm, Yb, and

Lu) under atmospherically controlled conditions are needed to augment the data presently available.

Acknowledgements

The United States Department of Energy is acknowledged for partial financial support of this project. Mr. Nils Swanson and Dr. Peter Schenck are thanked for assistance with the phase diagram graphics.

References

[1] A. Goyal, D.P. Norton, J.D. Budai, M. Paranthaman, E.D. Specht, D.M. Kroeger, D.K. Christen, Q. He, B. Saffian, F.A. List, D.F. Lee, P.M. Martin, C.E. Klabunde, E. Hartfield, V.K. Sikka, Appl. Phys. Lett. 69 (12) (1996) 1795.
[2] M. Paranthaman, C. Park, X. Cui, A. Goyal, D.F. Lee, P.M. Martin, T.G. Chirayil, D.T. Verebelyi, D.P. Norton, D.K. Christen, D.M. Kroeger, J. Mater. Res. 15 (12) (2000) 2647.
[3] R.P. Reade, P. Berdahl, R.E. Russo, S.M. Garrison, Appl. Phys. Lett. 61 (18) (1992) 2231.
[4] S.R. Foltyn, P. Tiwari, R.C. Dye, M.Q. Le, X.D. Wu, Appl. Phys. Lett. 63 (13) (1993) 1849.
[5] M. Bauer, R. Semerad, H. Kinder, IEEE Trans. Appl. Supercond. 9 (2) (1999) 1502.
[6] J.L. MacManus-Driscoll, Advanced Materials VCH Verlagsgesellschaft, (May 1997) 9 (6) (1997) 456–473.
[7] W. Wong-Ng, B. Paretzkin, E.R. Fuller Jr., J. Solid State Chem. 85 (1) (1990) 117.
[8] J.E. Ullman, R.W. McCallum, J.D. Verhoeven, J. Mater. Res. 4 (4) (1989) 752.
[9] M. Murakami, S.-I. Yoo, T. Higuchi, N. Sakai, J. Weltz, N. Koshizuka, S. Tanaka, Jpn. J. Appl. Phys. 33 (5B) (1994) L715.
[10] W. Wong-Ng, L.P. Cook, J. Suh, R. Coutts, J.K. Stalick, I. Levin, Q. Huang, J. Solid State Chem. 173 (2) (2003) 476.
[11] W. Wong-Ng, L.P. Cook, J. Suh, J.A. Kaduk, Physcia C 405 (2004) 47.
[12] W. Wong-Ng, L.P. Cook, J. Suh, Physica C 377 (2002) 107.
[13] W. Wong-Ng, L.P. Cook, J. Suh, Solid State Sci. 6 (1–2) (2004) 1211.
[14] W. Przybylo, K. Fitzner, Mater. Res. Bull. 30 (11) (1995) 1413.
[15] S.A. Hodorowicz, A. Lasocha, W. Lasocha, H.A. Eick, J. Solid State Chem. 75 (2) (1988) 270.
[16] C.N. Pieczulewski, J.E. McAdams, T.O. Mason, J. Am. Ceram. Soc. 73 (10) (1990) 3088.
[17] E. Hodorowicz, S.A. Hodorowicz, H.A. Eick, J. Solid State Chem. 84 (1991) 401.
[18] H. Ishizuka, Y. Idemoto, K. Fucki, Physica C 195 (1–2) (1992) 145.
[19] E. Hodorowicz, S.A. Hodorowicz, C. Raymond, H.A. Eick, J. Solid State Chem. 98 (1) (1992) 187.
[20] Y.L. Zhang, J.K. Liang, X.R. Chen, G.H. Rao, H.B. Liu, Y.M. Ni, D.N. Zheng, S.S. Xie, J. Less-Common Met. 146 (1989) 121.
[21] K. Osamura, W. Zhang, Z. Metallkd. 84 (8) (1993) 522.
[22] J.J. Ritter, Powder Diffract. 3 (1) (1988) 30.
[23] PDF, Powder Diffraction File, produced by International Centre for Diffraction Data (ICDD), 12 Campus Blvd., Newtown Square, PA 19073–3273, USA.
[24] W. Wong-Ng, L.P. Cook, Powder Diffract. 9 (4) (1994) 280.
[25] W. Wong-Ng, K.L. Davis, R.S. Roth, J. Amer. Ceram. Soc. 71 (2) (1988) C64.
[26] J.L. Luce, A.M. Stacy, Chem. Mater. 9 (7) (1997) 1508.
[27] D.M. Deleeuw, H.A. Mutsaers, C. Langereis, H.C.A. Smoorenburg, P.J. Rommers, Physica C 152 (1988) 39.
[28] J. Thompson, J.D. FitzGerald, R.L. Withers, P.J. Barlow, J.S. Anderson, Mater. Res. Bull. 24 (1989) 505.
[29] S. Petricek, N. Bukovec, P. Bukovec, J. Solid State Chem. 99 (1992) 58.
[30] K.G. Frase, D.R. Clarke, Adv. Ceram Mater. 2 (3B) (1987) 295.
[31] F. Abbattista, M. Vallino, D. Mazza, Mater. Chem. Phys. 21 (1989) 521.
[32] F. Abbattista, M. Vallino, D. Mazza, M.L. Borlera, C. Brisi, Mater. Chem. Phys. 20 (2) (1988) 191.
[33] R.D. Shannon, Acta Crystallogr. A32 (1976) 751.
[34] W. Wong-Ng, B. Paretzkin, Set 42-1497, Powder Diffraction File, produced by ICDD, 12 Campus Blvd., Newtown Square, PA 19073–3273, USA, 1991.
[35] J. Stalick, W. Wong-Ng, Mater. Lett. 9 (10) (1990) 401.
[36] R.S. Roth, C.J. Rawn, F. Beech, J.D. Whitler, J.O. Anderson, in: M.F. Yan (Ed.), Ceramic Superconductors II, American Ceramic Society, Westerville, OH, 1988, p. 13.
[37] T. Uzumaki, K. Hashimoto, N. Kamehara, Physica C 202 (1992) 175.
[38] T. Ishiguro, N. Ishizuma, N. Mizutani, M. Kato, J. Solid State Chem. 49 (1983) 232.
[39] W. Zhang, K. Osamura, Physica C 174 (1991) 126.
[40] Y.T. Zhu, E.J. Peterson, P.S. Baldonado, J.Y. Coulter, D.E. Peterson, F.M. Muller, J. Phys. Chem. Solid 59 (8) (1998) 1331.
[41] M. Vallino, D. Mazza, F. Abbattista, J. Less-Common Met. 170 (1) (1991) 83.
[42] W. Wong-Ng, M.A. Kuchinski, H.F. McMurdie, B. Paretzkin, Powder Diffract. 4 (1989) 2.
[43] R.M. Hazen, L.W. Finger, R.I. Angel, C.T. Prewitt, N.L. Ross, H.L. Mao, C.G. Hadidiacos, Phys. Rev. B 35 (13) (1987) 7238.
[44] S.F. Watkins, F.R. Fronczek, K.S. Wheelock, R.G. Goodrich, W.O. Hamilton, W.W. Johnson, Acta Cryst. C44 (1988) 3.
[45] W. Wong-Ng, B. Paretzkin, Set 42-1495, Powder Diffraction File, produced by International Centre for Diffraction Data (ICDD), 12 Campus Blvd., Newtown Square, PA 19073–3273, USA.
[46] W. Wong-Ng, B. Paretzkin, Set 39-1399, Powder Diffraction File, produced by International Centre for Diffraction Data (ICDD), 12 Campus Blvd., Newtown Square, PA 19073–3273, USA, 1988.
[47] H. Müller-Buschbaum, O. Schrandt, J. Alloys Compd. 191 (1) (1993) 151.
[48] J.L. Garcia-Munoz, J. Rodriguez-Carvajal, J. Solid State Chem. 115 (2) (1995) 324.
[49] H. Okada, M. Takano, Y. Takede, Physica C 166 (1990) 111.
[50] Y.T. Zhu, E.J. Peterson, P.S. Baldonado, J.Y. Coulter, D.E. Peterson, F.M. Muller, J. Mater. Res. 14 (2) (1999) 334.
[51] W. Wong-Ng, B. Paretzkin, Set 42-1494, Powder Diffraction File, produced by International Centre for Diffraction Data (ICDD), 12 Campus Blvd., Newtown Square, PA 19073–3273, USA, 1991.
[52] L.M. Kovba, L.N. Lykova, E.V. Antipov, Russ. J. Inorg. Chem. 28 (1983) 409.
[53] K. Spitsyn, Dokl. Chem. 180 (1968) 516.
[54] W. Wong-Ng, H.F. McMurdie, B. Paretzkin, Y. Zheng, C. Hubbard, A.L. Dragoo, J.M. Stewart, Powder Diffract. 3 (1988) 48.
[55] H. Müller-Buschbaum, M. Scheikowski, Z. Anorg. Allg. Chem. 591 (12) (1990) 181.
[56] J. Krueger, H. Müller-Buschbaum, Z. Anorg. Allg. Chem. 512 (5) (1984) 59.
[57] J. Krueger, H. Müller-Buschbaum, Rev. Chim. Miner. 20 (4–5) (1983) 456.
[58] Y. Zhu, E.J. Peterson, P.S. Baldonado, J.Y. Coulter, D.E. Peterson, F.M. Muller, J. Alloys Compd. 281 (1998) 137.
[59] S.N. Koshcheeva, V.A. Fotiev, A.A. Fotiev, V.G. Zubkov, Izv. Akad. Nauk SSSR, Neorg. Mater. 26 (7) (1990) 1491, Inorg. Mater. (Engl. Transl.) 26 (7) 1267.
[60] H. Ouchi, M. Ito, Mater. Sci. Monogr.: High Temp. Supercond. 70 (1991) 489.
[61] R.X. Liang, T. Nakamura, Jpn. J. Appl. Phys. Part 2 27 (7) (1988) L1277.
[62] S.A. Hodorowicz, A. Lasocha, W. Lasocha, A. Chodorowicz, H.A. Eick, Acta Phys. Pol. A75 (3) (1989) 437.

[63] J.K. Liang, X.L. Chen, S. Wu, J. zhao, Y.L. Zhang, S.S. Xie, Solid State Commun. 74 (6) (1990) 509.
[64] E. Hodorowicz, S.A. Hodorowicz, H.A. Eick, Physica C 158 (1–2) (1989) 127.
[65] J.K. Liang, X.T. Xu, G.H. Rao, S. Xie, X. Shao, Z. Duan, J. Phys. D 20 (10) (1987) 1324.
[66] S.A. Hodorowicz, A. Chodorowicz-Bak, J. Czerwonka, E. Hodorowicz, W. Lasocha, H.A. Eick, J. Solid State Chem. 92 (2) (1991) 480.

Nature of the transient BaF_2-related phases in the "BaF_2" processing of $Ba_2YCu_3O_{7-x}$ superconductors

W. Wong-Ng,[a] I. Levin, and L. P. Cook
Ceramics Division, National Institute of Standards and Technology, Gaithersburg, Maryland 20899

R. Feenstra
Condensed Matter Sciences Division, Oak Ridge National Laboratory, Oak Ridge, Tennessee 37831

(Received 14 November 2005; accepted 25 January 2006; published online 10 March 2006)

Transient BaF_2-based oxyfluoride phases are thought to play a critical role in the formation of the *c*-textured $Ba_2YCu_3O_{7-x}$ layers of coated conductors. *In situ* high-temperature x-ray diffraction from the precursor films containing pure BaF_2 as well as pseudobinary BaF_2-Y, BaF_2-Cu, and Y–Cu mixtures and heat treated in water vapor under reduced conditions revealed that the transient BaF_2-based superstructures, similar to those observed during formation of $Ba_2Cu_3O_{7-x}$, develop even from the pure BaF_2 precursor. These superstructures results from the dissolution of oxygen in BaF_2 leading to formation of the oxyfluoride phase, $Ba(F_{2-2x}\square_x)O_x$, with an ordered arrangement of O, F, and F vacancies. © *2006 American Institute of Physics*. [DOI: 10.1063/1.2184757]

The *ex situ* "BaF_2" process,[1,2] which is one of the most successful processes for manufacturing of long-length $Ba_2YCu_3O_{7-x}$ (Y-213) coated conductors, involves a low-temperature deposition of precursor layers onto a substrate using either a fast rate *e*-beam deposition or solution methods. High quality films/tapes have been produced using both $SrTiO_3$ substrates and rolling-assisted biaxially textured substrates.[3–6] Detailed understanding of the phase formation sequence during the *ex situ* "BaF_2" conversion process is important for producing homogeneous tapes with reproducible properties.

The overall process of formation of the Y-213 phase from the (BaF_2+Y+Cu) amorphous mixture can be expressed as $(2BaF_2+Y+3Cu)(\text{amorphous})+2H_2O(g)+(2\frac{1}{2}-\frac{1}{2}x)O_2(g)\rightarrow Ba_2YCu_3O_{7-x}(s)+4HF(g)$;[7,8] that is, the process consists of a series of oxidation/hydration reactions involving BaF_2, Y, and Cu. The cubic BaF_2-like (BF) oxyfluoride $Ba(F_{2-2x}\square_x)O_x$ ($a_{BF}\approx 6.2$ Å)[9] crystallizes from the amorphous precursor around $T=300$ °C. Further heating above $T=550$ °C, produces a BaF_2-related superstructure (SS) having lattice parameters ($a_{ss}\approx a_{BF}\sqrt{6}/2$, $b_{ss}\approx a_{BF}\sqrt{2}/2$, and $c_{ss}\approx a_{BF}\sqrt{3}$)[10–12] and a signature x-ray diffraction reflection at $2\theta\approx 25°$. Wu *et al.*[10] attributed the formation of this superstructure to the dissolution of Y in the BaF_2 with the 2:1 ordering of Ba and Y. Based on the similarity between the c_{ss} and the *c* parameter of Y-213 phase, Wu *et al.*[10,12] suggested that the $(Ba_2Y)F_yO_x$ superstructure provides a template for the nucleation of Y-213 phase and is therefore essential for the epitaxial growth of the superconducting phase. The goal of the present work is to clarify the origin of the transient BaF_2-based superstructure through *in situ* studies of phase formation in the precursor systems BaF_2-Y, BaF_2-Cu, BaF_2-Cu, and BaF_2.

Four different films, 0.7 μm thick, were used in these studies: Film No. 1 (BaF_2+Y[Ba:Y=2:1]), Film No. 2 (BaF_2+Cu[Ba:Cu=2:3]), Film No. 3 (Y+Cu[Y:Cu=1:3]), and Film No. 4 (BaF_2). The cation ratios were selected according to Ba:Y:Cu=2:1:3. The precursors were deposited at ~100 °C by electron beam evaporation of Cu (metal), Y (metal), and BaF_2 on single crystal $SrTiO_3$ substrates.[3] The compositions were derived from calibrated readings of the evaporation rate monitors and inductively coupled plasma (ICP) analysis. The details of the experimental setup for the *ex situ* conversion anneal were reported previously.[7] X-ray diffraction confirmed that two of the as-deposited films were amorphous (Film Nos. 1 and 3), whereas two others (Films Nos. 2 and 4) contained a crystalline BaF_2 phase. The films were relatively stable in air;[2] however, as a precaution, the films were kept in a dry box prior to the high-temperature x-ray diffraction experiments.

In situ studies of phase formation were conducted in a Siemens D5000 θ-θ x-ray diffractometer[13] equipped with a high-temperature furnace, a position sensitive detector, and a custom-designed gas flow apparatus.[7] Cu K_α radiation was used. The sample, mounted on a Pt heating band using alumina paste, was ramped from room temperature to 700 °C and the x-ray diffraction patterns were collected every 50 °C in the 14°–40° 2θ range for 6 min per scan. Finally, the temperature was elevated to 735 °C and multiple x-ray scans, each 6 min long, were collected until no further changes in the diffraction patterns could be observed. The experiments were conducted under a flow of (He +0.1 % O_2) bubbled through the saturated aqueous NaCl solution (9.9 mol % NaCl at 22 °C) to avoid condensation. Selected samples were examined in a transmission electron microscope operated at 200 kV. The cross-sectional specimens were prepared by conventional sectioning, polishing and dimpling (both sides) to a thickness of 25 μm. The thinning was continued in a Gatan PIPS (5 kV, 4.5°)[1] until perforation occurred.

In the BaF_2-Y-H_2O system (Film No. 1, Fig. 1), the onset of crystallization for the BaF_2-like phase occurs around 250 °C as inferred from the appearance of the 111_{BF} reflection. The formation of a BaF_2-related superstructure, similar to that observed in the BaF_2-Cu-Y precursors at $T\approx 600$ °C, is evident from the signature diffraction peak at $2\theta\approx 25°$; this peak is present through 735 °C. At 700 °C, the peaks indicated in Fig. 1 as 2′ and 2 can be indexed according to the pseudo-orthorhombic ($\beta\approx 90°$) cell with

[a]Electronic mail: winnie.wong-ng@nist.gov

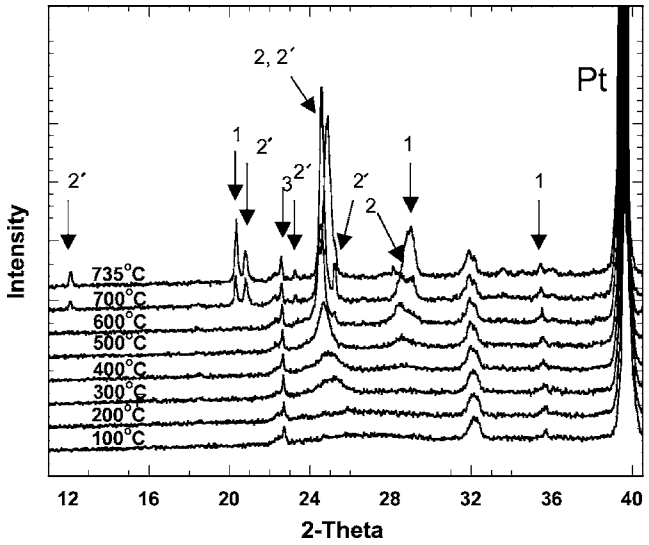

FIG. 1. X-ray diffraction pattern of Film No. 1 (BaF_2-Y-H_2O) as a function of temperature (1-Y_2O_3, 2-cubic BaF_2-like $Ba(F_{2-2x}\square_x)O_x$, 2′-$Ba(F_{2-2x}\square_x)O_x$ superstructure, 3-$SrTiO_3$).

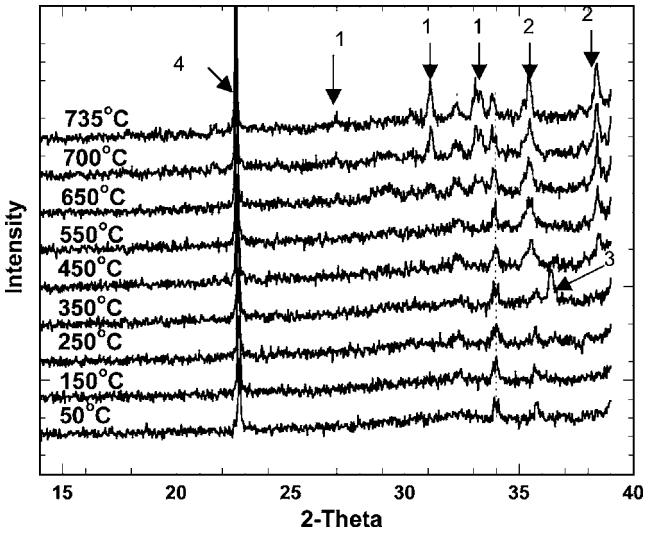

FIG. 3. X-ray diffraction pattern of Film No. 3 ($Y-Cu-H_2O$) as a function of temperature (1-$Y_2Cu_2O_5$, 2-CuO, 3-Cu_2O, 4-$SrTiO_3$).

$a \approx a_{BF}\sqrt{6}/2 \approx 7.3$ Å, $b \approx a_{BF}/\sqrt{2} \approx 4.3$ Å, and $c \approx a_{BF}\sqrt{3} \approx 10.9$ Å, ($\mathbf{k}_1 = 1/6[1\bar{1}2]^*$, $\mathbf{k}_2 = [1\bar{1}0]^*$, and $\mathbf{k}_3 = 1/3[111]^*$, where the asterisk refers to a reciprocal space). The 111_{BF} reflection is indexed as the 003 reflection of the superlattice. The barium oxyfluoride can be described using the general formula $Ba(F_{2-2x}\square_x)O_x$, where $\square$ denotes F vacancies that are generated to maintain charge balance. The formation of $Ba(F_{2-2x}\square_x)O_x$ occurs via an overall reaction: $BaF_2 + Y + \frac{3}{4}O_2 + xH_2O \rightarrow Ba(F_{2-2x}\square_x)O_x + \frac{1}{2}Y_2O_3 + 2xHF\uparrow$.

The BaF_2-Cu films, as deposited, contained a crystalline BaF_2-like phase. Heating these films above 600 °C in the presence of H_2O produced a $Ba(F_{2-2x}\square_x)O_x$ superstructure similar to that observed in the BaF_2-Y system (see peaks 2′ in Fig. 2). At $T \approx 700$ °C, $BaCuO_2$ forms. Interestingly, the low angle diffraction peak at 2θ around 12° is missing in the BaF_2-Cu film (Fig. 2) at 735 °C and occurs at 700–735 °C for the BaF_2-Y system (Fig. 1). The overall reaction in this system can be described as $2BaF_2 + 2Cu + 3/2O_2 + xH_2O \rightarrow Ba(F_{2-2x}\square_x)O_x + BaCuO_2 + CuO + (2+2x)HF\uparrow$.

As expected, annealing the Y–Cu precursors under water vapor (Film No. 3) produced $Y_2Cu_2O_5$ at $T \approx 650$ °C (Fig. 3). No x-ray reflections at $2\theta \approx 25°$ were observed in the Y–Cu films, which suggests that the superstructure giving rise to this reflection in the two previous precursors is associated with the BaF_2-based phase.

Annealing the pure BaF_2 precursor film in water vapor (Film No. 4) yielded a similar superstructure with the same signature diffraction peak at $\approx 25°$ 2θ (Fig. 4). These results confirm that the BaF_2-based superstructure observed in the BaF_2-Cu-Y, BaF_2-Cu, and BaF_2-Y films is associated with the ordering of F, O, and anion vacancies in the oxyfluoride phase $Ba(F_{2-2x}\square_x)O_x$ rather than with the ordering of Ba and Y/Cu. The representative electron diffraction pattern for the BaF_2 film quenched from 600 °C is shown in Fig. 5. This pattern was recorded from a single grain along the $\langle 110 \rangle_{BF}$ zone axis orientation. The superlattice reflections at $k = \frac{1}{3}[111]^*_{BF} \approx 10.7$ Å are indicated. The diffraction can be

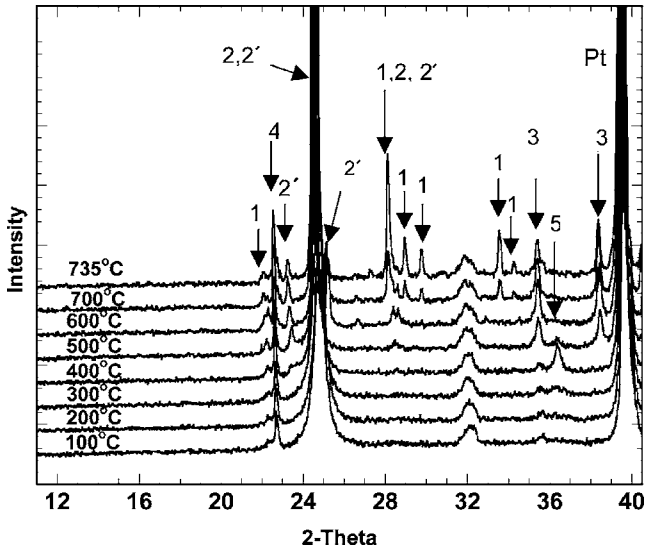

FIG. 2. X-ray diffraction pattern of Film No. 2 (BaF_2-Cu-H_2O) as a function of temperature (1-$BaCuO_2$, 2-cubic BaF_2-like $Ba(F_{2-2x}\square_x)O_x$, 2′-$Ba(F_{2-2x}\square_x)O_x$ superstructure, 3-CuO, 4-$SrTiO_3$, 5-Cu_2O).

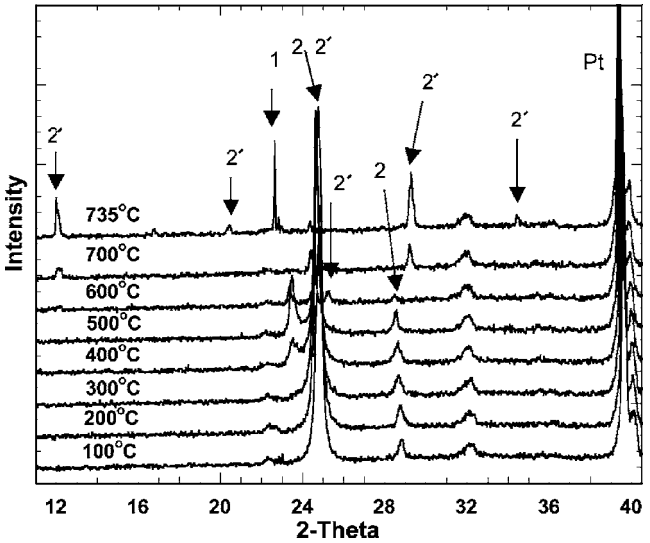

FIG. 4. X-ray diffraction pattern of Film No. 4 (BaF_2-H_2O) as a function of temperature (1-$SrTiO_3$, 2-cubic BaF_2-like $Ba(F_{2-2x}\square_x)O_x$, 2′-$Ba(F_{2-2x}\square_x)O_x$ superstructure).

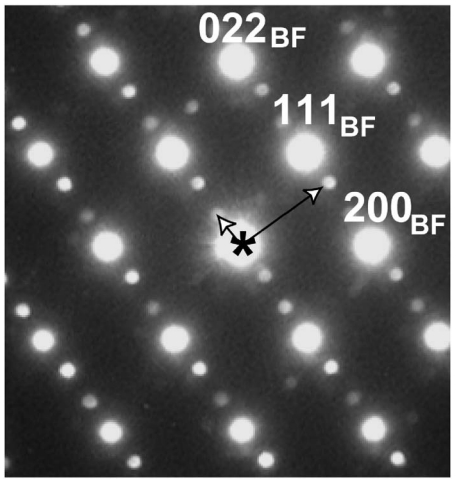

FIG. 5. Representative $\langle 110\rangle_{BF}$ zone axis electron diffraction pattern recorded from the single grain (Film No. 4) in the BaF_2 film quenched from 600 °C after annealing in water vapor. The superlattice reflections at $k=\frac{1}{3}[111]^*_{BF}$ (BF represents barium fluorite) are indicated.

described according to a hexagonal unit cell with the lattice parameters $a_{ss}=a_{BF}/\sqrt{2}$ and $c_{ss}=a_{BF}\times\sqrt{3}$, and $P\bar{3}m1$ (No. 164) symmetry (Fig. 6). The ordering, which occurs along the $[111]_{BF}$ direction (ordering vector $\mathbf{k}=\frac{1}{3}[111]^*_{BF}$), can be attributed to the alternating double layers of $[(F/\square)Ba_4]$ and $[OBa_4]$ tetrahedra (a disordered distribution of the F vacancies in the $[(F/\square)Ba_4]$ layers is assumed). Similar O/F ordering has been reported previously for a stoichiometric YOF phase;[14] however, in YOF, the 1:1 ratio of O and F required doubling of the c lattice ($c_{ss}\approx 2\times a_{dis}\times\sqrt{3}$; "dis" stands for disordered). Increasing both oxygen and F-vacancy concentrations in $Ba(F_{2-2x}\square_x)O_x$ with increasing temperatures likely induces additional ordering of the F vacancies, causing further symmetry reduction from $P\bar{3}m1$ to

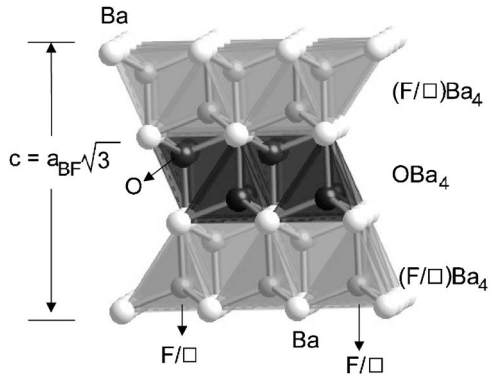

FIG. 6. Structural model of the $Ba(F_{2-2x}\square_x)O_x$ phase showing the alternating double layers of $[(F/\square)Ba_4]$ and $[OBa_4]$ tetrahedra. The ordering occurs along the $[111]^*_{BF}$ direction (ordering vector $\mathbf{k}=\frac{1}{3}[111]^*_{BF}$). A disordered distribution of the F vacancies is assumed.

$P2_1/m$ ($a_{ss}=a_{BF}\sqrt{6}/2$, $b_{ss}=a_{BF}/\sqrt{2}$, $c_{ss}=a_{BF}\times\sqrt{3}$, $\beta\approx 90°$) or lower.[7] For example, at 735 °C, one observes additional low angle diffraction peaks. The formation of $Ba(F_{2-2x}\square_x)O_x$ in this system can be described as $BaF_2+xH_2O\rightarrow Ba(F_{2-2x}\square_x)O_x+2xHF\uparrow$.

The $Ba(F_{2-2x}\square_x)O_x$ phase is metastable since it cannot be obtained in the bulk form.[15] Our results demonstrate that the formation of the transient BaF_2-based superstructures during the "BaF_2 process" is related to the anion ordering in the oxyfluoride $Ba(F_{2-2x}\square_x)O_x$ and occurs even in the absence of Y and Cu. The O/F ratio in this phase increases continuously during processing. The O/F/□ ordering is similar to that observed in the stoichiometric YOF; however, the periodicities of the resulting superstructures are different due to the different anion ratios in the Ba- and Y-based compounds. The details of anion ordering in the barium oxyfluorides require further investigation, as does their role in the nucleation of the c-textured high-T_c superconductor Y-213 phase.

The authors acknowledge the partial support from the US Department of Energy (DOE), and the valuable discussions with Dr. Mas Suenaga of Brookhaven National Laboratory.

[1] S.-W. Chan, B. G. Bagley, L. H. Greene, M. Giroud, W. L. Feldmann, K. R. Jenkin, II, and B. J. Wilkins, Appl. Phys. Lett. **53**, 1443 (1988).
[2] R. Feenstra, T. B. Lindemer, J. D. Budai, and M. D. Galloway, J. Appl. Phys. **69**, 6569 (1991).
[3] R. Feenstra, A. A. Gapud, F. A. List, E. D. Specht, D. K. Christen, T. G. Holesinger, and D. M. Feldman, IEEE Trans. Appl. Supercond. **15**, 2803 (2005).
[4] M. W. Rupich, W. Zhang, X. Li, T. Kodenkandath, D. T. Verebelyi, U. Schoop, C. Thieme, M. Teplitsky, J. Lynch, N. Nguyen, E. Siegal, J. Scudiere, V. Maroni, K. Venkataraman, D. Miller, and T. G. Holesinger, Physica C **412–414**, 877 (2004).
[5] X. Li, M. W. Rupich, W. Zhang, N. Nguyen, T. Kodenkandath, U. Schoop, D. T. Verebelyi, C. Thieme, M. Jowett, P. N. Arendt, S. R. Foltyn, T. G. Holesinger, T. Aytug, D. K. Christen, and M. P. Paranthaman, Physica C **390**, 249 (2003).
[6] T. Araki and I. Hirabayashi, Supercond. Sci. Technol. **16**, R71 (2003).
[7] W. Wong-Ng, I. Levin, R. Feenstra, L. P. Cook, and M. Vaudin, Supercond. Sci. Technol. **17**, S548 (2004).
[8] W. Wong-Ng, I. Levin, M. Vaudin, R. Feenstra, L. P. Cook, and J. P. Cline, Adv. X-ray Analysis 46, 257 (2002).
[9] A. H. Swanson and E. Tatge, Natl. Bur. Stand. Circ. (U. S.) **539**, 539 (1953).
[10] L. Wu, Y. Zhu, V. F. Solovyov, H. J. Wiesmann, A. R. Moodenbaugh, R. L. Sabatini, and M. Suenaga, J. Mater. Res. **16**, 2869 (2001).
[11] F. A. List, E. D. Specht, L. Heatherly, K. J. Leonard, S. Sathamurthy, and D. M. Kroeger, Physica C **391**, 350 (2003).
[12] L. Wu, V. F. Solovyov, H. J. Wiesmann, Y. Zhu, and M. Suenaga, Appl. Phys. Lett. **80**, 419 (2002).
[13] The identification of any commercial product or trade name does not imply endorsement or recommendation by the National Institute of Standards and Technology.
[14] I. Levin, Q. Z. Huang, L. P. Cook, and W. Wong-Ng, Eur. J. Inorg. Chem., 87–91 (2005).
[15] W. Wong-Ng, L. P. Cook, and Z. Yang (unpublished data).

Melting investigation of the system BaF_2–BaO–½Y_2O_3–CuO_x–H_2O

2005 Supercond. Sci. Technol. 18 442

(http://iopscience.iop.org/0953-2048/18/4/012)

INSTITUTE OF PHYSICS PUBLISHING SUPERCONDUCTOR SCIENCE AND TECHNOLOGY

Supercond. Sci. Technol. **18** (2005) 442–453 doi:10.1088/0953-2048/18/4/012

Melting investigation of the system BaF_2–BaO–$\frac{1}{2}Y_2O_3$–CuO_x–H_2O

W Wong-Ng[1], L P Cook[1], J Suh[1], I Levin[1] and R Feenstra[2]

[1] Ceramics Division, National Institute of Standards and Technology, Gaithersburg, MD 20899, USA
[2] Condensed Matter Sciences Division, Oak Ridge National Laboratory, Oak Ridge, TN 37831, USA

Received 22 September 2004, in final form 8 November 2004
Published 8 February 2005
Online at stacks.iop.org/SUST/18/442

Abstract

In order to understand low-temperature melting during the 'BaF_2 process', equilibria in the quaternary Ba, Y, Cu//O, F reciprocal system have been investigated using a compositional model which can be represented as a trigonal prism. This prism is comprised of three tetrahedra: BaF_2–YF_3–CuF_2–CuO_x, BaF_2–YF_3–$\frac{1}{2}Y_2O_3$–CuO_x, and BaF_2–BaO–$\frac{1}{2}Y_2O_3$–CuO_x. Systematic differential thermal analysis (DTA) studies of compositions spaced along compositional vectors extending from the fluoride end of the prism to the oxide end gave evidence of low-melting liquids (<600 °C) near the fluorine-rich region in the BaF_2–YF_3–CuF_2–CuO_x tetrahedron. In the intermediate BaF_2–YF_3–$\frac{1}{2}Y_2O_3$–CuO_x tetrahedron, a low-temperature DTA peak (550–570 °C) was also identified; this has been shown to be due to a reversible phase transformation in crystalline YOF. In the oxide-rich BaF_2–BaO–$\frac{1}{2}Y_2O_3$–CuO_x tetrahedron, where, in the presence of water vapour, the principal defluorination process is generally thought to occur, the lowest melting temperature observed was 815 °C at $p_{O_2} = 20$ Pa and $p_{H_2O} = 2.1$ kPa. However, published observations on films undergoing the BaF_2 process have suggested the presence of an amorphous phase thought to be a liquid at ⩽735 °C. Based on our results, the low-melting liquids reported in the literature do not appear to exist as a stable liquid phase in the BaF_2–BaO–$\frac{1}{2}Y_2O_3$–CuO_x–H_2O system under the conditions of our experiments. Rather, the formation of low-melting liquid in Ba–Y–Cu–O–F films at ⩽735 °C may require (a) relatively fluorine-rich compositions, (b) metastable melting, (c) formation of hydroxide- or hydroxyfluoride-based liquids, or (d) some combination thereof.

1. Introduction

With the advent of coated conductor technologies for processing high-T_c superconductors for wire and cable applications [1–7], there has been a renewal of interest in superconductors based on $Ba_2YCu_3O_x$ (Y-213) and $Ba_2RCu_3O_x$ (R-213, R = lanthanides). Relative to (Bi, Pb)-2223 (Bi(Pb):Sr:Ca:Cu:O = 2:2:2:3) superconductors, which are normally processed by the powder-in-tube method [8–10], $Ba_2YCu_3O_{6+x}$ can be more readily deposited on metal tapes, and the resulting materials show substantially improved current-carrying capability under applied magnetic field. Three successful technologies for producing textured substrates for coated conductor applications have been developed: (1) ion-beam-assisted deposition (IBAD) [1, 2], (2) rolling-assisted bi-axially textured substrate (RABiTS) [3–5], and (3) inclined substrate deposition (ISD) [6, 7]. As with all high-T_c applications, the issues of cost and performance are closely linked to the optimized processing of these materials. An important requirement for commercial applications is the production of long-length tapes.

The 'BaF_2 *ex situ*' method, investigated by a number of laboratories [11–34], is one of the promising methods

for producing long-length coated conductors. This process involves the low-temperature deposition of precursor layers using either high-rate e-beam evaporation of Y, BaF_2, and Cu onto a substrate, or the use of solution/sol–gel techniques to deposit equivalent compositions, followed by a post-annealing at high temperature in the presence of H_2O vapour under reduced oxygen partial pressure. The *ex situ* method has the potential for producing high-quality, long-length, high-J_c, high-T_c $Ba_2YCu_3O_x$ superconductors on textured substrates prepared by any of the three principal methods mentioned above. The separation of the deposition and post-processing steps inherent in this method may lead to increased throughput. An advantage of using the e-beam technique for precursor deposition is the elimination of carbonate contamination from the deposition stage, as all the barium is present as BaF_2 from the beginning.

The BaF_2 process dates back to 1987, when Mankiewich *et al* [11] reported the use of BaF_2 to prepare evaporated precursor films. In the following year, a trifluoroacetate (TFA) sol–gel method for preparing the precursor was demonstrated by Gupta *et al* [12]. In the same year, Chan *et al* [13] described a reaction model using H_2O to decompose the BaF_2. They also emphasized the importance of removing the product HF for speeding up the reaction. In 1990, a research group at Massachusetts Institute of Technology (MIT) successfully produced high-J_c, *c*-axis-aligned Y-213 coatings by the TFA method [14, 15]. Some beneficial effects of processing under reduced oxygen partial pressure were also noted. The TFA *ex situ* method was further developed during the 1990s [17–19]. In 1991, Feenstra *et al* [16], who worked with the e-beam *ex situ* method, reported on the phase stability of Y-213 at reduced oxygen partial pressure down to 10^{-4} atm. Use of reduced p_{O_2} allowed lowering of the processing temperature to 700–750 °C. By 1999, Feenstra *et al* [20] had demonstrated high-J_c *c*-axis-oriented Y-213 on CeO_2 buffer layers. This represented the first successful 'coated conductor' result. At about the same time, Solovyov and Suenaga [21] achieved success in preparing thicker (5 μm) Y-213 coatings with high J_c on single-crystal substrates. In 2001, Lee *et al* [22] showed the feasibility of a continuous process for producing long coated conductor tapes using the e-beam BaF_2 *ex situ* approach. Over the past decade, additional groups have pursued refinements in the BaF_2 process, using both sol–gel and e-beam techniques, to obtain tapes with improved texture and properties [23–31]. Recently, Ichinose *et al* investigated YBCO film growth by post-annealing of precursor films containing BaF_2 at low p_{O_2}, but without the presence of water vapour [32–34].

A major requirement for advancement of the BaF_2 *ex situ* process, so that the rate of conversion may be increased, is an improved understanding of the reaction process by which fluoride-containing precursors are converted to $Ba_2YCu_3O_x$. The overall conversion reaction of oxidized precursors can be approximated by

$$2BaF_2 + \tfrac{1}{2}Y_2O_3 + 3CuO + 2H_2O(g) + \tfrac{1}{2}xO_2(g) \rightarrow Ba_2YCu_3O_{6.5+x}(s) + 4HF(g). \quad (1)$$

On the left-hand side of reaction (1) the first three substances are present in the as-deposited oxidized film as a nano-scale mixture. As shown in figure 1, the conversion process can be considered as compositional migration of the precursor from the BaF_2–$\frac{1}{2}Y_2O_3$–CuO_x plane to the bottom BaO–$\frac{1}{2}Y_2O_3$–CuO_x plane in the presence of water vapour. This migration occurs during the *ex situ* step, when water vapour is introduced at elevated temperatures to cause the defluorination reaction to occur. Since gaseous HF is present on the product side, it must be removed to a level lower than the equilibrium value of p_{HF} at a given p_{H_2O} for the reaction to proceed. One of the major issues is the role of low-temperature melting. A liquid has been inferred, by the Brookhaven research group, on the basis of transmission electron microscopy observations on reacted specimens processed below 735 °C [31].

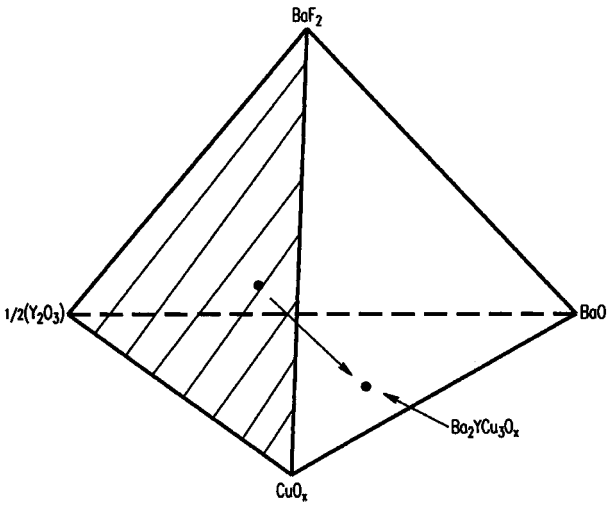

Figure 1. Schematic drawing of the quaternary system BaF_2–$\frac{1}{2}Y_2O_3$–YF_3–CuO_x. In the presence of water, the composition of the precursor film migrates through the interior and becomes $Ba_2YCu_3O_x$.

In order to make the 'BaF_2 process' commercially viable, it is critical to be able to fully control the process. A complete understanding of the details of the process, including the intermediate phases formed, is essential for controlling film properties. Since it is possible that the growth of the Y-213 film could be assisted by the presence of a low-temperature liquid, several investigations have been conducted (including the use of high-temperature x-ray diffraction (HTXRD)) to understand the intermediate phase formation mechanism, and to search for evidence of intermediate low-melting liquid [17, 24, 31]. An amorphous layer (with a Ba:Y:Cu cation ratio of ≈2:1:1.5) situated between the Y-213 product and the untransformed precursor has been observed on intermediate *ex situ* films (designated as the BNL films) deposited on $SrTiO_3$ and CeO_2 substrates at 735 °C [24, 31]. The presence of a low-temperature liquid could be important for enhancing the formation of Y-213 through chemical mobility and for improving texture of the Y-213 films. On the other hand, too much liquid could have a detrimental effect on properties [35].

Our overall research objectives are to provide phase equilibrium diagrams needed to optimize processing of Ba–Y–Cu–F–O materials and to assist in the application of this information to coated conductor processing issues. In particular, it is important to understand the influence of low-temperature melts on the formation of the Y-213 superconductor, as well as the role of liquid phase epitaxy [36–38]. Regardless of whether any observed processing

liquids are stable, metastable, or transient non-equilibrium phases, the equilibrium phase relations serve as an important frame of reference. Preliminary studies of the presence of low-temperature liquids have been reported from our laboratory [39, 40]. This paper presents further description of our investigations in the BaF_2–BaO–$\frac{1}{2}Y_2O_3$–CuO_x–H_2O system and in the related fluoride-rich systems, including both subsolidus phase assemblages and melting events.

2. Experimental details[3]

2.1. Approach for multi-dimensional phase equilibria studies

As noted above, evidence for an amorphous phase with Ba:Y:Cu ≈ 2:1:1.5 has been reported in the literature [31]. We have examined melting of this composition by preparing 2:1:1.5 bulk compositions and investigating their behaviour as a function of temperature in the presence of water vapour. For comparison, we have also examined compositions with Ba:Y:Cu = 2:1:3, corresponding to the idealized bulk composition of a precursor film, under similar conditions. During the *ex situ* conversion process, the F/O ratio of the precursor film decreases as the conversion takes place. Under certain conditions, films may initially have greater F/O ratios than would normally be prepared by the e-beam method using BaF_2, Y, and Cu sources, for example through use of the TFA method [41]. To model the complete range of F/O ratios potentially possible during the BaF_2 *ex situ* conversion process, it is necessary to consider phase equilibria in the Ba, Y, Cu//O, F quaternary reciprocal system. Our preliminary work [40] illustrated the use of a triangular prism to represent this reciprocal system (figure 2). The oxides are represented at the base, and fluorides at the top. On the basis of Gibbs energy minimization computations involving the prism end members [42], the prism can be divided into three constituent tetrahedra. The BaF_2–BaO–$\frac{1}{2}Y_2O_3$–CuO_x system forms the lower tetrahedron (within which the final defluorination of the precursor film takes place). The other two tetrahedra are BaF_2–YF_3–CuF_2–CuO_x and BaF_2–YF_3–$\frac{1}{2}Y_2O_3$–CuO_x. The two Ba:Y:Cu ratios of interest, 2:1:1.5, and 2:1:3, correspond to vertical lines extending through these tetrahedra from the base to the top of the prism. We have prepared compositions for melting studies with different F/O ratios at regular intervals along these two Ba:Y:Cu compositional vectors, or isopleths.

For most precursor compositions prepared using the e-beam method, the BaF_2–BaO–$\frac{1}{2}Y_2O_3$–CuO_x tetrahedron is where the conversion into the Y-213 phase occurs, as described by equation (1). Consequently, further studies on melt occurrence in this system were conducted. In addition to samples prepared along the two isopleths, as described above, a more detailed exploration of the eutectic phase relationships of the ternary BaO–$\frac{1}{2}Y_2O_3$–CuO_x subsystem, which forms the basal plane of the quaternary BaF_2–BaO–$\frac{1}{2}Y_2O_3$–CuO_x tetrahedron, was completed. The latter were conducted as a function of oxygen partial pressure, and also with the addition of BaF_2 and H_2O.

[3] Certain commercial equipment, instruments, or materials are identified in this paper in order to specify the experimental procedure adequately. Such identification is not intended to imply recommendation or endorsement by the National Institute of Standards and Technology, nor is it intended to imply that the materials or equipment identified are necessarily the best available for the purpose.

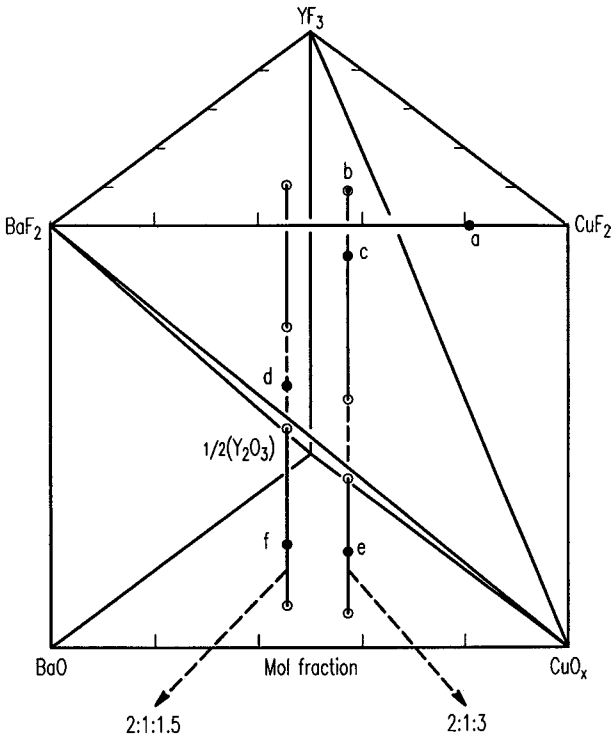

Figure 2. Triangular prism used to represent the full reciprocal Ba, Y, Cu//O, F. Two compositional vectors with Ba:Y:Cu = 2:1:3 and 2:1:1.5 are illustrated. Letters refer to compositions discussed in the text.

2.2. Sample preparation

2.2.1. Compositions along the Ba:Y:Cu = 2:1:3 and 2:1:1.5 vectors. Several of the components of the Ba, Y, Cu//O, F system, most notably BaO and CuF_2, are atmospherically sensitive, and so all materials preparation was conducted in an argon-filled glovebox (<0.1 Pa contaminants) to prevent atmospheric reaction. Starting materials for the experiments were reagent grade $BaCO_3$, Y_2O_3, CuO, CuF_2, YF_3, and optical quality single-crystal BaF_2 (which was ground to powder). The $BaCO_3$ was used to prepare BaO by vacuum decomposition. All starting materials were verified as single phase by powder x-ray diffraction (XRD). All materials were weighed as fine powders and thoroughly mixed repeatedly with a mortar and pestle. Two master batches of fluoride with Ba:Y:Cu of 2:1:3 and 2:1:1.5, and two batches of oxides with the same cation ratios, were prepared. Using these master batches, 20 compositions with different mole fraction ratios of the fluoride and oxide end members (F%: 5, 10, 15, 20, 25, 30, 35, 40, 45, 50, 55, 60, 65, 70, 75, 80, 85, 90, 95, 100) were then prepared along each of the two iso-cationic vectors. Each sample was thus a mixture of three oxides and three fluorides. The samples were then intimately mixed and homogenized. Figure 2 shows the two compositional vectors that correspond to the cation ratios Ba:Y:Cu = 2:1:3 and Ba:Y:Cu = 2:1:1.5. From the base triangle to the top, compositions vary from the oxide-rich to the fluoride-rich end.

2.2.2. Eutectic melting in the BaO–BaF_2–$\frac{1}{2}Y_2O_3$–CuO_x system, with addition of BaF_2 and H_2O. Materials preparation was also conducted in an argon-filled glovebox to

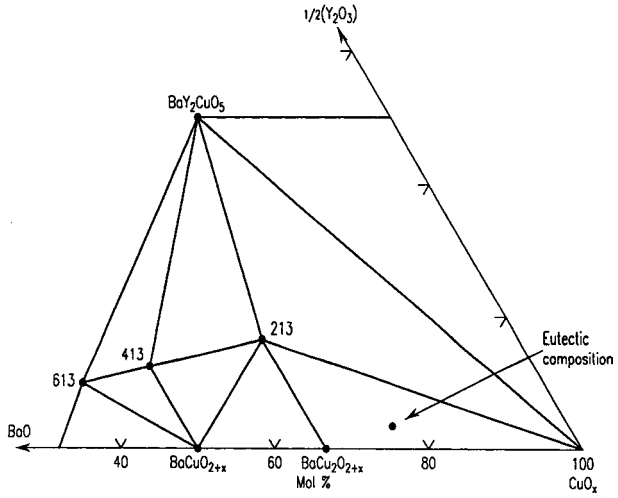

Figure 3. The eutectic melt region of the system BaO–$\frac{1}{2}Y_2O_3$–CuO_x. The symbols 213, 413, and 613 refer to the Ba:Y:Cu ratios of relevant Ba–Y–Cu–O compounds.

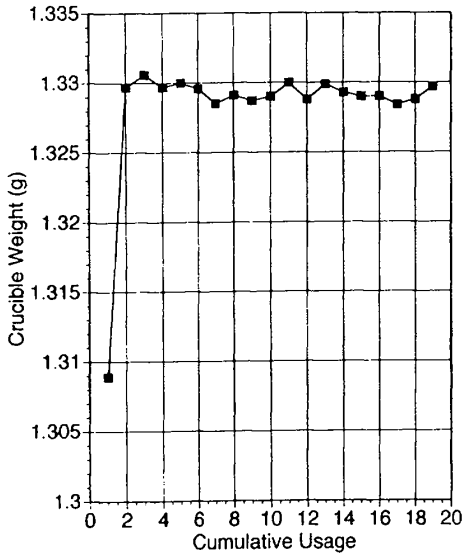

Figure 4. Weight change of a representative Pt DTA crucible after each use.

prevent atmospheric reaction. A single starting composition in the system BaO–$\frac{1}{2}Y_2O_3$–CuO_x was chosen for this study, corresponding to $Ba_{25}Y_5Cu_{70}O_x$. This composition was prepared by calcination at 800 °C in CO_2- and H_2O-scrubbed air, and was found to consist of a three-phase mixture of $BaCuO_{2+x}$, $Ba_2YCu_3O_x$ and CuO. It lies in the lowest-melting region of the system BaO–$\frac{1}{2}Y_2O_3$–CuO_x near the eutectic [43] (figure 3). To study the effect of BaF_2, a second composition was prepared from the first by adding 20% mole fraction BaF_2 and mixing it thoroughly with a mortar and pestle. The sample was calcined at 800 °C in scrubbed air for several days.

2.3. Choice of container

An important experimental issue for the study of the Ba, Y, Cu//O, F system concerns container reaction. Although we have generally used MgO crucibles for oxide high-T_c experiments to minimize container reaction [44], the presence of fluorides presents a different set of problems. For example, MgO reacts with CuF_2 or YF_3 to form MgF_2 and CuO_x or Y_2O_3. Platinum, frequently a container of choice for fluorides, is known to react with base metal oxides under reducing conditions, and to react with BaO under oxidizing conditions. While there is no perfect container material, platinum appears to be the best compromise under the conditions of our experiments. To monitor the reaction of our Pt differential thermal analysis (DTA) cells, we followed the weight change of the crucibles after each use (figure 4). It was observed that although the crucibles experienced a slight weight gain during the first usage, subsequent experiments produced only negligible weight change, indicating that after the initial saturation with Ba–Y–Cu there was essentially no further compositional interaction.

2.4. Differential thermal analysis/thermogravimetric analysis (DTA/TGA)

Simultaneous differential thermal analysis and thermogravimetric analysis (DTA/TGA) were used to study thermal events and to perform annealing of samples under atmospherically controlled conditions. Most experiments utilized primarily the DTA signal; the TGA signal was useful primarily in following oxygen gain/loss associated with the CuO_x component.

DTA/TGA experiments were performed using an electronically upgraded Mettler TA-1 system fitted with an Anatech digital control and readout system enclosed in an argon-filled glovebox, a feature which eliminated atmospheric contamination during loading of the samples. The DTA/TGA apparatus was calibrated against the α/β-quartz transition (571 °C) and the melting point of NaCl (801 °C), and temperatures reported in this study have a standard uncertainty of ±5 °C. Event temperatures were determined as the intersection of the baseline with the extrapolated linear portion of the rising DTA peak. Oxygen partial pressure during DTA/TGA was controlled using analysed Ar/O_2 mixtures, except as noted. During the experiments of type (2), below, gas mixtures were continuously passed through the sample region at a rate of 150 mℓ min^{-1}, and the oxygen pressure at the outlet of the DTA/TGA system was periodically checked with a zirconia sensor described in *2.4.2*. Oxygen pressures reported in this study have a relative expanded uncertainty of ±10% in the 1 kPa–0.1 MPa range and ±20% in the 10 Pa–1 kPa range.

2.4.1. DTA/TGA of compositions along the Ba:Y:Cu = 2:1:3 and 2:1:1.5 vectors. Because the oxidation/reduction state of CuO_x-containing samples changes with temperature as well as by interaction with ambient p_{O_2}, the net effect is that under the relatively low p_{O_2} of interest in this set of our experiments the samples effectively controlled the ambient p_{O_2}. Most samples contained CuO as starting material. The experiments along the two compositional vectors were completed in flowing argon (except as noted); given the slow kinetics of dissociation of CuO to Cu_2O, the oxygen partial pressure of samples in these experiments was effectively that of the CuO/Cu_2O equilibrium. After several exploratory experiments, a three-step DTA program was chosen for all 40 compositions and the end members: (1) 25–950 °C at 10 °C min^{-1} (pre-reaction); (2) 950–450 °C at 10 °C min^{-1} (cooling); (3) 450–1150 °C at 10 °C min^{-1} (measurement). This program resulted

in reaction of the unstable, energetic starting combinations during step 1, as evidenced by strong exotherms at <500 °C for most compositions. During cooling step 2, exotherms were interpreted as indicating either the presence of melt, or phase transformation of a solid component, which was then generally confirmed by corresponding endotherms on subsequent heating during final step 3.

2.4.2. DTA/TGA of eutectic melting in the BaO–BaF_2–$\frac{1}{2}Y_2O_3$–CuO_x system, with addition of BaF_2 and H_2O. DTA/TGA experiments were carried out by allowing the finely powdered sample (∼50 mg) to equilibrate in the given atmosphere at 700 °C until no further weight change was observed (generally 1 h was sufficient), followed by ramping through the melting point at 10 °C min^{-1}. For experiments at $p_{O_2} \geqslant 1$ kPa, a TGA effect (mass loss), which correlated with the DTA effect produced by melting, was generally observed. At lower p_{O_2}, the TGA effects were very weak or absent entirely. Water was introduced into the DTA/TGA system by tapping a portion of the inlet flow of the Ar/O_2 mixture and passing it through a two-stage bubbler containing an aqueous solution saturated with NaCl. The first stage of the bubbler served to pre-saturate the gas prior to the second stage, where a very fine dispersion of bubbles was produced, with a long path through the solution, assuring an equilibrium value of p_{H_2O}. At 22 °C this value corresponds to $p_{H_2O} = 2.1$ kPa. After passing through the bubbler, the H_2O-saturated Ar/O_2 mixture exited through a Pt tube positioned in the hot zone directly over the sample, which was contained in an 8 mm diameter MgO crucible. Experiments were conducted at various flow rates and, by noting that above a certain flow rate there was no additional effect on the melting points by further increases in flow rate, it was assumed that for the proper range of flow rates the value of p_{H_2O} at the sample was essentially the saturated value of 2.1 kPa. Based on these experiments, a flow rate for the H_2O-saturated gas of 50 mℓ min^{-1} was used for all experiments. To confirm selected DTA/TGA data points, isothermal experiments were performed at 5 °C intervals, followed by cooling and visual observation of products. This allowed an independent determination of melting points, which agreed well with DTA/TGA data.

2.5. X-ray diffraction

X-ray powder diffraction was used to identify the phases synthesized and to confirm phase purity. A computer-controlled automated diffractometer equipped with a θ-compensation slit and Cu Kα radiation was operated at 45 kV and 40 mA. The radiation was detected by a scintillation counter and solid-state amplifier. The Siemens software package and later the MDI Jade software package were used for data collection. Reference x-ray diffraction patterns of the Powder Diffraction File (PDF)[4] were used for performing phase identification.

A high-temperature Siemens 5000 x-ray diffractometer equipped with both a scintillation counter and a position sensitive detector (PSD) was modified for the present study by adding a gas flow apparatus. This apparatus includes a series of bubblers containing NaCl-saturated water at room temperature and an oxygen analyser. Helium gas containing ≈100 $\mu\ell\ \ell^{-1}$ O_2 (100 ppm by volume) was flowed through the bubblers, resulting in a gas stream with $p_{H_2O} = 2.1$ kPa, and passed directly over the sample in the enclosed furnace chamber. Because of the θ–θ geometry, the specimen remained fixed in a horizontal position during the experiments. Cu Kα radiation was used for the studies.

[4] Powder Diffraction File (PDF), produced by International Centre for Diffraction Centre (ICDD), Newtown Square, PA 19081.

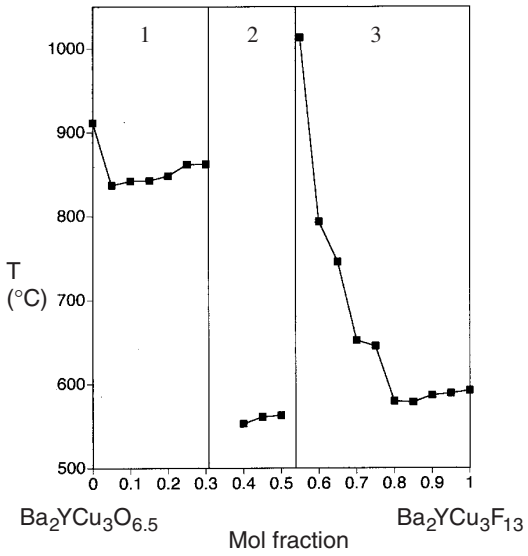

Figure 5. DTA temperatures as a function of mole fraction (%) of fluoride end-member along the Ba:Y:Cu = 2:1:3 composition vector. The numerical labels '1, 2, and 3' in each section refer to the volumes of BaF_2–BaO–$\frac{1}{2}Y_2O_3$–CuO_x, BaF_2–YF_3–$\frac{1}{2}Y_2O_3$–CuO_x, and BaF_2–YF_3–CuF_2–CuO_x, respectively.

3. Results and discussion

Results of phase equilibria of the reciprocal system Ba, Y, Cu//O, F will be described systematically according to the three subsystems: BaF_2–CuF_2–YF_3–CuO_x, BaF_2–$\frac{1}{2}Y_2O_3$–YF_3–CuO_x, and BaF_2–BaO–$\frac{1}{2}Y_2O_3$–CuO_x. The discussion includes phase relations of phases participating in melting reactions, as well as crystal chemistry and phase relations of phases of interest. A discussion of the implications of the results to the 'BaF_2 process' will follow.

3.1. Phase equilibria of the Ba, Y, Cu//O, F system

Figures 5 and 6 show the plots of the minimum DTA temperatures (which may or may not correspond to the minimum melting temperatures of these samples) versus mole fraction of the end-member oxide and fluoride for Ba:Y:Cu = 2:1:3, and for Ba:Y:Cu = 2:1:1.5 respectively (under 100% Ar). With progression along the 2:1:3 composition line, the bulk compositions pass successively through each of the constituent tetrahedron of figure 2. For example, the compositions in section 1 of figure 5 correspond to the compositions in the tetrahedron BaO–BaF_2–$\frac{1}{2}Y_2O_3$–CuO_x. The DTA temperatures of the compositions in section 1 are relatively high, in the 800–900 °C range. However, in sections 2 and 3 (BaF_2–$\frac{1}{2}Y_2O_3$–YF_3–CuO_x and

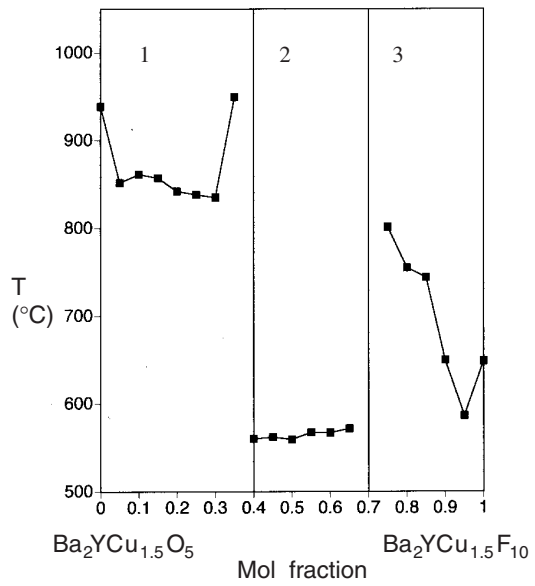

Figure 6. DTA temperatures as a function of mole fraction (%) of fluoride end member along the Ba:Y:Cu = 2:1:1.5 composition vector. The numerical labels '1, 2, and 3' in each section refer to the volumes BaF_2–BaO–$\frac{1}{2}Y_2O_3$–CuO_x, BaF_2–YF_3–$\frac{1}{2}Y_2O_3$–CuO_x, and BaF_2–YF_3–CuF_2–CuO_x, respectively.

YF_3–CuF_2–BaF_2–CuO_x tetrahedra), an abrupt lowering of the DTA temperatures to less than 600 °C was observed. In figure 6, a similar trend of the DTA temperatures along the Ba:Y:Cu = 2:1:1.5 composition line (approximate composition of the amorphous layer of the BNL film) was observed. Further experiments were undertaken to determine if these events represented generation of low-melting liquids, or were due to solid state phase transformation.

3.1.1. The BaF_2–CuF_2–YF_3–CuO_x system

(i) BaF_2–CuF_2 subsystem. The phase equilibria of the binary BaF_2–CuF_2 subsystem of the BaF_2–CuF_2–YF_3–CuO_x system was investigated by Samouel in 1970 [45], and a low-melting eutectic liquid was reported below 620 °C at 27.5% mole fraction BaF_2 (composition (a) in the eutectic region of the BaF_2–CuF_2 subsystem (figure 2)). Our experiments have confirmed the existence of this low-melting liquid: a DTA event at 617 °C in Ar was observed using a composition of 27.5% mole fraction BaF_2. The optical micrograph of composition (a) which was heat treated at 620 °C in Ar in the DTA apparatus is shown in figure 7. There is clear evidence of melting. The melting reaction was determined to be

$$Ba_2Cu_5F_{14} + Ba_6Cu_7F_{26} \rightarrow \mathrm{L}.$$

According to Samouel [45], the four binary fluoride phases present in the phase diagram of the BaF_2–CuF_2 system were Ba_2CuF_6, $BaCuF_4$, $Ba_5Cu_6F_{22}$, and $Ba_2Cu_7F_{18}$. In a later report on the BaF_2–CuF_2–FeF_3 system [46], the composition of $Ba_5Cu_6F_{22}$ was redetermined to be $Ba_6Cu_7F_{26}$ (PDF 39-983), which is triclinic, with lattice parameters of $a = 15.562(4)$ Å, $b = 12.027(5)$ Å, $c = 5.950(2)$ Å, $\alpha = 90.95(2)°$, $\beta = 91.28(4)°$, and $\gamma = 90.05(2)°$. Based on the structure of

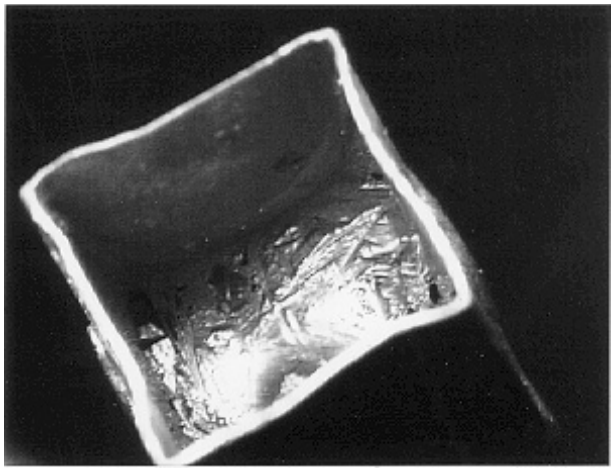

Figure 7. Optical micrograph of composition (a) in figure 2 (BaF_2:CuF_2 = 27.5:72.5) heated at 620 °C. Melting was observed.

the Zn analogue [47], it was predicted that the structure of $Ba_6Cu_7F_{26}$ also consists of a three-dimensional network which can be described as layers containing intergrown rutile and perovskite units. Currently, a structural investigation of this phase is underway in our laboratory. In 1986, another paper from the same research group [48] reported that instead of the previously reported $Ba_2Cu_7F_{18}$ (predicted based on the compound $Ba_2Zn_7O_{18}$), the correct formula of this phase should be $Ba_2Cu_5F_{14}$ (PDF 39-1291). $Ba_2Cu_5F_{14}$ is monoclinic ($C2/c$), $a = 18.170(2)$ Å, $b = 8.652(1)$ Å, $c = 10.328(1)$ Å, $\beta = 117.10(1)°$. The structure consists of complex layers of infinite edge-sharing chains of bi-octahedral units parallel to the (100) plane. Jahn–Teller distortion is associated with all Cu octahedra.

(ii) BaF_2–YF_3–CuF_2 subsystem. The initial melt temperature for composition (b) in the BaF_2:YF_3:CuF_2 system (end point of the Ba:Y:Cu = 2:1:3 composition line) was determined by DTA to be 592 °C (under Ar atmosphere). As expected, these temperatures are somewhat lower than the binary eutectic temperature of 617 °C as reported in the BaF_2–CuF_2 system. The melting reaction in this region appears to involve the phases $Ba_2Cu_5F_{14}$, $Ba_6Cu_7F_{26}$, and YF_3 (subsolidus phases present in composition (b) when annealed at 550 °C).

(iii) YF_3–CuF_2–BaF_2–CuO_x system. Within the YF_3–CuF_2–BaF_2–CuO_x tetrahedron, the temperature of the DTA thermal event for composition (c) along the 2:1:3 composition line (oxide/fluoride ratio of 15/85) further lowers from 592 to 579 °C, a temperature that corresponds to melting. From results of x-ray diffraction studies of samples annealed at 550 °C, the reaction which produces melt in the vicinity of composition (c) involves the four phases: YF_3, CuO, $Ba_2Cu_5O_{14}$, and $Ba_6Cu_7F_{26}$ [46–48].

From a number of observations, it appears that the melts of the interior fluoride–oxide systems are not as easy to observe as the cuprate type liquids in the BaO–$\frac{1}{2}Y_2O_3$–CuO_x system, which are dark and readily creep up the sides of the crucible. Figure 8 shows an optical micrograph of the Pt crucible that contains a sintered sample from loose powder of composition (c) at 700 °C. Surrounding the pellet in the corner of the

Table 1. Phase assemblages of selected compositions before and after annealing at 500 °C, 100 Pa (0.1% O_2) within the BaF_2–$\frac{1}{2}Y_2O_3$–YF_3–CuO_x subsystem.

Vol. no	Phase assemblage (before)	Phase assemblage (after)
1	$Y_2Cu_2O_5$–$\frac{1}{2}Y_2O_3$–$Ba_3Y_2F_{12}$–BaF_2	$Y_2Cu_2O_5$–YOF–$Ba_4Y_3F_{17}$(ss)–BaF_2
2	$Y_2Cu_2O_5$–$\frac{1}{2}Y_2O_3$–BaY_2F_8–$Ba_3Y_2F_{12}$	$Y_2Cu_2O_5$–YOF–$Ba_4Y_3F_{17}$(ss)–BaY_2F_8
3	$Y_2Cu_2O_5$–$\frac{1}{2}Y_2O_3$–YF_3–BaY_2F_8	$Y_2Cu_2O_5$, YOF–$Ba_4Y_3F_{17}$(ss)–CuO_x
4	$Y_2Cu_2O_5$–CuO_x–$Ba_3Y_2F_{12}$–BaF_2	$Y_2Cu_2O_5$–CuO_x–$Ba_4Y_3F_{17}$(ss)–BaF_2
5	$Y_2Cu_2O_5$–CuO_x–BaY_2F_8–$Ba_3Y_2F_{12}$	$Y_2Cu_2O_5$–CuO_x–BaY_2F_8–$Ba_4Y_3F_{17}$(ss)
6	$Y_2Cu_2O_5$–CuO_x–YF_3–BaY_2F_8	$Y_2Cu_2O_5$–CuO_x–YF_3–BaY_2F_8

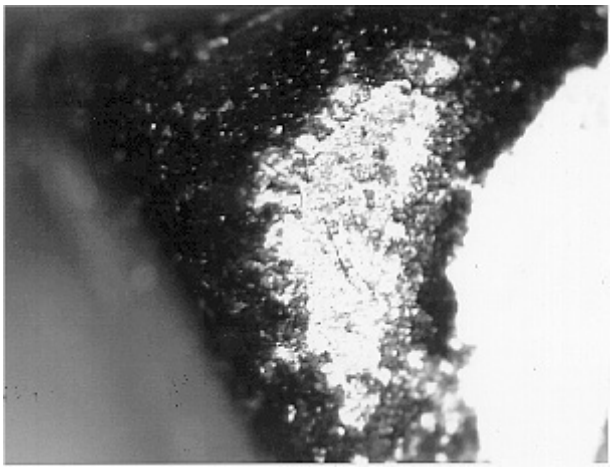

Figure 8. Optical micrograph of composition (c) in figure 2 (in the YF_3–CuF_2–BaF_2–CuO_x subsystem) heated at 700 °C. Evidence for melting can be observed.

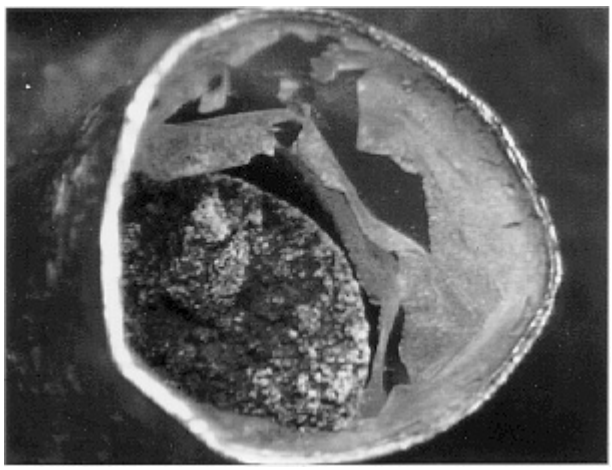

Figure 9. Optical micrograph of composition (d) in figure 2 (in the BaF_2–$\frac{1}{2}Y_2O_3$–YF_3–CuO_x subsystem) heated to 1150 °C (using Cu_2O).

crucible, an area interpreted as recrystallized melt can be detected.

3.1.2. The BaF_2–$\frac{1}{2}Y_2O_3$–YF_3–CuO_x system. In general, low-temperature DTA events were observed between 500 and 600 °C in this system. The next-higher-temperature events all take place at above 900 °C. Based on an observed DTA event at 576 °C, a sample with an oxide/fluoride ratio of 45/55 along the 2:1:1.5 vector was homogenized at 950 °C, cooled to 450 °C, reground and annealed at 650 °C. At that temperature, a somewhat sintered sample is observed but no melting was visible. The x-ray diffraction patterns of the sample annealed after 500 °C and after 650 °C did not show substantial differences that could be attributed to either melting or phase transformation. Both patterns indicated the presence of YOF, BaF_2, CuO, and $Ba_4Y_3F_{17}$. We did not find compelling evidence of sample melting at 725 °C, 825 °C, and even up to 925 °C; only continuous shrinkage of the sample due to sintering was observed.

To determine if reduced copper may affect the presence of liquid, we performed a DTA experiment using composition (d) but replacing CuO with Cu_2O. While the DTA onset temperature was also observed at around 567 °C, the size of the DTA peak appeared to be larger. However, no visible melt was observed. Figure 9 shows the optical micrograph of the interior of the Pt crucible after completion of the melting experiment with the Cu_2O-based starting material at 1150 °C. The white scale seen peeling from the crucible walls and encrusting the residual crystalline material is believed to be the result of a small amount of melt present at 1150 °C. The textural features suggest that the liquid had a relatively low surface tension.

In order to understand the nature of the low-temperature DTA event, we studied in more detail the subsolidus phase relationships in the BaF_2–$\frac{1}{2}Y_2O_3$–YF_3–CuO_x subsystem. For convenience, the tetrahedron was divided into six regions as shown in table 1, namely, $Y_2Cu_2O_5$–$\frac{1}{2}Y_2O_3$–$Ba_3Y_2F_{12}$–BaF_2 (vol. 1), $Y_2Cu_2O_5$–$\frac{1}{2}Y_2O_3$–BaY_2F_8–$Ba_3Y_2F_{12}$ (vol. 2), $Y_2Cu_2O_5$–$\frac{1}{2}Y_2O_3$–YF_3–BaY_2F_8 (vol. 3), $Y_2Cu_2O_5$–CuO_x–$Ba_3Y_2F_{12}$–BaF_2 (vol. 4), $Y_2Cu_2O_5$–CuO_x–BaY_2F_8–$Ba_3Y_2F_{12}$ (vol. 5), and $Y_2Cu_2O_5$–CuO_x–YF_3–BaY_2F_8 (vol. 6). According to the binary phase diagram of the BaF_2–YF_3 system [49, 50], $Ba_3Y_2F_{12}$ was reported to be the end member of a trigonally distorted fluorite solid solution [45]. Equi-molar mixtures of the boundary phases were prepared for each region and were equilibrated (with two regrinds) at 500 °C. The equilibrium phases found in these six volumes after the annealing were established by x-ray diffraction and are listed in table 1. These four-phase volumes are consistent with each other and do not overlap. Schematic drawings of these equilibrium volumes are shown in figure 10.

Results of DTA experiments under 0.1% O_2 confirmed that, among the six regions, a low-temperature event was found in regions 1, 2 and 3 at around 570–580 °C. A more detailed study was conducted of the composition in the selected region 3. After equilibration, this composition was found to lie in the four-phase field: $Y_2Cu_2O_5$–YOF–$Ba_4Y_3F_{17}$ solid solution [51]–CuO_x (Cu_2O). However, no visible melting

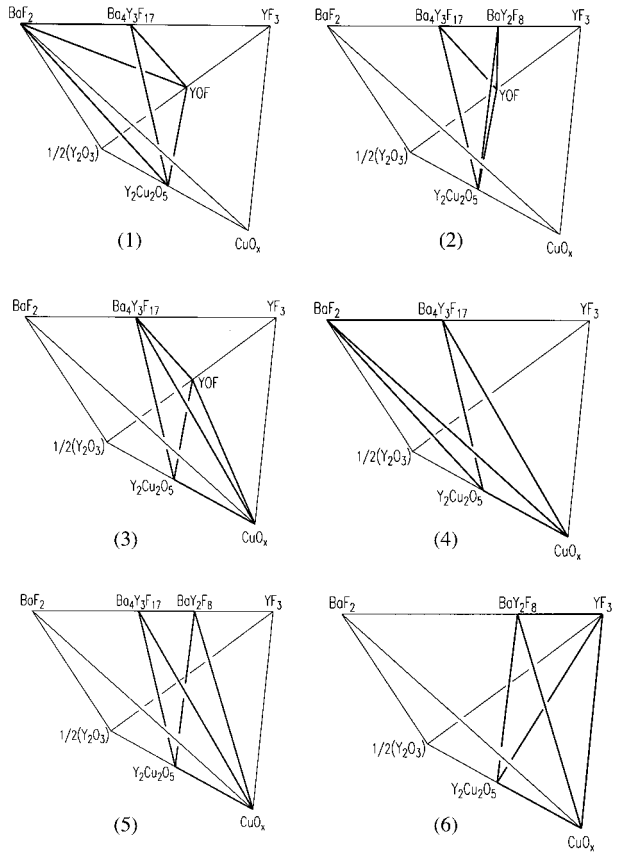

Figure 10. A schematic diagram of the six equilibrium phase assemblages prepared inside the BaF_2–$\frac{1}{2}Y_2O_3$–YF_3–CuO_x subsystem. Volumes 1, 2, and 3 show the presence of YOF.

was observed with the sample after an annealing at 650 °C. The x-ray patterns obtained at 500 and 650 °C did not show substantial differences. Subsequently, high-temperature x-ray diffraction study was used to further investigate the source of the DTA peak.

Figure 11 shows the results of high-temperature x-ray diffraction study of composition 3 at 550 and 600 °C. It illustrates the merging of the two sets of diffraction peaks into one between these two temperatures. These peaks were identified to be due to the presence of YOF [52–56]. The observation of peaks merging, together with the fact that among the six volumes that we studied volumes 1, 2 and 3 are the ones that contain the YOF phase, suggests the low-temperature DTA event is probably due to the phase transformation of YOF. YOF has been reported to have both the rhomobohedral and tetragonal structures; both are superstructures based upon the fluorite structure type [57]. Zachariasen [53] reported that the homogeneity range for the tetrahedral phase extends from the ideal composition YOF to 60% mole fraction of YOF and 40% mole fraction of YF_3. The rhombohedral phase corresponds to the exact composition YOF.

In order to understand in more detail the nature of the phase transformation of YOF, a single-phase sample of YOF was prepared for high-temperature x-ray diffraction and high-temperature neutron diffraction study. In figure 12, a reversible transformation occurring between 550 and 575 °C [58] is shown by the high-temperature x-ray diffraction data. In parallel to the diffraction experiments, we also performed

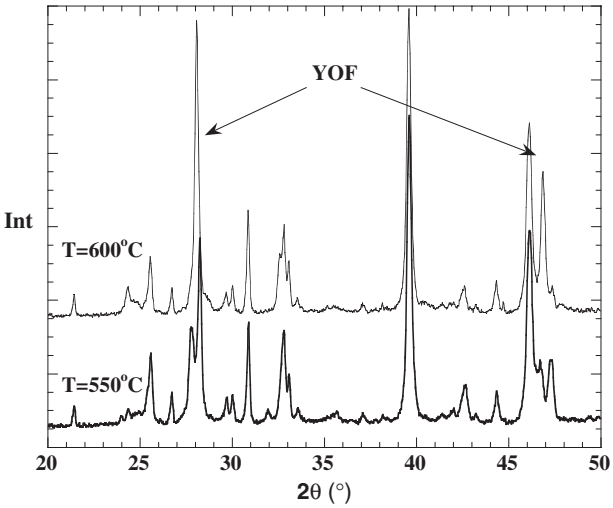

Figure 11. Merging of the two sets of diffraction peaks of composition 3 (corresponding to the phase YOF [52–56]) into one at a temperature between 500 and 600 °C.

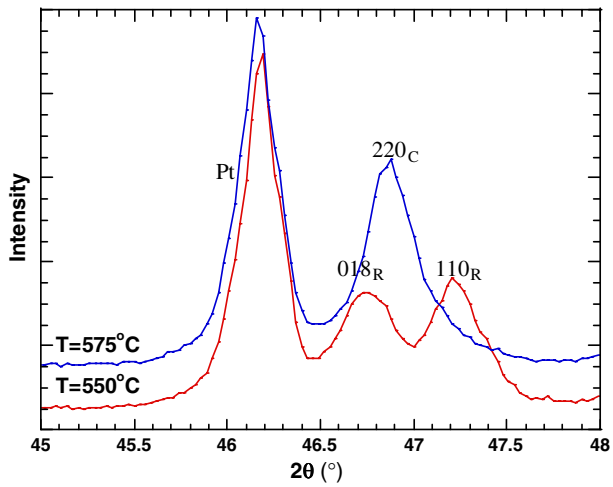

Figure 12. High-temperature x-ray diffraction study of YOF showing the changing of peaks from a doublet into a single peak between 500 and 600 °C.

(This figure is in colour only in the electronic version)

quenching experiments [59, 60]. Samples were annealed at 500 and 630 °C, and then quenched into a liquid-nitrogen-cooled copper cold well through which helium gas was rapidly passed. Subsequent x-ray diffraction patterns (figure 13) of the helium-quenched samples showed similar patterns for both quench temperatures, with only the rhombohedral phase present. The higher-temperature phase was not preserved even by rapid quenching. A detailed study of the phase transformation of YOF and a structure determination using high-temperature neutron diffraction showed the transformation to be of the order–disorder type [58].

3.1.3. The BaF_2–BaO–$\frac{1}{2}Y_2O_3$–CuO_x system

(i) Compositions along the 2:1:3 and 2:1:1.5 vectors. As shown in figures 5 and 6, the lowest DTA events

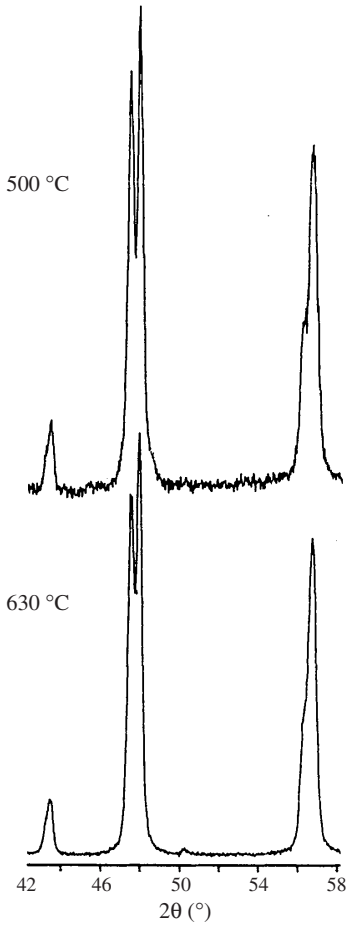

Figure 13. X-ray diffraction patterns of quenched YOF samples at 500 and at 630 °C. The split peaks near the 2θ region of 40° are retained in these patterns.

of the compositions along the vectors corresponding to Ba:Y:Cu = 2:1:3 and Ba:Y:Cu = 2:1:1.5 are at rather high temperatures (>800 °C). Along both the 2:1:3 and the 2:1:1.5 vectors, compositions with an F:O ratio of 20:80 (compositions 'e' and 'f' in figure 2, respectively) were annealed at 800 °C. Results of x-ray diffraction studies show these compositions to be inside different phase fields. Composition 'e' was found to lie in the $Ba_2YCu_3O_{6+x}$–CuO_x–BaY_2CuO_5–BaF_2 four-phase region, while composition 'f' was found to lie close to the $Ba_2YCu_3O_{6+z}$–$BaCuO_{2+x}$–BaF_2 tie-plane.

Results of DTA/TGA experiments conducted under $p_{O_2} = 100$ Pa indicated the lowest-temperature events for compositions 'e' and 'f' to be 848 and 880 °C, respectively, in the anhydrous samples. We have also studied the effect of water on the melting temperatures of these samples, to determine if the initial melting temperatures are substantially lowered by the presence of water vapour at $p_{H_2O} = 2.1$ kPa. Although the presence of water vapour lowered the melting temperatures significantly in both cases (from 848 to 828 °C in composition 'e', and from 880 to 867 °C in composition 'f'), melting temperatures did not extend as low as 750 °C, where BaF_2 *ex situ* processing typically occurs.

(ii) Effect of addition of water and BaF_2 on eutectic melting in the BaO–$\frac{1}{2}Y_2O_3$–CuO_x system as a function of p_{O_2}. The composition that we chose for this specific study was confirmed to be inside the eutectic region of the basal BaO–$\frac{1}{2}Y_2O_3$–CuO_x system. The x-ray diffraction pattern of this composition (with added BaF_2) calcined at 800 °C showed the presence of BaF_2, $BaCuO_{2+x}$, $Ba_2YCu_3O_x$ and CuO_x (figure 3), indicating that no additional solid phases were formed due to the presence of fluoride.

Results for different sets of experiments as a function of oxygen partial pressure are plotted individually in figures 14(a)–(d). In these temperature versus log p_{O_2} plots, we have included as a reference the CuO/Cu_2O equilibrium, calculated from literature data. Data for the eutectic melting without BaF_2 or H_2O are shown in figure 14(a). With decreasing p_{O_2}, the melting point shows a regular decrease, from 917 °C at $p_{O_2} = 0.1$ MPa to 838 °C at $p_{O_2} = 1$ kPa. Below $p_{O_2} = 1$ kPa there appears to be no further decrease in melting temperature down to $p_{O_2} = 20$ Pa; instead, there may actually be a slight increase. The melting point data can be approximated as two linear segments (presumably there is slight curvature, as for CuO/Cu_2O). Also shown in figure 14(a) is a weak thermal event, which occurs prior to melting. This was also observed in the experiments of figures 14(b)–(d), which leads us to postulate an additional equilibrium, represented by the short unconnected line. Figure 14(b), which includes the data of figure 14(a) for comparison, shows the effect of adding BaF_2 on the eutectic melting. The melting curve with BaF_2, while sub-parallel, shows the same abrupt change in slope at $p_{O_2} = 1$ kPa, and is consistently displaced to lower temperatures by ≈5–15 °C over its length. In figure 14(c), the effect of water at $p_{H_2O} = 2.1$ kPa is shown. Although the scatter in the data is somewhat greater, there is an unambiguous lowering of the melting point. This lowering effect is somewhat greater at higher p_{O_2} than at lower p_{O_2}, but the curve fitted to the data corresponds to, on average, a melting point lowering of ≈10–20 °C. The curve shows a change in slope similar to that observed for the previous experiments. The combined effects of BaF_2 and H_2O are shown in the data of figure 14(d).

As figures 14(a)–(d) indicate, the amount of eutectic melting point depression caused by the addition of BaF_2, H_2O, or a combination, while consistent, is relatively small and does not exceed 30 °C, and the abrupt change in slope at $p_{O_2} = 1$ kPa is preserved. This suggests that only small amounts of BaF_2 and H_2O enter the liquid phase, perhaps no more than a few % mole fraction. The curves in figure 14(d) summarize the melting temperature of the samples without H_2O or BaF_2 (from $p_{O_2} = 0.1$ MPa to 20 Pa) (curve a), and with the presence of both H_2O and BaF_2 (curve b). Even with the presence of both BaF_2 and H_2O, the lowest melting temperature was found to be 815 °C at $p_{O_2} = 20$ Pa, which is substantially above 735 °C, the temperature at which the amorphous phase was observed in BNL films [31]. Therefore the low-melting liquid suggested by observations on the BNL films does not appear to exist as a stable phase in the BaF_2–BaO–$\frac{1}{2}Y_2O_3$–CuO_x system under the experimental conditions described. There are several possible explanations. It may be that metastable melts are involved in processing [39]. If so, it would be expected that these would have a relationship to the equilibrium melts in the system BaF_2–BaO–$\frac{1}{2}Y_2O_3$–CuO_x–H_2O. This relationship could be controlled by the extrapolation of equilibrium curves such as those in figure 14(d).

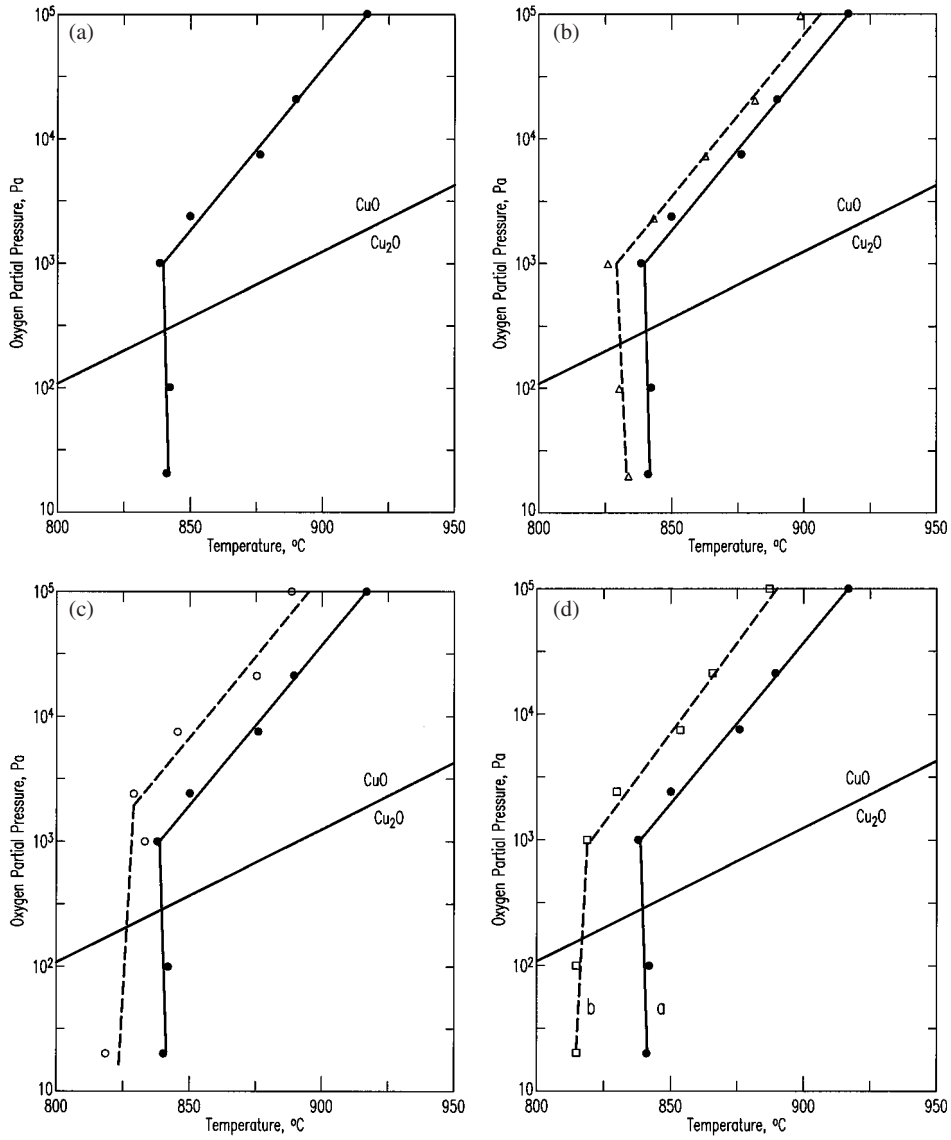

Figure 14. Eutectic melting in the system BaO–$\frac{1}{2}Y_2O_3$–CuO_x at various oxygen partial pressures: (a) without BaF_2 or H_2O; (b) with BaF_2; (c) with H_2O; and (d) with BaF_2 and H_2O (curve a without BaF_2 or H_2O, and curve b with BaF_2 and H_2O). The CuO/Cu_2O equilibrium is shown for reference.

3.2. Implications for processing

We have described evidence for low-temperature melting. The low-temperature melts that have been determined so far appear to lie in the BaF_2–CuF_2–YF_3–CuO_x system (upper tetrahedron in figure 2), and therefore have a greater fluorine content than compositions on the BaF_2–$\frac{1}{2}Y_2O_3$–CuO plane. Ideally, *ex situ* precursor films, especially those prepared by the e-beam process, would have a composition plotting on this plane; however, if the film stoichiometry varies, it is conceivable that oxide/fluoride phase compatibilities in the central or upper portions of the prism of figure 2 could come into play, if only in a transitory manner. A precursor film deviating locally in composition from this plane towards the fluorine-rich direction in figure 2 could produce a low-temperature melt due to local inhomogeneity. It is possible that the amorphous layer observed in the BNL film was produced by a liquid that was originally relatively fluorine rich, and was subsequently defluorinated during reaction with H_2O.

For precursor films prepared by the TFA process, it is likely that initial compositions would be fluoride rich relative to the BaF_2–$\frac{1}{2}Y_2O_3$–CuO plane [41]. TFA films therefore seem to offer an increased potential for the generation of low-temperature liquids, relative to e-beam-produced films. Consequently, there is the possibility that presence of low-temperature melts could be controlled, by careful selection of processing routes.

Other routes for generation of low-melting liquids include metastable melting, surface-stabilized liquids, and hydroxy- or hydroxyfluoride-stabilized liquids. Metastable melting is not unlikely, given the highly unstable nature of the fine-grained precursor films in the presence of water at elevated temperatures. Metastable melting is related to the equilibrium thermodynamics of the system, and would be expected to bear a predictable relation to the stable equilibria. Surface energetics are known to be important in the *ex situ* process, and are largely responsible for the formation of textured films—hence, it is likely that surface stabilization could also play

a role in the generation of low-temperature melts. Finally, $Ba(OH)_2$ has a low melting point, and so the generation of hydroxy- or hydroxyfluoride-stabilized liquids at relatively low temperatures must also be considered [61]. The role of $Ba(OH)_2$ in low-temperature melting is currently being investigated in our laboratory. It is also possible that given the multiplicity of processing routes and the variation in starting precursor compositions there could be multiple mechanisms for the production of low-melting liquids.

4. Summary and future work

We have presented evidence for liquids melting below 600 °C on the fluorine-rich side of the BaF_2–$\frac{1}{2}Y_2O_3$–CuO_x plane in the Ba, Y, Cu//O, F reciprocal system; these melts occur in the fluorine-rich BaF_2–CuF_2–YF_3–CuO_x subsystem. The low-temperature DTA events (500–600 °C) which we observed in the intermediate BaF_2–$\frac{1}{2}Y_2O_3$–YF_3–CuO subsystem were determined, using high-temperature x-ray and neutron diffraction studies, to be due to a rapid reversible phase transformation in the YOF phase. In the oxide-rich BaF_2–BaO–$\frac{1}{2}Y_2O_3$–CuO_x subsystem, in which the conversion of e-beam-deposited 'BaF_2' precursor films to the $Ba_2YCu_3O_x$ superconductor phase ideally takes place, all observed melting events occurred above 800 °C at 100 Pa O_2, even with the presence of water vapour at $p_{H_2O} = 2.1$ kPa. We conclude that low-melting liquids postulated to form at temperatures $\leqslant$735 °C under BaF_2 *ex situ* processing conditions are not related to equilibrium melts in the BaF_2–BaO–$\frac{1}{2}Y_2O_3$–CuO_x subsystem under the conditions of our experiments. The role that the thin-film processing environment plays in the generation of liquids, perhaps through kinetically favoured metastable or transient melting routes, or through energetically favoured surface stabilization, needs to be considered.

Also, due to the presence of water, there is a possibility that $Ba(OH)_2$ may play a role in the phase equilibria that gives rise to low-melting liquids [61]. Future work will investigate phase equilibria in the $Ba(OH)_2$–BaF_2–$\frac{1}{2}Y_2O_3$–CuO_x system. Furthermore, in order to fully understand the origin of liquids in the complex Ba, Y, Cu//F, O reciprocal system, a more detailed understanding of the phase equilibria of the subsystems, including those with mixed anions, is important.

Acknowledgments

This work has been partially supported by the US Department of Energy. We are grateful for valuable discussions with Dr M Suenaga of the Brookhaven National Laboratory. We acknowledge the graphical assistance of Mr Nils Swanson of the American Ceramic Society. Dr Jonathan Storer of 3M Corporation is acknowledged for providing the single-crystal BaF_2 that was used as starting material.

References

[1] Foltyn S R, Peterson E J, Coulter J Y, Arendt P N, Jia Q X, Dowden P C, Maley M P, Wu X D and Peterson D E 1997 *J. Mater. Res.* **12** 2941
[2] Iijima Y, Hosaka M, Tanabe N, Sadakata N, Saitoh T, Kohno O and Takeda K 1997 *J. Mater. Res.* **12** 2913
[3] Goyal A *et al* 1996 *Appl. Phys. Lett.* **69** 1795
[4] Paranthaman M *et al* 2000 *J. Mater. Res.* **15** 2647
[5] Goyal A *et al* 2001 *Physica* C **357** 903
[6] Balachandran U 2001 Practical superconductivity development for electrical power applications *Annual Report for FY 2001* Argonne National Laboratory ANL-02/03
[7] Balachandran U 2002 Practical superconductivity development for electrical power applications *Quarterly Report for January–March 2002* Argonne National Laboratory
[8] Kaufman D Y, Lanagan M T, Dorris S E, Dawley J T, Bloom I D, Hash M C, Chen N, DeGuire M R and Poeppel R B 1993 *Appl. Supercond.* **1** 81–91
[9] Balachandran U, Iyer A N, Haldar P, Hoehn J G Jr and Motowidlo L R 1994 *Proc. 4th Int. Conf. and Exhibition: World Congr. on Superconductivity (Orlando, FL, June–July 1994)* vol II, ed K Kristen and C Burnham pp 639–49
[10] Sandhage K H, Riley G N Jr and Carter W 1991 *J. Met.* **43** 21
[11] Mankiewich P M, Scofield J H, Skocpol W J, Howard R E, Dayem A H and Good E 1987 *Appl. Phys. Lett.* **51** 1753
[12] Gupta A, Jagannathan R, Cooper E I, Giess E A, Landman J I and Hussey B W 1988 *Appl. Phys. Lett.* **52** 2077
[13] Chan S-W, Bagley B G, Greene L H, Giroud M, Feldmann W L, Jenkin K R II and Wilkins B J 1988 *Appl. Phys. Lett.* **53** 1443
[14] McIntyre P C and Cima M 1990 *J. Mater. Res.* **5** 4183
[15] McIntye P C, Cima M J, Liebenberg D H and Francavilla T L 1991 *Appl. Phys. Lett.* **58** 2033
[16] Feenstra R, Lindemer T B, Budai J D and Galloway M D 1991 *J. Appl. Phys.* **69** 6569
[17] McIntye P C and Cima M J 1994 *J. Mater. Res.* **9** 2219
[18] McIntye P C, Cima M J, Smith J A and Hallock R B 1992 *J. Appl. Phys.* **71** 1868
[19] McIntye P C, Cima M J and Roshko A 1995 *J. Appl. Phys.* **77** 5263
[20] Feenstra R 1999 *US Patent Specification* 5,972,847
[21] Solovyov V F and Suenaga M 1998 *Physica* C **309** 269
[22] Lee D F 2000 *DOE Peer Review (Washington DC, July 2000)*
[23] Solovyov V F, Wiesmann H J, Wu L-J, Zhu Y and Suenaga M 2000 *Appl. Phys. Lett.* **76** 1911
[24] Yamada Y, Kim S, Araki T, Takahashi Y, Yuasa T, Kurosaki H, Hirabayashi I, Iijima Y and Takeda K 2001 *Physica* C **357** 1007
[25] Takahashi Y, Araki T, Yamagiwa K, Yamada Y, Kim S B, Iijima Y, Takeda K and Hirabayashi I 2001 *Physica* C **357–360** 1003–6
[26] Honjo T, Fuj H, Huang D, Nakamura Y, Izumi T and Shiohara Y 2001 *Physica* C **357–360** 999
[27] Li Q *et al* 2001 *Physica* C **357–360** 987
[28] Jee Y-A, Li M, Ma B, Maroni V A, Fisher B L and Balachandran U 2001 *Physica* C **356** 297
[29] Honjo Y, Fuji H, Huang C, Nakamura Y, Izumi T and Shiohara Y 2001 *Physica* C **357–360** 999–1002
[30] Lu S W, List F A, Lee D F, Cui X, Paranthaman M, King B W, Kroeger D M, Goyal A, Martin P M and Ericson R E 2001 *Supercond. Sci. Technol.* **14** 218–23
[31] Wu L, Zhu Y, Solovyov V F, Weismann H J, Moodenbaugh A R, Sabatini R L and Suenaga M 2001 *J. Mater. Res.* **16** 2869
[32] Ichinose A, Kikuchi A, Tachikawa K and Akita S 2001 *Physica* C **357–360** 995–8
[33] Ichinose A, Kikuchi A, Tachikawa K, Akita S and Inoue K 2002 *Supercond. Sci. Technol.* **15** 262–8
[34] Ichinose A, Kiss A, Kikuchi A, Tachikawa K, Akita S and Inoue K 2003 *Supercond. Sci. Technol.* **16** 398–401
[35] Feenstra R, Holesinger T and Thomas D 2003 *Department of Energy Superconductivity Program Peer Review, Session 'Strategy Research' (Washington DC, July 2003)*
[36] Yao X, Izumi T, Hobara N, Nakamura Y, Izumi T and Shiohara Y 2001 *Physica* C **357–360** 1063
[37] Hobara N *et al* 2001 *Physica* C **257–360** 1038
[38] Izumi T *et al* 2001 *Physica* C **357–360** 1027

[39] Cook L P, Wong-Ng W and Suh J 2001 *High-Temperature Superconductors—Crystal Chemistry, Processing and Properties* (*Materials Research Society Proceedings* vol 659) ed U Balachandran, H C Freyhardt, T Izumi and D C Labalestier (Pittsburg, PA: Materials Research Society) p II4.8.1
[40] Wong-Ng W and Cook L P 2002 *Materials for High-Temperature Superconductor Technologies* (*Materials Research Society Symp. Proc.* vol 689) ed M P Paranthaman, M W Rupich, K Salama, J Mannhart and T Hasegawa (Warrendale, PA: Materials Research Society) p 337
[41] Yoshizami M, Seteznev I and Cima M J 2003 *Physica* C **403** 191
[42] Bale C W, Chartrand P, Degterov S A, Eriksson G, Hack K, Mahfoud R B, Melancon J, Pelton A D and Peterson S 2002 Factsage thermochemical software and databases *CALPHAD* **26** 189–228
[43] Wong-Ng W and Cook L P 1995 *J. Am. Ceram. Soc.* **77** 1883
[44] Wong-Ng W and Cook L P 1998 *J. Res. Natl Inst. Stand. Technol.* **103** 379
[45] Samouel M 1970 *C.R. Acad. Sci.* C **270** 1805
[46] Samouel M 1985 *Rev. Chim. Miner.* **22** 84
[47] Renaudin J, Samouel M, Leblanc M, de Kozak A and Ferey G 1985 *J. Solid State Chem.* **59** 103–10
[48] de Kozak A, Samouel M, Renaudin J and Ferey G 1986 *Rev. Chim. Miner.* **23** 352
[49] Ippolitov E G and Maklachko A G 1970 *Izv. Akad. Nauk SSSR Neorg. Mater.* **6** 146–8
[50] Sobolev B P and Tkachenko N L 1982 *J. Less-Common Met.* **85** 155–70
[51] Maksimov B A 1996 *Kristallografiya* **41** 51
[52] Hund Von F 1951 *Z. Anorg. Allg. Chem.* **265** 65
[53] Zachariasen W H 1951 *Acta Crystallogr.* **4** 231
[54] Bevan D J M and Mann A W 1975 *Acta Crystallogr.* B **31** 1406
[55] Bevan D J M, Mohyla J, Hoskins B F and Steen R J 1990 *Int. J. Solid State Inorg. Chem.* **27** 451–65
[56] Schmid S 1998 *Acta Crystallogr.* B **54** 391–8
[57] Swanson H E and Tatge E 1953 *NBS Circular no 539* vol 1 (Washington, DC: US Government Printing Office) p 70
[58] Levin I, Huang Q, Wong-Ng W and Cook L P 2004 *Eur. J. Inorg. Chem.* at press
[59] Wong-Ng W, Cook L P, Chiang C K, Swartzendruber L, Bennett L H, Blendell J E and Minor D 1988 *J. Mater. Res.* **3** 832
[60] Wong-Ng W and Cook L P 1991 Superconductivity in ceramic superconductors II *Ceramic Transactions* vol 18, ed K M Nair, U Balachandran, Y-M Chiang and A Bhalla (Westerville, OH: American Ceramic Society) p 73
[61] Cook L P, Wong-Ng W and Feenstra R 2004 *J. Res. Natl Inst. Stand. Technol.* at press

Thermodynamics of MgB_2—by Calorimetry and Knudsen Thermogravimetry

L. P. Cook, R. Klein, W. Wong-Ng, Q. Huang, R. A. Ribeiro, and P. C. Canfield

***Abstract*—The vapor pressure of MgB_2, corresponding to the reaction, $2\ MgB_2(cr) \rightarrow MgB_4(cr) + Mg(g)$, has been measured by Knudsen effusion vacuum thermogravimetry. The vapor pressure over the range 600°C–850°C can be expressed as: $\log p_{mg}(Pa) = -1.129141\ (10000/T) + 7.328161$, where T is the temperature in Kelvin. By extrapolation, the 0.1 MPa decomposition temperature of MgB_2 is estimated to be 1268°C. In a separate calorimetric investigation on the same material, using the isoperibol solution method, we measured the enthalpy of formation of MgB_2, $\Delta_f H^\circ_{MgB2}\ (298.15)$, to be $-(155.9 \pm 14.2)\ kJ \cdot mol^{-1}$. By combining the vapor pressure data and the enthalpy data, the Mg-rich part of the Mg-B phase diagram can be calculated. The measured vapor pressures are approximately an order of magnitude higher than those derived from published thermodynamic data. The lower limit of Mg pressures for the deposition of high-purity MgB_2 thin films at any given temperature may therefore be at a higher value than previously thought.**

***Index Terms*—Enthalpy of formation, MgB_2, phase diagram, thermodynamics, vapor pressure.**

I. Introduction

THE MgB_2 superconductor, with a nominal 39 K onset T_c [1], offers promise because of reduced weak link behavior [2] and the possibility of relatively low-cost wire production by a powder-in-(Fe)tube method [3]. Various dopants are being explored to improve the flux pinning characteristics [4]. As a basis for further investigations of this type, it is helpful to have detailed knowledge of the intrinsic properties of undoped MgB_2, including thermodynamic properties. Vapor pressure and enthalpy of formation are two of the most basic properties, and have direct application to the physical vapor deposition of MgB_2 thin films, and to the construction of an equilibrium Mg-B phase diagram.

II. Previous Work and Goal of Present Study

To date, White [5] has apparently made the sole determination of the enthalpy of formation of MgB_2. As the description of the experimental procedures and the original data were not available to us, it was not possible to accurately assess the data from [5]. Therefore, one of the goals of the present study is to make a measurement of the enthalpy of formation of $MgB_2(cr)$, $\Delta_f H^\circ_{MgB2}\ (298.15)$, for comparison with this early work.

An Mg-B phase diagram, with estimated fields of stability for MgB_2, MgB_4 and MgB_7 was published in [6]. More recently Liu *et al.* [7] calculated an Mg-B phase diagram using available thermodynamic data, and also estimated a $\log p_{Mg}$—temperature stability field for MgB_2. As these calculations were based in part on the early thermodynamic data mentioned above, a second goal of the present study is to directly measure the vapor pressure of MgB_2, for purposes of comparison.

III. Experimental Procedures[1]

The MgB_2 sample investigated in this study was prepared by combining elemental Mg and isotopically pure ^{11}B in a sealed Ta capsule and heating to produce Mg vapor, which completely reacted with the B to produce MgB_2 [8]. The material was removed from the Ta capsule in an Ar-filled glovebox (<1 ppm contaminants), comminuted, and loaded into containers for calorimetry and thermogravimetry in the glovebox. The X-ray pattern of this material indicated its single phase nature, which was substantiated by neutron Rietveld refinement. There was no indication in the neutron refinement of nonstoichiometry or of oxygen in solid solution.

The vapor pressure of MgB_2 was determined by the Knudsen effusion method [9] using a MgO cell with a 0.5 mm orifice. Rates of mass loss as a function of temperature were determined thermogravimetrically using a Mettler TA1 thermoanalyzer with Anatech instrumental control firmware and data acquisition electronics. Uncertainty in mass loss rates was $< \pm 1\%$ (standard error of estimate). During the experiments, background pressure was maintained at ≈2.7 mPa by dual diffusion pumps and a liquid nitrogen cold trap. The thermoanalyzer thermocouple was calibrated against the melting point of Au; reported temperatures have $< \pm 5°C$ uncertainty (standard error of estimate). The operation of the Knudsen effusion cell apparatus was checked using Mg metal, and the vapor pressures obtained over the temperature range 350°C to 550°C agreed within experimental error with vapor pressures calculated from generally accepted thermodynamic data for Mg [10].

Manuscript received November 1, 2004. This work was supported in part by the US Department of Energy.

L. P. Cook, R. Klein, W. Wong-Ng, and Q. Huang are with the Materials Science and Engineering Laboratory, National Institute of Standards and Technology (NIST), Gaithersburg, MD 20899 USA (e-mail: lawrence.cook@nist.gov).

R. A. Ribeiro and P. C. Canfield are with Ames Laboratory, Iowa State University, Ames, IA 50010 USA (e-mail: canfield@ameslab.gov).

Digital Object Identifier 10.1109/TASC.2005.848809

[1]Certain commercial equipment, instruments, or materials are identified in this paper to foster understanding. Such identification does not imply recommendation or endorsement by NIST, nor does it imply that the materials or equipment identified are necessarily the best available for the purpose.

The enthalpy of formation of $MgB_2(cr)$ was determined by isoperibol solution calorimetry, using an LKB 8700 calorimeter, as described in [11]. The calorimeter accuracy was checked by measuring the enthalpy of reaction of tris(hydroxymethyl) aminomethane, NIST standard reference material 724a, with 0.1N HCl. The value obtained was in excellent agreement with the certified value. Calorimetric measurements of the enthalpy of reaction of Mg(cr), B(amorphous), and $MgB_2(cr)$ with 5.5 dm^{-1} HNO_3 were combined via a Hess cycle to establish the value of $\Delta_f H^\circ_{MgB2}$ (298.15). Literature data for the conversion of B (amorphous) to B(cr) [10] was used to complete the Hess cycle.

IV. Results

The measured vapor pressures of MgB_2 are shown in Fig. 1, where they have been fit by the following expression: $\log p_{mg}(Pa) = -1.129\,141\ (10000/T) + 7.328\,161$, where T is the temperature in Kelvin. While there is some scatter, the fit is reasonably good, with $R^2 = 0.98$. The scatter may be due in part to the fact that data were collected on both increasing and decreasing temperature steps, with temperatures selected in semi-random fashion, in order to average out thermally-induced kinetic effects associated with the vaporization process. There does not appear to be any indication in the data of a compositional effect, i.e., as the vaporization process continued, it generated pressures described by the fitted curve of Fig. 1, even as the composition became progressively depleted in Mg. If there were solid solution present in MgB_2, then it would be expected that the data in Fig. 1 would have a broader spread, and could be best fit by several semi-parallel lines, each corresponding to a different solid solution composition produced by progressive Mg loss. However no such grouping of the data according to amount of Mg lost was observed. The vaporization process was terminated after a mass loss of 17%, which would correspond to a product with 2% (mole fraction) $MgB_2 + 98\%$ (mole fraction) MgB_4. X-ray powder diffraction of the product showed it to be a mixture of predominantly MgB_4 and minor MgB_2, with no other phases detected, indicating that the vaporization process occurred according to the equilibrium reaction: $2\ MgB_2(cr) \rightarrow MgB_4(cr) + Mg(g)$. In other samples, including some obtained commercially, presence of MgO among the vaporization products is thought to indicate entry of oxygen into the MgB_2 during its synthesis. Results of vapor pressure measurements on these materials will be published elsewhere [12].

Our experimental calorimetric data[2] for the reaction of Mg(cr), B(amorphous), and $MgB_2(cr)$ with HNO_3 were combined with literature data for the amorphous/crystalline transition in B according to the reactions below, where $\Delta_r H_m$ designates the enthalpy per mole of solid reactant:

$$Mg(cr) + HNO_3(5.5\ mol \cdot dm^{-3}) = products,\quad \Delta_r H_m = -(625.9 \pm 3.4)\ kJ \cdot mol^1 \tag{1}$$

$$B(amorphous) + HNO_3(5.5\ mol \cdot dm^{-3}) = products,\quad \Delta_r H_m = -(464.3 \pm 6.3)\ kJ \cdot mol^{-1} \tag{2}$$

[2]Measurement uncertainties are expressed as ± one standard deviation of the mean.

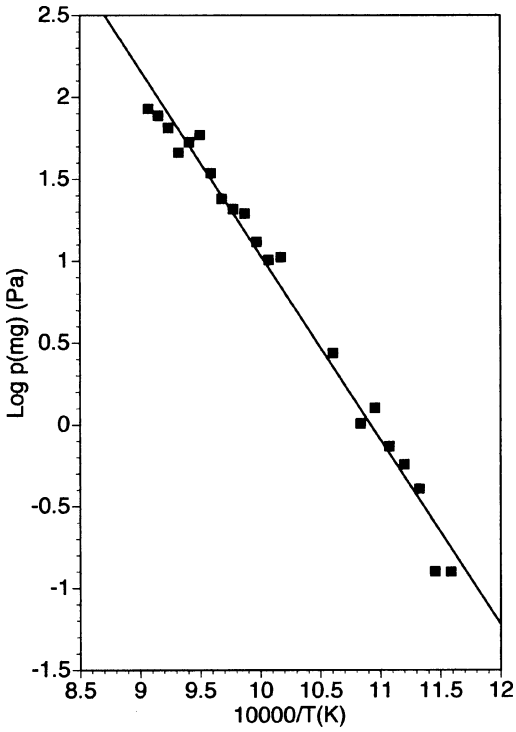

Fig. 1. Vapor pressure of MgB_2, as measured by Knudsen effusion vacuum thermogravimetry.

$$B(cr) = B(amorphous),\ \Delta_r H_m = (3.8 \pm 5)\ kJ \cdot mol^{-1}[10] \tag{3}$$

$$MgB_2(cr) + HNO_3(5.5\ mol \cdot dm^{-3}) = products,\quad \Delta_r H_m = -(1391.0 \pm 13.9)\ kJ \cdot mol^{-1} \tag{4}$$

These reactions define the enthalpy of formation of $MgB_2(cr)$, by application of the appropriate Hess cycle: $-\Delta_r H_m(4) + 2\Delta_r H_m(2) + 2\Delta_r H_m(3) + \Delta_r H_m(1) = \Delta_f H^\circ_{MgB2}(298.15) = -(155.9 \pm 14.2)\ kJ \cdot mol^{-1}$. A more complete data set will be published elsewhere [13], together with measurements on other samples with lesser purity.

V. Discussion

The vapor pressure data can be combined with the measurement of $\Delta_f H^\circ_{MgB2}$ (298.15) to produce a calculated phase diagram [14] at 0.1 MPa for the Mg-rich part of the Mg-B phase diagram, as shown in Fig. 2. This diagram indicates a decomposition temperature of 1268°C for MgB_2, significantly lower than that estimated in [6] and calculated in [7]. Calculation of Fig. 2 has required adjustments in the thermodynamic properties of MgB_4 as published in the literature [10], to allow production of a diagram consistent with our data for MgB_2. Our value of $\Delta_f H^\circ_{MgB2}$ (298.15), $-(155.9 \pm 14.2)\ kJ \cdot mol^{-1}$, is more than twice the literature value of $-(74.8 \pm 3.8)\ kJ \cdot mol^{-1}$ [5], [10]. Without access to a complete description of the earlier work, a full explanation of the difference is not possible. However, based on our calculation of Fig. 2, it is also likely that the enthalpy of formation of MgB_4 is significantly more negative than reported in the literature. Fig. 2 was calculated assuming negligible solubility of MgB_2 in the Mg/MgB_2 eutectic. This

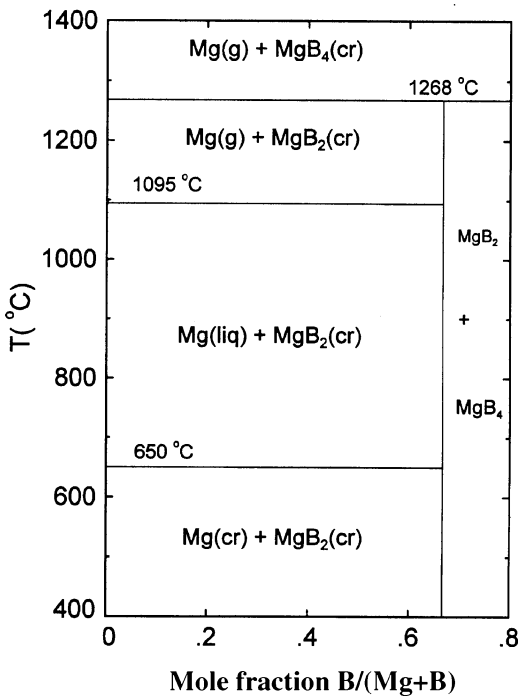

Fig. 2. Calculated phase diagram for the Mg-rich part of the Mg-B system at 0.1 MPa total pressure.

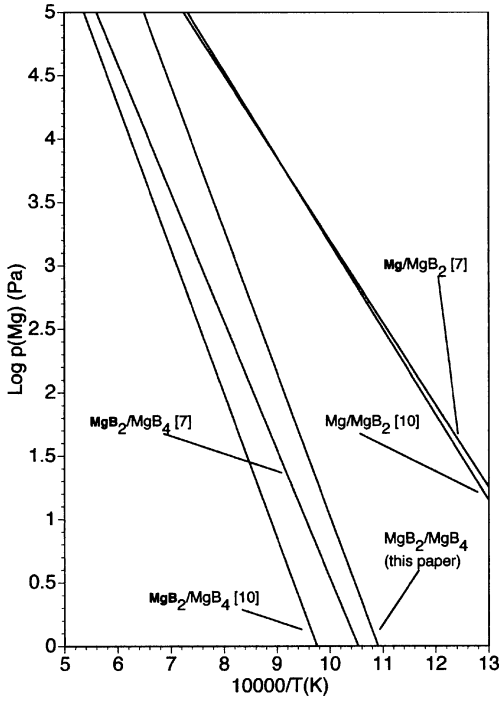

Fig. 3. Comparison of literature data on MgB_2 stability with the present study.

assumption was supported by our observation that there was no detectable lowering of the melting point of Mg in the presence of MgB_2.

Our measured vapor pressure curve is plotted together with literature data in Fig. 3, where it can be seen that our data are approximately an order of magnitude higher than the curve calculated from the literature data [10] for the MgB_2/MgB_4 equilibrium. Our measurements are also significantly higher than the calculated curve of [7]. The practical implication is that, for production of high purity MgB_2, higher Mg pressures must be employed than would be suggested by the literature data. However, if less pure MgB_2 is desired, as is currently sought for some applications requiring improved flux pinning, then it is possible that successful processing may be achieved at lower Mg pressures than the curve in Fig. 1, in the presence of suitable dopants.

VI. Summary

Using well-characterized, stoichiometric MgB_2, with no detectable oxygen impurities, we have measured the Mg pressure over $MgB_2(cr)$ as a function of temperature over the range 600°C to 850°C. From this data, we have developed an expression that can be extrapolated to give an MgB_2 decomposition temperature of 1268°C at 0.1 MPa. We have performed calorimetric studies on the same material, resulting in a new determination of $\Delta_f H^\circ_{MgB2}$ (298.15), which differs significantly from the literature value. The thermodynamic properties of other Mg-borides will require reevaluation before a reliable phase diagram can be constructed for the complete range of Mg-B compositions.

References

[1] J. Nagamatsu, N. Nakagawa, T. Muranaka, Y. Zenitani, and J. Akimitsu, "Superconductivity at 39 K in magnesium diboride," *Nature*, vol. 410, pp. 63–64, 2001.

[2] D. C. Larbalestier, L. D. Cooley, M. O. Rikel, A. A. Polyanskii, J. Jiang, S. Patnaik, X. Y. Cai, D. M. Feldmann, A. Gurevich, A. Squitieri, M. T. Naus, C. B. Eom, E. E. Hellstrom, R. J. Cava, K. A. Regan, N. Rogado, M. A. Hayward, T. He, J. S. Slusky, P. Halifah, K. Inumaru, and M. Hass, "Strongly linked current flow in polycrystalline forms of the superconductor MgB_2," *Nature*, vol. 410, pp. 186–189, 2001.

[3] R. Flukiger, H. L. Suo, N. Musolino, C. Beneduce, P. Toulemonde, and P. Lezza, "Superconducting properties of MgB_2 tapes and wires," *Physica C*, vol. 385, pp. 286–305, 2003.

[4] X. L. Wang, S. Soltanian, M. James, M. J. Qin, J. Horvat, Q. W. Yao, H. K. Liu, and S. X. Dou, "Significant enhancement of critical current density and flux pinning in MgB_2 with Nano- SiC, Si, and C doping," *Physica C*, vol. 408-10, pp. 63–67, 2004.

[5] D. White, Olin Mathieson Chemical Corporation, Technical Research Report MCC-1023-TR-222, 1956.

[6] T. B. Massalski, Ed., *Binary Alloy Phase Diagrams*, 2nd ed. Materials Park, OH: ASM International, 1992, vol. 1, p. 498.

[7] Z.-K. Liu, D. G. Schlom, Q. Li, and X. X. Xi, "Thermodynamics of the Mg-B system: implications for the deposition of MgB_2 thin films," *Appl. Phys. Lett.*, vol. 78, pp. 3678–3680, 2001.

[8] S. L. Bud'ko, G. Lapertot, C. Petrovic, C. E. Cunningham, N. Anderson, and P. C. Canfield, "Boron isotope effect in superconducting MgB_2," *Phys. Rev. Lett.*, vol. 86, pp. 1877–1880, 2001.

[9] K. D. Carlson, "The Knudsen effusion method," in *The Characterization of High-Temperature Vapors*, J. L. Margrave, Ed. New York: Wiley, 1967, pp. 115–129.

[10] M. W. Chase Jr., "NIST-JANAF thermochemical tables, 4th edition," *J. Phys. Chem. Ref. Data,* Monograph no. 9, 1952 pp., 1998.

[11] R. Klein, L. P. Cook, and W. Wong-Ng, "Enthalpies of formation of $SrPbO_3$ and Sr_2PbO_4," *J. Chem. Thermod.*, vol. 34, pp. 2083–2092, 2002.

[12] L. P. Cook, R. Klein, W. Wong-Ng, Q. Huang, R. A. Ribeiro, and P. C. Canfield, "Knudsen effusion thermogravimetry of MgB_2," *Thermochim. Acta*, submitted for publication.

[13] R. Klein, L. P. Cook, W. Wong-Ng, Q. Huang, R. A. Ribeiro, and P. C. Canfield, "Enthalpy of formation of MgB_2," *J. Chem. Thermod.*, submitted for publication.

[14] C. W. Bale, P. Chartrand, S. A. Degterov, K. Hack, R. Ben Mahfoud, J. Melancon, A. D. Pelton, and S. Petersen, "FactSage thermochemical software and databases," *CalPhad*, vol. 26, pp. 189–228, 2002.

Strain effects on point defects and chain-oxygen order-disorder transition in 123 cuprate compounds

Haibin Su*
Department of Materials Science and Engineering, SUNY at Stony Brook, Stony Brook, New York 11794, USA

David O. Welch†
Department of Materials Science, Brookhaven National Laboratory, Upton, New York 11973, USA

Winnie Wong-Ng‡
Ceramics Division, NIST, Gaithersburg, Maryland 20899, USA
(Received 22 March 2004; published 24 August 2004)

The energetics of Schottky defects in 123 cuprate superconductor series $R\mathrm{Ba_2Cu_3O_7}$ (where R = lanthandies) and $\mathrm{Y}A_2\mathrm{Cu_3O_7}$ (A = alkali earths), were found to have unusual relations if one considers only the volumetric strain. Our calculations reveal the effect of nonuniform changes of interatomic distances within the R-123 structures, introduced by doping homovalent elements, on the Schottky defect formation energy. The energy of formation of Frenkel pair defects, which is an elementary disordering event, in 123 compounds can be substantially altered under both stress and chemical doping. Scaling the oxygen-oxygen short-range repulsive parameter using the calculated formation energy of Frenkel pair defects, the transition temperature between orthorhombic and tetragonal phases is computed by quasichemical approximations (QCA's). The theoretical results illustrate the same trend as the experimental measurements in that the larger the ionic radius of R, the lower the orthorhombic/tetragonal phase transition temperature. This study provides strong evidence of the strain effects on order-disorder transition due to oxygens in the CuO chain sites.

DOI: 10.1103/PhysRevB.70.054517 PACS number(s): 74.25.Bt, 64.60.Cn, 61.10.−i

I. INTRODUCTION

It is well known that during the fabrication process of superconductor materials, a variety of point defects, such as substitution and interstitial impurities, vacancies, and cation-disorder are involved. These defects have a large effect on the properties of superconductors.[1] In type-II superconductors, high critical current densities can be achieved by the presence of high-density defects which will provide suitable pinning centers for the magnetic flux lines. The ideal size of defects for flux line pinning should be comparable to the superconducting coherence length. For cuprates such as $\mathrm{YBa_2Cu_3O_{7-\delta}}$ (Y-123), the coherence lengths are in the order of tens of Å while the conventional superconductors have a coherence length of several thousand Å. Thus atomic-scale structural inhomogeneities such as point defects and columnar defects can play an important role in flux-line pinning.[2] An increasing number of applications of the 123-type high-T_c superconductors use materials other than Y-123. For example, in many bulk forms and multilayer applications, Y is replaced by Nd, Sm, or other rare-earth (R) elements . Doping $\mathrm{YBa_2Cu_3O_{7-\delta}}$ with Ca, Sr, or other alkaline earth (A) elements has also been shown to improve bulk and grain boundary transport and other properties.[3–5]

Since it is well known that strain effects are important in the studies of point defects, it is expected that studies of strain effects on point defects for series of $R\mathrm{Ba_2Cu_3O_{7-\delta}}$ (R-123) compounds will be important for practical applications of superconductivity. In particular, the concentration and ordering of oxygen vacancies have significant effects on the superconducting properties. For Y-123, the superconducting temperature T_c depends on the oxygen stoichiometry. As an example of a generic doping curve in cuprates,[6,7] when δ is larger than around 0.7, the crystal loses superconductivity. However, if δ is smaller than 0.7, the compound is superconducting. It is generally believed that higher oxygen content can create more holes in the structure. When δ is between 0.1 and 0.7, the crystal is in the underdoped region, and T_c increases with increasing hole concentration. When the oxygen content is in the proper range, T_c is above the boiling point of liquid nitrogen. However, if more holes are created, the T_c value decreases instead, and the crystal is in an overdoped region.

Oxygen ordering in the Cu-O chains of the 123 structure gives rise to further complex structures.[8,9] Even when the average occupancies of oxygen sites remain constant, the occupation at chain and antichain sites can vary. Jorgensen *et al.*[10] observed that the superconducting transition temperature in Y-123 changes as a function of time following the quenching experiment while the oxygen content is fixed. This demonstrates that the specific ordering of the oxygen atoms in the basal plane is another important parameter that controls T_c in the Y-123 system.[11] The ordering process in the Cu-O chain is the origin of the structural transition between tetragonal and orthorhombic phases in the 123 structure, which has been extensively studied since the discovery of Y-123.[12–15] Structural transition of Y-123 is strongly affected by external pressure as well.[16–19] In addition, there are systematic results reported by Wong-Ng and co-workers[20–22] showing that the orthorhombic/tetragonal phase transition temperatures in R-123 can be scaled approximately linearly with the ionic radius of R^{3+}. The above experimental obser-

vations indicate that lattice strain may play an important role in phase transition, which has not been investigated theoretically and systematically so far.

In this paper, we plan to study the effects of homovalent substitutions at Y and Ba sites, and hydrostatic pressure on the order-disorder transition theoretically. Considering large stress fields due to dislocations around grain boundaries, this study will also provide valuable information for understanding the transport properties in the vicinity of grain boundaries. First we briefly explain methods used in atomistic simulations. Secondly, we focus on the effects of strain on Schottky defects and related phenomena for a series of homovalent substitutions at Y and Ba sites of $YBa_2Cu_3O_{7-\delta}$. Although the 123 structure is not stable in the Ca and Sr analogs under ambient pressure,[23–25] partial substitution of Sr on the Ba site has been reported.[4,23,26–28] Finally, strain effects on chain-oxygen order-disorder transition of $RBa_2Cu_3O_{7-\delta}$ will be investigated.

II. ATOMISTIC SIMULATION METHODS

Since the parent compounds of high-T_c cuprate superconductors can be considered as charge-transfer insulators, ionic bonding can be assumed to have a large contribution to the lattice energy. Methods used to study atomistic phenonmena in conventional oxides can therefore be applied to study cuprates. The cuprates become superconductors at a proper doping level and temperature. However, the charge carrier density is very low compared with that of conventional metals. In addition, the charge carriers are confined within copper-oxygen planes. Consequently, the screening effect is not as strong as that of conventional metals. The lattice energy calculated from ionic models is somewhat overestimated. The point defect's energy is also slightly overestimated due to the omission of screening effect in metallic region of the phase diagram, which can be improved by including polarization effects in the shell model.[29] Many previous theoretical investigations are based on this type of ionic model (for example, see Refs. 30–34).

Several pair-potential sets of shell model parameters have been determined for Y-123 by Baetzold.[31,32] To systematically study homovalent substitutions on Y and Ba sites, a consistent set of shell model parameters using the data set for $YBa_2Cu_3O_7$ (Ref. 31) was further developed to account for the dependence of the Born repulsion of the two ions on their net charges, on outer electronic configurations,[35,36] and on the common "r^3 law" between polarizability and radius.[37] The "virtual crystal method" is applied here to interpret experimental data of mixing two types of elements on one site. This method essentially is, for the purpose of calculating average structural and elastic properties, to approximate the mixture of two ions distributed over one sublattice by identical average "virtual ions." It allows the incorporation of compositional changes at the atomic level, but ignores explicit effects of disorder. For instance, when Ba^{2+} is partially replaced by Sr^{2+} in experiments, the composition-weighted average value of the two ions' radii is taken to approximate that of each virtual divalent ion. After constructing a consistent interatomic pair potential set,[38] we used the "general utility lattice program" (GULP),[39] which integrates the above modeling methods at an atomistic scale, to study lattice energy, elastic constants, and lattice dynamic properties. In summary, our calculations are based on short-range potentials of the Buckingham-type, long-range Coulomb potentials, and displacement-induced deformations of the electronic charge density in the framework of a shell model.

III. SCHOTTKY DEFECTS IN 123 COMPOUNDS

Any deviation in a crystal from a perfect structure is an imperfection. The simplest imperfection is a lattice vacancy, which is a missing atom or ion, known as a Schottky defect. Schottky defects involve "multiple" vacancies while preserving electrical neutrality. Regardless of how a Schottky defect is created, it is necessary to expend a certain amount of work per atom to take it to the surface. We calculated point defect energy by the Mott-Littleton approach.[40,41] Some vacancies are at anionic sites and others at the cationic sites. For Y-213, the defect reaction is given as follows:

$$YBa_2Cu_3O_7 \rightarrow V_Y^{-3} + 2V_{Ba}^{-2} + 3V_{Cu}^{-2} + 7V_O^{+13/7}; \qquad (1)$$

where V represents a vacancy. According to mass action law, the equilibrium constant (K) at a finite temperature can be written as

$$K = c(V_Y^{-3})c(V_{Ba}^{-2})^2c(V_{Cu}^{-2})^3c(V_O^{+13/7})^7 = \bar{c}^{13}, \qquad (2)$$

where c is the equilibrium concentration of vacancies and $\bar{c}$ is the average concentration of vacancies. The equilibrium concentration of the vacancy j, c_j, can be computed from Boltzmann statistics as

$$c_j = N_j \exp\left(\frac{-E_{v_j}}{kT}\right), \qquad (3)$$

where N_j is the number of atom j per unit volume and E_{v_j} is the energy required to take atom j from its lattice site inside the crystal to a site on the surface. Substituting the equilibrium concentraions of vacancies into Eq. (2), we obtain the expression for the average concentration of vacancies $\bar{c}$ as follows:

$$\bar{c} = N \exp\left(\frac{-\bar{E}_{\text{Schottky}}}{kT}\right), \qquad (4)$$

where N is the number of formula units per unit volume and $\bar{E}_{\text{Schottky}}$ is given, in terms of the formation energy of individual vacancy (an ion is removed to infinity instead of the surface of crystals) and lattice energy E^{lattice}, as

$$\bar{E}_{\text{Schottky}} = \frac{\sum_i E_i^{\text{vacancy}} + E^{\text{lattice}}}{13}. \qquad (5)$$

In R-123, the absolute value of site potential decreases continuously with increasing ion radius at the Y site, which is consistent with applying external tensile pressure. Usually, the change of short-range repulsion is less significant than that of the Madelung site potential. In general, the smaller absolute site potential value is favorable for lowering va-

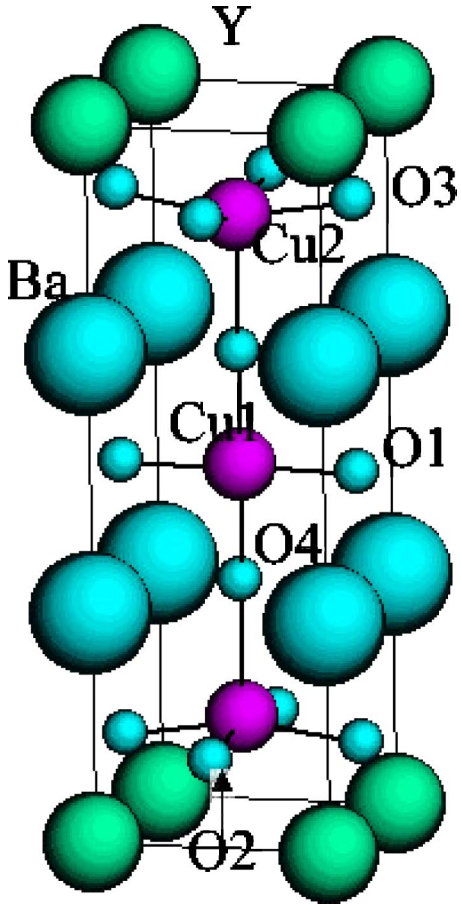

FIG. 1. Crystal structure of $YBa_2Cu_3O_7$.

cancy energy, and vice versa. Furthermore, an increase of the total volume leads to the expansion of effective relaxation space so that the vacancy energy can further decrease due to the relaxation of the atoms. In the shell model, the electronic polarization due to the electronic relaxation also lowers the defect energy. In $YA_2Cu_3O_7$ (*A*-123), as the radius of the ion at *A* sites becomes larger, a similar phenomenon is observed. In both $RBa_2Cu_3O_7$ and $YA_2Cu_3O_7$, the lower Schottky defects formation energies are always associated with the larger volume. This indicates that the volume of formation of Schottky defects is positive, or the volume of the entire crystal expands during the formation of Schottky defects.

As shown in Fig. 1, the complex structure of 123 compounds can be roughly divided into six layers along the *c* axis direction: *R*-CuO_2(Cu2)-BaO-CuO(Cu1)-BaO-CuO_2-*R*. For the sake of simplicity, the distances between planes are represented by the separations of cations projected along the *c* axis. The external and internal strains are computed with Y-123 as a reference. Replacing Y^{3+} by larger R^{3+} ions leads to positive external strains, indicating the dimensions of the cell expand as increasing *R* size. The more interesting observations are the changes of internal parameters within the unit cell. The variance of internal strains provide direct information of the changes of layers' separations in *R* series. The interatomic distances vary quite differently with ionic radius in the *R*-123 and *A*-123 series.[38] For instance, the distance of *R*-CuO_2 becomes larger with increasing *R* size, which is expected from the change of short-range repulsion of *R*-O. However, even when the entire cell volume increases as the *R* ion becomes larger, some parts of unit cell contract such as interlayer separations between CuO_2(Cu2)-BaO and BaO-CuO(Cu1) (or, bond lengths of Cu2-O4 and Cu1-O4). Consequently, the average energy of the point defect only decreases slightly because of the existing compressive blocks within the structure as plotted in Fig. 1. In the *A*-123 series, when Ba^{2+} is (partially) replaced by smaller A^{2+}, the variances of external and internal strains are of the same sign, reflecting a somewhat "even" expansion of the entire structure. The difference between *R*-123 and *A*-123 is reflected by the changes of *A*-*A* and Cu1-Cu2 distances. Unlike those in *R*-123, for *A*-123 both distances become larger with increasing *A* size. The different changes of internal strains due to doping at either Y or Ba sites governs the absolute value of slope of Schottky defects of *R*-123 and *A*-123 (see Fig. 2). In the previous studies,[42] they found interesting correlations between dopant radius and energy of solution in $YBa_2Cu_3O_7$. The trend of subsituting divalent cation for barium matches well with that in the Schottky defect energy of $YA_2Cu_3O_7$. However, there exist clear different trends between replacing yttrium by trivalent ions in $YBa_2Cu_3O_7$ and that in the Schottky defect energy of $RBa_2Cu_3O_7$. The reason is that the parent structure is fixed for former case, so that the trivalent ion larger than yttrium leads to more energy of solution. One the other hand, the Schottky defect has to consider all the atoms in the unit cell. Unless the structures change more or less "homogeneously," the energy of solution at one specific site may evolve differently from the Schottky defect energy.

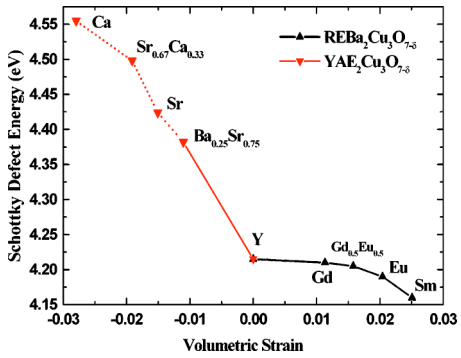

FIG. 2. Schottky defects formation energy vs volumetric strain. The volumetric strain is defined as $(V-V_0)/V_0$, where V_0 is the volume of Y-123 compound. All volumes are obtained by optimizing cell parameters and internal coordinates to minimize the total energy. The solid solutions are treated by the "virtual crystal method."

Recall that the relation between cell volume, bulk modulus of *R*-123, and the trend of thermal expansion coefficients are also the manifestation of the complexity of the 123 structure.[38] There is an "unusual" relation between Schottky defects formation energy and $B\Omega$ (where B is bulk modulus and Ω is the mean volume per atom) of *R*-123 in Fig. 3. As reported by Varotsos,[43] the Schottky defects formation energy is proportional to $B\Omega$ for elemental and binary crystals. While this relation appears to be obeyed by the *A*-123 series, it is violated by the *R*-123 series. The possible reason is still

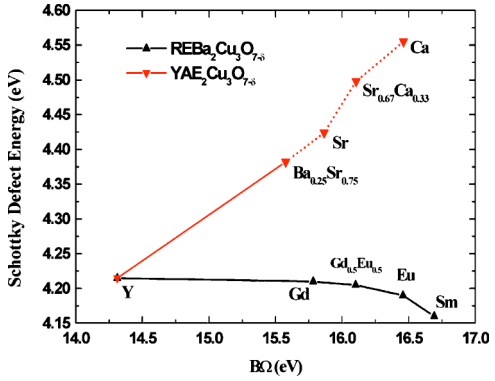

FIG. 3. Schottky defects formation energy vs $B\Omega$ of 123 compounds. B is the bulk modulus and Ω is the mean volume per atom of 123 compounds. Both B and Ω are calculated from the optimized structures with minimal total energy. The solid solutions are treated by the "virtual crystal method."

the non-uniform changes of the interatomic distances within the unit cell for R-123. We have studied the trend of melting temperature of R-123 by "Lindemann law,"[44,45] and found that the vibrations along the c axis are the most important modes to determine the melting temperatures while the isotropic approximation fails to yield correct results.[38] Here, we take another approach to investigate the relation between melting temperatures and formation energies of Schottky defects. Kurosawa[46] gave a direct correlation between them, which is listed in Table I. While it appears that a smaller Schottky defect formation energy can lower the melting temperature of simple binary significantly, it has not been proved to be true for compounds with complex structure. Note that the predominant point defect could be Frenkel defect rather than Schottky defect in some complex structures. However, Schottky defect energy provides an unambiguous measure on the average cohesive strength. For example, despite the Schottky defect formation energy of Sm-123 is smaller than that of Y-123, Sm-123 has a higher melting temperature. It is necessary to study internal strains rather than volumetric strains in order to obtain a detailed analysis of the thermodynamic properties of compounds with complex structures. In general, we found that the signs of the slopes $(dE_{\text{Schottky}}/d\epsilon_v)$ of R-123 and A-123 in Fig. 2 are the same. The difference between these two slopes and the "unusual" relationships between Schottky defects formation energies and $B\Omega$ and melting temperatures of R-123 compounds all reflect the complexity of the crystal structure.

IV. CHAIN-OXYGEN ORDER-DISORDER TRANSITION

The oxygen content is an important parameter for superconductivity in cuprates. In addition, the distribution (ordering) of oxygen atoms among the atomic sites strongly affects T_c. The order-disorder transition of chain oxygen has been extensively studied both experimentally and theoretically.[8,9,12–15] Raman studies show that there exists a pressure-induced ordering phenomenon.[19] The strain effect on this transition has not been investigated theoretically in a systematic fashion. Here we focus on the effects of homo valent substitutions at Y and Ba sites, and hydrostatic pressure on the order-disorder transition.

In the quasi chemical approximation (QCA),[12,15] the short-range order is characterized by the fraction number of near-neighbor pair sites occupied by oxygen-oxygen pairs $p=N_{oo}/4N$, where N is the number of sites on each of the sublattice α and β, and N_{oo} is the number of oxygen-oxygen near neighbor pairs. The long-range order parameter S is defined such that the fractional site occupancy on sublattice β is $c(1+S)$, while that on sublattice α is $c(1-S)$ where c is the fractional site occupancy averaged over both sublattices. (Note that for $YBa_2Cu_3O_{7-\delta}$, c is 0.5 when δ is zero; i.e., $\delta=1-2c$.)

The partition function is given by

$$Z(T)=\sum_{R_\alpha}\sum_{q_{\alpha\alpha}} g(R_\alpha,q_{\alpha\alpha})e^{-W(R_\alpha,q_{\alpha\alpha})/kT}, \tag{6}$$

where $R_\alpha=N(1+S)/4$, $q_{\alpha\alpha}$ is the probability of pairs $\alpha\alpha$, and $g(R_\alpha,q_{\alpha\alpha})$ is proportional to the total number of ways one can divide N entities into four groups of $\alpha\alpha,\alpha\beta,\beta\alpha$, and $\beta\beta$ pairs. The configuration energy is denoted as $W(R_\alpha,q_{\alpha\alpha})$. As usual, we may replace each sum by its maximum term in the summation for the system of a great many assemblies. Hence, we have

$$Z(T)=\sum_{R_\alpha} g(R_\alpha,\bar{q}_{\alpha\alpha})e^{-W(R_\alpha,\bar{q}_{\alpha\alpha})/kT}, \tag{7}$$

in which the most probable value $\bar{q}_{\alpha\alpha}$ of $q_{\alpha\alpha}$ is determined by

$$\frac{\partial}{\partial \bar{q}_{\alpha\alpha}}\left(\ln g(R_\alpha,\bar{q}_{\alpha\alpha})-\frac{W(R_\alpha,\bar{q}_{\alpha\alpha})}{kT}\right)=0. \tag{8}$$

There are three unknowns for a given value of temperature T and oxygen partial pressure P_{O_2}: c,S,p. Three equations involving these three unknowns are obtained by requiring that (1) the chemical potential of oxygen atoms is the same on both sublattices, (2) the chemical potential of oxygen atoms is the same in the solid and in the gas phase (which consists mostly of diatomic molecules but has an equilibrium concentration of atomic oxygen), and (3) the free energy of the system is a minimum with respect to the fractional number of oxygen-oxygen pairs. The following deri-

TABLE I. The Schottky defects formation energy and melting temperature of binary and R-123 compounds. The data of binary compounds are from Ref. 46. The melting temperature data of R-123 are from Ref. 47.

Crystal	NaF	NaCl	NaBr	MgO	CaO	SrO	Crystal	YBCO	GdBCO	EuBCO	SmBCO
$\bar{E}_{\text{Schottky}}$(eV)	2.5	2.2	2.0	6.3	5.5	5.0	$\bar{E}_{\text{Schottky}}$(eV)	4.22	4.21	4.20	4.16
T_{melting}(K)	1259	1073	1018	3070	2850	2700	T_{melting}(K)	1250	1290	1300	1325

vations follow the similar procedure as described in Ref. 48. Using the above conditions, QCA yields

$$\ln\left(\frac{c(1+S)-p}{c(1-S)-p}\right)=\frac{3}{4}\ln\left(\frac{(1+S)[1-c(1-S)]}{(1-S)[1-c(1+S)]}\right), \quad (9)$$

$$\ln\left[\left(\frac{1-c(1+S)}{c(1+S)}\right)^3\left(\frac{c(1+S)-p}{1-2c+p}\right)^4\right] = \ln\left[\left(\frac{P_{O_2}}{\xi}\right)^{1/2}\frac{1}{(kT)^{7/4}}\right]-\frac{\epsilon+1/2E_d}{kT}, \quad (10)$$

$$\frac{v}{kT}=\ln\left(\frac{[c(1+S)-p][c(1-S)-p]}{p(1-2c+p)}\right), \quad (11)$$

where ϵ is the energy to remove an oxygen atom from the gas and place it in the lattice, v is the repulsion energy between near-neighbor oxygens, E_d is the dissociation energy of one oxygen molecule, ξ is equal to 4.144×10^{19} Pa(eV)$^{-7/2}$. The desired values of c, S, and p are obtained for given values of T and P_{O_2}, by simultaneously solving the above equations. We note that the order-disorder transition temperature T_{od} is related to the oxygen-oxygen repulsion energy v and the value of the average site occupancy c at this temperature by

$$\frac{v}{kT_{OD}}=\ln\left(\frac{16c(1-c)}{1-4(1-2c)^2}\right). \quad (12)$$

Frenkel defects involve an atom displaced from its normal site into an interstitial site. If the interstitial site is chosen as antichain site for 123 compounds, this Frenkel pair is closely related to chain-oxygen order-disorder transition. Forming a Frenkel pair in an otherwise perfect crystal is an elementary disordering event. As the disordering proceeds, it is important to account for defect-defect interactions. Using Mott-Littleton approach, we have computed the isolated Frenkel pair formation energy for RBa$_2$Cu$_3$O$_7$, YA_2Cu$_3$O$_7$, and Y-123 under hydrostatic pressure. We found that this formation energy increases in compressive regions and decreases in tensile regions under hydrostatic pressure. This is the origin of ordering under stress. From the systematic investigation of the phonon spectral characteristics with the application of pressure,[19] it was observed that the changes induced by the hydrostatic pressure have a strong effect on chain ordering. Results of our calculations are consistent with the reported observation. Figure 4 shows the plots of the Frenkel pair formation energy versus lattice strain (volumetric strain) for both the R series and the A series. These two plots demonstrate a similar trend and they form a well-connected smooth curve. The similar behavior of the curve for the R and A series (with chemical doping) and the curve for Y-123 (with hydrostatic pressure) indicates that the oxygen disordering energy is dominated by lattice strain, which is expected if the short range repulsion terms dominate the energy required to form the oxygen interstitial ion.

Furthermore, scaling the oxygen-oxygen short-range repulsive energy by the calculated Frenkel Pair formation energy, the transition temperature between orthorhombic and tetragonal phases is computed based on Eq. (12). The transition temperature of YBa$_2$Cu$_3$O$_{7-\delta}$ was used as a reference. The results are plotted in Fig. 5 with the experimental data taken from Refs. 20–22. There exists observable difference (around 100 K) between theory and experiment in the Nd-123 system.[22] It has been determined experimentally that the orthorhombic-to-tetragonal phase transition in the R-123 series take place at an oxygen composition in the range of 6.4 (Er) to 6.83 (Nd), not all at 6.5 (Y).[20–22] The change of oxygen content leads to the change of structure such as lattice parameters and atomic positions,[8,9] which in turn alters the formation energy of Frenkel pairs. Since we set the reference transition temperature to be the value in Y-123 case, this corresponds to the transition at oxygen content being 6.5. If we track the whole process of order-disorder transition starting from fully oxygenated case, the total oxygen content decreases until the transition is finished. The formation energy of Frenkel pairs decreases also as anisotropy in the ab plane [defined as $(b-a)/a$] reduces. Note that the transition occurs at oxygen content being 6.83 in a Nd-123 system, this indicates the anisotropy in Nd-123 remains higher compared with Y-123. Therefore, the formation energy of Frenkel pairs

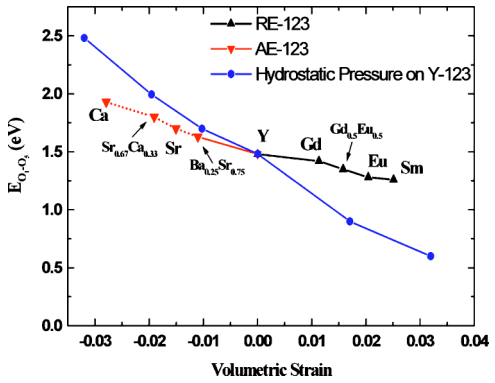

FIG. 4. Frenkel pair formation energy vs volumetric strain for 123 compounds. The energy corresponds to moving one chain oxygen into an antichain site. All volumes are obtained by optimizing cell parameters and internal coordinates to minimize the total energy. The solid solutions are treated by the "virtual crystal method."

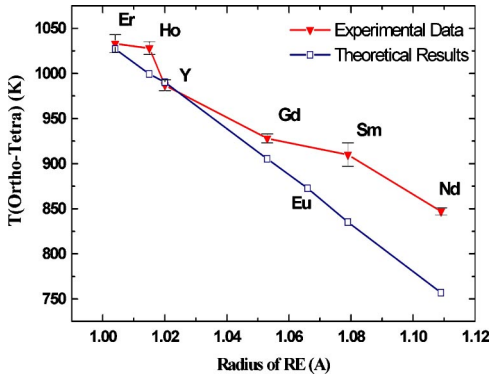

FIG. 5. Chain-oxygen order-disorder transition temperature of RBa$_2$Cu$_3$O$_7$. The theoretical data are calculated by using the transition temperature of YBa$_2$Cu$_3$O$_{7-\delta}$ as a reference. The experimental data are from Refs. 20–22. The error bars indicate the temperature range measured by x-ray diffraction.

decreases less than that in Y-123 during the whole process of transition as observed experimently. This means that in our "simple" model the transition temperature for Nd-123 is underestimated. But, the remarkable thing is that using such a simple model, the trend of the theoretical results agree well with the experimental measurements. It is seen that stress and "chemical pressure" can substantially alter the degree of disorder. This study provides a clear evidence for the effects of strain on order-disorder transition. Previous studies also show there are quite rich microstructures resulting from this orthorhombic-to-tetragonal phase transition: for instance, twin structures and related twinning dislocations,[49,50] tweed morphology caused mainly by (110) and $(\bar{1}10)$ shear displacements.[1] In particularly, our results can be applied further to deduce that strain near edge dislocations in low angle grain boundaries,[51] which can also have a significant effect on the degree of ordering in cuprate materials. For example, the interactions between point defects and strain fields due to dislocations and/or grain boundaries can affect the distribution of point defects, and the content and degree of order of oxygen atoms.[38]

V. CONCLUSIONS

Based on the Mott-Littleton approach we studied the Schottky defect formation energy in the 123 phase as a function of volumetric strain. Generally, a more expanded lattice favors a lower Schottky defect formation energy, and vice verse. The difference of slopes $(d\mathrm{E}_{\mathrm{Schottky}}/d\epsilon)$ between *R*-123 and $YA_2Cu_3O_{7-\delta}$, the "unusual" relation between Schottky defects formation energies and $B\Omega$ and melt temperatures of *R*-123 compounds all reflect the complexity of the crystal structure of 123 compounds.

Our study also illustrates the importance of strain effects on the orthorhombic/tetragonal phase transition in the *R*-123 compounds. We have calculated the formation energy of Frenkel pair defects as a function of volumetric strain for $RBa_2Cu_3O_7$ and $YA_2Cu_3O_7$, and for $YBa_2Cu_3O_7$ under hydrostatic pressure. Our calculations show good agreement with experimental observations in that pressure favors ordering of the CuO chains. For example, the Frenkel pair formation energy indeed increases significantly (around -0.25 eV/0.01 volumetric strain) under compression. Based on a quasichemical approach, the orthorhombic/tetragonal transition temperatures for *R*-123 have been computed by scaling the effective oxygen-oxygen short-range repulsive energy in the CuO chain using the Frenkel pair formation energy. The calculated results agree with experimental data in that the larger the ionic size of *R*, the lower the orthorhombic/tetragonal phase transition temperature.

ACKNOWLEDGMENTS

The work at NIST was partially supported by the U.S. Department of Energy (DOE). The work at Brookhaven National Laboratory was performed under the auspices of the Division of Materials Sciences, Office of Science, U.S. Department of Energy under Contract No. DE-AC-02-98CH10886.

*Present address: Beckman Institute 139-74, California Institute of Technology, Pasadena, CA 91125. Electronic address: hbsu@wag.caltech.edu

†Electronic address: dwelch@bnl.gov

‡Electronic address: winnie.wong-ng@nist.gov

[1] Z. X. Cai and Y. Zhu, *Microstructures and Structural Defects in High-Temperature Superconductors* (World Scientific, Singapore, 1998).

[2] P. D. Yang and C. M. Lieber, Science **273**, 1836 (1996).

[3] J. B. Langhorn, M. A. Black, and P. J. McGinn, Mater. Lett. **41**, 289 (1999).

[4] F. Licci, A. Gauzzi, M. Marezio, G. P. Radaelli, R. Masini, and C. Chaillout-Bougerol, Phys. Rev. B **58**, 15 208 (1998).

[5] H. Hilgenkamp and J. Mannhart, Rev. Mod. Phys. **74**, 485 (2002).

[6] H. B. Zhang and H. S. Sato, Phys. Rev. Lett. **70**, 1697 (1993).

[7] J. L. Tallon, C. Bernhard, H. Shaked, R. L. Hitterman, and J. D. Jorgensen, Phys. Rev. B **51**, 12 911 (1995).

[8] R. J. Cava, B. Batlogg, C. H. Chen, E. A. Rietman, S. M. Zahurak, and D. Werder, Nature (London) **329**, 423 (1987).

[9] R. J. Cava, B. Batlogg, C. H. Chen, E. A. Rietman, S. M. Zahurak, and D. Werder, Phys. Rev. B **36**, 5719 (1987).

[10] J. D. Jorgensen, S. Pei, P. Lightfoot, H. Shi, A. P. Paulikas, and B. W. Veal, Physica C **167**, 571 (1990).

[11] H. F. Poulsen, N. H. Andersen, J. V. Andersen, H. Bohr, and O. G. Mouritsen, Nature (London) **349**, 594 (1991).

[12] H. Bakker, D. O. Welch, and O. W. Lazareth, Solid State Commun. **64**, 237 (1987).

[13] D. Defontaine, L. T. Wille, and S. C. Moss, Phys. Rev. B **36**, 5709 (1987).

[14] A. G. Khachaturyan, S. V. Semenovskaya, and J. W. Morris, Phys. Rev. B **37**, 2243 (1988).

[15] H. Bakker, J. P. A. Westerveld, D. M. R. Locascio, and D. O. Welch, Physica C **157**, 25 (1989).

[16] W. H. Fietz, R. Quenzel, H. A. Ludwig, K. Grube, S. I. Schlachter, F. W. Hornung, T. Wolf, A. Erb, M. Klaser, and G. MullerVogt, Physica C **270**, 258 (1996).

[17] S. Sadewasser, Y. Wang, J. S. Schilling, H. Zheng, A. P. Paulikas, and B. W. Veal, Phys. Rev. B **56**, 14 168 (1997).

[18] S. Sadewasser, J. S. Schilling, A. P. Paulikas, and B. W. Veal, Phys. Rev. B **61**, 741 (2000).

[19] E. Liarokapis, D. Lampakis, T. Nishizaki, and C. Panagopoulos, High Press. Res. **18**, 109 (2000).

[20] W. Wong-Ng, L. P. Cook, C. K. Chiang, L. Swartzendruber, and L. H. Bennett, in *Advances in Ceramic Materials and Ceramic Superconductor II*, edited by M. F. Yan (American Ceramic Society, Westerville, OH, 1988), Vol. II, p. 27.

[21] W. Wong-Ng, L. P. Cook, C. K. Chiang, M. D. Vaudin, D. L. Kaiser, F. Beech, L. Swartzen-druber, L. H. Bennett, and E. R. Fuller, Jr., in *High Temperature Superconducting Compounds:*

Processing & Related Properties, edited by S. H. Whang and A. DasGupta (The Minerals, Metals and Materials Society, Warrendale, PA, 1989), Vol. II, p. 553.
[22] W. Wong-Ng, L. P. Cook, H. B. Su, D. O. Welch, C. K. Chiang, and L. Bennett (unpublished).
[23] R. S. Roth, C. J. Rawn, J. D. Whitler, C. K. Chiang, and W. K. Wong-Ng, J. Am. Ceram. Soc. **72**, 395 (1989).
[24] B. Okai, Jpn. J. Appl. Phys., Part 2 **29**, L2180 (1990).
[25] P. K. Davies, E. Caignol, and T. King, J. Am. Ceram. Soc. **74**, 569 (1991).
[26] Y. Cao, T. L. Hudson, Y. S. Wang, S. H. Xu, Y. Y. Xue, and C. W. Chu, Phys. Rev. B **58**, 11 201 (1998).
[27] H. G. Lee, A. P. Litvinchuk, M. V. Abrashev, M. N. Iliev, S. H. Xu, and C. W. Chu, J. Phys. Chem. Solids **59**, 1994 (1998).
[28] M. Marezio, E. Gilioli, P. G. Radaelli, A. Gauzzi, and F. Licci, Physica C **341**, 375 (2000).
[29] B. G. Dick and A. W. Overhauser, Phys. Rev. **112**, 90 (1958).
[30] S. L. Chaplot, Phys. Rev. B **37**, 7435 (1988).
[31] R. C. Baetzold, Phys. Rev. B **38**, 11 304 (1988).
[32] R. C. Baetzold, Phys. Rev. B **42**, 56 (1990).
[33] S. Valkealahti and D. O. Welch, Physica C **162**, 540 (1989).
[34] N. F. Wright and W. H. Butler, Phys. Rev. B **42**, 4219 (1990).
[35] L. Pauling, Z. Kristallogr. **67**, 377 (1928).
[36] M. P. Tosi, Solid State Phys. **16**, 1 (1964).
[37] K. D. Bonin and V. V. Kresin, *Electric-Dipole Polarizabilities of Atoms, Molecules, and Clusters* (World Scientific, Singapore, 1997).
[38] H. B. Su, Ph.D. thesis, SUNY at Stony Brook, 2002.
[39] J. D. Gale, J. Chem. Soc., Faraday Trans. **93**, 629 (1997).
[40] N. F. Mott and M. J. Littleton, Trans. Faraday Soc. **34**, 485 (1938).
[41] N. F. Mott and R. W. Gurney, *Electronic Processes in Ionic Crystals* (Oxford University Press, Oxford, 1948).
[42] M. S. Islam and R. C. Baetzold, Phys. Rev. B **40**, 10 926 (1989).
[43] P. Varotsos and W. Ludwig, Phys. Rev. B **18**, 2683 (1978).
[44] J. J. Gilvarry, Phys. Rev. **102**, 308 (1956).
[45] J. P. Poirier, *Introduction to the Physics of the Earth's Interior* (Cambridge University Press, Cambridge, 1991).
[46] T. Kurosawa, J. Phys. Soc. Jpn. **12**, 338 (1957).
[47] K. Osamura and W. Zhang, Z. Metallkd. **84**, 522 (1993).
[48] T. Muto and Y. Takagi, Solid State Phys. **1**, 194 (1955).
[49] V. S. Boyko, S. W. Chan, and M. Chopra, Phys. Rev. B **63**, 224521 (2001).
[50] S. W. Chan and V. S. Boyko, Phys. Rev. B **53**, 16 579 (1996).
[51] H. Kung, J. P. Hirth, S. R. Foltyn, P. N. Arendt, Q. X. Jia, and M. P. Maley, Philos. Mag. Lett. **81**, 85 (2001).

ELSEVIER

Physica C 377 (2002) 107–113

PHYSICA C

www.elsevier.com/locate/physc

Subsolidus phase relationships of the $BaO–Y_2O_3–CuO_x$ system under carbonate-free conditions at $p_{O_2} = 100$ Pa and at $p_{O_2} = 21$ kPa

W. Wong-Ng [a,*], L.P. Cook [a], J. Suh [b]

[a] *Ceramics Division, Materials Science and Engineering Laboratory, National Institute of Standards and Technology (NIST), 100 Bureau Dr., Gaithersburg, MD 20899, USA*

[b] *Department of Geology, University of Maryland, College Park, MD 20742, USA*

Received 3 September 2001; received in revised form 9 October 2001; accepted 10 October 2001

Abstract

Current applications of $BaO–Y_2O_3–CuO_x$ phase equilibria are focused on the use of coated-conductor technology for fabrication of superconducting tape. Although such processing is typically carried out with carbonate-free high T_c precursors, the majority of phase equilibrium studies completed to date have utilized $BaCO_3$-derived starting materials. The present study reports results of a $BaO–Y_2O_3–CuO_x$ phase equilibrium investigation at two oxygen pressures using carbonate-free precursors based on BaO. Special apparatus and procedures for handling these atmospherically sensitive compositions are described. Experimental results were used to establish tie-lines in the BaO-rich part of the phase diagram, and have confirmed a difference in tie-line distribution among the $Ba_2YCu_3O_x$, $Ba_4YCu_3O_x$, BaY_2CuO_5, and $BaCuO_{2+x}$ phases under carbonate-free conditions relative to those obtained using $BaCO_3$-derived starting materials. By reducing p_{O_2} from 21 kPa to 100 Pa under carbonate-free conditions, an additional tie-line change among the phases $Ba_2YCu_3O_x$, $Ba_4YCu_3O_x$, $Ba_6YCu_3O_x$, and BaY_2CuO_5 was observed. These differences can be applied to coated-conductor processing of $Ba_2YCu_3O_x$ superconducting tapes.
Published by Elsevier Science B.V.

PACS: 74.70; 74.25.D
Keywords: $BaO–Y_2O_3–CuO_x$; Phase diagrams; Carbonate-free; Superconductors

1. Introduction

Following the discovery of high T_c superconducting oxides in 1986, considerable progress in the relevant materials science and engineering has been achieved. In the area of wire and tape fabrication, intensive research has led to the design and development of first generation powder-in-tube (PIT) Bi–Pb–Sr–Ca–Cu–O (BSCCO) tapes [1–5]. Current efforts in first-generation wire and tape research and development are focused on improving processing routes to minimize the cost of production. More recently, second-generation high T_c

* Corresponding author. Tel.: +1-301-975-5791; fax: +1-301-975-5334.
E-mail address: winnie.wong-ng@nist.gov (W. Wong-Ng).

0921-4534/01/$ - see front matter Published by Elsevier Science B.V.
PII: S0921-4534(01)01124-8

superconductor tapes deposited on flexible coated conductors have received increasing attention [6–10]. These superconductors are based on BaO–Y_2O_3–CuO_x materials, including lanthanide-substituted variants. The Ba–Y–Cu–O materials are relatively more isotropic when compared with BSCCO-based superconductors, and can retain current carrying ability at liquid nitrogen temperature under high magnetic fields. Therefore, such coated-conductor superconductors have great commercial potential for electric utility and high magnetic field applications. These superconductors are also expected to be more economical to produce.

Because of the potential advantages of coated-conductor superconductors, a renewed research interest in the entire family of the $Ba_2RCu_3O_x$ materials (R = Y and lanthanide elements) has developed. The BaO–Y_2O_3–CuO_x system is one of the high T_c systems most extensively investigated since the discovery of the 90 K superconductor, $Ba_2YCu_3O_{6+x}$ [11,12]. A large number of phase diagrams are available in literature; however, the majority were prepared using $BaCO_3$ [13–23], partly because it is difficult to handle BaO. The presence of CO_3^{2-} gave rise to extraneous phases (e.g., oxycarbonates) in the system, either directly from solid carbonate starting materials, or indirectly by contact with atmospheric CO_2. While a few diagrams are reported as having been constructed using BaO, $Ba(NO_3)_2$ and BaO_2 [24–34], these were not prepared entirely under atmospherically controlled conditions, and are not totally consistent with each other.

The goal of this paper is to provide subsolidus phase diagrams of the carbonate-free BaO–Y_2O_3–CuO system at $p_{O_2} = 21$ kPa (875–900 °C) and at $p_{O_2} = 100$ Pa (800–810 °C) by using BaO as a source for Ba. By studying the phase equilibria at these oxygen pressures, the effect of lowering p_{O_2} to the values prevailing in coated-conductor processing can be established. As the crystal chemistry and crystal structure of compounds of the BaO–Y_2O_3–CuO system have been studied extensively [13–35], this paper will not repeat these details, except for selected comments, when appropriate. Emphasis will be placed on the occurrence of phases and phase compatibilities, which form the basis for processing.

2. Experimental

BaO starting material was produced from $BaCO_3$ (99.99% purity, metals basis) by vacuum calcination in a specially designed vertical tube furnace. An MgO crucible containing ~15 g of $BaCO_3$ was suspended in the hot zone of the furnace, and the furnace was evacuated to a pressure of ~10 μm Hg or less by a high capacity mechanical pump. The following heating schedule was used: room temperature to 1300 °C in 20 h; isothermal at 1300 °C for 10 h; 1300 °C to room temperature in 20 h. During the vacuum calcination the pressure typically increased to ~200 μm Hg as CO_2 was evolved, and then rapidly returned to ~10 μm Hg or less as the decomposition of the $BaCO_3$ was completed. After cooling, the BaO was lowered through an interlock into a transfer vessel. It was then transported to an Ar-filled glovebox equipped with a recirculating purifier, which continually removed atmospheric contaminants from the Ar to <1 ppm by volume. Fig. 1 shows the X-ray diffraction pattern of the single-phase cubic BaO obtained. This X-ray pattern was obtained using a hermetic cell designed for air-sensitive materials [36]. All sample weighings, homogenizations and pressings of pellets were performed inside the glovebox. Pelletized samples were placed inside individual MgO crucibles for annealing in a

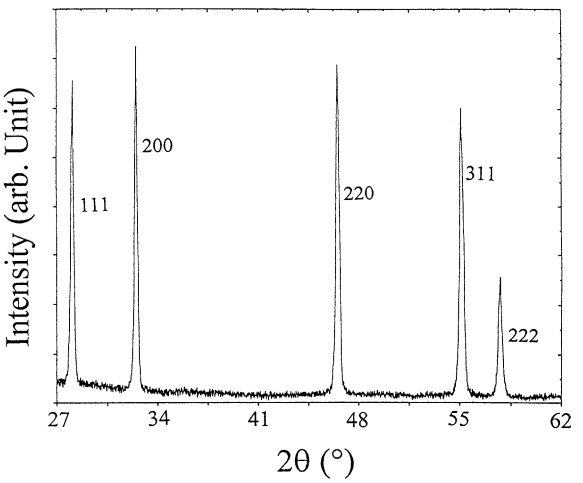

Fig. 1. X-ray diffraction pattern of cubic BaO, obtained by vacuum calcination of $BaCO_3$.

horizontal box-type controlled-atmosphere furnace. Transfer from the glovebox to the box furnace and vice versa was achieved via a second transfer vessel and an interlock system attached to the furnace.

Samples of 26 compositions for each atmosphere (a total of 52 samples (Table 1)) were prepared using the solid state sintering method. Stoichiometric amounts of BaO, Y_2O_3 (99.99% purity, metals basis), and CuO (99.99% purity, metals basis) were mixed and pressed into pellets, and annealed in the box furnace. During the annealings, oxygen pressure of Ar/O_2 mixtures was controlled using a mass flow meter and monitored at both the inlet and outlet of the furnace using a zirconia oxygen sensor. Samples were annealed at 875–900 °C for the experiments at $p_{O_2} = 21$ kPa (corresponding to air), and at 800–810 °C for the experiments at $p_{O_2} = 100$ Pa (0.1% O_2 by volume). Intermediate grindings and pelletizations took place until no further changes were detected in the powder X-ray diffraction patterns. The hermetic cell was used for all X-ray diffraction characterization of samples in this study. Samples were processed for a total time of about three weeks each.

Table 1
Compositions (listed in mol fraction %) of 26 samples for each atmosphere (at $p_{O_2} = 21$ kPa and at $p_{O_2} = 100$ Pa) prepared for phase equilibrium studies in the $BaO–Y_2O_3–CuO_x$ system

#	BaO	$(1/2)Y_2O_3$	CuO
1	60	10	30
2	50	16.67	33.33
3	65	17.5	17.5
4	70	5	25
5	60	5	35
6	54	8	38
7	50	18	32
8	40	40	20
9	45	10	45
10	40	20	40
11	35	60	5
12	20	70	10
13	25	25	50
14	40	5	55
15	25	5	70
16	10	35	55
17	10	65	25
18	50	25	25
19	55	35	10
20	45	40	15
21	45	27.5	27.5
22	45	45	10
23	31.67	18.33	50
24	58	11	31
25	52	12	36
26	63.33	3.33	33.34

3. Results and discussion

Figs. 2 and 3 show the phase diagrams of the $BaO–Y_2O_3–CuO_x$ system prepared at $p_{O_2} = 21$ kPa (875–900 °C) and at $p_{O_2} = 100$ Pa (800–810 °C). The diagrams are relatively straightforward, but are different from those prepared using $BaCO_3$ [10–23], particularly in the Ba-rich region. In the following sections, we will describe briefly the compounds formed and the phase relationships determined.

3.1. Compounds formed in the $BaO–Y_2O_3–CuO_x$ systems

The phases formed at $p_{O_2} = 21$ kPa and at $p_{O_2} = 100$ Pa are similar, except those in the associated binary $BaO–CuO_x$ system.

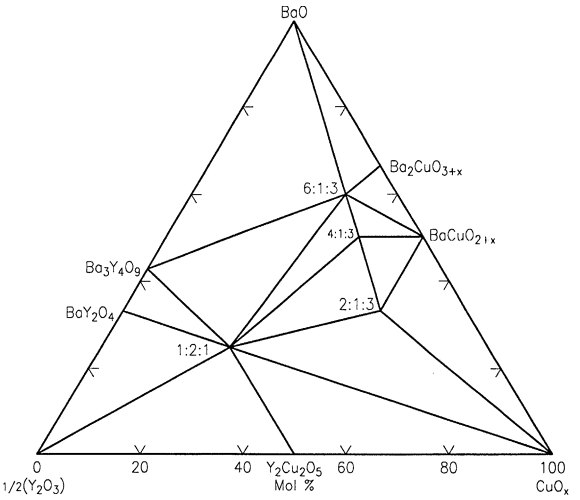

Fig. 2. Phase diagram of the $BaO–(1/2)Y_2O_3–CuO_x$ system prepared at $p_{O_2} = 21$ kPa (875–900 °C). In this diagram, the symbols (2:1:3), (4:1:3), (6:1:3) and (1:2:1) are used to represent the phases BaY_2CuO_5, $Ba_4YCu_3O_x$, $Ba_6YCu_3O_x$ and BaY_2CuO_5, respectively.

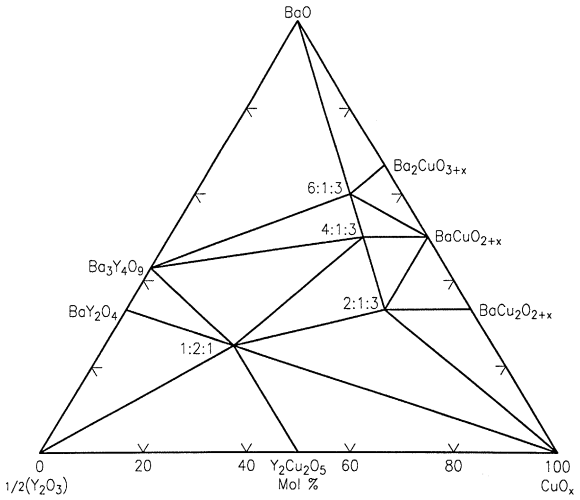

Fig. 3. Phase diagram of the BaO–(1/2)Y_2O_3–CuO_x system prepared at $p_{O_2} = 100$ Pa (800–810 °C). Symbols are shown in Fig. 2.

3.1.1. The BaO–CuO_x system

In this binary system, the compounds Ba_2CuO_{3+x} [35–37] and $BaCuO_{2+x}$ [38] were found to be stable both at $p_{O_2} = 21$ kPa and at $p_{O_2} = 100$ Pa. As the ionic size of Ba and Y is rather different, no solid solution of the $(Ba_{2-x}Y_x)CuO_{3+z}$ type was observed, in contrast to the BaO–Nd_2O_3–CuO system [34,39]. Furthermore, there was no evidence of the existence of the $Ba_2Cu_3O_{5+x}$ [40] or $Ba_3Cu_5O_{8+x}$ [40] phases. At $p_{O_2} = 100$ Pa the reduced phase $BaCu_2O_{2+x}$ was observed in addition to Ba_2CuO_{3+x} and $BaCuO_{2+x}$. The Ba_2CuO_{3+x} phase cannot be prepared in the presence of moisture and carbonate. The Ba_3CuO_4 phase, reported by Frase and Clarke [27] and Abbattista et al. [24,35] to be stable under very reduced conditions, was not detected in the present study.

3.1.2. The BaO–Y_2O_3 system

Under atmospherically controlled conditions, the oxycarbonates reported in the BaO–Y_2O_3–CuO_x system investigated with $BaCO_3$-derived starting materials are not stable. In the BaO–Y_2O_3 system, only $Ba_3Y_4O_9$ and BaY_2O_4 were found, instead of the four phases ($Ba_3Y_4O_9$, BaY_2O_4, $Ba_2Y_2O_5$ and $Ba_4Y_2O_9$) reported in Ref. [14]. The phases "$Ba_2Y_2O_5$" and "$Ba_4Y_2O_9$" have been determined to be oxycarbonates, corresponding to $Ba_2Y_2O_5 \cdot CO_2$ and $Ba_4Y_2O_9 \cdot 2CO_2$ [26], and therefore were not found in the present study. According to Abbattista et al. [35] and De Leeuw et al. [26], these phases dissociate according to the following equations:

$$3Ba_2Y_2O_5 \cdot CO_2 \leftrightarrow 2BaY_2O_4 + Ba_4Y_2O_7 \cdot CO_2$$

$$2Ba_4Y_2O_7 \cdot CO_2 \leftrightarrow Ba_3Y_4O_9 + 5BaO + 2CO_2$$

3.1.3. The Y_2O_3–CuO system

In the binary Y_2O_3–CuO_x diagrams, only the $Y_2Cu_2O_5$ phase was observed both at $p_{O_2} = 21$ kPa and at $p_{O_2} = 100$ Pa. The R_2CuO_4 type phase only exists when R is relatively large (lanthanides with ionic radius $r > r^{3+}_{Dy}$) [41]. The oxygen partial pressure of 100 Pa presumably was not sufficiently low for the reduced $YCuO_2$ phase [42,43] to be stable.

3.1.4. The BaO–Y_2O_3–CuO system

A total of four ternary oxides ($Ba_2YCu_3O_{6+x}$ (2:1:3), $Ba_4YCu_3O_x$ (4:1:3), $Ba_6YCu_3O_x$ (6:1:3), and the 'green' phase BaY_2CuO_5 (1:2:1)) was found in the BaO–Y_2O_3–CuO system under both processing conditions. The occurrence of the compounds $Ba_4YCu_3O_x$ and $Ba_6YCu_3O_x$ in the BaO-rich part of the diagram agrees with that reported by Abbattista et al. [24], and Osamura and Zhang [34]. A number of other reported phases near the Ba-rich end are a result of the use of barium carbonate [13,14,26].

Although solid solution has been reported in the lanthanide-containing $Ba_{2-x}R_{1+x}Cu_3O_{6+x}$ phases, in the system BaO–Y_2O_3–CuO_x, the $Ba_2YCu_3O_{6+x}$ (2:1:3) phase is a point compound with respect to cation content. In the lanthanide-containing phases, with relatively larger size of R (R = La, Nd, Sm, Eu, and Gd), the Shannon ionic radii of Ba (1.52 Å (ten-fold coordination [41])) and R (1.053 to 1.16 Å from Gd to La, eight-fold coordination) are more comparable, relative to the smaller Y ion (1.019 Å).

The $Ba_2YCu_3O_{6+x}$ phase is tetragonal P4/mmm when quenched from 900, and 810 °C. The structure of $Ba_4YCu_3O_{6+x}$ was reported to be of the cubic oxygen-defect perovskite type [24], and that of the orthorhombic $Ba_6YCu_3O_{6+x}$ phase is of the

$SrTi_2O_4$-type (layered perovskite structure) [24]. The structure of the BaY_2CuO_5 "green" phase, orthorhombic with space group Pnma, has been studied extensively [44–46].

3.2. Phase compatibilities

While differences in oxygen partial pressure did not affect the phase formation of the BaO–Y_2O_3–CuO system, the tie-line relationships at $p_{O_2} = 21$ kPa (875–900 °C) and at $p_{O_2} = 100$ Pa (800–810 °C) are somewhat different. The main difference concerns the relations between the $Ba_6YCu_3O_x$, $Ba_4YCu_3O_x$, $Ba_3Y_4O_9$ and BaY_2CuO_5 phases. At $p_{O_2} = 21$ kPa, the BaY_2CuO_5 phase was found to be compatible with the $Ba_6YCu_3O_x$ phase, whereas at $p_{O_2} = 100$ Pa, the tie-line was found to switch over to $Ba_3Y_4O_9$–$Ba_4YCu_3O_x$ instead.

The tie-lines determined in the CuO- and Y_2O_3-rich part of the phase diagrams are in agreement with most other diagrams, whether prepared using $BaCO_3$, BaO_2, BaO, or $Ba(NO_3)_2$. However, the region of the diagram near BaO corner is substantially different. Among the diagrams reported in the literature, our results agree most closely with those reported by Abbittista et al. [35], and by Osamura and Zhang [34]. These reported diagrams were prepared using either BaO_2 or $Ba(NO_3)_2$, and are shown in Fig. 4. The similarities arise from the fact that the phases described in these diagrams are the same as those reported in the present paper. However, the tie-line relationships near the 2:1:3 phase are different. These tie-line relations involve the four phases, $Ba_2YCu_3O_{6+x}$, BaY_2CuO_5, $BaCuO_{2+x}$ and $Ba_4YCu_3O_x$. In the present study, the $Ba_2YCu_3O_{6+x}$ phase is found to be compatible with the $Ba_4YCu_3O_x$ phase, whereas the literature studies indicate a tie-line between $BaCuO_{2+x}$ and BaY_2CuO_5 [34,35]. Fig. 5 shows an X-ray powder pattern of a composition within the three-phase region $BaCuO_{2+x}$—2:1:3—4:1:3. The presence of these three phases and the absence of the green phase (1:2:1) in this X-ray pattern clearly indicate their phase compatibility (Figs. 1 and 2), and rule against a tie-line between $BaCuO_2$ and BaY_2CuO_5. The formation of the tie-line between 2:1:3 and 4:1:3 was also reported in our previous investigation of the melting equilibria of the BaO–Y_2O_3–CuO system [47]. The majority of literature studies were not conducted entirely under atmospherically controlled conditions, and it is clear that the presence of CO_2 affects the tie-line relationships. For applications of phase equilibria to coated-conductor processing, phase diagrams constructed

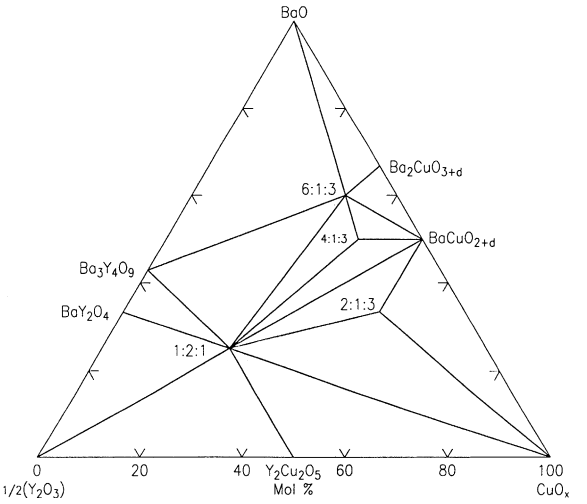

Fig. 4. Subsolidus phase diagram of the BaO–(1/2)Y_2O_3–CuO_x system reported by Osamura and Zhang [34], and Abbattista et al. [35] showing tie-line between $BaCuO_2$ and the 'green phase' BaY_2CuO_5. Symbols are shown in Fig. 2.

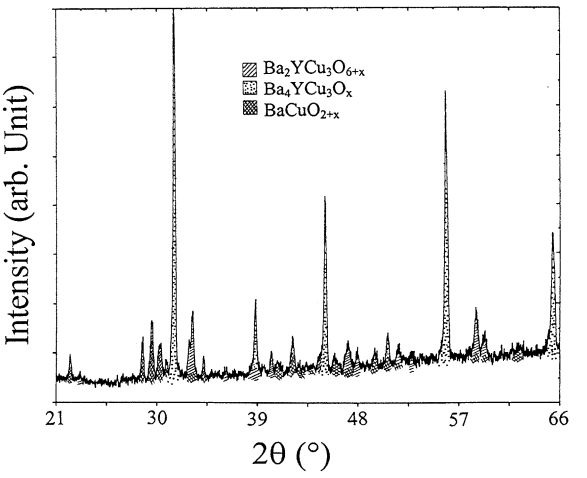

Fig. 5. X-ray diffraction pattern of the composition (Ba:Y:Cu = 45:10:45) showing the presence of three phases: $Ba_2YCu_3O_{6+x}$, $BaCuO_{2+x}$ and $Ba_4YCu_3O_x$.

under carbonate-free conditions should be employed.

4. Summary

We have investigated the phase relationships of the $BaO–Y_2O_3–CuO_x$ system at $p_{O_2} = 21$ kPa (875–900 °C) and at $p_{O_2} = 100$ Pa (800–810 °C). The latter condition was selected to match the deposition conditions prevailing during coated-conductor deposition. While the phases formed agree with those reported by Osamura and Zhang [34], and by Abbittista et al. [35]; the tie-line relationships among the four phases, BaY_2CuO_5, $Ba_2YCu_3O_x$, $BaCuO_{2+x}$ and $Ba_4YCu_3O_x$ are different. The presence of CO_2 appears to affect the tie-line relationships. The phase relationships of these systems at $p_{O_2} = 21$ kPa and at $p_{O_2} = 100$ Pa mainly differ in the four-phase region delineated by BaY_2CuO_5, $Ba_6YCu_3O_x$, $Ba_3Y_4O_9$ and $Ba_4YCu_3O_x$.

Since phase diagrams of the $BaO–R_2O_3–CuO_x$ (R = lanthanides) systems are important for future coated-conductor development, systematic studies of these diagrams under various atmospheric conditions are planned. A comparison of these diagrams with that of the Y-system will be carried out.

Acknowledgements

The US Department of Energy is provided partial financial support of this project. Mr. N. Swanson is thanked for his assistance with the phase diagram graphics.

References

[1] J.O. Willis, R.D. Ray II, T.G. Holesinger, R. Zhou, K.V. Salazar, J.Y. Coulter, J.J. Gingert, D.S. Phillips, D.E. Peterson, Proceedings of the Seventh US/Japan Workshop on High Temperature Superconductors, Tsukuba, Japan, 22–24 October, 1995.

[2] U. Balachandran, Impact of recent advances in synthesis and processing of ceramic superconductors, in: W. Wong-Ng, U. Balachandran, A.S. Bhalla (Eds.), Ceramic Transactions 84, American Ceramic Society, Westerville, OH, 1998, p. 157.

[3] U. Balachandran, A.N. Iyer, P. Haldar, J.G. Hoehn Jr., L.R. Motowidlo, in: K. Kristen, C. Burnham (Eds.), Proceedings of the Fourth International Conference and Exhibition: World Congress on Superconductivity, Orlando, FL, vol. II, June 27–July 1 1994, pp. 639–649.

[4] D.Y. Kaufman, M.T. Lanagan, S.E. Dorris, J.T. Dawley, I.D. Bloom, M.C. Hash, N. Chen, M.R. DeGuire, R.B. Poeppel, Appl. Supercond. 1 (1/2) (1993) 81.

[5] K. Sato, T. Hikata, H. Mukai, M. Ueyama, N. shibata, T. Kato, T. Masuda, M. Nagata, K. Iwata, T. Mitsui, IEEE Trans. Mag. 27 (1991) 1231.

[6] A. Goyal, D.P. Norton, J.D. Budal, M. Paranthama, E.D. Specht, D.M. Kroeger, D.K. Christen, Q. He, B. Saffian, F.A. List, D.F. Lee, P.M. Martin, C.E. Klabunde, E. Hartfield, V.K. Sikka, Appl. Phys. Lett. 69 (12) (1996) 1795.

[7] M. Paranthaman, C. Park, X. Cui, A. Goyal, D.F. Lee, P.M. Martin, T.G. Chirayil, D.T. Verebelyi, D.P. Norton, D.K. Christen, D.M. Kroeger, J. Mater. Res. 15 (12) (2000) 2647.

[8] Q. He, D.K. Christen, J.D. Budai, E.D. Specht, D.E. Lee, A. Goyal, D.P. Norton, M. Paranthaman, F.A. List, D.M. Kroeger, Physica C 275 (1997) 155.

[9] R.P. Reade, P. Berdahl, R.E. Russo, S.M. Garrison, Appl. Phys. Lett. 61 (18) (1992) 2231.

[10] S.R. Foltyn, P. Tiwari, R.C. Dye, M.Q. Le, X.D. Wu, Appl. Phys. Lett. 63 (13) (1993) 1849.

[11] M.K. Wu, L.R. Ashburn, C.J. Torng, P.H. Hov, L.R. Meng, L. Gao, Z.J. Huang, Y. Wang, C.W. Chu, Phys. Rev. Lett. B 58 (1987) 908.

[12] R.J. Cava, B. Batlogg, R.B. van Dover, D.W. Murphy, S. Sunshine, T. Siegrist, J.R. Remeika, E.A. Rietman, S. Zahurak, G.P. Espinosa, Phys. Rev. Lett. B 58 (1987) 1676.

[13] W. Reichelt, H. Wilhelm, G. Foersterling, H. Oppermann, Crysta. Res. Technol. 24 (2) (1989) K26.

[14] R.S. Roth, C.J. Rawn, F. Beech, J.D. Whitler, J.O. Anderson, in: M.F. Yan (Ed.), Ceramic Superconductors II, American Ceramic Society, Westerville, OH, 1988, pp. 13–26.

[15] G. Wang, S.N. Song, J.B. Ketterson, T.O. Mason, K.R. Poeppelmeier, J. Am. Ceram. Soc. 70 (7) (1987) C165.

[16] J. Hahn, T.O. Mason, S.J. Hwu, K.R. Poeppelmeier, Chemtronics 2 (3) (1987) 126.

[17] H. Fjellvaag, P. Karen, A. Kjekshus, Acta Chem. Scand. Ser. A 41 (5) (1987) 283.

[18] S.F. Pashin, E.V. Antipov, L.M. Kovba, Yu.Ya. Skolis, Sverkhprovodimost: Fiz. Khim. Tekh. 2 (7) (1989) 102.

[19] J. Przyluski, K. Borowiec, K.K. Kolbrecka, Mater. Sci. Monogr. 60 (1989) 195 (Adv. Solid State Chem.).

[20] K. Borowiec, J. Przyluski, K.K. Kolbrecka, Eur. J. Solid State Inorg. Chem. 27 (1–2) (1990) 333.

[21] I.A. Saltykova, N.N. Baranova, V.P. Barkhatov, I.N. Dubrovina, V.F. Balakirev, Sverkhprovodimost: Fiz. Khim. Tekh. 3 (6) (1990) 1250 (part 2).

[22] W. Zhang, K. Osamura, Z. Metallkd. 82 (5) (1991) 408.

[23] K.W. Schlegel, G. Foersterling, Mater. Sci. Forum, 133–136 Proceedings of the Second European Powder Diffraction Conference, Part 2, 1993, p. 841.
[24] F. Abbattista, M. Vallino, D. Mazza, Mater. Chem. Phys. 21 (1989) 521.
[25] Y. Ikeda, M. Takano, Y. Band, H. Kitaguchi, J. Takada, Y. Miura, A. Osaka, K. Takahashi, Funti oyobi Funmatsu Yakin 34 (10) (1987) 580.
[26] D.M. De Leeuw, C.A.H.A. Mutsaers, C. Langereis, H.C.A. Smoorenburg, P.J. Rommers, Physica C 152 (1988) 39.
[27] K.G. Frase, D.R. Clarke, Adv. Ceram. Mater. 2 (3B) (1987) 295.
[28] K.G. Frase, E.G. Liniger, D.R. Clarke, J. Am. Ceram. Soc. 70 (9) (1987) C204.
[29] M.M. Oleksienko, N.N. Matyushenko, L.F. Verkhorobin, V.V. Derevyanko, V.N. Golovin, S.D. Lavrinenko, in: H.W. Weer (Ed.), Proc. SPIE—Int. Soc. Opt. Eng. No. 948, Plenum Publishing, New York, 1988, pp. 107–112.
[30] W. Zhang, K. Osamura, Physica C 190 (4) (1992) 396.
[31] W. Zhang, K. Osamura, Physica C 185–189 (1991) 501 (part 1).
[32] E.L. Brosha, F.H. Garzon, I.D. Raistrick, P.K. Davis, J. Am. Ceram. Soc. 78 (7) (1995) 1745.
[33] J.P. Lawanier, J.K. Meen, D. Elthon, J. Am. Ceram. Soc. 79 (2) (1996) 533.
[34] K. Osamura, W. Zhang, Z. Metallkd. 84 (1993) 8.
[35] F. Abbattista, M. Vallino, D. Mazza, M. Lucco-Borler, C. Brisi, Mater. Chem. Phys. 20 (2) (1988) 191.
[36] J.J. Ritter, Powd. Diffr. 3 (1) (1988) 30.
[37] W. Wong-Ng, K. Davis, R.S. Roth, J. Am. Ceram. Soc. 71 (2) (1988) C64.
[38] R. Kipka, H.K. Muler-Buschbaum, Z. Naturforsch Teil B 32 (1977) 121.
[39] F. Abbattista, D. Mazza, M. Vallino, Eur. J. Solid State Inorg. Chem. (Suppl.) 28 (1991) 649.
[40] W. Wong-Ng, L.P. Cook, Powd. Diffr. 9 (4) (1994) 280.
[41] R.D. Shannon, Acta Crystallogr. A 32 (1976) 751.
[42] T. Ishiguro, J. Solid State Chem. 49 (1983) 232.
[43] B.U. Koehler, M. Janse, Z. Anorg. Allg. Chem. 543 (1986) 73.
[44] R.M. Hazen, L.W. Finger, R.A. Angel, C.T. Prewitt, N.L. Ross, H.K. Mao, C.G. Hadidiacos, Phys. Rev. B 35 (1987) 7238.
[45] S.F. Watkins, F.R. Fronczek, K.S. Wheelock, R.G. Goodrich, W.O. Hamilton, W.W. Johnson, Acta Cryst. C 44 (1988) 3.
[46] W. Wong-Ng, M.A. Kuchinski, H.F. McMurdie, B. Paretzkin, Powd. Diffr. 4 (1989) 1.
[47] W. Wong-Ng, L.P. Cook, J. Res. Natl. Inst. Stand. Technol. 103 (1998) 379.

Journal of
MATERIALS RESEARCH

Effect of Ag on the primary phase field of the high-T_c (Bi,Pb)-2223 superconductor

W. Wong-Ng and L.P. Cook
Ceramics Division, National Institute of Standards and Technology, Gaithersburg, Maryland 20899

W. Greenwood
University of Maryland, College Park, Maryland 20742

A. Kearsley
Mathematical and Computational Science Division, National Institute of Standards and Technology, Gaithersburg, Maryland 20899

(Received 30 July 1999; accepted 1 December 1999)

The subsolidus equilibria and the primary phase field (crystallization field) of the 110 K high-T_c (Bi,Pb)-2223 ([Bi,Pb]:Sr:Ca:Cu) phase have been determined in the presence of Ag under a 92.5% Ar/7.5% O_2 atmosphere (volume fraction). A total of 29 six-phase volumes that include both the (Bi,Pb)-2223 and Ag phases was observed. These subsolidus volumes are similar to those observed without the presence of Ag. The compositional range of initial melts of these volumes (mole fraction basis) covers $BiO_{1.5}$ from 5.6% to 25.3%, PbO from 0.4% to 13.8%, SrO from 8.4% to 31.9%, CaO from 12.2% to 33.3%, CuO from 21.7% to 40.9%, and $AgO_{0.5}$ from 1.2% to 6.3%. Based on these data, the primary crystallization field for the (Bi,Pb)-2223 phase in the presence of Ag was constructed using the convex hull technique. A section through this "volume" was portrayed by holding the $AgO_{0.5}$, SrO, and CaO components at the median value of the 29 compositions while allowing projection on the other three axes ($BiO_{1.5}$, PbO, and CuO). The net effect of Ag on the melt composition is a reduction in the PbO concentration and an increase in the SrO content. Applications of the liquidus data are also discussed.

I. INTRODUCTION

In recent years, extensive research and development efforts have been focused on the commercial applications of the 80 K high-T_c superconductor 2212 phase in the Bi–Sr–Ca–Cu–O system, and on the 110 K high-T_c superconductor (Bi,Pb)-2223 phase in the (Bi,Pb)–Sr–Ca–Cu–O (BSCCO) system. These applications include transmission cables, motors, generators, transformers, magnets, fault current limiters, and energy storage systems. One of the obstacles that prevents large-scale commercial application of these high-T_c products is the cost of production. In order to realize the full commercial potential, the performance of the superconductor components, which is closely related to cost, must be optimized. The BSCCO high-T_c components are largely prepared in wire or tape form using powder-in-tube (PIT),[1–3] or the powder/wire-in-tube (PWIT)[4] methods. The PIT technique involves a multistep process of filling silver tubing with high-T_c superconductor BSCCO powder, followed by repeated packing, cold drawing, rolling, and thermal processing. The PWIT tapes are developed by packing both powder and wires into a silver tube. Grain alignment in both methods is frequently achieved because of the presence of liquid. The resulting products often show significantly improved superconducting properties as a result of this melting/alignment phenomenon.[5–11] Therefore, melting information is important for industrial tape and wire application of the BSCCO system high-T_c superconductors.

A primary objective of the National Institute of Standards and Technology (NIST) phase-equilibrium program on the high-T_c superconductors is the determination of the portions of the phase diagrams of the BSCCO system that are relevant to the melt equilibria of the Pb-free 2212 and (Bi,Pb)-2223 phases. Previously the subsolidus phase relationships and primary phase fields of the 2212[12] and the (Bi,Pb)-2223[13,14] phases, and phase equilibria of various PbO-containing subsystems such as that of PbO–SrO–CaO,[15] PbO–CaO–CuO,[16] and Bi_2O_3–PbO–CuO[17] have been determined. Since Ag tubing is employed during PIT processing, and Ag is also being used with (Bi,Pb)-2223 to form composites, the effect of Ag on phase equilibria of the BSCCO system must be considered. The goal of the present study is to determine the effect of Ag on the primary phase field of (Bi,Pb)-2223 with regard to the melting temperatures and oxide composition of melts.

A. Primary phase field

1. General description and approach

A primary phase is the first crystalline phase to appear on cooling a composition from the liquid state; or conversely, the last crystalline phase to disappear on heating a composition to melting. A primary phase field is the locus of all compositions in a phase diagram having a common primary phase. The primary phase field of a binary phase is a line; for a ternary phase, it is a surface, and for a quarternary phase, it can be described as a volume. Therefore in the four-component Pb-free BSCCO system, the primary phase field of the 2212 phase is a volume.[12] For the Pb-doped (Bi,Pb)-2223 phase and (Bi,Pb)-2223 phase with the presence of Ag, the primary phase fields are described as hypervolumes in five- and six-component systems, respectively.[13,14]

The basic procedure for obtaining the primary phase field of a given phase "A" in an "n" component system is summarized in the following steps: (i) Identify all compounds in subsolidus equilibrium with A, (ii) determine all n-phase compatibility regions which involve phase A and determine which n-phase compatibility regions are stable up to the solidus, (iii) obtain solidus temperatures by differential thermal analysis (DTA) for each n-phase compatibility region, (iv) sample and analyze the composition of the first liquid formed upon heating each stable n-phase assemblage to the solidus, and (v) construct an outline of the primary phase field using compositions of the first liquids to appear.

2. Primary phase field of (Bi,Pb)-2223 without Ag

Because of the importance of the (Bi,Pb)-2223 phase in the high-T_c industry, a relatively extensive amount of research has been conducted. A brief review of literature data and the primary phase field of the (Bi,Pb)-2223 phase without the presence of Ag was reported recently.[14] (Bi,Pb)-2223 was found to be in equilibrium with 11 phases, including (Ca,Sr)O, CuO, 0*x*21($Ca_{2-x}Sr_xCuO_3$), 2201 [$(Bi,Pb)_2Sr_{2-x}Ca_xCuO_z$], 11 9 *x* 5 [$(Bi,Pb)_{2.2}Sr_{1.8-x}Ca_xCuO_z$], 1*x*20 [$(Ca,Sr)_2PbO_4$], 0 14 *x* 24 ($Sr_{14-x}Ca_xCu_{24}O_{41}$), 2310 [$Bi_2(Sr,Ca)_4O_z$], 0*x*11 [$(Ca_{1-x}Sr_x)CuO_2$, Ca rich], 3221 [$(Pb, Bi)_3Sr_2Ca_2CuO_x$] 0*x*11′ [$(Ca_{1-x}Sr_x)CuO_2$, Ca poor)].

In these symbols, *x* is used to represent the amount of mutual substitution of the Ca and Sr sites.

At 810 to 820 °C in a volume fraction of 7.5% O_2 (92.5% Ar) 29 five-phase volumes that involve the (Bi,Pb)-2223 phase were found to be mutually stable in a topologically consistent manner.[14] Among them, a total of 16 volumes consist of 2223-2212 as a pair. The 1*x*20 phase was also found to have a wide stability region, and occurred in 15 volumes. Consequently, this phase is often found to be an impurity phase, along with the 2212, during the preparation of 2223.

The range of melt compositions observed for these volumes (mole-fraction basis) was 7.3–28.0% $BiO_{1.5}$, 1.2–19.4% PbO, 11.3–27.8% SrO, 9.8–30.8% CaO, and 17.1–47.0% CuO. These 29 initial melt compositions of the five-phase volumes were used to construct the (Bi,Pb)-2223 primary phase field by employing the convex hull technique.[18] The result is a well-formed closed volume in five-dimensional space. Using the isopleth projection method, a section made by holding the SrO and CaO values constant at the median values for the 29 data points is shown in Fig. 1.

B. Effect of Ag on processing of (Bi,Pb)-2223

There have been numerous literature reports concerning the processing of high-T_c phases with Ag. In addition to employing Ag as the sheath material of the PIT tubing, the use of silver as an additive is also widespread in BSCCO tape and wire processing. Various benefits and the effect of Ag on microstructure and superconducting properties in Ag/Bi-based tapes are summarized in Refs.[19–38] The beneficial effects of silver doping include the following: improved densification due to the presence of low temperature liquid;[20] improved grain morphology by elimination of necking, cracking, and sausaging;[21,27] better grain-to-grain connectivity and intergranular critical current;[21] better flux pinning;[22] enhanced texturing;[23–25] accelerated phase formation;[26] and improved mechanical properties (strength, flexibility, and fracture toughness).[19,31] The increased wettability and quantity of melt offer significant advantages for processing of BSSCO/Ag composite tapes in that the liquid may heal mechanical damage incurred during the deformation process.

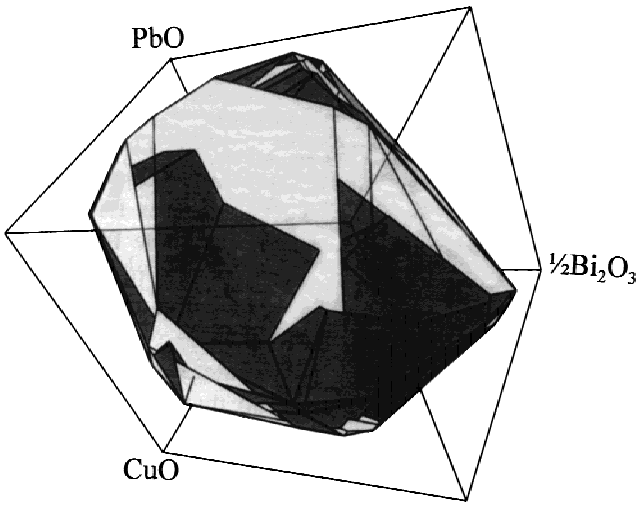

FIG. 1. An isoplethal section through the (Bi,Pb)-2223 primary phase field[14] made by holding the SrO and CaO values constant at the median values for the 29 data points (mole fraction of SrO and CaO = 21.3% and 18.8%, respectively). The (Bi,Pb)-2223 primary phase field forms a closed volume in five-dimensional space.

The influence of silver is especially important at the silver–superconductor interface. There is evidence for preferential formation of the (Bi,Pb)-2223 phase at the Ag interface in Ag-sheathed tapes, and the thin superconducting layer region next to the silver sheath has been shown to carry most of the supercurrent in the tape.[28–30]

C. Previous studies of BSCCO/Ag phase equilibria

The effect of Ag on equilibria of the 2212 and 2223 phases has been investigated extensively.[38–49] For example, MacManus-Driscoll and Brevman[39] found Ag to be present in the melts of the Bi-2212 and (Bi,Pb)-2223 phases. Majewski *et al.*[40,41] found that the temperature of the complete melting of 2212 decreased significantly from about 895 to 865 °C when Ag was added up to mole fraction of about 40% (mass fraction <10% of Ag). Wong-Ng *et al.*[12] found that Ag enters into all liquids in equilibrium with the 2212 phase at a mole fraction level of 2% to 8%. Also, small amounts of Cu, Bi, and Pb were found to alloy in the Ag, which may have a significant effect on processing.

Liquid and solid solubility of Ag in 2212 and its melts was studied by McCallum *et al.*[42] They found that solid solubility of Ag in 2212 was less than detection limits, but that Ag depressed the melting temperature of mixtures with the 2212 phase by 15 to 30 °C, through formation of a eutectic. They also found liquid immiscibility between oxide and Ag liquid at all temperatures. Two eutectics were found. For the Ag-rich side, the eutectic occurs at an atomic fraction of about 98%. For the oxide-rich side the eutectic occurs at about 860 °C, with about 4% Ag in the liquid.

Partial phase diagrams of the systems PbO–Ag, CuO–Ag, and PbO–CuO–Ag have been presented by Shao *et al.*,[43] Hu *et al.*,[44] and Liu *et al.*[45] The authors showed that reactions between CuO and Ag produced immiscible liquids: CuO + Ag → L2 (932 °C) and CuO + L2 → L1 (964 °C). It was also shown that the Ag melting point decreased in the presence of CuO. In the PbO–Ag system, a peritectic reaction takes place at 950 °C, where solid Ag and two immiscible liquid phases L1 and L2 coexist in the composition range with mole fraction of Ag from 11.65% to 95.70%. The eutectic reaction corresponds to CuO + PbO + Ag → L, with a melt composition of 12.04% Ag and 16.35% CuO.

Osamura and Maruyama[46] investigated phase relationships in Ag/2223 tapes and found that the 2223 phase formed only between 830 and 870 °C. They also constructed projections of the phase equilibria on isothermal quasiternary Bi_2O_3–(SrO + CaO)–CuO sections. Electromotive force measurements by Tetenbaum *et al.*[47] showed that (Bi,Pb)-2223 in a silver sheath is stable at 815 °C for oxygen partial pressures between 2.03×10^3 Pa and 13.2×10^3 Pa. Moon *et al.*[48] studied the thermal instability of (Bi,Pb)-2223 in contact with Ag at 830 to 905 °C under flowing air and also under 5 vol% O_2. They found that upon annealing at conditions under which the (Bi,Pb)-2223 phase was stable, the Ag/(Bi,Pb)-2223 interface was unstable and formed several decomposition phases. When annealed at the incongruent melting of 2223, Ag dissolved into and diffused through the liquid, influencing the (Bi,Pb)-2223 decomposition. Specimens annealed on silver at 885 to 905 °C in air or 865 to 905 °C under 5 vol% O_2 showed an incongruent melting reaction summarized as (Bi,Pb)-2223 → $(Ca,Sr)_2CuO_3$ + $(Ca,Sr)CuO_2$ + L.

Thermodynamic optimization of the Ag–Bi–Sr–Ca–Cu–O system using the calculated phase-diagram (CALPHAD) method has been reported by Assal.[49] Studies were performed on the Ag–O, Ag–Bi–O, Ag–Cu–O, Ag–Sr–Cu–O, Ag–Ca–Cu–O, and Ag–Bi–Sr–Ca–Cu–O systems.

II. EXPERIMENTAL METHODS

A. Sample preparation

The samples studied in the BSCCO system were prepared by the solid-state calcining technique. Table I shows the symbols and compositions of compounds prepared and used. To study the effect of Ag on both subsolidus and melting equilibria of (Bi,Pb)-2223, the first step was to find out the subsolidus relationships of Ag with phases that are likely to be in equilibrium with 2223, and for this samples were prepared as indicated in Table II. The next step was to determine the equilibria of a series of three-phase mixtures involving Ag, 2223, and a third component, with samples prepared as indicated in Table III. All silver-containing samples were prepared with about 30 wt% Ag.

In order to determine subsolidus relationships in the presence of Ag, Ag was mixed in with each of the 29 five-phase assemblages determined for the Ag-free system. Over a period of 4 days, repeated pelletizations and calcinings with intermediate grindings took place under 7.5 vol% O_2 at about 810 °C. The choice of temperature range for calcining was based on the report by Carter *et al.*[50] that the thermal stability of the (Bi,Pb)-2223 phase contained within an Ag sheath, and at $p_{O2} = 7.60 \times 10^3$ Pa, extended over the range of ≈805 to 835 °C, and that it decomposed to 2212, CuO, and Ca_2PbO_4 at 800 °C.[51] All samples were characterized by powder x-ray diffraction in order to confirm that the six-phase compatibilities persisted at that specific temperature.

B. Melt characterization

For the melting characterization, we have adopted the procedure which we devised previously for the study of the Ba–Y–Cu–O system. The details of this procedure

have been documented elsewhere.[52–54] The various steps can be summarized as follows: (i) Differential thermal analysis/thermal gravimetric analysis (DTA/TGA) is used to obtain indication of thermal events; (ii) samples are annealed in 7.5 vol% O_2 using MgO crucibles, and quenched in liquid-nitrogen-cooled helium for further characterization; (iii) solid residual phases and selected wick materials [see step (v)] are characterized by x-ray powder diffraction to identify the crystallized phases present; (iv) scanning electron microscopy (SEM) and x-ray mapping are used to study the microstructure of the quenched materials; and (v) sampling of liquid is performed by using a porous MgO wick added to the quench experiments for quantitative compositional analysis by energy-dispersive x-ray spectrometry (EDS).[55,56] The standards used for microanalysis were $Bi_2Sr_{1.5}Ca_{1.5}Cu_2O_z$, (Pb,Zr)$TiO_3$, and metallic Ag. Analytical uncertainties (one standard deviation) are estimated at <10% relative. Uncertainties in DTA temperatures quoted in this paper are estimated at less than ±7 °C (one standard deviation).

TABLE I. Symbols and compositions of compounds used in this study.

Symbol	([Bi,Pb]:Sr:Ca:Cu)	Representative compositions
2223	(2:2:2:3)	$(Bi_{1.8}Pb_{0.4})Sr_2Ca_{2.2}Cu_3O_z$
2212	(2:2:1:2)	$(Bi_{1.9}Pb_{0.1})Sr_{1.5}Ca_{1.5}Cu_2O_z$
014*x*24	(0:14:*x*:24)	$Sr_7Ca_7Cu_{24}O_{41}$
0*x*21	(0:*x*:2:1)	$(Ca_{1.9}Sr_{0.1})CuO_3$
3221	(3:2:2:1)	$Bi_{0.5}Pb_3Sr_2Ca_2CuO_z$
2310	(2:3:1:0)	$Bi_{27.82}Pb_{6.18}Sr_{49.5}Ca_{16.5}O_z$
2201	(2:2:0:1)	$Bi_{1.64}Pb_{0.36}Sr_2CuO_z$
119*x*5	(11:9:*x*:5)	$Bi_{1.8}Pb_{0.4}Sr_{1.6}Ca_{0.2}CuO_z$
0*x*11	(0:*x*:1:1)	$(Ca_{0.86}Sr_{0.14})CuO_2$
0*x*11′	(0:*x*:1:1′)	$(Ca_{0.5}Sr_{0.5})CuO_2$
4805	(4:8:0:5)	$Bi_{3.4}Pb_{0.72}Sr_8Cu_5O_z$
11900	(10:8:0:0)	$Bi_{10}Sr_8O_x$
2110	(14:6:6:0)	$Bi_{14}Sr_6Ca_6O_x$
1*x*20	(1:*x*:2:0)	$(Ca_{1.9}Sr_{0.1})_2PbO_4$
$Bi_2Ca_2O_5$		$Bi_2Ca_2O_5$
$CaBi_2O_4$		$CaBi_2O_4$
$Bi_2Sr_3O_x$		$Bi_2Sr_3O_x$
$SrPbO_3$		$SrPbO_3$
$Bi_{0.8}Sr_{0.1}Ca_{0.1}O_x$		$Bi_{0.8}Sr_{0.1}Ca_{0.1}O_x$
$BiSr_3O_x$		$BiSr_3O_x$
CaO		CaO
CuO		CuO

TABLE II. Two-phase starting compositions and x-ray diffraction results at 805 to 810 °C under 7.5 vol% O_2.

Starting composition	X-ray results
Ag-2223	Ag-2223
Ag-2310	Ag-2310
Ag–CuO	Ag–CuO
Ag-4805	Ag-4805
Ag-0*x*11	Ag-0*x*11
Ag–CaO	Ag–CaO
Ag-119*x*5	Ag-119*x*5
Ag-0*x*21	Ag-0*x*21
Ag–$SrPbO_3$	Ag–$SrPbO_3$
Ag-2201	Ag-2201-119*x*5
Ag-014*x*24	Ag-014*x*24
Ag-11900	Ag-11900
Ag-2212	Ag-2212
Ag-0*x*11′	Ag-0*x*11′
Ag–$Bi_2Sr_3O_x$	Ag-2310
Ag-1*x*20	Ag-1*x*20
Ag-3221	Ag-3221
Ag–$Bi_2Ca_2O_5$	Ag–$Bi_2Ca_2O_5$
Ag-2110	Melted
Ag–$CaBi_2O_4$	Melted

III. RESULTS AND DISCUSSION

X-ray results (Tables II and III) showed that the presence of Ag does not produce new phases, or alter the subsolidus relationships for two- and three-phase assemblages at about 810 °C. Results of equilibration of Ag with various phases that are likely in equilibrium with (Bi,Pb)-2223, and also in the presence of (Bi-Pb)-2223, indicated only the 11 phases as described earlier in the Ag-free system are in equilibrium with (Bi,Pb)-2223 + Ag, namely: (Ca,Sr)O, CuO, 0*x*21, 11 9 *x* 5/2201, 2110, 0 14 *x* 24, 2310, 1*x*20, 2310, 0*x*11, and 0*x*11′.

The compounds in the Bi–Sr–Ca–Cu–Ag–O system include a large number of complicated series of ternary and quarternary solid solutions. Therefore, a large number of two-phase tie-line bundles, three-phase tie-plane "stacks," and four- and five-phase tie volumes separate the six-phase volumes involving solid solutions. The

TABLE III. Three-phase starting compositions and x-ray diffraction results of samples annealed at 815 °C under 7.5 vol% O_2.

Starting composition	X-ray diffraction results
Ag-2223-2310	Ag-2223-2310
Ag-2223–CuO	Ag-2223–CuO
Ag-2223-4805	Ag-2310-2201-2212
Ag-2223-0*x*11	Ag-2223-0*x*11
Ag-2223–CaO	Ag-2223–CaO
Ag-2223-119*x*5	Ag-2223-119*x*5
Ag-2223-2201	Ag-2223-2212-119*x*5
Ag-2223-0*x*21	Ag-2223-0*x*21-1*x*20
Ag-2223–$SrPbO_3$	Ag-3221-119*x*5
Ag-2223-014*x*24	Ag-2223-119*x*5-014*x*24
Ag-2223–$BiSr_3O_x$	Ag-2310-1*x*20
Ag-2223-11900	Ag-2310-11900
Ag-2223–$(Bi_{1.6}Pb_{.36})Sr_3O_6$	Ag-2310-014*x*24-119*x*5
Ag-2223-2212	Ag-2223-2212
Ag-2223-0*x*11′	Ag-2223-0*x*11′
Ag-2223–$Bi_2Sr_3O_x$	Ag-2223-2310-2212
Ag-2223-4805	Ag-2310-4805
Ag-2223–1*x*20	Ag-2223-1*x*20
Ag-2223-3221	Ag-2223-3221
Ag-2223–$Bi_2Ca_2O_5$	Melted
Ag-2223–$Bi_{0.8}Sr_{0.1}Ca_{0.1}O_x$	Melted
Ag-2223-2110	Melted

2223-phase compatibilities include a number of relatively "flat," or shallow, six-phase equilibrium volumes. For each of the six-phase assemblages, the exact compositions of coexisting solid solutions are thermodynamically defined, and it is not necessary to specify them when discussing phase compatibilities.

A. Six-phase equilibria

The subsolidus relationships of the five-phase volumes that involve 2223 were found to remain the same with the addition of Ag as a sixth phase. As given in Table IV, x-ray results showed that the presence of Ag does not alter the subsolidus relationships in these multiphase assemblages at about 810 °C. There was also no indication that Ag enters into the 2223 phase under subsolidus conditions, in agreement with literature data.[8,23] The 29 equilibrium volumes are shown in Table IV, along with the DTA temperatures associated with the initial melting and the annealing and quenching temperatures at which liquids were sampled by the wicking technique. For comparison, temperature data pertaining to the 29 volumes without Ag are also listed in this table.

B. Effect of Ag on melting equilibria

The presence of Ag was found to depress the melting temperature of each of the 29 five-phase volumes as shown in Table IV. As indicated in Fig. 2, the melting temperatures were found to be depressed in a range of 2 to 25 °C with the addition of Ag. Quite a few volumes have relatively low initial melting temperatures, for example, three volumes have initial melting temperature lower than 820 °C: 2223–2212–0*x*21–1*x*20–CuO (818 °C), 2223–CuO–1*x*20–0*x*11′–014*x*24 (814 °C), and 2223–0*x*11′–3221–1*x*20–0*x*11 (818 °C).

From quantitative EDS measurements, the initial melt compositions of the 29 volumes were obtained, as indicated in Table V. Ag was found to dissolve in the liquid, presumably as $AgO_{0.5}$. The range of melt compositions for these volumes (mole fraction basis) was measured as

TABLE IV. DTA temperature of the 29 five-phase (without Ag) and six-phase (with Ag) volumes that contained (Bi,Pb)-2223 in 7.5 vol% O_2.

		DTA[a]	Quench[b]	DTA[a]	Quench[b]
		T(°C)	T(°C)	T(°C)	T(°C)
ID no.	Five-phase equilibrium	(No Ag)		(with Ag)	
1	2223-2212-1*x*20-119*x*5-2310	827	830	825	830
2	2223-2212-1*x*20-2310-CaO	830	835	825	827
3	2223-2212-0*x*21-1*x*20-CuO	837	840	818	821
4	2223-2212-1*x*20-0*x*11-3221	838	842	825	827
5	2223-2212-1*x*20-CuO-0*x*11	839	842	828	831
6	2223-2212-0*x*21-014*x*24-CuO	840	850	837	840
7	2223-2212-014*x*24-1*x*20-119*x*5	840	845	838	842
8	2223-2212-2310-0*x*11-3221	842	845	840	843
9	2223-2212-119*x*5-0*x*11-CuO	842	846	836	838
10	2223-2212-014*x*24-119*x*5-CuO	845	850	838	842
11	2223-2212-014*x*24-0*x*21-1*x*20	846	851	838	839
12	2223-2212-3221-CaO-1*x*20	848	852	830	834
13	2223-2212-0*x*11-2310-119*x*5	850	853	845	848
14	2223-2212-0*x*11-0*x*11′-CuO	850	855	827	834
15	2223-2212-0*x*11-0*x*11′-2310	853	858	835	840
16	2223-2212-3221-CaO-2310	865	870	840	843
17	2223-1*x*20-CuO-0*x*21-014*x*24	828	831	823	826
18	2223-1*x*20-CaO-0*x*11′-2310	832	835	830	833
19	2223-1*x*20-CaO-0*x*11′-3221	831	833	829	835
20	2223-CuO-1*x*20-0*x*11′-01424	816	818	814	820
21	2223-2310-1*x*20-014*x*24-0*x*11′	832	835	830	836
22	2223-0*x*11′CuO-1*x*20-0*x*11	838	841	827	831
23	2223-0*x*11′-3221-1*x*20-0*x*11	820	823	818	822
24	2223-0*x*11′-CaO-0*x*11-3221	830	833	828	833
25	2223-0*x*11′-CaO-2310-0*x*11[c]	840	845	835	838
26	2223-0*x*11′-2310-0*x*11-119*x*5[c]	848	853	840	844
27	2223-0*x*11′-2310-119*x*5-014*x*24	827	832	824	830
28	2223-0*x*11′-014*x*24-119*x*5-CuO[c]	840	845	835	839
29	2223-2310-3221-CaO-0*x*11[c]	838	840	836	840

[a]Indicates initial melting; combined standard uncertainty <6 °C.
[b]Indicates temperature of melt wicking sampling experiments; combined standard uncertainty <6 °C.
[c]Small amount of 2212 phase is also present in these volumes.

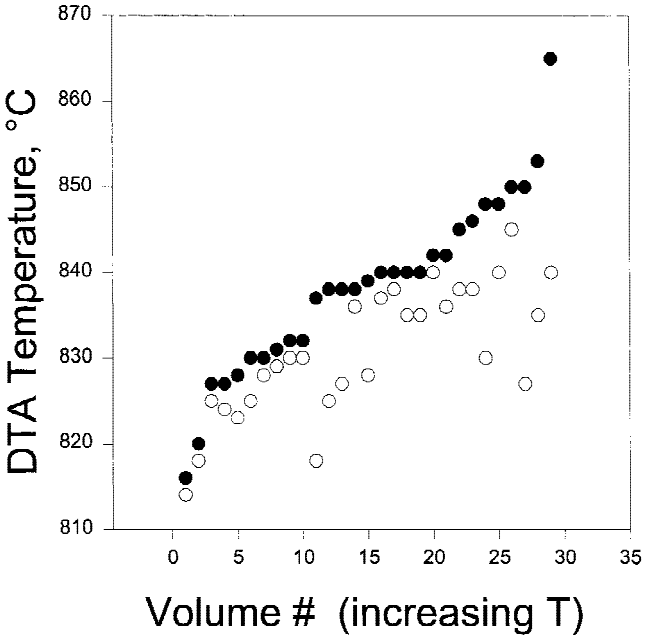

FIG. 2. Initial melting temperatures of the 29 five-phase volumes with and without the presence of Ag under 7.5 vol% O_2. These volumes are arranged in order of increasing temperature. Filled circles are without Ag, open circles are with Ag. A systematic lowering of the melting temperatures due to the presence of Ag is observed.

5.6%–25.3% $BiO_{1.5}$, 0.4%–13.8% PbO, 8.4%–31.9% SrO, 12.2%–33.3% CaO, 21.7%–40.9% CuO, and 1.2%–6.3% $AgO_{0.5}$. As noted, $AgO_{0.5}$ was consistently present in the liquid. Although PbO is present in the liquid of every volume, the concentration of PbO is the least among the five other oxide components, followed by SrO. The concentration of the CuO component was the highest. The PbO mole fraction varied from 0.4% to 13.8%, with the lower values corresponding to volumes lacking Pb-rich compounds and the higher values corresponding to volumes containing the Pb-rich 3221 phase.

In order to compare the liquid compositions in the five-component (Bi,Pb)–Sr–Ca–Cu–oxide and six-component (Bi,Pb)–Sr–Ca–Cu–Ag–oxide systems, the compositions in the six-component system were renormalized without Ag. The results of comparison of each element are shown in Figs. 3–7. In order to observe possible trends, the volumes are rearranged according to increasing concentration of each particular element. It is seen that in the case of $BiO_{1.5}$, CaO, and CuO, no particular trend was observed, and the data are rather scattered. The range of melt composition is similar in the $BiO_{1.5}$ and CaO cases, with and without Ag.

TABLE V. Liquid compositions (mole fraction basis) of the 29 five- and six-phase volumes which contain (Bi,Pb)-2223 in the systems $\frac{1}{2}Bi_2O_3$–PbO–SrO–CaO–CuO and $\frac{1}{2}Bi_2O_3$–PbO–SrO–CaO–CuO–Ag. Values have a relative standard uncertainty of 10%.

ID	No Ag					With Ag					
no.	$BiO_{1.5}$	PbO	SrO	CaO	CuO	$BiO_{1.5}$	PbO	SrO	CaO	CuO	Ag
1	23.6	7.6	26.3	25.4	17.1	25.3	4.4	17.4	23.5	26.0	3.4
2	23.0	7.3	27.1	23.5	19.1	23.3	7.7	25.9	18.0	22.1	3.0
3	18.5	14.4	16.3	14.2	36.6	20.0	6.4	18.7	25.2	24.2	5.5
4	19.9	14.0	19.9	15.4	30.8	14.7	7.3	22.7	17.3	32.8	5.2
5	15.0	10.0	16.0	12.0	47.0	21.8	12.3	8.4	20.8	34.5	2.2
6	28.0	3.2	17.1	21.6	30.1	12.6	1.4	21.3	31.1	30.9	2.7
7	20.2	6.5	20.8	22.2	30.3	22.1	6.5	24.6	14.1	29.4	3.3
8	13.5	4.1	27.8	26.4	28.2	20.9	6.1	25.8	15.8	27.9	3.5
9	17.2	2.7	19.9	28.7	31.5	22.7	4.5	23.8	12.2	34.2	2.6
10	21.4	2.8	24.0	20.9	30.9	20.8	9.2	20.7	12.9	32.5	3.9
11	17.0	11.0	16.2	17.9	37.9	23.3	3.3	21.8	14.3	34.3	3.0
12	19.3	10.2	23.7	18.4	28.4	24.4	9.4	22.3	12.8	28.1	3.0
13	21.6	4.7	24.5	26.2	23.0	20.9	2.4	25.4	23.1	24.3	3.9
14	21.8	1.2	21.7	18.3	37.0	10.4	1.2	22.1	24.4	36.7	5.2
15	25.3	2.3	22.7	17.3	32.4	15.1	2.1	24.0	19.5	36.6	2.7
16	20.4	7.6	20.9	25.8	25.3	21.7	8.4	23.2	16.8	27.7	2.2
17	10.4	18.2	11.3	20.6	39.5	17.4	11.5	18.1	15.3	35.6	2.1
18	20.8	12.8	23.5	15.4	27.5	12.6	4.4	31.9	27.6	21.6	1.9
19	15.8	16.9	24.1	15.2	28.0	13.4	5.7	29.7	22.8	26.6	1.8
20	13.8	16.9	20.2	15.7	33.4	17.7	8.6	20.1	12.5	35.1	6.0
21	18.8	15.9	23.4	12.0	29.9	7.4	2.4	27.9	28.5	31.2	2.6
22	7.3	16.7	12.6	20.4	43.0	14.0	13.8	16.1	12.9	38.6	4.6
23	16.6	18.7	18.3	14.1	32.3	5.6	1.4	20.0	30.3	40.9	1.8
24	17.0	19.4	15.1	15.3	33.2	10.2	5.7	24.4	25.4	31.5	2.8
25	12.4	1.6	26.5	30.8	28.7	8.9	0.4	23.6	18.1	45.8	3.2
26	27.6	2.1	24.8	13.4	32.1	23.3	3.9	22.5	18.3	29.5	2.5
27	19.9	4.1	23.0	15.8	37.2	15.8	2.3	29.2	22.0	24.4	6.3
28	23.4	1.6	24.1	10.5	40.4	20.0	4.2	22.1	15.0	34.7	4.0
29	15.4	16.9	25.2	9.8	32.7	9.6	3.1	27.0	33.3	25.8	1.2

It should be pointed out that in most volumes the PbO concentration in liquid decreased when Ag was added. On the other hand, the SrO concentration of most of the volumes increased with Ag addition, as indicated in Fig. 5. There appears to be some correlation of PbO and $AgO_{0.5}$ concentration in the liquid. The Shannon ionic radii[57] of Ag^{1+}, Pb^{2+}, and Sr^{2+} are quite similar (Ag^{1+} 1.15 Å, Pb^{2+} 1.19 Å, and Sr^{2+} 1.18 Å). Although the liquid structure could be quite complicated, similar ionic radii appear to suggest that Ag^{1+} could replace Pb^{2+} in the liquid, perhaps with accompanying changes in the oxygen stoichiometry.

C. Primary phase field of (Bi,Pb)-2223 with the presence of Ag

The 29 compositions of the six-phase volumes were modeled using the convex hull technique,[18] a mathematical tool often used in computational geometry. Given a collection of points (or data) the convex hull is the smallest convex set of points that contains all of the given points, or defines the extent of the compositional space. All the 29 points lie either on, or close to, the convex hull. The result indicates a well-formed, closed volume in six-dimensional space. The convex hull is defined by the equation

$$\mathbf{Ax} - \mathbf{b} \leqslant 0 \quad . \tag{1}$$

A is a matrix describing the faces, **b** is a matrix describing the position of the faces relative to the origin in

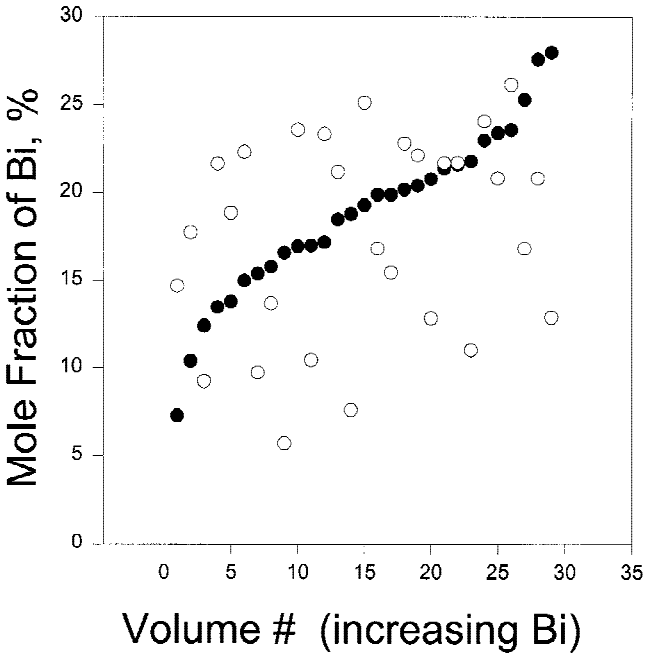

FIG. 3. Concentration of $BiO_{1.5}$ in the initial melt of the 29 six-phase volumes. The order of these volumes is rearranged according to increasing concentration of Bi in the volumes without Ag. Filled circles are without Ag, open circles are with Ag. The addition of Ag has no systematic effect on $BiO_{1.5}$.

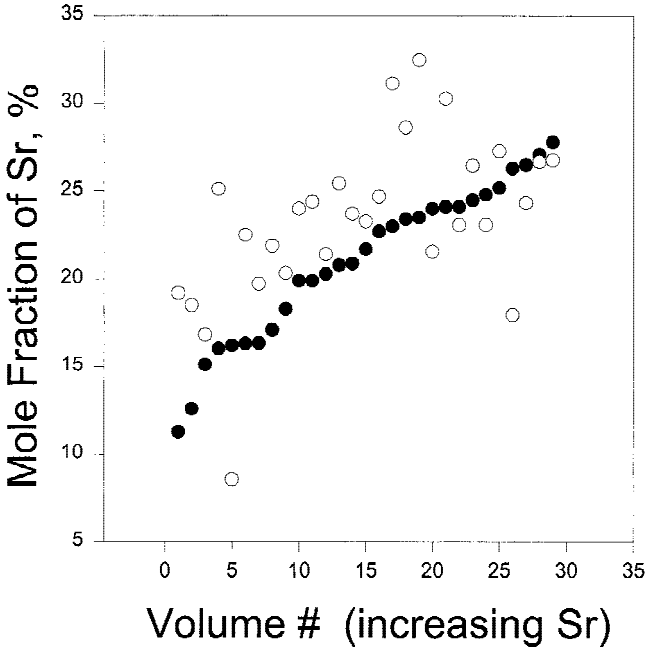

FIG. 4. Concentration of SrO in the initial melt of the 29 six-phase volumes. The order of these volumes is rearranged according to increasing concentration of SrO in the volumes without Ag. Filled circles are without Ag, open circles are with Ag. SrO concentrations for most of the volumes increased with Ag addition.

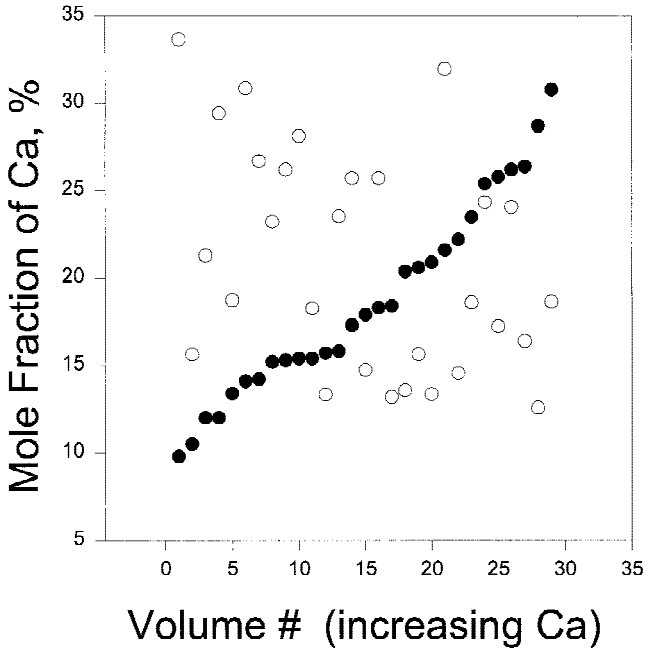

FIG. 5. Concentration of CaO in the initial melt of the 29 six-phase volumes. The order of these volumes is rearranged according to increasing concentration of Ca in the volumes without Ag. Filled circles are without Ag, open circles are with Ag. The addition of Ag has no systematic effect on CaO.

six-component space, and **x** is a vector referring to the coordinates of any given point. The values of **A** and **b** are determined using a "sweeping algorithm." Using this algorithm a convex hull is created by finding first the triangle connecting three of the points, then one point is added at a time until all 29 points are considered. During addition of each point, the values of **A** and of **b** in the equation above are changed correspondingly. At the completion of the mathematical manipulation, the matrix **A** has a dimension of $k \times 6$, where k is the number of faces in the convex hull. The matrix **b** has the length of k. In the present model, k has a value of 547.

To graphically represent the primary phase field of this multidimensional volume, and to give a general sense of the "shape," the isopleth projection method, which uses a section of constant composition through the phase space, was employed. Figure 8 shows an isoplethal section made by holding the $AgO_{0.5}$, SrO, and CaO values constant at the median values for the 29 data points, with the remaining oxides shown on the three cartesian axes represented by PbO, $BiO_{1.5}$, and CuO. The median value was determined to be (mole fraction basis) 17.11% $BiO_{1.5}$, 5.53% PbO, 22.77% SrO, 20.13% CaO, 31.15% CuO, and 3.30% $AgO_{0.5}$. A comparison of this shape with that of the five-component system without Ag (Fig. 1) shows that it is much more flattened in the direction of PbO, indicating a lesser amount of Pb in the liquid.

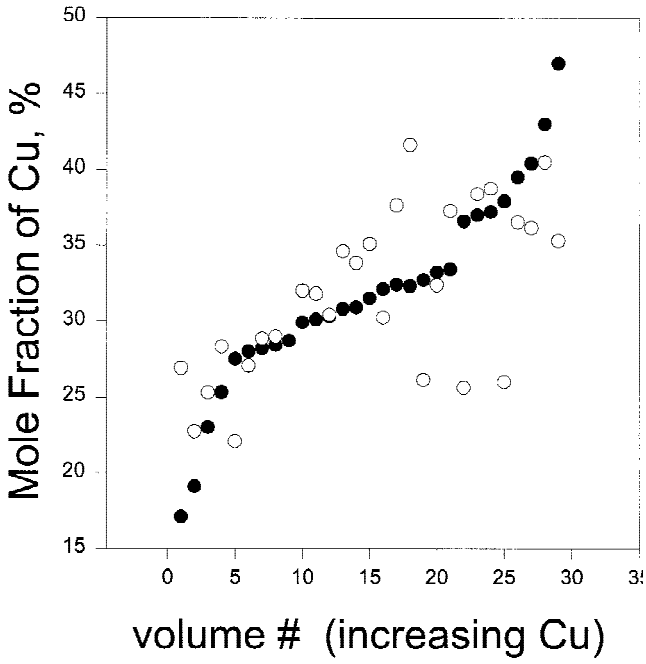

FIG. 6. Concentration of CuO in the initial melt of the 29 six-phase volumes. The order of these volumes is rearranged according to increasing concentration of CuO in the volumes without Ag. Filled circles are without Ag, open circles are with Ag. The addition of Ag has no systematic effect on CuO.

D. Applications of Ag–liquid data to processing

The primary phase field provides a compositional region which can be used as a guide for crystal growth and for melt processing. Similar application of the 2212 pri-

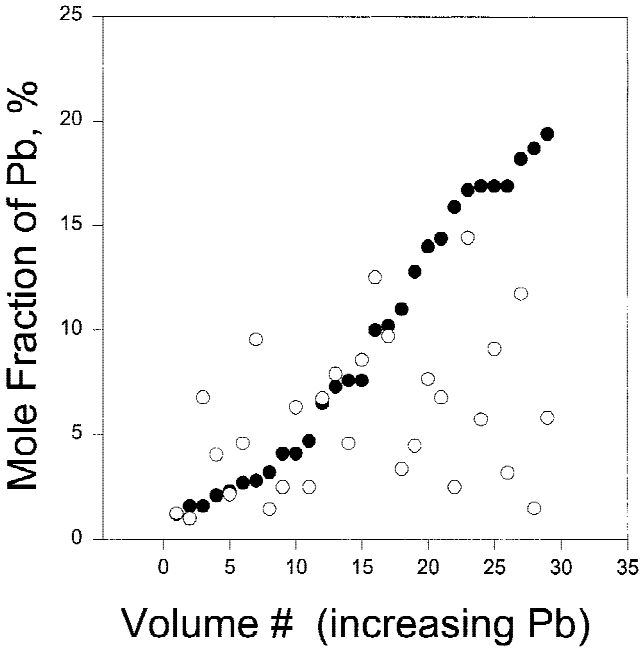

FIG. 7. Concentration of PbO in the initial melt of the 29 six-phase volumes. The order of these volumes is rearranged according to increasing concentration of PbO in the volumes without Ag. Filled circles are without Ag, open circles are with Ag. It was observed that the PbO concentration in most volumes decreased when Ag was added.

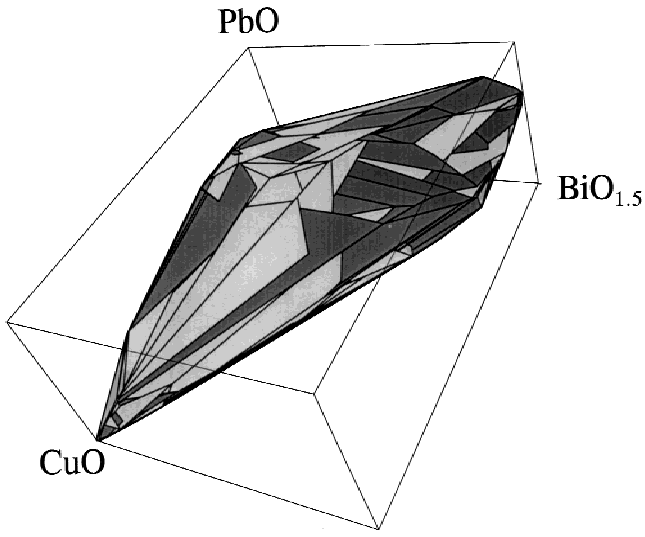

FIG. 8. The primary phase field of the Pb-2223 phase with the presence of Ag. An isoplethal section made by holding the SrO, CaO, and Ag values constant at the median values for the 29 data points (mole fraction of SrO, CaO, and $AgO_{0.5}$ = 22.8%, 20.1%, and 3.3%, respectively). While maintaining the same orientation as that in Fig. 1, this diagram is flattened in the PbO direction, indicating less Pb in the liquid.

mary phase field has been reported.[58] When starting with a composition prepared within the Pb-free 2212 primary phase field, even with a crystallization scheme using a relatively rapid cooling rate (½ degree/min), we were able to obtain a sample with microstructure dominated by relatively large 2212 crystals. On the other hand, a composition that was prepared outside this field gave a microstructure with large calcium cuprate crystals, and much less of the 2212 phase. Applying the same principle during processing of the 2223 phase, compositions falling outside the primary phase field should be avoided, as they would be expected to produce large primary crystals of unwanted phases.

Equation (1) can be used to determine if a given composition lies inside or outside the Pb-2223 primary phase field. If all components of the difference matrix between the two matrices [**Ax** − **b**] are negative, then the particular composition is within the volume. If all components are 0 then the composition is on the surface, and if any component is positive, the composition is outside. Table VI shows an example of two compositions illustrating where the composition occurs relative to the primary phase field. Composition I was found to lie inside the volume because, using the matrix manipulation, all components of **Ax** − **b** were found to be negative. Composition II was found outside the volume because 112 out of 579 components are positive.

Since the presence of liquid is important for texturing, using the data associated with the 29 six-phase volumes, one can design compositions for processing. Each of these 29 volumes gives an initial melting temperature and initial melt composition which is quite different from the others. For example, some have high Pb contents, which could produce melts with different surface tensions and viscosities than the rest, perhaps beneficial for the production of textured superconductors.

Advances in computer technology provide an effective means of data dissemination and a vehicle for interactive calculations. In order to facilitate the use of primary phase field data for the BSCCO superconductors, we are developing a World Wide Web page. Users will be able to determine whether a trial composition is within a given primary phase field.

IV. SUMMARY

We have illustrated the general procedure used to obtain the primary phase field of a multicomponent system. The subsolidus phase equilibria and initial liquid melt compositions of a complete set of 29 six-component (Bi,Pb)-2223 volumes in the presence of Ag were obtained. These volumes are consistent with each other. Ag was found to occur in the liquid phases and to lower the melting temperatures of the 29 equilibrium volumes from 2 to 25 °C. The range of melt compositions for the 29 volumes expressed in mole fraction is 5.6–25.3% $BiO_{1.5}$, 0.4–13.8% PbO; 8.4–31.9% SrO; 12.2–33.3% CaO, 21.7–40.9% CuO, and 1.2–6.3% $AgO_{0.5}$. Although only a relatively small amount of Ag dissolved in the liquid, between 1% and 6%, its presence affects the concentration of other components in liquid, especially Pb and Sr.

TABLE VI. Compositions (mole fraction) used to illustrate the use of the primary phase field O (Bi,Pb)-2223 + Ag.

	Bi	Pb	Sr	Ca	Cu	Ag
I.	17.41	5.69	22.75	20.21	30.63	3.31
II.	30.00	10.00	10.00	20.00	25.00	5.00

The six-component primary phase field was constructed using the liquid compositions of the initial melts of the 29 six-phase volumes. This field represents compositional regions where liquids can be found in equilibrium with 2223. A comparison of the isoplethal section obtained by holding the SrO, CaO, and $AgO_{0.5}$ concentration at the median of the 29 volumes with that of the five-component system without Ag showed that it is much more flattened in the direction of PbO, indicating reduced concentrations of PbO in the liquid.

The depression of the melting points of all 29 volumes resulting from entry of silver into the liquid allows melt processing at lower temperatures compared to systems without Ag. Conversely, processing at a lower temperature is required in the presence of Ag if only solid-state reactions are desired during a certain processing step. Since Ag dissolves in the liquid to a small extent, there may be a thinning effect on the wall of the Ag tubing. In order for the Ag tubing to maintain stability, one approach would be to presaturate the bulk composition with the required amount of Ag.

REFERENCES

1. D.Y. Kaufman, M.T. Lanagan, S.E. Dorris, J.T. Dawley, I.D. Bloom, M.C. Hash, N. Chen, M.R. DeGuire, and R.B. Poeppel, Appl. Supercond. **1,** 81 (1993).
2. U. Balachandran, A.N. Iyer, P. Haldar, J.G. Hoehn, Jr., and L.R. Motowidlo, in *Proceedings of The Fourth International Conference and Exhibition: World Congress on Superconductivity,* Orlando, FL, June 27–July 1, 1994, edited by K. Kristen and C. Burnham, (World Congress on Superconductivity, Houston, TX, 1994), Vol. II, p. 639.
3. K.H. Sandhage, G.N. Riley, Jr., and W. Carter, J. Met. **43,** 21 (1991).
4. R. Zeng, H.K. Liu, and S.X. Dou, Physica C **300,** 49 (1998).
5. T.D. Aksenova, P.V. Bratukhin S.V. Shavkin, V.L. Melnkov, E.V. Antipova, N.E. Khlebova, and A.K. Shikov, Physica C **205,** 271 (1993).
6. J.S. Luo, N. Merchant, V.A. Maroni, S.E. Dorris, M.T. Lanagan, and B.S. Tani, J. Am. Ceram. Soc. **78,** 2785 (1995).
7. W.J. Kim, S.C. Kwon, H.G. Lee, G.W. Hong, and I.H. Kuk, Supercond. Sci. Technol. **11,** 250 (1998).
8. M.T. Mlchevsky, P.L. Yill, and L. Gherardi, Appl. Supercond. **2,** 33 (1994).
9. N. Merchant, J.S. Luo, V.A. Maroni, G.N. Riley, and W.L. Carter, Appl. Phys. Lett. **65,** 1039 (1994).

10. J. Müller, O. Eibl, B. Fischer, and P. Herzog, Supercond. Sci. Technol. **11,** 238 (1998).
11. Y.S. Sung and E.E. Hellstrom, Physica C **255,** 266 (1995).
12. W. Wong-Ng, L.P. Cook, and F. Jiang, J. Am. Ceram. Soc. **81,** 1829 (1998).
13. W. Wong-Ng, L.P. Cook, F. Jiang, W. Greenwood, U. Balachandran, and M. Lanagan, J. Mater. Res. **12,** 2855 (1977).
14. W. Wong-Ng, L.P. Cook, and A. Kearsley, J. Res. Natl. Inst. Stand. Technol. **104,** 277 (1999).
15. W. Wong-Ng, L.P. Cook, and F. Jiang, Physica C **272,** 87 (1996).
16. W. Wong-Ng, L.P. Cook, W. Greenwood, and F. Jiang, Physica C **279,** 31 (1997).
17. W. Wong-Ng, F. Jiang, and L.P. Cook, J. Appl. Supercond. **4,** 385 (1997).
18. C.B. Barber, D.P. Dobkin, and H. Huhdanpaa, ACM Trans. on Mathematical Software **22,** 469 (1996).
19. J. Joo, J.P. Singh, T. Warzynski, A. Grow, and R.B. Poeppel, Applied Supercond. **2,** 401 (1994).
20. M.T. Mlchevsky, P.L. Villa, and L. Gherardi, Appl. Supercond. **2,** 35 (1994).
21. T.E. Jones, W.C. McGinnis, E.W. Jacobs, R.D. Boss, P.M. Thibado, J.S. Briggs, and W.E. Glad, Physica C **201,** 279 (1992).
22. Q.Y. Hu, H.W. Weber, F.M. Sauerzopf, G.W. Schulz, R.M. Schalk, H.W. Neumuller, and S.X. Dou, Appl. Phys. Lett. **65,** 3008 (1994).
23. J.S. Luo, N. Merchant, V.A. Maroni, G.N. Riley, Jr., and W.L. Carter, Appl. Phys. Lett. **63,** 690 (1993).
24. I.S. Oh and K. Mukherjee, Physica C **227,** 197 (1994).
25. N. Merchant, J.S. Luo, V.A. Maroni, G.N. Riley Jr., and W.L. Carter, Appl. Phys. Lett. **65,** 1039 (1994).
26. S.X. Dou, H.K. Liu, Y.C. Guo, R. Bhasale, Q.Y. Hu, E. Babic, and I. Kusevic, Appl. Supercond. **2,** 191 (1994).
27. R. Zhou, W.L. Hults, R.J. Sebring, J.F. Bingert, J.Y. Coulter, J.O. Willis, and J.L. Smith, Physica C **255,** 275 (1995).
28. Y. Feng, Y.E. High, D.C. Larbalestier, Y.S. Sung, and E.E. Hellstrom, Appl. Phys. Lett. **62,** 1553 (1993).
29. Y. Yamada, J.Q. Xu, J. Kessler, E. Seibt, W. Goldacker, W. Jahn, and R. Flukiger, Physica C **185–189,** 2483 (1991).
30. M. Lelovic, P. Krishmaraj, N.G. Eror, and U. Balacjandran, Physica C **242,** 246 (1995).
31. J.P. Singh, J. Joo, N. Vasabthamohan, and R.B. Poeppel, J. Mater. Res. **8,** 2458 (1993).
32. D.C. Larbalestier, X.Y. Cai, Y. Feng, H. Edelman, A. Umezawa, G.N. Riley, Jr., and W.L. Carter, Physica C **221,** 299 (1994).
33. S.X. Dou, Y.C. Guo, R.K. Wang, M. Ionescu, H.K. Liu, E. Babic, and I. Kusevic, IEEE Trans. Appl. Supercond. **5,** 1830 (1995).
34. Y.S. Sung and E.E. Helstrom, Physica C **255,** 266 (1993).
35. J.S. Luo, N. Merchant, V.A. Marni, D.M. Gruen, B.S. Tani, W.L. Carter, G.N. Riley Jr., and K.H. Sandhage, J. Appl. Phys. **72,** 2385 (1992).
36. Y.C. Guo, H.K. Liu, and S.X. Dou, J. Mater. Res. **8,** 2187 (1993).
37. A. Oota, T. Horio, K. Ohba, and K. Iwasaki, J. Appl. Phys. **71,** 5997 (1992).
38. R. Funahashi, I. Matsubara, K. Ueno, and H. Ishikawa, Physica C **311,** 107 (1999).
39. J.I. MacManus-Driscoll and J.C. Bravman, J. Am. Ceram. Soc. **77,** 2305 (1994).
40. P. Majewski, A. Sotelo, H. Szillat, S. Kaesche, and F. Aldinger, Physica C **275,** 47 (1997).
41. P. Majewski, Supercond. Sci. Technol. **10,** 453 (1997).
42. R.W. McCallum, K.W. Dennis, L. Margulies, and M.J. Kramer, in *Proceedings of the 1993 Fall TMS Meetings,* edited by U. Balachandran, E.W. Collings, and A. Goyal (TMS, Warrendale, PA, 1993), p. 195.
43. Z.B. Shao, K.R. Liu, and L.Q. Liu, J. Am. Ceram. Soc. **76,** 2663 (1993).
44. Q.Y. Hu, H.W. Weber, F.M. Sauerzopf, G.W. Schulz, R.M. Schalk, H.W. Neumuller, and S.X. Dou, Appl. Phys. Lett. **65,** 3008 (1994).
45. H.K. Liu, S.X. Dou, M. Ionescu, Z.B. Shao, K.R. Liu, and L.Q. Liu, J. Mater. Res. **10,** 2933 (1995).
46. K. Osamura and T. Maruyama, *Proceedings of the Fifth U.S.-Japan Workshop on High T_c Superconductors,* edited by K. Tachikawa, organized by New Superconducting Materials Forum (The Society of Non-Traditional Technology, Tsukuba, Japan, Nov. 1992), p. 75.
47. M. Tetenbaum, M. Hash, B.S. Tani, J.S. Luo, and V.A. Maroni, Physica C **249,** 396 (1995).
48. R.J. Moon, K.P. Trumble, and K.J. Bowman, J. Mater. Res. **14,** 652 (1999).
49. J. Assal, Doctoral Thesis, Swiss Federal Institute of Technology, Zurich, Switzerland (1998).
50. W.L. Carter, G.N. Riley, J.S. Luo, N. Merchant, and V.A. Maroni, Appl. Supercond. **1,** 1523 (1993).
51. J.S. Luo, N. Merchant, V.A. Maroni, D.M. Gruen, B.S. Tani, W.L. Carter, G.N. Riley, Jr., and K.H. Sandhage, J. Appl. Phys. **72,** 2385 (1992).
52. W. Wong-Ng and L.P. Cook, in *Superconductivity and Ceramic Superconductors II* (Ceramic Trans. **18,** American Ceramic Society, Westerville, OH, 1991), p. 73.
53. W. Wong-Ng and L.P. Cook, Adv. X-ray Anal. **35,** 633 (1992).
54. W. Wong-Ng and L.P. Cook, J. Amer. Ceram. Soc. **77,** 1883 (1994).
55. K.F.J. Heinrich, *Electron Beam X-Ray Microanalysis* (Van Nostrand Reinhold, New York, 1981), p. 578.
56. C.E. Fiori, C.R. Swyt, and R.L. Myklebust, NIST/NIH Desktop Spectrum Analyzer Program and X-Ray Database, NIST Standard Reference Database No. 36 NIST, Gaithersburg, MD, (1991).
57. R.D. Shannon and C.T. Prewitt, Acta Crystallogr. **25,** 925 (1969).
58. L.P. Cook and W. Wong-Ng, in *Impact of Recent Advances in Synthesis and Processing of Ceramic Superconductors,* edited by W. Wong-Ng, U. Balachandran, and A.S. Bhalla (Ceram. Trans. **84,** American Ceramics Society, Westerville, OH, 1998), p. 71.

Volume 104, Number 3, May–June 1999
Journal of Research of the National Institute of Standards and Technology

[J. Res. Natl. Inst. Stand. Technol. **104**, 277 (1999)]

Primary Phase Field of the Pb-*Doped* 2223 *High-T_c Superconductor in the* (Bi, Pb)-Sr-Ca-Cu-O *System*

Volume 104 Number 3 May–June 1999

W. Wong-Ng, L. P. Cook, and A. Kearsley

National Institute of Standards and Technology,
Gaithersburg, MD 20899-0001

and

W. Greenwood

University of Maryland,
College Park, MD 20742

Both liquidus and subsolidus phase equilibrium data are of central importance for applications of high temperature superconductors in the (Bi, Pb)-Sr-Ca-Cu-O system, including material synthesis, melt processing and single crystal growth. The subsolidus equilibria of the 110 K high-T_c Pb-doped 2223 ([Bi, Pb], Sr, Ca, Cu) phase and the location of the primary phase field (crystallization field) have been determined in this study. For the quantitative determination of liquidus data, a wicking technique was developed to capture the melt for quantitative microchemical analysis. A total of 29 five-phase volumes that include the 2223 phase as a component was obtained. The initial melt compositions of these volumes range from a mole fraction of 7.3 % to 28.0 % for Bi, 11.3 % to 27.8 % for Sr, 1.2 % to 19.4 % for Pb, 9.8 % to 30.8 % for Ca, and 17.1 % to 47.0 % for Cu. Based on these data, the crystallization field for the 2223 phase was constructed using the convex hull technique. A section of this "volume" was obtained by holding two components of the composition at the median value, allowing projection on the other three axes to show the extent of the field.

Key words: high-T_c superconductor; Pb-doped 2223; BSCCO; phase equilibria; primary phase field.

Accepted: April 19, 1999

Available online: http://www.nist.gov/jres

1. Introduction

The rapid pace of applied research on the high-T_c superconductors has continued since their initial discovery in the Bi-Sr-Ca-Cu-O (BSCCO) system [1]. To date, many prototype products have been developed, and large scale applications are possible [2]. In the Pb-free BSCCO system, it is well known that it is relatively easy to prepare the 80 K 2212 (Bi:Sr:Ca:Cu) compound in nominal single-phase form. By contrast, the processing window for the Pb-free 2223 phase is narrow, and obtaining a commercially significant amount of single-phase material is difficult. Partial doping of Bi with Pb, on the other hand, can stabilize the phase formation of the Pb-doped 110 K 2223 ([Bi, Pb]:Sr:Ca:Cu) superconductors [5–10]. Therefore, industrial processing of high-T_c superconductor materials has focused primarily on advancing the commercial potential of the Pb-free 2212 and the Pb-doped 2223 superconductors for wire and tape applications. For simplicity, in this paper, we will refer to the Pb-doped phase simply as 2223.

1.1 Powder-in-Tube Processing Technique

In recent years, various fabrication techniques of the BSCCO 2212 and 2223 superconductor wires and tapes were developed [11–14]. Among them, the powder-in-tube (PIT) technique was found to be most viable. This technique involves a multistep process of filling Ag tubing with high-T_c BSCCO powder, followed by repeated packing, cold drawing, rolling, and thermal processing. The presence of a liquid phase enhances the growth and preferred orientation of micaceous superconductor grains, and often leads to grain alignment. Significantly improved superconducting properties as a result of this melting/alignment phenomenon, and of the presence of Ag, were obtained [15–21]. The tapes produced by these methods have demonstrated a capacity to support high critical currents in high magnetic fields [3,22,23]. Therefore, the PIT technique offers a promising route to the industrial-scale fabrication of long-length, high-quality superconducting cables for electric power and high-field magnetic applications. These BSCCO super-

conductors show further improvements in properties with the introduction of artificial pinning centers [24, 25].

1.2 Phase Equilibrium Data

Phase diagrams provide fundamental processing maps, and it is therefore essential to have data on all aspects of the phase relationships in the BSCCO system, including solid-state homogeneity regions, melting equilibria, and the location of the primary phase crystallization fields of the high-T_c phases in the BSCCO system. Information on melting and on the primary phase field is an invaluable guide in the optimization of 2223 ceramics through melt processing, and it also provides a framework for the interpretation of transient and metastable liquids. To date, while melt data are relatively plentiful for the Pb-free 2212 phase [26–28], only limited data are available for the Pb-doped 2223 phase [29–33].

1.2.1. Phase Equilibrium Data

Because of the importance of the 2223 phase in the high-T_c industry, a relatively extensive amount of research has been conducted. These studies included the mechanisms and kinetics of 2223 phase formation [34–48], phase formation in reaction couples [49], the location of the 2223 homogeneity region [50–56], the thermal stability of the Pb-2223 phase as a function of oxygen partial pressure [57–58], and the influence of oxygen partial pressure and reaction time on the formation of the 2223 phase [69–75]. With regard to phase diagram studies, because the Bi-Pb-Sr-Ca-Cu-O system is a five-component oxide system, a complete investigation requires extensive effort. Thus far, many studies have concentrated on small regions pertaining to the Pb-2223 phase [56, 76–86]. For example, Toledano et al. [76] treated 2223 equilibria with reference to the quasi-quaternary $(Bi_{1.8}Pb_{0.4})O_x$–CaO-SrO-CuO system. Strobel et al. [77, 78] studied the phase diagram of the $Bi_{1.6}Pb_{0.4}Sr_2CuO_6$-$CaCuO_2$ system, which includes $Bi_{1.6}Pb_{0.4}SrCa_{n-1}Cu_nO_{2n+4+z}$, at temperatures between 825 °C and 1000 °C. Osamura and Maruyama [79] investigated phase relationships in Ag/2223 tapes and found that the 2223 phase formed only between 830 °C and 870 °C. They constructed projections of the phase equilibria on isothermal quasi-ternary Bi_2O_3-(SrO+CaO)-CuO sections. Kaesche et al. [56, 80] discussed isothermal sections at 850 °C and 865 °C, using CuO (mole fraction fixed at 37 %), SrO, CaO and $(Bi/Pb)_2O_3$ as components. MacManus-Driscoll and Yi [86] reported the phase equilibria near (Bi, Pb)-2223 as a function of oxygen partial pressure. In their study, the phases in equilibirum with 2223 are in general in agreement with Kaesche et al. [56, 80] and Wong-Ng et al. [87] except for the (Ca, Sr) CuO_2 and 119 × 5 phases (In these symbols, x is used to represent the amount of Ca being substituted into the Sr site).

To date, many reported equilibria are expressed, as a convenient way, as projections made by combining Bi and Pb, or Ca and Sr. However, since these elements do not substitute ideally for each other, or to the same extent in all of the compounds that are in equilibrium with the 2223 phase, it is not totally accurate to represent the results in this manner.

Presently, there is still a need for data to complete the subsolidus equilibria and the primary crystallization field of the 2223 phase. The primary objective of the NIST high-T_c phase diagram project is to develop the portions of the phase diagrams that are relevant to the processing of the 2223 compounds. This paper summarizes the determination of a complete set of the five-phase subsolidus equilibrium assemblages that contain the 2223 phase, and the determination of the primary phase field of the 2223 phase. These studies were conducted under a volume fraction of 7.5 % O_2/92.5 % Ar atmosphere.

1.2.2 Previous Work at NIST

1.2.2.1. Phases in Equilibrium With the Pb-2223 Phase

Bernik has studied the influence of starting composition ($Bi_{2+d-x}Pb_xSr_2Ca_2Cu_3O_z$) on the formation of the "pure" 2223 phase. A single phase region for 2223 was mapped on a plot of the mole fraction of Pb versus (Bi+Pb) [88]. In samples with nominal composition of $Bi_{2+d-x}Pb_xSr_2Ca_2Cu_3O_z$ ($d = 0$), 2223 forms when $x \geq 0.2$. The 2223 phase coexists with 2212 in the range $0.2 \leq x \leq 0.4$ after annealing at 855 °C for 100 h. Some $(Ca, Sr)_2CuO_3$ was also found. When $x > 0.4$, 2223 along with $(Pb, Bi)_{1.4}(Sr, Ca)_3Cu_{0.77}O_z$ were found in these samples. The 2223 phase can be formed from starting mole fraction compositions with less than 10 % Bi replaced by Pb, provided (Bi + Pb) > 2. The 2201 phase coexists with 2223 when (Bi + Pb) > 2.3 and Pb > 0.1. As a summary, the single 2223 phase region in samples with composition $Bi_{2+d-x}Pb_xSr_2Ca_2Cu_3O_z$ is proposed as $0.3 < x < 0.45$, $0.05 \leq d \leq 0.35$, $2.05 <$ (Bi, Pb) < 2.35.

In a subsequent separate study, compositions that are in equilibrium with the 2223 phase were determined [87]. From extensive x-ray diffraction results, 11 phases which include binary, ternary, and quaternary oxides were found to be in equilibrium with the 2223 phase at 810 °C to 820 °C (Table 1) [87]. In order to describe phase equilibria of various phases, it is useful to

designate the complicated BSCCO formulas with simplified abbreviations, which are presented in Table 1. These designations are strictly for convenience, and are not meant to precisely convey the stoichiometric formulas. The equilibrium phases were (Ca, Sr)O, CuO, 0x21 ($[Ca, Sr]_2CuO_3$), 119x5 ($[Bi, Pb]_{2.2}Sr_{1.8-x}Ca_xCuO_z$), 014$x$24 ($Sr_{14-x}Ca_xCu_{24}O_{41}$), 2310 ($Bi_2[Sr, Ca]_4)O_z$, 2201 $(Bi, Pb)_2Sr_{2-x}Ca_xCuO_z$, 0$x$11 ($Sr_{1-x}Ca_x)CuO_2$, Ca-rich and Ca-poor), 1x20 ($[Ca, Sr]_2PbO_4$), and 3221 ($[PbBi]_3Sr_2Ca_2CuO_z$).

Table 1. Symbols and compositions of compounds prepared and used in this study

Symbol	([Bi,Pb]:Sr:Ca:Cu)	Representative compositions
2223	(2:2:2:3)	$(Bi_{1.8}Pb_{0.4})Sr_2Ca_{2.2}Cu_3O_z$
2212	(2:2:1:2)	$(Bi_{1.9}Pb_{0.1})Sr_{1.5}Ca_{1.5}Cu_2O_z$
014x24	(0:14:x:24)	$Sr_7Ca_7Cu_{24}O_{41}$
0x21	(0:x:2:1)	$(Ca_{1.9}Sr_{0.1})CuO_3$
3221	(3:2:2:1)	$Bi_{0.5}Pb_3Sr_2Ca_2CuO_z$
2310	(2:3:1:0)	$Bi_{27.82}Pb_{6.18}Sr_{49.5}Ca_{16.5}O_z$
2201	(2:2:0:1)	$Bi_{1.64}Pb_{0.36}Sr_2CuO_z$
119x5	(11:9:x:5)	$Bi_{1.8}Pb_{0.4}Sr_{1.6}Ca_{0.2}CuO_z$
0x11	(0:x:1:1)	$(Ca_{0.86}Sr_{0.14})CuO_2$
0x11'	(0:x:1:1')	$(Ca_{0.5}Sr_{0.5})CuO_2$
4805	(4:8:0:5)	$Bi_{3.4}Pb_{0.72}Sr_8Cu_5O_z$
CaO		CaO
CuO		CuO
1x20	(l:x:2:0)	$(Ca_{1.9}Sr_{0.1})PbO_4$

The 014x24 phase is a solid solution in which Ca can substitute into the Sr site up to x = 7 [89, 90]. The 3221 phase is referred to as the Bi-doped "451" solid solution by Daesche et al. [56, 80]. It was initially discovered by Kitakuchi et al. [91] and studied in detail by Luo et al. [92]. The Ca_2PbO_4 (1x20) phase was found to form an extensive solid solution with Sr_2PbO_4. A complete solid solution and the Rietveld refinement studies of (Ca, $Sr)_2PbO_4$ have been reported by Kitakuchi et a. [91] and Wong-Ng et al. [93, 94]. Calcium was found to incorporate into the Raveau 11905 phase [95], to give a solid solution with the general formula of $Bi_{2.2+x}Sr_{1.8-x-y}Ca_yCu_{1\pm w}O_z$ (119x5), where $0 < x < 0.5$. Both the 119x5 and 2201 phases can be indexed on different monoclinic cells [96]. Because of the close proximity of these two phases, they will not be distinguished and will be referred to as 119x5. The 2310 solid solution has an approximate formula of $Bi_2(Sr, Ca)_4O_z$ and exists in high and low-temperature forms [97]. The high-temperature form, which is in equilibrium with the 119x5, 2212, and 2223 superconductors, is monoclinic, with space group Pc. Both the two different structure types of $(Ca, Sr)CuO_2$ (0x11 and 0x11') [98] were found to be in equilibrium with Pb-2223. The Ca-rich 0x11 phase is orthorhombic, whereas the 0x11' phase is tetragonal.

1.2.2.2 Extent of Pb-Substitution

In order to study Pb incorporation in various Bi-containing compounds, a series of samples of the 2212, 4805, 119x5, 2201, and 2310 phases was prepared by assuming the same Bi/Pb ratio as in the 2223 phase, namely 1.8/0.4 [87]. These samples have stoichiometry of $Bi_{27.82}Pb_{6.18}Sr_{49.5}Ca_{16.5}O_x$(2310), $Bi_{1.8}Pb_{0.4}Sr_{1.6}Ca_{0.2}CuO_x$ (119x5), $Bi_{1.64}Pb_{0.36}Sr_2CuO_x$ (2201), $Bi_{1.64}Pb_{0.36}Sr_{1.5}Ca_{1.5}Cu_2O_x$ (2212), and $Bi_{3.28}Pb_{0.72}Sr_8Cu_5O_x$ (4805). Results of the synthesis of the Pb-doped 2212 phase showed the presence of the $(Ca, Sr)_2PbO_4$ impurity. With trial amounts of Pb = 0.1, 0.2 and 0.3 in $Bi_{2-x}Pb_xSr_{1.5}Ca_{1.5}Cu_2O_x$, it was found that Pb substitutes at the ≈ 0.1 mol level into the Bi site, and, subsequently, the Pb = 0.1 sample was used (Table 1). Lead was found not to substitute in the 4805 phase, and the 4805 phase was not in equilibrium with 2223. The other phases (2310, 119x5, and 2201) all form solid solutions with Pb at a ratio of 1.8/0.4.

1.2.2.3. Five Phase Equilibrium Volumes of 2223–2212

Based on the 11 phases that are in equilibrium with the 2223 phase, the possibility of various five-phase volumes is immense. According to the combinatorial formula

$$C = k!/[m!(k-m)!], \quad (1)$$

which gives the number of combinations C of k objects taken m at a time, there are 330 potential five-phase combinations that contain four of the 11 phases with 2223. This is a number too large to handle by trial and error. However, the number of possibilities for initial investigation was narrowed considerably by choosing only combinations that contain both 2212 and 2223 phases. The number of initial possibilities is thereby reduced by a factor of nearly 3. Because of the requirements for self consistency of these volumes, for example, to avoid overlapping phase space, the number of possibilities that remained for evaluation diminished rapidly as experimental data were accumulated. Coexistence with 2212 phase was chosen to be studied first, not only because it is an important 80 K superconductor, but also because during the formation of the 2223 phase, the 2212 phase is one of the precursors formed before the 2223 phase appears [34,35,43]. Furthermore, processing of the 2223 phase often results in the presence of the 2212 phase. A precise knowledge of the relationships of the 2212 and 2223 phases with other phases will significantly enhance our understanding of 2223-phase formation and processing. Sixteen such volumes were determined. After the 2223 + 2212

subsolidus was determined, the remaining 2223 subsolidus volumes could be added in a similar way.

1.3. General Approach to Obtaining the Primary Phase Field

By definition, a primary phase is the first crystalline phase to appear on cooling a composition from the liquid state. A primary phase field is the locus of all compositions in a phase diagram having a common primary phase. The primary phase field of a binary phase is a line, that of a ternary phase is a surface, and that of a quaternary phase can be described as a volume. Therefore, in the four-component Pb-free BSCCO system, the primary phase field of the 2212 phase is represented by a volume, and for the 2223 phase, the primary phase field is a multidimensional volume.

In order to obtain the primary phase field of a given phase of interest, the first step is to determine all compounds that are in equilibrium with the phase of interest. Next, the multiphase compatibility regions involving this phase are identified. For example, in a ternary system, one would determine all three-phase compatibility regions involving the ternary phase of interest, and four-phase compatibility regions in a quaternary system, and five-phase volumes in a five-component system, respectively. For each of the compatibility regions, the onset melting temperature is then determined. The compositions of the first liquid formed in each of these regions will determine the outline of the primary phase field. The method of locating the primary phase field has been illustrated and discussed in detail previously with reference to the Pb-free 2212 phase [26].

2. Experimental Method

Samples for this investigation were prepared by the solid-state calcining technique. Stoichiometric starting mixtures of PbO, Bi_2O_3, $SrCO_3$, $CaCO_3$, and CuO were homogenized, pressed, and heat treated at temperatures corresponding to the stable range of phase formation, based on available phase diagram information. Approximately 30 g of the 2223 phase were prepared by using the composition $Bi_{1.8}Pb_{0.4}Sr_2Ca_{2.2}Cu_3O_z$. The heat treatment process for this composition, which was performed in air, was as follows: 840 °C, 24 h; 850 °C, 24 h; 855 °C, 40 h; 860 °C, 40 h; and 855 °C, 120 h. Powder x-ray diffraction was used to confirm the phase formation.

2.1. Five-Phase Equilibria Involving the Pb-2223 Phase

The eleven phases as discussed above were used as starting materials for preparing five-phase mixtures that contained the 2223 phase. Table 2 lists the 80 five-phase samples which we have studied for determining a complete set of five-phase volumes. These samples were prepared by mixing approximately equal volumes of the phases, pelletizing, and calcining them at 810 °C–820 °C for 2 days in a 7.5 % O_2 atmosphere, followed by grinding, repelletizing, and reheating at the same temperature for another 2 days with intermediate grindings. The choice of temperature range for calcining was based on the report by Carter et al. [67] that the thermal stability of the 2223 phase contained within a Ag sheath extended over the range of ≈ 805 °C to 835 °C at $p_{O_2} = 7.61 \times 10^3$ MPa (0.075 atm), and that it decomposed to 2212, CuO, and Ca_2PbO_4 at 800 °C [22]. After heat treatment, all samples were subjected to powder x-ray diffraction to confirm that the five-phase compatibilities persisted.

2.2. Determination of Liquid Composition

The procedure for obtaining compositions of melts that are produced during initial melting of multiphase volumes has been documented elsewhere [26]. The various steps can be summarized as follows: (1) DTA/thermogravimetric analysis studies were conducted to obtain an indication of thermal events. Initial melting temperatures of the five-phase assemblages were measured by differential thermal analysis (DTA) with ≈ 50 mg of annealed sample contained in a MgO crucible at a scan speed of 4 °C/min under a flowing atmosphere of 7.5 % O_2/92.5 % Ar. Melting temperatures (during the heating cycle) obtained by DTA were chosen as the intercept of the extrapolated baseline with the linearized slope of the rising peak. (2) To capture liquid, a small piece of MgO wick was mixed in with the sample, which was placed in a MgO crucible and annealed in the appropriate atmosphere (air, or volume fraction of 7.5 % O_2 + 92.5 % Ar). (3) Samples were annealed in purified air and were quenched in liquid-nitrogen-cooled helium for further characterization. (4) Powder x-ray characterization was performed on solid residual phases and on selected wick material to identify the crystallized melt. (5) SEM examination and x-ray mapping were conducted to study the microstructure of the quenched materials. (6) Quantitative energy dispersive x-ray spectrometry (EDS) was applied to obtain the composition of the melt captured in the quenched wick and the compositions of crystalline phases. The EDS data were reduced according to conventional methods [99] via the DTSA software package [100], which incorporates several advanced features for spectral manipulation and quantification. The standards used for microanalysis were $Bi_2Sr_{1.5}Ca_{1.5}Cu_2O_z$ and (Pb, Zr)TiO_3. Analytical uncertainties (one standard deviation) are estimated at < 10 % relative. Uncertainties in

DTA temperatures quoted in this paper are estimated a $< \pm 7$ °C (one standard deviation).

Table 2. Results of heat-treatment of 81 five-phase mixtures

Starting composition	X-ray analysis of results
2223-2212-1*x*20-119*x*5-2310[a]	2223-2212-1*x*20-119*x*5-2310
2223-2212-1*x*20-2310-CaO[a]	2223-2212-1*x*20-2310-CaO
2223-2212-0*x*21-1*x*20-CuO[a]	2223-2212-0*x*21-1*x*20-CuO
2223-2212-0*x*21-3221-CuO	2223-2212-0*x*21-1*x*20-CuO
2223-2212-1*x*20-CuO-CaO	2223-2212-0*x*21-1*x*20-CuO
2223-2212-1*x*20-0*x*11-3221[a]	2223-2212-1*x*20-0*x*11-3221
2223-2212-1*x*20-CuO-*x*11[a]	2223-2212-1*x*20-CuO-0*x*11
2223-2212-0*x*21-014*x*24-CuO[a]	2223-2212-0*x*21-014*x*24-CuO
2223-2212-014*x*24-1*x*20-119*x*5[a]	2223-2212-014*x*24-1*x*20-119*x*5
2223-2212-11*x*5-1*x*20-0*x*11	2223-2212-1*x*20-119*x*5-014*x*24
2223-2212-2310-0*x*11-3221[a]	2223-2212-2310-0*x*11-3221
2223-2212-119*x*5-0*x*11'-CuO[a]	2223-2212-119*x*5-0*x*11-CuO
2223-2212-014*x*24-119*x*5-CuO[a]	2223-2212-014*x*24-119*x*5-CuO
2223-2212-014*x*24-3221-CuO	2223-2212-014*x*24-CuO-119*x*5
2223-2212-0*x*11-014*x*24-CuO	2223-2212-014*x*24-CuO-119*x*5
2223-2212-014*x*24-0*x*21-1*x*20[a]	2223-2212-014*x*24-0*x*21-1*x*20
2223-2212-0*x*21-1*x*20-014*x*24	2223-2212-0*x*21-1*x*20-014*x*24
2223-2212-3221-CaO-1*x*20[a]	2223-2212-3221-CaO-1*x*20
2223-2212-CaO-0*x*11'-3221	2223-2212-3221-CaO-1*x*20
2223-2212-0*x*11-2310-119*x*5[a]	2223-2212-0*x*11-2310-119*x*5
2223-2212-3221-CaO-2310[a]	2223-2212-3221-CaO-2310
2223-2212-3221-0*x*11'-119*x*5	2223-2212-3221-CaO-2310
2223-2212-0*x*11-0*x*11'-2310[a]	2223-2212-0*x*11-0*x*11'-2310
2223-2212-3221-0*x*11'-0x11	2223-2212-0*x*11-0*x*11'-2310
2223-2212-0*x*11-0x11'-CuO[a]	2223-2212-0*x*11-0*x*11'-CuO
2223-1*x*20-CuO-0*x*21-014*x*24[a]	2223-1*x*20-CuO-0*x*21-014*x*24
2223-1*x*20-CaO-0*x*11'-2310[a]	2223-1*x*20-CaO-0*x*11'-2310
2223-1*x*20-CaO-0*x*11'-3221[a]	2223-1*x*20-CaO-0*x*11'-3221
2223-CuO-1*x*20-0*x*11'-014*x*24[a]	2223-CuO-1*x*20-0*x*11'-014*x*24
2223-2310-1*x*20-014*x*24-0*x*11'[a]	2223-2310-1*x*20-014*x*24-0*x*11'
2223-0*x*11'CuO-1*x*20-0*x*11[a]	2223-0*x*11'CuO-1*x*20-0*x*11
2223-0*x*11'-3221-1*x*20-0*x*11[a]	2223-0*x*11'-3221-1*x*20-0*x*11
2223-0*x*11'-CaO-0*x*11-3221[a]	2223-0*x*11'-CaO-0*x*11-3221
2223-0*x*11'-CaO-2310-0*x*11[a]	2223-0*x*11'-CaO-2310-0*x*11
2223-0x11'-2310-0*x*11-119*x*5[a]	2223-0*x*11'-2310-0*x*11-119*x*5
2223-0*x*11'-2310-119*x*5-014*x*24[a]	2223-0*x*11'-2310-119x5-014*x*24
2223-0*x*11'-014*x*24-119*x*5-CuO[a]	2223-0*x*11'-014*x*24-119*x*5-CuO
2223-2310-3221-CaO-0*x*11[a]	2223-2310-3221-CaO-0*x*11
2223-1*x*20-CuO-014*x*24-119*x*5	2223-2212-1*x*20-CuO
2223-1*x*20-CuO-0*x*11-119*x*5	2223-2212-1*x*20-CuO
2223-1*x*20-0*x*11-119*x*5-2310	2223-2212-1*x*20-2310
2223-1x20-0x11-2310-3221	2223-2212-1*x*20-0*x*11
2223-1*x*20-CaO-3221-2310[a]	2223-2212-1*x*20-CaO-2310
2223-CaO-3221-2310-1*x*20	2223-2212-1*x*20-2310-CaO
2223-1*x*20-119*x*5-014*x*24-2310	2223-2212-2310-1*x*20-119*x*5
2223-1*x*20-CuO-014*x*24-2310	2223-2212-1*x*20-CuO
2223-1*x*20-CuO-0*x*11-2310	2223-2212-1*x*20-CuO
2223-CuO-0*x*11-119*x*5-014*x*24	2223-2212-2310-119*x*5
2223-CaO-2310-3221-0*x*11	2212-3221-CaO-2310
2223-2310-0*x*11-014*x*24-119*x*5	2223-2212-0*x*11-2310-119*x*5
2223-2310-1*x*20-CuO-0*x*11	2223-2212-1*x*20-CuO-0*x*11
2223-2310-0*x*11-CuO-119*x*5	2223-2212-CuO-119x5
2223-2310-1*x*20-CuO-014*x*24	2223-1*x*20-CuO-014*x*24
2223-2310-0*x*11-CuO-014*x*24[b]	2223-CuO-2310-0*x*11
2223-2212-0*x*11-0*x*11'-119*x*5	2223-2212-0*x*11-0*x*11'
2223-119*x*5-2310-1*x*20-0*x*11'	2223-2212-1*x*20-2310

Table 2. Results of heat-treatment of 81 five-phase mixtures—Continued

Starting composition	X-ray analysis of results
2223-014*x*24-1*x*20-0*x*11'-CuO	2223-2212-1*x*20-CuO-0*x*21
2223-2212-1*x*20-0*x*21-3221	2223-2212-1*x*20-3221
2223-2212-0*x*11'-0*x*11-119*x*5	2223-2212-0*x*11'-0*x*11
2223-2212-0*x*11-CuO-119*x*5	2223-2212-0*x*11-CuO
2223-2212-0*x*11-0*x*21-3221	2223-2212-3221-0*x*11
2223-2212-3221-0*x*11-CuO	2212-2310-0*x*11-119*x*5
2223-2212-1*x*20-0*x*11'-CuO	2223-2212-1*x*20-CuO
2223-2212-2310-CuO-1*x*20	2223-2212-1*x*20-CuO
2223-2212-1*x*20-119*x*5-CaO	2212-CaO-2310-1*x*20
2223-2212-1*x*20-0*x*11-119*x*5	2223-2212-1*x*20-0*x*11
2223-2212-014*x*24-3221-1*x*20	2223-2212-014*x*24-1*x*20
2223-2212-1*x*20-3221-CuO	3221-CuO-119*x*5
2223-2212-014*x*24-3221-CuO	3221-CuO-119*x*5-014*x*24
2223-2212-014*x*24-0*x*21-3221	2212-3221-014*x*24-0*x*21
2223-2212-1*x*20-119*x*5-3221	2212-3221-1*x*20-119*x*5
2223-2212-119*x*5-3221-CuO	2212-119*x*5-3221-CuO
2223-2212-3221-0*x*11-119*x*5	2223-2212-3221-0*x*21
2223-2212-014*x*24-1*x*20-CaO[b]	2223-2212-014*x*24-1*x*20-CaO
2223-2212-1*x*20-CaO-0*x*11[b]	2223-2212-1*x*20-CaO-0*x*11
2223-2212-014*x*24-0*x*11-1*x*20	2223-2212-0*x*11-1*x*20
2223-2212-CaO-2310-0*x*11'	2223-2212-0*x*11'-2310
2223-2212-0*x*11'-119*x*5-2310	2223-2212-2310-CaO
2223-2212-2310-3221-014*x*24	2223-2310-3221-014*x*24
2223-2212-2310-CaO-0*x*11'	2223-2212-2310-CaO

[a] Samples interpreted as representing equilibrium subsolidus volumes.
[b] Metastable volumes.

3. Results and Discussion

This section focuses on the description of the complicated five-phase equilibrium volumes, the first liquids that are associated with these volumes, and the construction of the Pb-2223 primary phase field.

3.1. Five-Phase Compatibilities of Pb-2223 at 810 °C to 820 °C in 7.5 % O_2

The compounds in the Bi-Pb-Sr-Ca-Cu-O system include a complicated series of binary, ternary, quaternary, and five-component solid solutions. Therefore, a large number of two phase tie-line bundles and stacks of three-phase tie planes exist. In the following discussion, the exact equilibrium compositions of the solid solutions that participate in specific equilibria are not specified. Also, because of the large number of phases, and closely spaced phase compositions, the 2223 phase compatibilities include a number of relatively “flat,” or shallow, five-phase equilibrium volumes. This implies that in certain regions of the phase diagram, a small variation in composition or temperature can lead to a dramatic change in the phase equilibrium assemblage.

Among the 80 five-phase starting mixtures that were prepared and annealed at 810 °C to 820 °C in 7.5 % volume fraction of O_2, 29 five-phase volumes that involve the 2223 phase were found to be mutually stable in a topologically consistent manner, as indicated in Table 2. The volumes which are marked with ([a]) were those that form a consistent set. The remaining volumes were found to either result in a smaller number of components, or to be metastable as a result of reactions to produce other assemblages or because of conflict with the remaining set. There are a few volumes (marked with the symbol "M"), however, that also contain a small amount of the 2212 phase in addition to the reported five phases.

These 29 subsolidus volumes are consistent with each other in that each volume shares a given side with no more than one other (Table 3). Among them, there are a total of 16 volumes which contain of 2223-2212 as a pair. Because the 2212 and 2223 phases have similar structures (members of the same homologous series), and the 2212 phase is a precursor for the formation of the 2223 phase, it is not surprising that their mutual solid-state compatibilities are extensive. There are a total of nine five-phase volumes that contained the 2223 + CuO pair, nine five-phase volumes that contain the 2223 + 014x24 pair, and four five-phase volumes that contain the 2223 + $(Ca, Sr)_2CuO_3$ pair. The number of volumes for the latter two pairs is much smaller than for the 2223 + 2212 pair. This is so because CuO and $(Ca, Sr)_2CuO_3$ are one- and three-component oxide phases, respectively, whereas 2212 is a five-component phase (when it contains lead) that lies nearer to the center of the system.

Table 3. Twenty-nine five-phase equilibrium volumes that contain the 2223 phase prepared in 7.5 % volume fraction O_2. Differential thermal analysis (DTA) temperatures indicate initial melting, quench temperatures (Qch) indicate temperature of the melt wick sampling experiments

Five-phase equilibrium[a]		DTA t (°C)[b]	Qch t (°C)[c]	Melt composition (mole fraction, %)[d]				
				$BiO_{1.5}$	PbO	SrO	CaO	CuO
1	2223-2212-1*x*20-119*x*5-2310	827	830	23.6	7.6	26.3	25.4	17.1
2	2223-2212-1*x*20-2310-CaO	830	835	23.0	7.3	27.1	23.5	19.1
3	2223-2212-0*x*21-1*x*20-CuO	837	840	18.5	14.4	16.3	14.2	36.6
4	2223-2212-1*x*20-0*x*11-3221	838	842	19.9	14.0	19.9	15.4	30.8
5	2223-2212-1*x*20-CuO-0*x*11	839	842	15.0	10.0	16.0	12.0	47.0
6	2223-2212-0*x*21-014*x*24-CuO	845	850	28.0	3.2	17.1	21.6	30.1
7	2223-2212-014*x*24-1*x*20-119*x*5	840	845	20.2	6.5	20.8	22.2	30.3
8	2223-2212-2310-0*x*11-3221	842	845	13.5	4.1	27.8	26.4	28.2
9	2223-2212-119x5-0*x*11-CuO	842	846	17.2	2.7	19.9	28.7	31.5
10	2223-2212-014*x*24-119*x*5-CuO	845	850	21.4	2.8	24.0	20.9	30.9
11	2223-2212-014*x*24-0*x*21-1*x*20	846	851	17.0	11.0	16.2	17.9	37.9
12	2223-2212-3221-CaO-1*x*20	848	852	19.3	10.2	23.7	18.4	28.4
13	2223-2212-0*x*11-2310-119*x*5	850	853	21.6	4.7	24.5	26.2	23.0
14	2223-2212-0*x*11-0*x*11'-CuO	850	855	21.8	1.2	21.7	18.3	37.0
15	2223-2212-0*x*11-0*x*11'-2310	853	858	25.3	2.3	22.7	17.3	32.4
16	2223-2212-3221-CaO-2310	865	870	20.4	7.6	20.9	25.8	25.3
17	2223-1*x*20-CuO-0*x*21-014*x*24	828	831	10.4	18.2	11.3	20.6	39.5
18	2223-1*x*20-CaO-0*x*11'-2310	832	835	20.8	12.8	23.5	15.4	27.5
19	2223-1*x*20-CaO-0*x*11'-3221	831	833	15.8	16.9	24.1	15.2	28.0
20	2223-CuO-1*x*20-0*x*11'-01424	816	818	13.8	16.9	20.3	15.7	33.4
21	2223-2310-1*x*20-014*x*24-0*x*11'	832	835	18.8	15.9	23.4	12.0	29.9
22	2223-0*x*11'CuO-1*x*20-0*x*11	838	841	7.3	16.7	12.6	20.4	43.0
23	2223-0*x*11'-3221-1*x*20-0*x*11	820	823	16.6	18.7	18.3	14.1	32.3
24	2223-0*x*11'-CaO-0*x*11-3221	830	833	17.0	19.4	15.1	15.3	33.2
25	2223-0*x*11'-CaO-2310-0*x*11	840	845	12.4	1.6	26.5	30.8	28.7
26	2223-0*x*11'-2310-0*x*11-119*x*5	848	853	27.6	2.1	24.8	13.4	32.1
27	2223-0*x*11'-2310-119*x*5-014*x*24	827	823	19.9	4.1	23.0	15.8	37.2
28	2223-0*x*11'-014*x*24-119*x*5-CuO	840	845	23.4	1.6	24.1	10.5	40.4
29	2223-2310-3221-CaO-0*x*11	838	840	15.4	16.9	25.2	9.8	32.7

[a] See Table 1 for symbols and compositions.
[b] Indicates initial melting; combined standard uncertainty < 6 °C.
[c] Indicates temperature of melt wick sampling experiments, combined standard uncertainty < 6 °C.
[d] For mole fractions > 10 %, the relative standard uncertainty is < 2.5 %; for mole fraction < 10 %, it is < 5.0 %.

This gives it access to a much larger number of phases. The 1*x*20 ([Ca, Sr]$_2$PbO$_4$) phase was also found to have a wide stability region, and occurred in eight of the 16 volumes. Consequently, this phase is often found to be an impurity phase, along with the 2212 phase, during the preparation of 2223.

A comparison of the five-phase volumes of Table 3 with results in the existing literature indicates both similarities and differences. For example, Kaesche et al. [56, 80] reported two five-phase volumes involving the 2223 phase: 0*x*21-CuO-014*x*24-2212-2223 and 3221-014*x*24-CuO-2212-2223. Our results agree with the first volume; however, we found that the latter volume was converted into the 2223-2212-014*x*24-CuO-119*x*5 assemblage. Undoubtedly, many factors influenced the experimental results, including the sensitivity of the phase assemblages to processing conditions, the sluggish kinetics of phase formation, and the very closely spaced phase stability fields of the high-T_c phases. Furthermore, our samples were studied under 7.5 % volume fraction of O_2 at ≈ 810 °C and the samples of Kaesche et al. [56, 80] were investigated in air (22.1 % O_2). This difference in conditions may be the cause of the differences in the observed equilibria.

3.2. Initial Melting of the Five-Phase Volumes

The DTA temperatures (in 7.5 % O_2) of initial melting for each of the 29 five-phase volumes are also listed in Table 3, along with the temperatures at which the sample was quenched, and the compositions of initial melts that are based on EDS analyses of the MgO wicks. These DTA temperatures range from 816 °C for the assemblage 2223-CuO-1*x*20-0*x*11'-014*x*24, to 865 °C for the assemblage 2223-2212-3221-CaO-2310. This spread of approximately 40 °C is much smaller than the ≈ 70 °C spread observed in the four-phase volumes that contain the Pb-free 2212 phase [26].

The solidus of the five-phase volumes is defined by the temperatures at which the first liquids appear on heating. The solidus temperatures are useful for two main purposes. They indicate the maximum temperatures available for equilibrium solid-state processing of 2223 in each five-phase volume, and they also indicate the range of temperatures over which equilibrium liquids are available for 2223 processing. Below 816 °C, no stable equilibrium liquids are available for 2223 processing in equilibrium with 2212. Above 865 °C, which is the highest initial melting temperature among these volumes, the compositions for which 2223 and liquid are in equilibrium with each other are severely restricted due to the expansion of the liquid field.

The range of melt compositions for these volumes expressed in mole fractions is $BiO_{1.5}$, 7.3 % to 28.0 %; PbO, 1.2 % to 19.4 %; SrO, 11.3 % to 27.8 %; CaO, 9.8 % to 30.8 %; and CuO, 17.1 % to 47.0 %. Although PbO is present in the liquid of every volume, the concentration of PbO is the least among the five oxide components, followed by SrO. The concentration of the CuO component has the highest value. The subsolidus volumes with relatively high PbO concentration give rise to higher PbO content in the melt. For example, in the five-phase volume 2223-0*x*11'-3221-1*x*20-0*x*11, which contains the PbO-rich phases $Bi_{0.5}Pb_3Sr_2Ca_2CuO_z$ and $(Ca_{1.9}Sr_{0.1})PbO_4$, the PbO concentration is relatively high (18.7 %). By contrast, for the volume 2223-2212-0*x*11-0*x*11'-CuO, where there is no PbO-containing compound other than a small amount of Pb substituted in the 2223, 2212 and 119x5 phases, the PbO content of the liquid is only 1.2 %.

3.3. The Primary Phase Field of the 2223 Phase

By analogy with our determination of the primary phase volume of the Pb-free phase [26], the 29 compositions of the five-phase volumes were modeled using a computational geometry technique based on forming a convex hull from the experimentally determined chemical compositions. This mathematical notion of a convex hull, the smallest convex set of points that contains all of the given data points, has been used in many physical science applications. In this case, the convex hull represents the extent of the compositional volume. This numerical procedure results in a well-formed, hyper-volume in five-dimensional space. It is important to note the requirement that chemical compositions sum to unity results in the loss of one degree of freedom. This explains the flat appearance of the three dimensional cross-sections. The convex hull is defined by the matrix equation

$$\boldsymbol{Ax} + \boldsymbol{b} \leq 0, \tag{2}$$

where $\boldsymbol{A}$ is a matrix whose rows define the unit normal vectors to the faces of the convex hull. Each element of the vector $\boldsymbol{b}$ defines the proximity of the given face to the origin (in this five-dimensional space). The vector $\boldsymbol{x}$ gives the coordinates corresponding to a given point. The matrix $\boldsymbol{A}$ and vector $\boldsymbol{b}$ can be found using a so-called "sweeping algorithm" that has been implemented and tested [101]. When the procedure is complete, the matrix $\boldsymbol{A}$ has dimension $k \times 5$ and the vector $\boldsymbol{b}$ has dimension $\boldsymbol{k}$ where $\boldsymbol{k}$ is the number of faces in the convex hull.

3.4 Graphical Representations

3.4.1. Subsolidus Phase Relationships

Since all of the 29 volumes in Table 3 are expressed in the five-component space, representing them is not straightforward. One way to view them is via a thermodynamic method, which involves projecting through the composition of a phase common to a group of assemblages. However, not all 29 volumes can be viewed simultaneously in this manner. In other words, one can view groups of volumes which contain a common compound plus the 2223 phase individually. As an example, the sixteen 2223-2212 volumes can be viewed together as a group [87]. For convenience, one can recast the coordinate system of simple conventional oxides into a system using 2310 (i.e., $Bi_2Sr_3CaO_7$), PbO, 2212 (e.g., $Bi_{2.0}Pb_{0.2}Sr_2CaCu_2O_z$), CaO, and CuO as reference according to the following equations:

$$
\begin{aligned}
n_{2212} &= 1.5(n_{\mathrm{BiO1.5}}) - 1.0(n_{\mathrm{SrO}}) \\
n_{\mathrm{PbO'}} &= -0.3(n_{\mathrm{BiO1.5}}) + 1.0(n_{\mathrm{PbO}}) + 0.2(n_{\mathrm{SrO}}) \\
n_{2310} &= -1.0(n_{\mathrm{BiO1.5}}) + 1.0(n_{\mathrm{SrO}}) \\
n_{\mathrm{CaO'}} &= -0.5(n_{\mathrm{BiO1.5}}) + 1.0(n_{\mathrm{CaO}}) \\
n_{\mathrm{CuO'}} &= -0.3(n_{\mathrm{BiO1.5}}) + 2.0(n_{\mathrm{SrO}}) + 1.0(n_{\mathrm{CuO}}), \qquad (3)
\end{aligned}
$$

where the quantity n is the amount of substance for each indicated component (The SI unit for n is mole). Projection through 2212 into a three-dimensional space is then carried out. The resulting sixteen volumes were found to fit well with each other in the 3-dimensional space without overlapping. Figure 1 shows how four out of the sixteen volumes fit with each other.

3.4.2. Primary Phase Field

To graphically represent the primary phase field and give a general sense of its "shape," we employ an isopleth projection technique. In this technique the five-dimensional convex hull is viewed in three-dimensions by holding two components of the composition fixed at their mean value. Figure 2 shows an isoplethal section made by holding the $BiO_{1.5}$ and PbO values constant at the median values for the 29 data points, with the remaining oxides shown on the three Cartesian axes. The view of the section of the 2223 primary phase field in Fig. 2 appears to have a broad oval shape.

It is interesting that the mean of the compositional analyses in Table 3 is close to the 2223 composition. Obviously, since 2223 melts incongruently, the 2223 composition cannot plot within the primary phase field. The position of the mean suggests that there may be more structure to the primary phase field than has been accounted for by the convex hull. There are two possibilities. If the primary phase field has a strongly curved concavo-convex shape about the 2223 stoichiometry, without actually enclosing it, then the convex hull fitting procedure, which doesn't allow for concavity, would fit a single surface around the entire ensemble. Alternatively, if the primary phase field actually consisted of a two-liquid field, split on opposite sides of the 2223 stoichiometry, the convex hull would again fit a single surface. These possiblities are undergoing further evaluation in our laboratories.

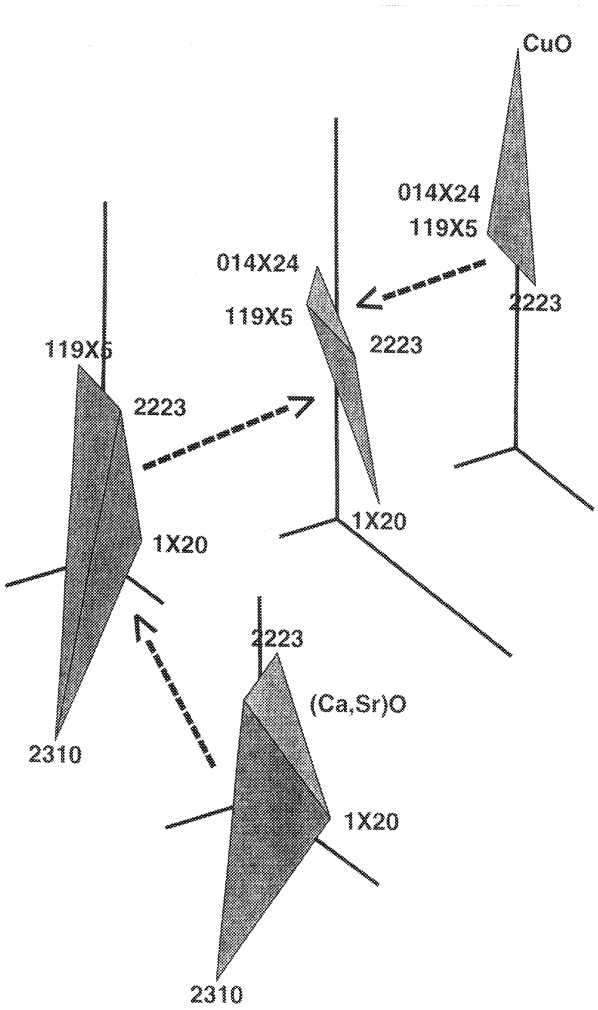

Fig. 1. An example of four of the 16 five-phase subsolidus assemblages, as projected through the 2212 phase. Arrows indicate how volumes are interconnected in these exploded views.

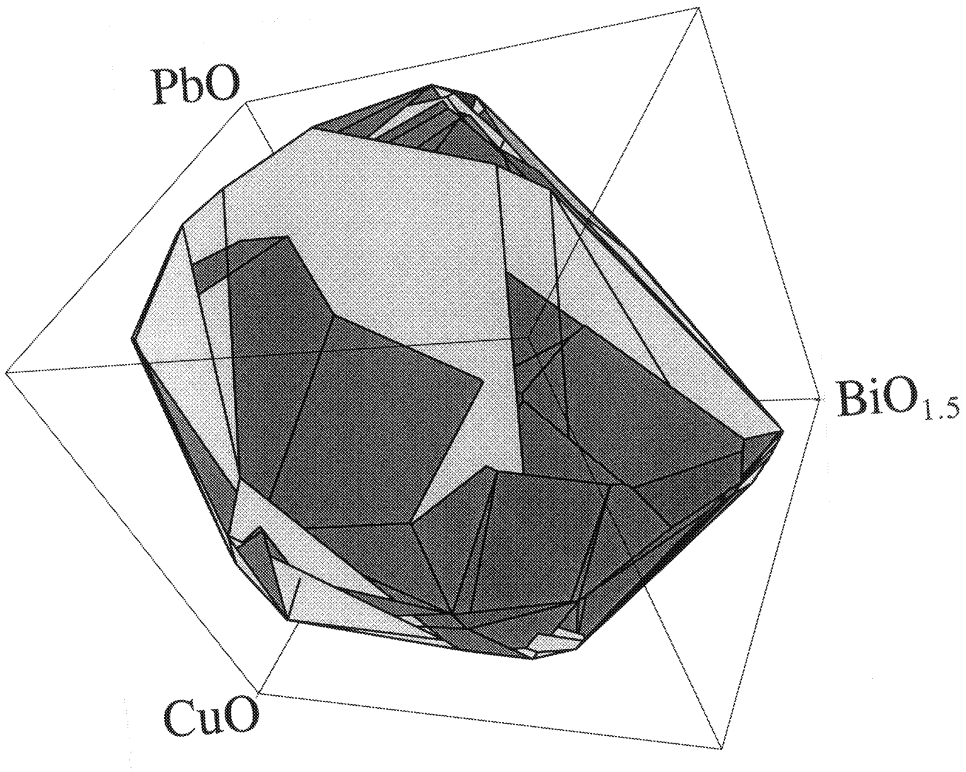

Fig. 2. The primary crystallization field of the Pb-2223 phase. An isoplethal section made by holding the $BiO_{1.5}$ and PbO values constant at the median mole fraction values for the 29 data points ($BiO_{1.5}$ = 20.4 %, and PbO = 6.9 %).

3.5. Application of the Primary Phase Field

The primary phase field provides a compositional region that one can use for crystal growth and for melt processing. In principle, when a composition is prepared within the limits defined by the primary phase field, crystals of 2223 will be the first to crystallize from the melt.

We have demonstrated previously that in the process of growing the Pb-free 2212 crystals [102], when one starts with a composition prepared within the primary phase field as shown in Fig. 3, even with a crystallization scheme using relatively rapid cooling rate (0.5 °C/min), we were able to obtain a sample with microstructure mostly dominated by the 2212 crystals. On the other hand, a composition that was prepared outside this field gave a microstructure that was mostly the calcium cuprate phase, with only a very small amount of the 2212 phase present. Applying the similar principle during the processing of the 2223 phase, compositions falling outside the primary phase field should be avoided, as they would be expected to produce large primary crystals of unwanted phases.

Equation (2) can be used to determine if a given composition lies inside the Pb-2223 primary phase field. If the difference of the two terms on the left side of the equation ($\boldsymbol{Ax} - \boldsymbol{b} \leq 0$) is negative, the particular composition lies inside the crystallization volume. If the value of all components is zero, the composition is on the surface; and if the value of any one component is positive, it is outside the volume. Compositions falling outside this volume should be avoided for the processing of the 2223 phase, as they would be expected to produce large primary crystals of unwanted phases. Table 4 shows an example of two compositions in order to illustrate whether the composition lies relative to the primary phase field. The first composition was found to lie inside the volume because from the matrix manipulation, all components of $\boldsymbol{Ax} - \boldsymbol{b}$ were found to be negative. The second composition was found to be outside the volume because 68 out of 200 elements are positive.

4. Summary and Future Needs

We have illustrated the general procedure of obtaining the primary phase fields of the five-component

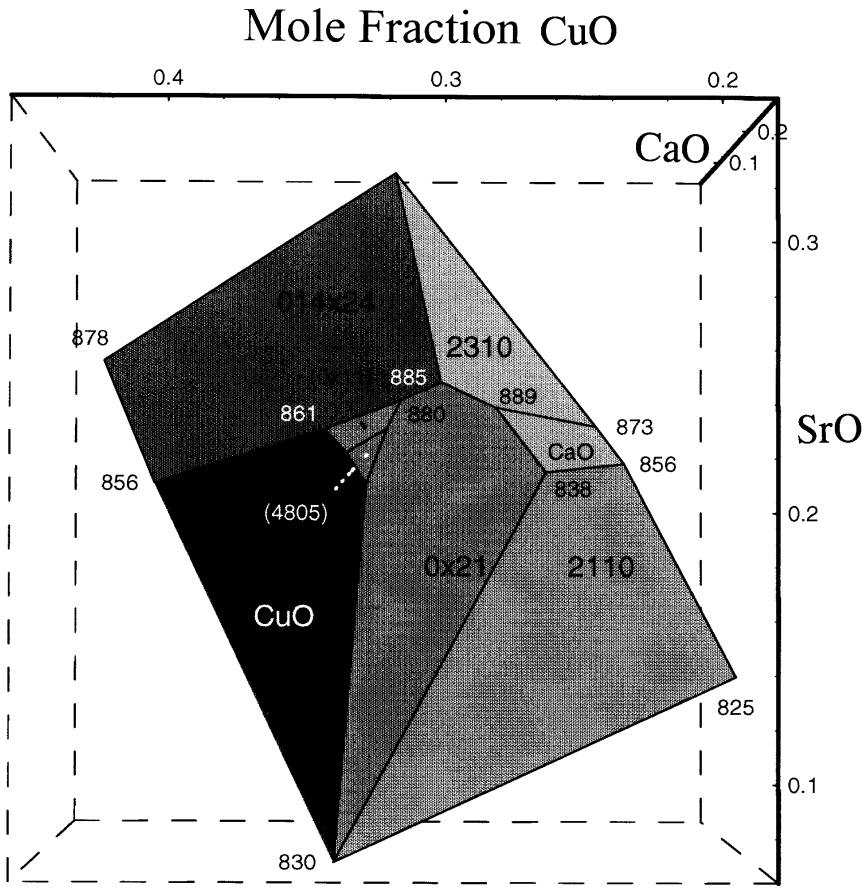

Fig. 3. Primary phase field of the 2212 phase in the BSCCO system. The onset melting temperatures are indicated at the corners.

Table 4. Compositions (expressed in mole fraction %) used to illustrate the use of the primary phase field of Pb-2223

Bi	Pb	Sr	Ca	Cu	$Ax - b$	Comments
21.82	1.20	21.66	18.32	37.01	all "–"	Inside volume
29.00	10.00	11.00	15.00	35.00	68 "+"	Outside volume

Pb-2223 phases. The subsolidus phase equilibria and liquid melt compositions of a complete set of 29 five-phase volumes that contain the Pb-2223 phase were obtained. These volumes are consistent with each other. The liquid compositions of the initial melts of these five-phase volumes have been measured and were used to construct the primary phase field. This field represents compositional regions where liquids can be found in equilibrium with the superconductors. It was found that, for these 29 volumes, the range of initial melt compositions expressed in mole fractions encompasses $BiO_{1.5}$: 7.3 % to 28.0 %; PbO: 1.2 % to 19.4 %; SrO: 11.3 % to 27.8 %; CaO: 9.8 % to 30.8 %; and CuO: 17.1 % to 47.0 %. A PbO component is present in the initial melt of every volume. The subsolidus volumes that contain PbO-rich phases give rise to melts with high PbO content.

The World Wide Web provides an excellent opportunity to give access to the primary phase field model described here. Presently, work is underway to construct a website where users can input various chemical compositions corresponding to experiments and, using java-based web technology, the convex hull procedure described here can be implemented and results displayed immediately. In this way, a user (potentially anywhere in the world) can employ this technique. The resulting polyhedra can be revolved in order to be viewed from different angles and used to make decisions relating to the shape. Also, it can be determined whether a trial composition is within the polyhedron.

Silver has been reported to enter the liquid phase, but, there was no indication that Ag enters into the 2223 phase under subsolidus subsolidus conditions [18, 98].

Acknowledgements

Dr. U. Balachrandran is thanked for the Pb-2223 sample used for the preparation of multiphase mixtures. This work was partially supported by the U.S. Department of Energy.

5. References

[1] Michel, C., Hervieu, M., Borel, M. M., Grandin, A., Deslandes, F., Provot, J., and Raveau, B., Z. Phys. B **68**, 421 (1987).
[2] U. Balachrandran, Impact of Recent Advances in Synthesis and Processing of Ceramic Superconductors, Ceramic Transactions **84**, W. Wong-Ng, U. Balachandran, and A. S. Bhalla, eds., Amer. Ceram. Soc. (1998) p. 157.
[3] A. P. Malozemoff, W. Carter, S. Fleshler, L. Fritzemeier, O. Li, L. Masur, P. Miles, D. Parker, R. Parrella, E. Podtburg, G. N. Riley, Jr., M. Rupich, J. Scudiere, and W. Zhang, Proceedings of Applied Superconductivity Conference, Palm Desert, CA. September 13–18, 1998, to be published.
[4] J. O. Willis, R. D. Ray II, T. G. Holesinger, R. Zhou, K. V. Salazar, J. Y. Coulter, J. J. Gingert, D. S. Phillips, and D. E. Peterson, Proceedings of the 7th US/Japan Workshop on High Temperature Superconductors, Tsukuba, Japan, October 22–24, 1995.
[5] P. Majewski, S. Kaesche, H.-L. Su, and F. Aldinger, Physica C **221**, 295 (1994).
[6] M. Boekhlt, D. Gotz, H. Idink, M. Fleuster, T. Hah, E. Woermann, and G. Guntherodt, Physica C **176**, 4207 (1991).
[7] Y. Ikeda, Z. Hiroi, H. Ito, S. Shimomura, M. Takano, and Y. Bando, Physica C **165**, 189 (1989).
[8] Y. Iwai, Y. Hoshi, H. Saito, and M. Takata, Physica C **170**, 319 (1990)
[9] Y. Wakata, T. Namba J. Takada, and T. Egi, Physica C **219**, 366 (1994).
[10] S. E. Dorris, M. A. Pitz, J. T. Dawley, and D. J. Trapp, J. Elect. Mater. **24** (12), 832 (1995).
[11] D. Y. Kaufman, M. T. Lanagan, S. E. Dorris, J. T. Dawley, I. D. Bloom, M. C. Hash, N. Chen, M. R. DeGuire, and R. B. Poeppel, Appl. Supercond. **1**(1/2), 81–91 (1993).
[12] U. Balachandran, A. N. Iyer, P. Haldar, J. G. Hoehn, Jr., and L. R. Motowidlo, Proceedings of The Fourth International Conference and Exhibition: World Congress on Superconductivity, Vol. II, K. Kristen and C. Burnham, eds., Orlando, FL, June 27–July 1, 1994, NASA, Linthicum Heights, MD, pp. 639–649.
[13] K. H. Sandhage, G. N. Riley, Jr., and W. Carter, J. Met. **43**, 21 (1991).
[14] K. Sato, T. Hikata, H. Mukai, M. Ueyama, N. Shibata, T. Kato, T. Masuda, M. Nagata, K. Iwata, and T. Mitsui, IEEE Trans. Mag. **27**, 1231 (1991).
[15] T. D. Aksenova, P. V. Bratukhin, S. V. Shavkin, and V. L. Melnkov, E. V. Antipova, N. E. Khlebova, and A. K. Shikov, Physica C **205**, 271 (1993).
[16] J. S. Luo, N. Merchant, V. A. Maroni, S. E. Dorris, M. T. Lanagan, and B. S. Tani, J. Am. Ceram. Soc. **78**, 2785 (1995).
[17] W. J. Kim, S. C. Kwon, H. G. Lee, G.W. Hong, and I. H. Kuk, Supercond. Sci. Technol. **11**, 250 (1998).
[18] M. T. Mlchevsky, P. L. Yill, and L. Gherardi, Appl. Supercond. **2**(1), 33 (1994).
[19] N. Merchant, J. S. Luo, V. A. Maroni, G. N. Riley, and W. L. Carter, Appl. Phys. Lett. **65** (8), 1039 (1994).
[20] J. Müller, O. Eibl, B. Fischer, and P. Herzog, Supercond. Sci. Technol. **11**, 238 (1998).
[21] Y. S. Sung and E. E. Hellstrom, Physica C **255**, 266 (1995).
[22] J. S. Luo, N. Merchant, V. A. Maroni, D. M. Gruen, B. S. Tani, W. L. Carter, G. N. Riley, Jr., and K. H. Sandhage, J. Appl. Phys. **72** (6), 2385 (1992).
[23] Q. Y. Hu, R. M. Schalk, H. W. Weber, H. K. Liu, R. K. Wang, C. Czurda, and S. X. Dou, J. Appl. Phys. **78**, 1123 (1995).
[24] Q. Y. Hu, H. W. Weber, F. M. Sauerzopf, G. W. Schulz, R. M. Schalk, H. W. Neumuller, and S. X. Dou, Appl. Phys. Lett. **65**, 3008 (1994).
[25] S. X. Dou, X. L. Wang, Y. C. Guo, Q. Y. Hu, P. Mikheenko, J. Horvat, M. Ionescu, and H. K. Liu, Superocnd. Sci. Technol. **10**, A52 (1997).
[26] W. Wong-Ng, L. P. Cook, and F. Jiang, J. Amer. Ceram. Soc. **81** (7), 1829 (1998).
[27] P. Majewski, Adv. Mater. **4**, 508 (1992).
[28] J. I. MacManus-Driscoll and J. C. Bravman, J. Am. Ceram. Soc. **77** (9), 2305 (1994).
[29] S. Kesche, P. Majewski, and F. Aldinger, J. Elect. Mater. **24** (12), 1829 (1995).
[30] S. Kesche, P. Majewski, and F. Aldinger, Z. Metallkd. **87**, 587 (1997).
[31] Y. S. Sung and E. E. Hellstrom, Physica C **255**, 266 (1995).
[32] K. Osamura and T. Maruyama, Proceedings of the fifth U.S.-Japan workshop on High T_c Superconductors, K. Tachikawa, ed., organized by New Superconducting Materials Forum, The Society of Non-Traditional Technology, Tsukuba, Japan, Nov. 1992, p. 75.
[33] Y. S. Sung and E. E. Hellstrom, Physica C **253**, 79 (1995).
[34] W. Wong-Ng and S. W. Freiman, Superconducting Glass-Ceramics in BSCCO: Fabrication and Its Application, Y. Abe, ed., Worldwide Publisher, Singapore (1997) p. 1.
[35] W. Wong-Ng and S. W. Freiman, Appl. Supercond. **2** (3/4), 163 (1994).
[36] M. Xu, D. K. Finnemore, U. Balachandran, and P. Haldar, J. Appl. Phys. **78** (1), 360 (1995).
[37] J. S. Luo, N. Merchant, V. A. Maroni, D. M. Gruen, B. S. Tani, W. L. Carter, and G. N. Riley, Jr., Appl. Supercond. **1**(1,2), 101 (1993).
[38] F. H. Chen, H. S. Koo, and T. Y. Tseng, Appl. Phys. Lett. **58** (6), 637 (1991).
[39] X.-H. Gao, D. Gao, J.-H. Li, J. Li, and S-F. Jiang, Physica C **229**, 124 (1994).
[40] X.-H. Gao, J. Li S-F Jiang, D. Gao, G-D Zheng, and S. Gao, Physica C **244**, 321 (1995).
[41] M. Wang, G. Xiong, X. Tang, and Z. Hong, Physica C **210**, 413 (1993).
[42] Z. X. Zhao and G. C. Che, Appl. Supercond. **2** (3,4), 227 (1994).
[43] Q. Y. Hu, H. K. Liu, and S. X. Dou, Physica C **250**, 7 (1995).
[44] S. Nhien and G. Desgardin, Physica C **272**, 309 (1996).
[45] J. S. Luo, N. Merchant, E. Escorcia-Aparicio, V. A. Maroni, B. S. Tani, W. L. Carter, and G. N. Riley, Jr., J. Mater. Res. **9** (12), 3059 (1994).
[45] J. S. Luo, N. Merchant, E. Escorcia-Aparicio, V. A. Maroni, B. S. Tani, W. L. Carter, and G. N. Riley, Jr., J. Mater. Res. **9** (12), 3059 (1994).
[46] J.-C. Grivel, D. Grindatto, G. Grasso, and R. Flükiger, Proceedings of the SMART Conference, Liége, Belgium, June 1997.
[47] R. Flükiger, J.-C. Grivel, G. Grasso, and D. Grindatto, in Adv. Cryo. Eng. Mater. Vol. 44B, ICMC, July 21, 1997, Portland, OR, U. Balachandran et al., ed., Plenum Press, NY (1998).

[48] J.-C. Grivel and R. Flükiger, Supercond. Sci. Technol. **11**, 288-298 (1998).
[49] J. L. MacManus-Driscoll and Z. Yi, Supercond. Sci. Technol. **10**, 970 (1998).
[50] J. S. Luo, F. Faudot, J-P. Chevalier, R. Portier, and D. Michel, J. Solid State Chem. **89**, 94 (1990).
[51] U. Endo and T. Kawai, J. Appl. Phys. **28**, L1163 (1989).
[52] U. Endo, S. Koyama, and T. Kawai, J. Appl. Phys **28** (2), l190 (1989).
[53] J. C. Toledano, D. Morin, J. Schneck, H. Faqir, O. Monnereau, G. Vacquier, P. Strobel, and V. Barnole, Physica C **253**, 53 (1995).
[54] G. N. Riley Jr., W. L. Carter, and K. H. Sandhage, Int. Workshop on Superconductivity, cosponsored by ISTEC and MRS, Honolulu, June 23–26, 1992, Materials Research Society, Warrendale, PA, p. 216.
[55] H. Sasakura, S. Minamigawa, K. Nakahigashi, M. Kogachi, S. Nakanishi, N. Fukoka, M. Yoshikaa, S. Noguchi, K. Okuda, and A. Yanase, Japn. J. Appl. Phys. **28**(7), L1163 (1989).
[56] S. Kaesche, P. Majewski, and F. Aldinger, J. Elect. Mater. **24** (12), 1829 (1995).
[57] Y. C. Guo, H. K. Liu, and S. X. Dou, Physica C **200**, 147 (1992).
[58] M. Xu, D. K. Finnemore, U. Balachandran, and P. Haldar, Appl. Phys. Lett. **68** (24), 3359 (1995).
[59] M. Xie, L. W. Zhang, T.G. Chen, X.T. Li, and J. Cai, Physica C **206**, 251 (1993).
[60] J. I. MacManus-Driscoll and J. C. Bravman, J. Am. Ceram. Soc. **77** (9), 2305 (1994).
[61] H. Zhang and H. Sato, Physica C **214**, 265 (1993).
[62] M. Tetenbaum, M. Hash, B. S. Tani, J. S. Luo, and V. A. Maroni, Physica C **246**, 396 (1995).
[63] M. Tetenbaum, M. Hash, B. S. Tani, J. S. Luo, and V. A. Maroni, Physica C **235-240**, 321 (1994).
[64] M. Xu, and D. K. Finnemore, J. Appl. Phys. **76** (2), 1111 (1994).
[65] A. P. Mozhaev, S. V. Chernyev, Y. V. Badun and M. S. Kuznetsov, J. Solid State Chem. **119**, 120 (1995).
[66] J.-C. Grivel and R. Flukiger, Physica C **235-240**, 505 (1994).
[67] W. L. Carter, G. N. Riley, J. S. Luo, N. Merchant, and V. A. Maroni, Appl. Supercond. **1** (10–12)1523 (1993).
[68] Y. B. Huang, G. F. de la Fuente, A. Larrea, and R. Navarro, Supercond. Sci. Tech. **7**, 759 (1994).
[69] J. A. Parrell, D.C. Larbalestier, G. N. Riley, Jr., Q. Li, W. L. Carter, R. D. Parrella, and M. Teplitsky, J. Mater. Res. **12** (11), 2997 (1997).
[70] U. Endo, S. Koyama, and T. Kawai, J. J. Appl. Phys. **27**, L1476 (1988).
[71] W. Wu and P. S. Nicholson, J. Mater. Res. **7**, 38 (1992).
[72] I. S. Oh. K. Mukherjee, Physica C **227**, 197 (1994).
[73] N. Merchant, J. S. Luo, V. A. Maroni, S. N. Sinha, G. N. Riley, Jr., and W. L. Carter, Appl. Supercond. **2** (3,4), 217 (1994).
[74] W. Zhu and P. S. Nicholson, J. Appl. Phys. **73** (12), 8423 (1993).
[75] F. Marti, G. Grasso, J.-C. Grivel, and R. Flükiger, Supercond. Sci. Technol. **11**, 485 (1998).
[76] J. C. Toledano, P. Strobel, D. Morin, J. Schneck, G. Vacquier, O. Monereau, V. Barnole, J. Primot, and T. Fournier, Appl. Supercond. **1** (3–6), 581 (1993).
[77] P. Strobel and T. Fournier, Physica C **164–165**, 519 (1990).
[78] P. Strobel, J. C. Toledano, D. Morin, J. Schneck, G. Vacquier, O. Monereau, J. Primot and T. Fournier, Physcia C **201**, 27 (1992).
[79] K. Osamura and T. Maruyama, Proceedings of the Society of Non-Traditional Technology, organized by the New Superconducting Materials Forum, Tsukuba, Japan, 1 (1992).
[80] S. Kaesche, P. Majewski, and F. Aldinger, Z. Metallkd. **87**, 587 (1997).
[81] D. Morin, P. Strobel, J. C. Toledano, J. Schneck, G. Vacquier, O. Monereau, J. Primot, and T. Fournier, Physica C **185-189**, 487 (1991).
[82] Y. Ikeda, H. Ito, S. Shimomura, Z. Hiroi, M. Takano, Y. Bando, J. Takada, K. Oda, H. Kitaguchi, Y. Miura, Y. Takeda, and T. Takada, Physica C **190**, 18 (1991).
[83] Y. S. Sung and E. E. Hellstrom, Physica C **253**,79 (1995).
[84] Y. T. Huang, W-N Wang, S-F Wu, C-Y Shei, W-M Hurng, W-H Lee, and P-T Wu, J. Amer. Ceram. Soc. **73** (11), 3507 (1990).
[85] P. Majewski, S. Kaesche, and F. Aldinger, J. Amer. Ceram. Soc. **80** (12) 1174 (1997).
[86] J. L. MacManus-Driscoll and Z. Yi, J. Am. Ceram. Soc. **81** (5), 1322 (1998).
[87] W. Wong-Ng, L. P. Cook, F. Jiang, W. Greenwood, U. Balachrandran, and M. Lanagan, J. Mater. Res. **12** [11], 2855 (1997).
[88] S. Bernik, Supercond. Sci. Technol. **10**, 671 (1997).
[89] T. Siegrist, S. Mahurak, D. W. Murphy, and R. S. Roth, Nature **334** (6179), 231 (1988).
[90] R. S. Roth, C. J. Rawn, J. J. Ritter, and B. P. Burton, J. Am. Ceram. Soc. **72** (8) 1545 (1989).
[91] H. Kitguchi, J. Takada, K. Oda, and Y. Miura, J. Mater. Res. **5** (7),1397 (1990).
[92] J. S. Luo, N. Merchant, V. A. Maroni, G. N. Riley, Jr., and W. L. Carter, Appl. Phys. Lett. **63** (5), 690 (1993).
[93] W. Wong-Ng, F. Jiang, and L. P. Cook, Physica C **272**, 87 (1996).
[94] W. Wong-Ng, J. A. Kaduk, and W. Greenwood, Powd. Diff. **13**(4), 232 (1998).
[95] W. Wong-Ng, L. P. Cook, and F. Jiang, Adv. X-Ray Anal. **39**, 731 (1997).
[96] R. S. Roth, C. J. Rawn, and L. A. Bendersky, J. Mater. Res. **5**, 46 (1990).
[97] C. J. Rawn, R. S. Roth, B. P. Burton, and M. D. Hill, J. Am. Ceram. Soc. **77** (8), 2173 (1994).
[98] R. S. Roth, C. J. Rawn, J. J. Ritter, and B. P. Burton, J. Am. Ceram. Soc. **72**, 1545 (1989).
[99] K. F. J. Heinrich, Electron Beam X-Ray Microanalysis, Van Nostrand Reinhold Co., New York (1981) p. 578.
[100] C. E. Fiori, C. R. Swyt, and R. L. Myklebust, NIST/NIH Desktop Spectrum Analyzer Program and X-Ray Database, NIST Standard Reference Database No. 36 (1991).
[101] C. B. Barber, D. P. Dobkin, and H. Huhdanpaa, The quickhull alogorithm for convex sets, The ACM Transaction on Mathematical Software **22** (4), 469 (1996).
[102] L. P. Cook and W. Wong-Ng, Impact of Recent Advances in Synthesis and Processing of Ceramic Superconductors, in Ceramic Transactions 84, W. Wong-Ng, U. Balachandran, and A. S. Bhalla, eds., Amer. Ceram. Soc. (1998) p. 41.

About the authors: *Winnie Wong-Ng is a reserach chemist in the Phase Equilibria group of the Ceramics Division, Materials Science and Engineering Laboratory at NIST, Gaithersburg. She has been actively engaged in research on the phase equilibria, crystallography and crystal chemistry of high temperature superconductor materials since 1986. Lawrence P. Cook is also a research scientist in the Phase Equilibria group of the Ceramics Division, Materials Science and Engineering Laboratory at NIST. His expertise includes differential thermal/thermogravimetric analysis, scanning electron microscopy/energy dispersive spectrometry and phase equilibria modelling. Anthony Kearlsey is a member of the Mathematical and Computational Science Division at NIST. His research involves developing numerical algorithms. In 1998, he was awarded a Presidential Early Career Award for his work on Numerical Methods for Optimization. W. Greenwood was a graduate student in the Geology Department of the University of Maryland, College Park. The authors have developed a unique method for quantitative determination of liquid compositions in equilibrium with the high-T_c superconductor materials, which is critical for the liquidus determination of these complicated multicomponent systems. The National Institute of Standards and Technology is an agency of the Technology Administration, U.S. Department of Commerce.*

JOURNAL OF SOLID STATE CHEMISTRY 85, 117–132 (1990)

Crystal Chemistry and Phase Equilibria Studies of the $BaO(BaCO_3)$–R_2O_3–CuO Systems. IV. Crystal Chemistry and Subsolidus Phase Relationship Studies of the CuO-Rich Region of the Ternary Diagrams, R = Lanthanides

WINNIE WONG-NG, BORIS PARETZKIN, AND EDWIN R. FULLER, JR.

Ceramics Division, IMSE, National Institute of Standards and Technology, Gaithersburg, Maryland 20899

Received August 16, 1989; in revised form November 20, 1989

In the $BaO(BaCO_3)$–R_2O_3–CuO systems, where R = lanthanides and yttrium, general trends of phase formation, solid solution formation, and phase relationships are correlated with the ionic size of R. In air at 950°C the phase relationships in the CuO-rich region of these ternary diagrams progressively change from the La system through the Nd, Sm, Eu, Gd, Y, Ho systems to the Er system. First, the La system has the greatest number of ternary compounds. Second, the superconductor material, $Ba_2RCu_3O_{6+x}$, exhibits a solid solution of $Ba_{2-z}R_{1+z}Cu_3O_{6+x}$ for the first half of the lanthanide elements with a range of formation which varies with the ionic size of R. Third, a trend is observed regarding the tie-line connections between BaR_2CuO_5, CuO, the phases $Ba_{2-z}R_{1+z}Cu_3O_{6+x}$, and the binary phase R_2CuO_4 or $R_2Cu_2O_5$. For the first half of the lanthanides, except for La, a compatibility join is found to connect R_2CuO_4 and the tetragonal end member of the $Ba_{2-z}R_{1+z}Cu_3O_{6+x}$ phase. In systems where R has a smaller ionic size, R = Eu and beyond, the tie-line connection switches to join the BaR_2CuO_5 phase and the CuO phase. For R = Dy and beyond, the binary phase R_2CuO_4 is replaced by the binary phase $R_2Cu_2O_5$.

Introduction

Despite recent worldwide efforts in superconductivity research, a lack of thorough fundamental understanding of the Ba–Y–Cu–O systems still remains. In addition, problems such as low critical current density, flux creep, and poor mechanical properties still render practical applications of these materials as a great challenge. The discovery that substitution of most lanthanide elements, R, for Y also produces a superconductor with a transition temperature ≈90 K (*1*, *30*) provides numerous alternative materials for investigations of possible desirable properties.

Since knowledge of phase equilibria and crystal chemistry is essential for controlling processing parameters and understanding material properties, systematic studies of the Ba–R–Cu–O systems are crucial. As part of an ongoing effort to understand the crystal chemistry and phase equilibria of the $BaO(BaCO_3)$–R_2O_3–CuO systems (*2*–*9*), we have initiated a systematic investigation of trends in phase formation and solid solution formation of selected binary and ternary compounds in the $BaO(BaCO_3)$–

0022-4596/90 $3.00

R_2O_3–CuO systems and trends in structural phase transformation between the orthorhombic and tetragonal phases of the superconductor material, $Ba_2RCu_3O_{6+x}$, as a function of the ionic size of the element R.

Solid solution formation for a material is also of technological importance. For example, one may control and correlate properties and processing parameters by varying the composition of the materials. In a recent study correlating superconducting properties with solid solution formation in the series $Ba_{2-z}R_{1+z}Cu_3O_{6+x}$, where R = Nd, Sm, Eu, and Gd, Blendell *et al.* (*9*) observed that the amount of substitution of a lanthanide for barium decreases regularly with the decreasing size of R^{3+}: the larger the mismatch of the ionic size between R^{3+} and Ba^{2+}, the narrower the extent of solid solution. The solid solution formation terminates at Gd, which seems to separate the different behavior of the earlier and later lanthanide elements. Recently, we have investigated the $Ba_{2-z}Sm_{1+z}Cu_3O_{6+x}$ and the $Ba_{2-z}La_{1+z}Cu_3O_{6+x}$ series and are able to establish a more general trend of solid solution formation. Current results are described herein.

Although solid solution members of the $Ba_{2-z}La_{1+z}Cu_3O_{6+x}$ system have been characterized by neutron diffraction by David *et al.* (*10*), Segré *et al.* (*11*), and Sunshine *et al.* (*12*), the solid solution range was not conclusively determined by these investigators and was assigned to be $z \lesssim 0.5$. Our studies of the solid solution formation of $Ba_{2-z}R_{1+z}Cu_3O_{6+x}$, where R = Nd, Eu, and Gd (*9*) indicated that the range of solid solution of the Nd system extends to $z \leq 0.7$. As the sizes of La^{3+} and Ba^{2+} are closer to each other than those of Nd^{3+} and Ba^{2+}, we expect the extent of solid solution in the La system to be greater or comparable to that of the Nd system. Accordingly, the range of solid solution of the $Ba_{2-z}La_{1+z}Cu_3O_{6+x}$ system was reinvestigated in the present work.

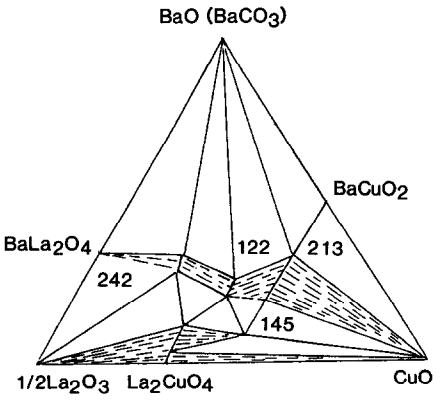

FIG. 1. Subsolidus phase diagram for the Ba–La–Cu–O system at 950°C in air, after Kilbanow *et al.* (*13*).

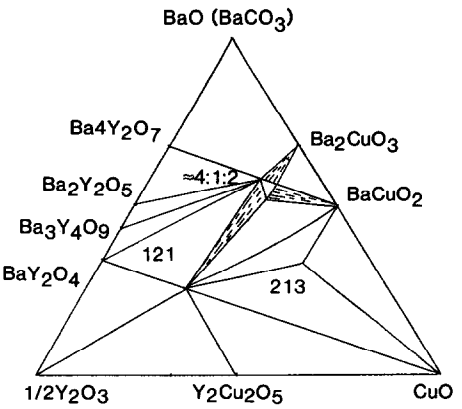

FIG. 2. Subsolidus phase diagram for the Ba–Y–Cu–O system at 950°C in air, after Roth *et al.* (*14*).

Ternary phase diagram studies of the Ba–La–Cu–O and Ba–Y–Cu–O systems at 950°C in air have been conducted by Kilbanow *et al.* (*13*) and Roth *et al.* (*14*), which are shown in Figs. 1 and 2, respectively. (Figure 1 has been modified to include present results.) Phase compatibility relationships are found to be substantially different for these two systems. The large difference in size of the La^{3+} and Y^{3+} ions undoubtedly has a great impact on their

crystal chemistry. Part of the goal of this study is to characterize and compare features of phase formation and phase relationships of compounds in the ternary phase diagrams of the $BaO(BACO_3)$–R_2O_3–CuO systems near the CuO corner.

Experimental

Solid state reaction techniques were employed for all sample preparation. Similar heat treatment procedures were adopted for all series of $Ba_{2-z}R_{1+z}Cu_3O_{6+x}$ materials. Table I shows the compositions prepared for the several solid solution series which we have investigated. Most compositions were prepared from stoichiometric mixtures of CuO, R_2O_3, and $BaCO_3$. In the case of R = La, $La(OH)_3$ was used instead of La_2O_3. Before each firing and annealing, the powder was pressed into pellets and placed on MgO single crystals, which were then set on a silica brick. The pellets were heat treated at both 850 and 900°C for 1 day, then fired in air at 950°C. Air-quenching was performed by removing the sample and brick together from the furnace and placing them on the bench top. Cooling time to room temperature for the sample was estimated to be about 3 to 5 min. Several regrindings and annealings took place until a single phase material was confirmed by the X-ray powder diffraction.

TABLE I

COMPOSITION, "z," OF SAMPLES $Ba_{2-z}R_{1+z}Cu_3O_{6+x}$ PREPARED AT 950°C IN AIR

R	z
La	0.0, 0.1, 0.2, 0.3, 0.4, 0.5, 0.6, 0.7, 0.8, 0.9, 1.0
Nd	0.0, 0.1, 0.2, 0.3, 0.4, 0.5, 0.6, 0.7, 0.8, 0.9, 1.0
Sm	0.0, 0.1, 0.2, 0.3, 0.4, 0.5, 0.6, 0.7, 0.8, 0.9, 1.0
Eu	−0.1, 0.0, 0.1, 0.2, 0.3, 0.4, 0.5, 0.6, 0.7, 0.8, 0.9, 1.0
Gd	0.0, 0.1, 0.2, 0.3, 0.5
Dy	0.0, 0.1, 0.2, 0.5
Y	0.0, 0.1, 0.5
Er	−0.1, 0.0, 0.1, 0.5
Lu	0.5

TABLE II

COMPOSITIONS NEAR THE CuO CORNERS PREPARED FOR THE TERNARY PHASE DIAGRAMS, $BaO:R_2O_3$:CuO, IN AIR

R	Compositions $BaO:\frac{1}{2}R_2O_3:CuO$
La	10:40:50, 20:40:40
Pr	10:40:50, 20:40:40
Nd	10:60:30, 15:50:35, 10:40:50, 15:15:70, 20:10:70, 20:10:70, 25:15:60, 25:40:35, 27:33:40, 30:30:40, 35:25:40, 18:37:45, 58:08:34, 53:13:34, 21:35:44, 25:28:47, 20:40:40
Sm	25:15:60, 15:15:70, 30:30:40, 10:60:30, 25:28:47, 28:25:47, 32:20:48, 10:40:50, 20:40:40
Eu	25:15:60, 15:15:70, 30:30:40, 10:60:30, 25:28:47, 28:25:47, 32:20:48, 10:40:50
Gd	30:30:40, 10:60:30, 25:15:60, 30:25:45, 10:40:50, 32:20:48, 34:18:48
Er	32:20:48, 10:50:40, 10:40:50, 15:30:55, 20:10:70, 25:25:50, 30:30:40, 35:30:35

To study phase relationships in the vicinity of the superconductor solid solution, $Ba_{2-z}R_{1+z}Cu_3O_{6+x}$, and the "green phase" compound, BaR_2CuO_5, compositions near the CuO corner of selected $BaO(BaCO_3)$–R_2O_3–CuO systems were also prepared. These compositions are indicated in Table II for the La, Pr, Nd, Sm, Eu, Gd, and Er systems. The Nd system was studied in more detail and will be reported separately (*4*). Most final sinterings were performed at 950°C and air-quenched. For compositions very close to the CuO corners, a temperature of 920°C was used instead to avoid melting. Tie-line relations were established by X-ray powder diffraction characterization.

Results and Discussion

Results of the ternary phase compatibility diagrams of the systems $BaO(BaCO_3)$–R_2O_3–CuO in the vicinity of the CuO corners, where R = La, Nd, Sm, Eu, Gd, Y, and Er are shown in Fig. 3. Since exact tie-line connection would require detailed lattice parameter determination, the tie lines connecting the solid solution series in this report are schematic only. Proceeding from the La system, which has the largest ionic size of R, toward the Er system with a smaller ionic size, a general trend of phase formation, solid solution formation, and phase relationship is found to be correlated with the ionic size of R. Several features of the progressive changes in the appearance of these ternary diagrams near the CuO corner will be discussed in detail below. In brief, these features are (1) the La system has the largest number of ternary compounds and solid solution series; this number decreases as the size of R decreases. (Although it has been reported by de Leeuw *et al.* (*15*) that if BaO_2 or $Ba(NO_3)_2$ are used other phases such as $Ba_4YCu_3O_{8.5}$ and $Ba_8Y_3Cu_5O_{1.5}$ also form, these phases have not been confirmed in this laboratory.) (2) The superconductor material, $Ba_2RCu_3O_{6+x}$, for the first half of the lanthanide elements, i.e., R = La, Nd, Sm, Eu, and Gd, which are relatively larger in size, exhibit a solid solution of $Ba_{2-z}R_{1+z}Cu_3O_{6+x}$ with a range of formation which decreases as the size of R decreases; this solid solution region terminates at Dy and beyond, where presumably the superconductor phase assumes a point stoichiometry; (3) A trend is observed regarding the tie-line connections between BaR_2CuO_5, CuO, the superconductor phases $Ba_{2-z}R_{1+z}Cu_3O_{6+x}$, and the binary phase R_2CuO_4, or $R_2Cu_2O_5$; note that the binary phase R_2CuO_4 is replaced by the binary phase $R_2Cu_2O_5$ after the tie-line connection changes.

Current results of phase formation for several series of compounds and solid solutions in the $BaO(BaCO_3)$–R_2O_3–CuO systems are discussed individually in the sections below. Following this, features of the tie-line relationship of the four phases near the CuO corner are discussed. Crystal stuctures for some of these phases are also discussed.

I. Phase Formation near CuO Corner

1. BaR_2CuO_5 and $Ba_{2+2x}R_{4-2x}Cu_{2-x}O_{10-2x}$ (1:2:1), R = La, Nd

Details of the phase formation of the 1:2:1 phases have been reported elsewhere (*5, 6, 16, 17*). In brief, under ambient conditions, the commonly known "green phase", or BaR_2CuO_5, has been prepared for R = Sm, Eu, Gd, Dy, Y, Er, Tm, Yb, and Lu. Among the oxides with a stable R^{3+} valence state, there is a size range of R for which this phase forms. However, this phase does not form with lanthanides of larger ionic size. For example, the formation of green phases for $R = La^{3+}$ and Nd^{3+} does not take place. The materials formed in this case are brown and are found to have a completely different crystal structure from that of the "green phase". While all green phase materials are orthorhombic with space group *Pbnm*(62), Z = 4, the "brown phases" tend to form solid solutions of $Ba_{2+2x}R_{4-2x}Cu_{2-x}O_{10-2x}$, with a tetragonal space group of *P*4/*mbm*(127). The solid solution range is $0.15 \leq x \leq 0.25$ for the La system and $0.0 \leq x \leq 0.1$ for the Nd system. Note that the La solid solution series does not include the stoichiometric compound with $x = 0$.

In the green phase structure, each yttrium ion is surrounded by seven oxygen atoms, as shown in Fig. 4. The framework can be considered as built up from distorted monocapped trigonal prisms, RO_7, which share one triangular face forming R_2O_{11} blocks. There is an apparent size limit, bounded by Sm, beyond which stability of

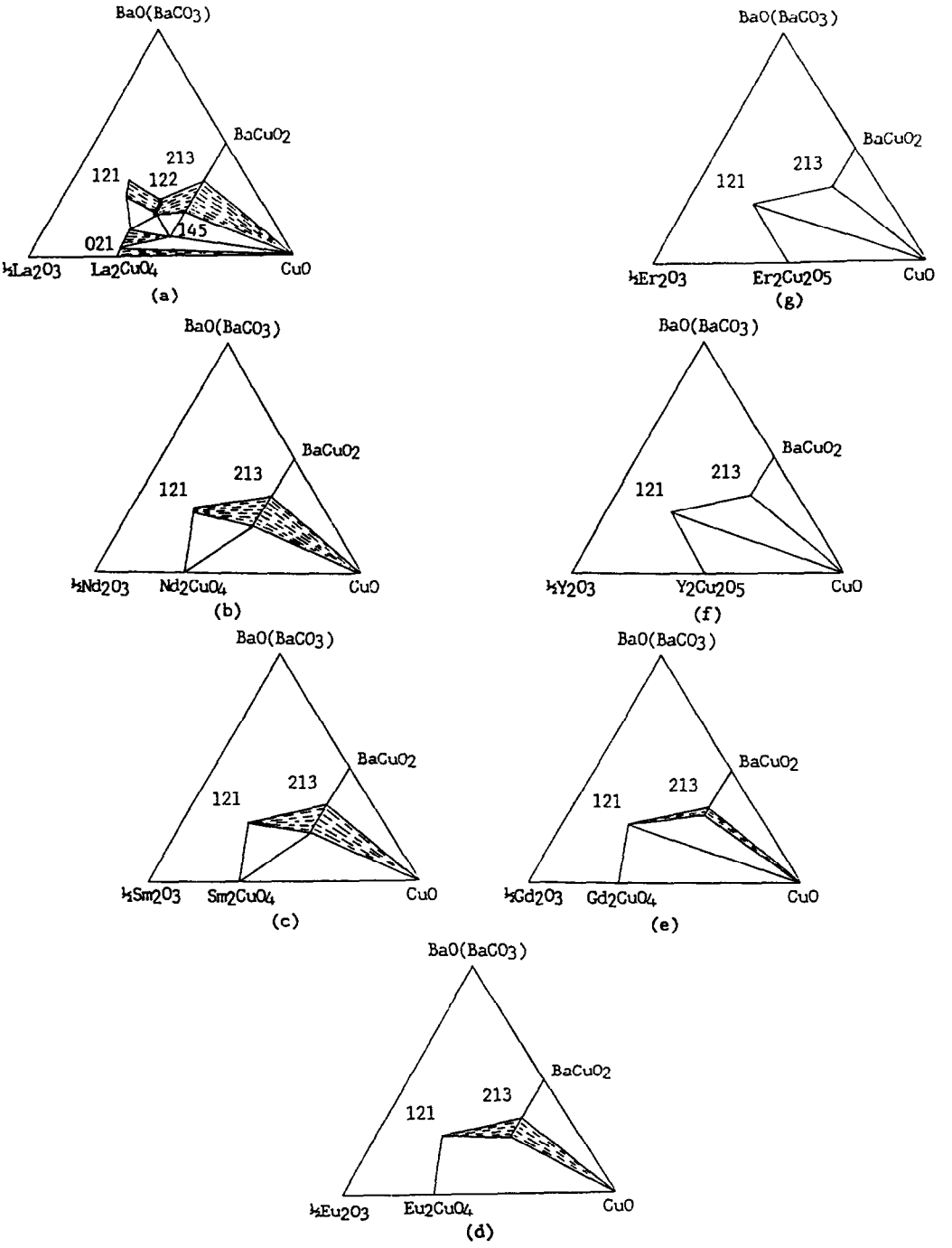

FIG. 3. Subsolidus phase compatibility diagrams of BaO–$\frac{1}{2}R_2O_3$–CuO near the CuO-rich region at 950°C in air for (a) La, (b) Nd, (c) Sm, (d) Eu, (e) Gd, (f) Y, and (g) Er.

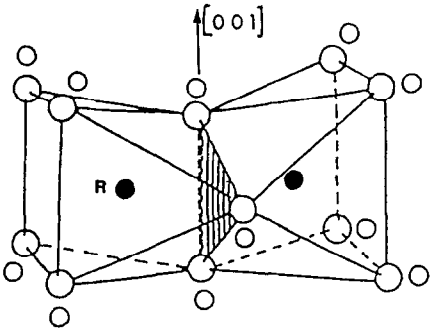

FIG. 4. Polyhedral environment of RO_7 and R_2O_{11} found in the structure of BaR_2CuO_5, R = Sm, Eu, Gd, Dy, Y, Ho, Er, Tm, Yb, and Lu.

the distorted monocapped trigonal prism, RO_7, is unattainable. The framework of the La and Nd materials is principally built from edge- and face-sharing RO_{10} and RO_8 polyhedra as illustrated in Figs. 5a and 5b. These octahedra and decahedra provide large enough space to accommodate the La^{3+} and Nd^{3+} ions.

2. $Ba_{2-z}R_{1+z}Cu_3O_{6+x}$ (2 : 1 : 3), R = La, Pr, Nd, Sm, Eu, and Gd

Results of the solid solution investigation of the R = La series show that the solid solution range indeed extends beyond z = 0.5. In Fig. 6, X-ray diffraction patterns of the $Ba_{2-z}La_{1+z}Cu_3O_{6+x}$ compositions with z = 0.5 to 0.9 are shown. A small number of peaks corresponding to $BaLa_4Cu_5O_{13+x}$ start to appear at $z \approx 0.8$. Figure 7 shows the X-ray powder diffraction patterns for selected compositions of $Ba_{2-z}Eu_{1+z}Cu_3O_{6+x}$, indicating a solid solution range of $z \leq 0.5$. The solid solution range is different for each of these series. The upper limit of the solid solution series is discernible by the presence of X-ray diffraction peaks from a different phase. For example, in the region around 2θ of 28–29° one detects the presence of the green phase BaR_2CuO_5 and CuO when R = Eu, Gd, and Er. The Sm samples show a solid solution range for $z \leq$ 0.7. The Gd sample, on the other hand, shows only a small range of $z \leq 0.2$. Solid solution ceases to exist at Dy, Er, and Y, or at least is less than $z \approx 0.1$, and this is so presumably also for superconductors with smaller R. The tendency of the solid solution formation is very great in the La system and the point compound $Ba_2LaCu_3O_{6+x}$ does not form; the lower limit of the solid solution is bounded by approximately $z >$ 0.1.

The size compatibility between the Ba^{2+} and R^{3+} is a predominant factor governing the formation of this solid solution. Shannon's ionic radii of lanthanides R^{3+}, where R = La, Pr, Nd, Sm, Eu, Gd, Dy, Y, and Er, using the coordination number of nine are listed in Tables III, IV, and V. Y is inserted according to its ionic size. The ionic radius of Ba^{2+} with a similar coordination environment is 0.147 nm, which is most comparable to that of La^{3+} of 0.122 nm. As the mismatch between R^{3+} and Ba^{2+} increases, the range of substitution decreases. Table III summarizes the approximate upper limit of the solid solution range of $Ba_{2-z}R_{1+z}Cu_3O_{6+x}$.

Another feature observed in all the $Ba_{2-z}R_{1+z}Cu_3O_{6+x}$ series is the structural phase transformation from an orthorhombic to a tetragonal structure as the value of

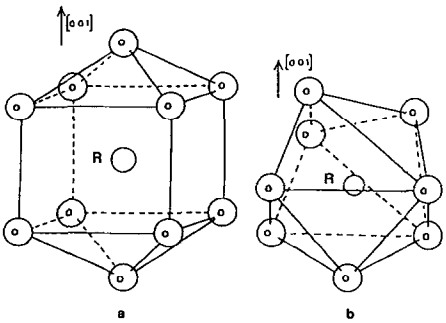

FIG. 5. Polyhedral environment of (a) RO_{10} and (b) RO_8 found in the structure of $Ba_{2+2x}R_{4-2x}Cu_{2-x}O_{10-2x}$, R = La and Nd.

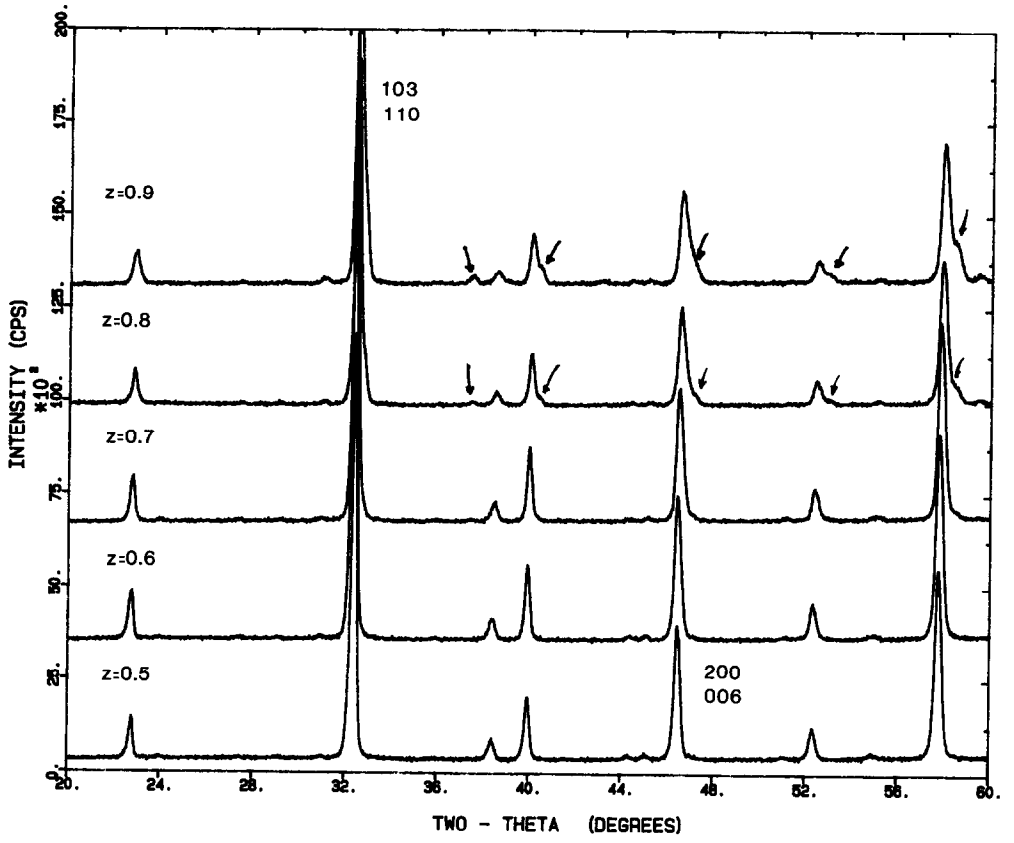

FIG. 6. X-ray diffraction patterns of $Ba_{2-z}La_{1+z}Cu_3O_{6+x}$. The appearance of the $BaLa_4Cu_5O_{13+x}$ phase is indicated by the arrows for z = 0.8 and 0.9.

z increases. Since the high temperature (950°C) phase is most likely the tetragonal structure (at least this is the case for R = Sm and Gd with z = 0 (*2, 3, 7*)), this transformation can depend on how the quenching is performed. Results discussed below only pertain to samples that were prepared at 950°C in air and air-quenched by pulling them from the furnace. The X-ray diffraction patterns of $Ba_{2-z}Eu_{1+z}Cu_3O_{6+x}$ shown in Fig. 7 illustrate the progressive changes of peak shape and convergence of multiplets into singlets going from the orthorhombic to the tetragonal structure. Phase transformation of the $Ba_{2-z}La_{1-z}Cu_3O_{6+x}$ series has been reported to take place at a z value of 0.15 (*12*). Our X-ray diffraction patterns are consistent with this result, showing a phase transformation at a z value between 0.1 and 0.2. For the Nd,

TABLE III

SOLID SOLUTION EXTENT OF $Ba_{2-z}R_{1+z}Cu_3O_{6+x}$

R	z	Ionic radius (nm)
La	≤ 0.7	0.1216
Nd	≤ 0.7	0.1163
Sm	≤ 0.7	0.1132
Eu	≤ 0.5	0.1120
Gd	≤ 0.2	0.1107

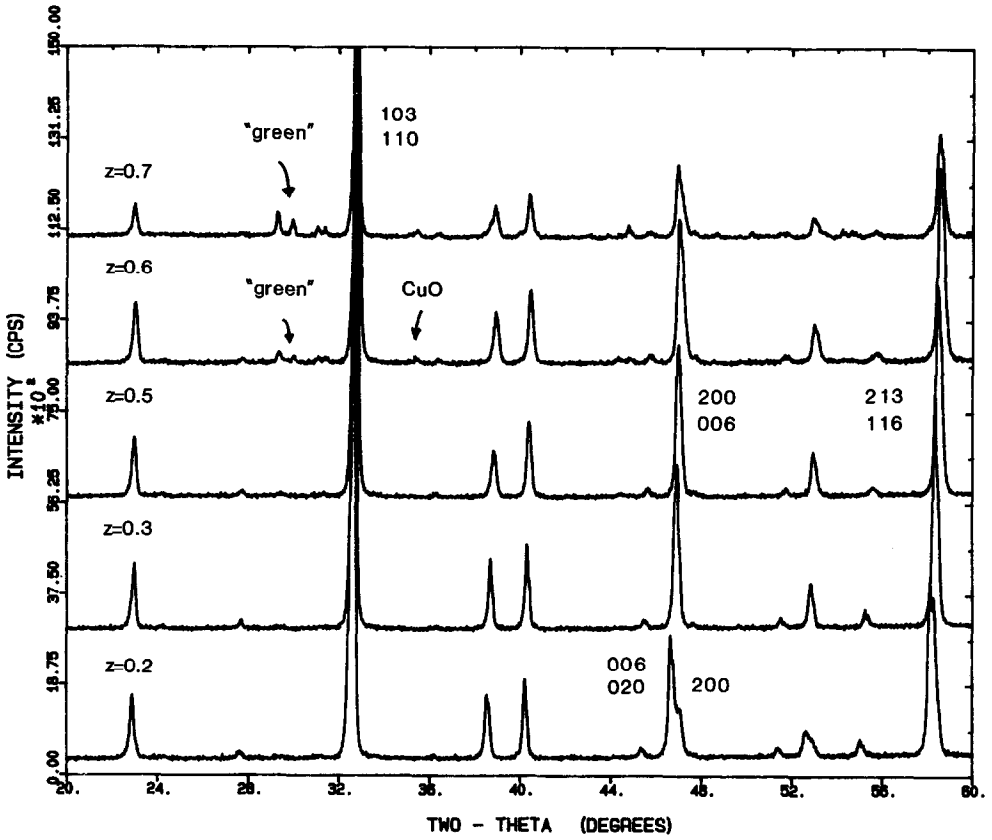

FIG. 7. X-ray diffraction patterns of $Ba_{2-z}Eu_{1+z}Cu_3O_{6+x}$.

Sm, and Eu series the corresponding z values for the structural phase transformation are approximately the same; all found to be between $z = 0.2$ and 0.3. As the samples in each $Ba_{2-z}R_{1+z}Cu_3O_{6+x}$ series were prepared at intervals in z of 0.1, we are not able to distinguish any differences at this stage. Whether the z value varies as a function of the size of R is a subject of interest to be investigated in the near future.

X-ray characterization and X-ray powder standard diffraction patterns of the tetragonal $Ba_{1.5}R_{1.5}Cu_3O_{7+x}$, with R = La, Pr, Nd, Sm, and Eu composition, has been reported (*8*). These tetragonal phases have up to 25% substitution of R in the Ba sites and therefore the chemical formula can be represented as $(Ba_{0.75}R_{0.25})_2RCu_3O_{7+x}$, or simply referred to as the $Ba_3R_3Cu_6O_{14+x}$ (336) composition. The crystallographic relationship of these five materials can be described as $a = b \approx \frac{1}{3}c$, indicating that as the R^{3+} ions replace the Ba^{2+} ions to an extent of 25% the unit cell content can be considered as a stack of three pseudo-cubes. The $Ba_3La_3Cu_6O_{14+x}$ system was first studied by Provost *et al.* (*18*) and the crystal structure has been determined by Sunshine *et al.* (*12*) using the neutron powder diffraction technique. This structure is similar to the structure of the superconductor $Ba_2YCu_3O_{6+x}$ except it is tetragonal with smaller unit cell volume, and with oxygen partially located at both the *a*- and *b*-basal axes. The struc-

tures of the Pr, Nd, Sm, and Eu analogs are presumably isostructural with the La compound because of the similarity of the X-ray diffraction patterns. Neutron diffraction study of the $Ba_3Nd_3Cu_6O_{14+x}$ phase is currently underway (*19*) to confirm the structure as well as the oxygen content of this material.

The superconductivity properties of the solid solution are currently being selectively investigated in terms of the ac magnetic susceptibility and critical current density measurements. For each series of materials a general trend of T_c diminishing as the z value increases has been observed. The T_c values, the fraction of superconductivity, and the critical current density are currently being studied and will be reported separately.

3. $BaR_4Cu_5O_{13+x}$ (*1 : 4 : 5*)

This oxygen defect perovskite is characterized by a mixed valence of Cu(II) and Cu(III) despite the presence of numerous oxygen vacancies. The La system appears to be the only one among the lanthanide systems that forms this black metallic conductor. The $BaLa_4Cu_5O_{13+x}$ compound is tetragonal with space group $P4/m$. The lattice parameters of a sample which was prepared in air at 950°C was found to have lattice parameters a = 0.86602(5) nm and c = 0.38629(3) nm (*20*) at approximately 25°C, which are closely related to that of the cubic perovskite: $a \approx a_p \sqrt{5}$ and $c = a_p$ = 3.8594. Michel *et al.* (*21*) described the framework $[Cu_5O_{13}]$ to be built up from corner-sharing CuO_5 pyramids and CuO_6 octahedra forming hexagonal tunnels and perovskite cages where the La^{3+} and Ba^{2+} ions are located in an ordered manner. Figure 8 (*22*) shows the structure of $BaLa_4Cu_5O_{13}$ in which each CuO octahedron shares four corners with four pyramids, and the two remaining corners with two other octahedra. Each pyramid is then connected to four other pyramids and one octahedron. Oxygen vacancies, which are found to be between pairs of CuO_5, form one-dimensional channels along the z-axis. The lanthanum ions are located in the hexagonal tunnels whereas the barium ions are located in the perovskite tunnels.

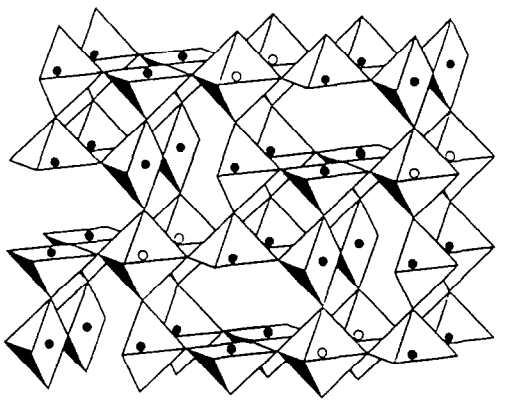

FIG. 8. Crystal structure of the compound $BaLa_4Cu_5O_{13}$ (*18*). The solid and open circles represent Cu atoms belonging to the CuO_5 pyramids and the CuO_6 octahedra, respectively. La^{3+} and Ba^{2+} ions are located in the hexagonal and perovskite tunnels, respectively. The z-axis points out of the plane of the paper.

4. $Ba_{1+x}R_{2-x}Cu_2O_{6-x/2}$ (*1 : 2 : 2*)

Among the $BaO : \frac{1}{2}R_2O_3 : CuO$ systems, the black 1 : 2 : 2 phase $BaR_2Cu_2O_6$ has only been prepared successfully in the La analog. The compounds $A_{1+x}La_{2-x}Cu_2O_{6-x/2}$ were first isolated by Nguyen *et al.* (*23*) with $0 \le x \le 0.14$ for A = Sr and x = 0.10 for A = Ca. These compounds are reported to be tetragonal with $a \approx 0.390$ nm and $c \approx 2.0$ nm and with a space group of $I4/mmm$. The structure, which is derived from that of $Sr_3Ti_2O_7$, can be described as an intergrowth of "oxygen-deficient, double-perovskite" layers and of SrO-type layers. These perovskite layers are indicated in Fig. 9. When A = Ba, the extent of solid solution has been found to be $0 \le x \le 0.20$ by Kilbanow *et al.* (*13*). X-ray diffraction studies and lattice parameter determination

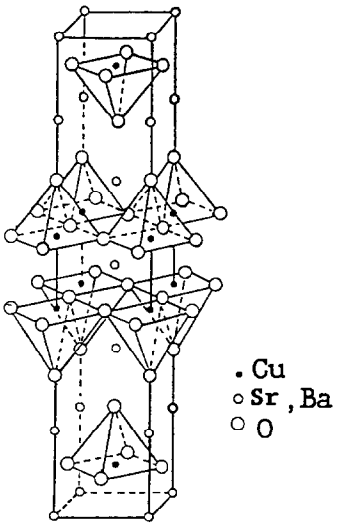

FIG. 9. Crystal structure of the compound $Sr_2La_4Cu_4O_{12}$ showing the oxygen-deficient double perovskite layers (Nguyen *et al.* (*19*)).

for the solid solution series $Ba_{1+x}La_{2-x}Cu_2O_{6-x/2}$ is currently being conducted.

5. R_2CuO_4 (0:2:1)

While all the R_2O_3:CuO systems contain only one binary compound at ambient atmosphere, there exist two distinctive compositions. Binary compounds of 2:1 composition with general formula R_2CuO_4 can be prepared with the lighter and larger size of R, for example with R = La, Pr, Nd, Sm, Eu, and Gd, whereas oxides in the second half of the lanthanide series tend to form a $2(\frac{1}{2}R_2O_3):2CuO$ binary compound $R_2Cu_2O_5$. Not all R_2CuO_4 phases are isostructural. For example, while La_2CuO_4 is orthorhombic with space group *CmCa* (*24*) and has the distorted K_2NiF_4-type structure as shown in Fig. 10, Pr_2CuO_4, Nd_2CuO_4, Sm_2CuO_4, Eu_2CuO_4, and Gd_2CuO_4 are tetragonal with space group *I4/mmm*. These tetragonal structures do not resemble the K_2NiF_4 type but have a coplanar Cu–O layer similar to that found in CaF_2-type structure (*25*). These features are illustrated in Fig. 10. Doping the La_2CuO_4 structure with a small amount of a 2+ ion such as Ba^{2+} and Sr^{2+} changes the structure from orthorhombic to tetragonal (*26, 27*) and results in a superconductor phase. Typical X-ray patterns of the orthorhombic and tetragonal R_2CuO_4 are illustrated with La_2CuO_4 and Nd_2CuO_4 in Fig. 11. Substantial differences of these patterns arising from totally different structures are obvious.

Solid solution formation of the composi-

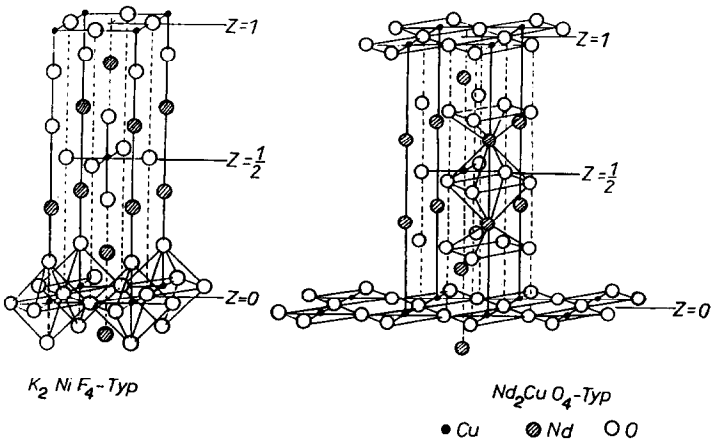

FIG. 10. Crystal structures of R_2CuO_4 for (a) R = La and (b) R = Pr, Nd, Sm, Eu, and Gd.

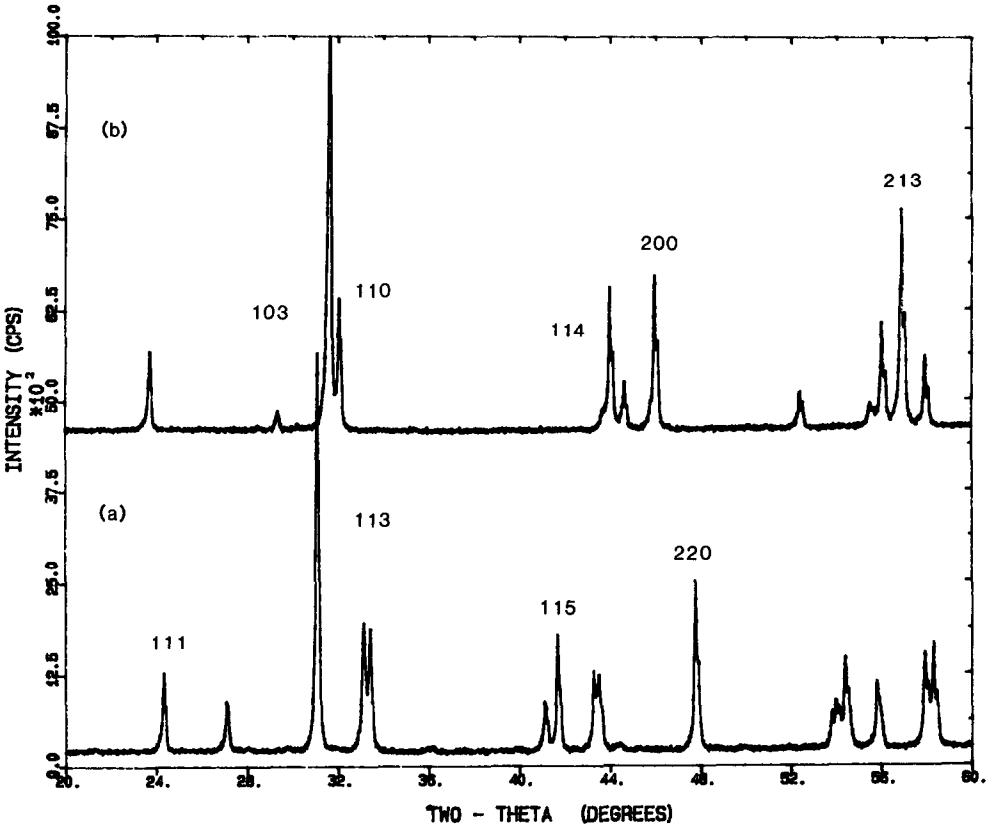

FIG. 11. X-ray diffraction patterns of (a) La_2CuO_4 and (b) Nd_2CuO_4.

tions $(R_{2-x}A_x)CuO_4$ with A = Ba has been studied with R = La (*12*) and that with a solid solution range of $0 \leq x \leq 0.25$ has been reported. This series gives rise to superconductor materials of T_c around 30 K (*28*). Substitution of Nd^{3+} and other smaller R^{3+} by Ba^{2+} in the R_2CuO_4 phases cannot be prepared (with $x \geq 0.1$).

Since crystallographic data are essential for phase characterization, Table IV summarizes these data and the corresponding Powder Diffraction File Number (PDF No.) (*29*) for the binary R_2CuO_4 phases which have been reported in the literature and from this work. The crystallographic data for the "green" and "brown" phases and the high T_c superconductor phases have been reported elsewhere (*5, 29–31*). Figure 12 illustrates a plot of the cell volume V of R_2CuO_4 versus the ionic radii of Shannon. The monotonic decrease in crystallographic volumes, as the ionic radii of the lanthanides decrease across the series, follows the well-known lanthanide contraction. The deviation from this linear dependence of the Gd compound may be due to the special stability associated with the half-filled Gd^{3+} ($4f^7$) f-subshell.

6. $R_2Cu_2O_5$ (0 : 1 : 1)

$R_2Cu_2O_5$ are greenish in color and can be prepared with the second half of the lanthanides, with R = Tb, Dy, Ho, Y, Er, Tm, Yb, and Lu. Structure determinations of

TABLE IV

CRYSTALLOGRAPHIC DATA FOR R_2CuO_4

Compound R_2CuO_4	Space group	Cell parameters a, b, c (nm)	Cell volume V (nm^3)	Density (g/cm^3)	Ionic radius R (nm)	PDF No.
La_2CuO_4	*Fmmm*	0.53556(6) 0.54011(9) 1.3149(5)	0.38035	7.079	0.1216	38-709
$(Ba_{.9}La_{.1})_2CuO_4$	*I4/mmm*	0.37754(6) 1.3236(14)	0.18866	7.130	0.1216	38-1308
Pr_2CuO_4	*I4/mmm*	0.3958 1.2288	0.19250	7.062	0.1179	22-245
Nd_2CuO_4	*I4/mmm*	0.394366(12) 1.21693(5) (at ≈25°C)	0.18926	7.300	0.1163	39-1390 (*32*)
Sm_2CuO_4	*I4/mmm*	0.3905 1.1938	0.18204	7.814	0.1132	24-998
Eu_2CuO_4	*I4/mmm*	0.3895 1.1887	0.18034	7.946	0.1120	24-399
Gd_2CuO_4	*I4/mmm*	0.3889 1.1861	0.17939	8.184	0.1107	24-422

$R_2Cu_2O_5$ have been controversial in the past 25 years. In 1964, Schmitz-DuMont and Kasper (*33*) identified $R_2Cu_2O_5$, where R = Y, Dy, Er, Yb, and Tb, to be orthorhombic double oxides having $In_2Cu_2O_5$-type structure. $In_2Cu_2O_5$ was later redetermined by Bergerhoff and Kasper (*34*) to be monoclinic with space group $P2$ and cell parame-

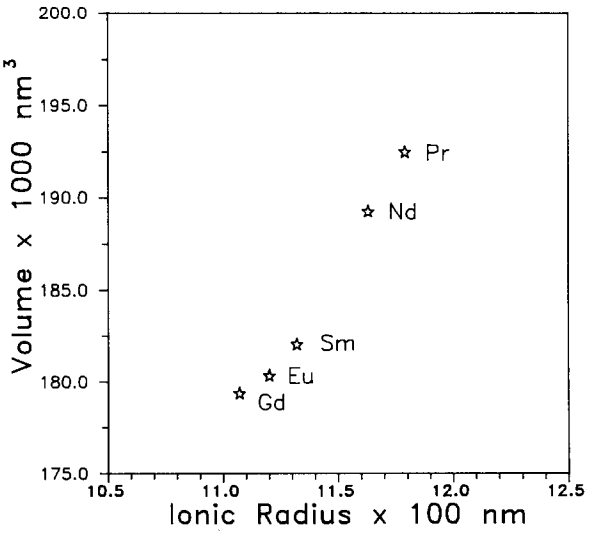

FIG. 12. Dependence of the unit cell volume of R_2CuO_4 on the ionic radius of R for R = Pr, Nd, Sm, Eu, and Gd.

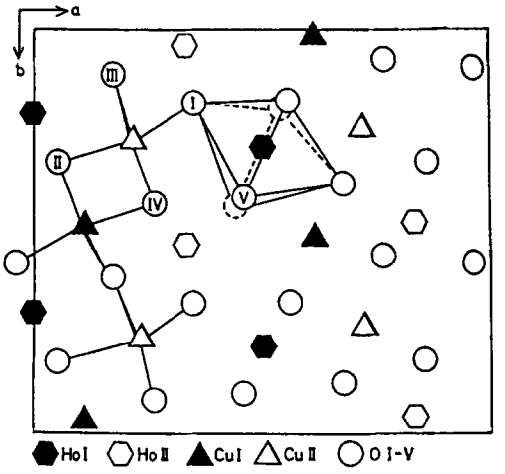

FIG. 13. Projection for $Ho_2Cu_2O_5$ along [001].

ters of a = 2.462, b = 1.0537, c = 0.3280 nm, and γ = 133°. The structure consists of a pseudo-orthorhombic framework of InO_6 polyhedra with the oxygen atoms at the corners.

In 1977, Freund and Muller-Buschbaum (*35*) reported the structure of the Ho analog, using single crystals obtained by melting the oxide mixture (2 CuO : 1 Ho_2O_3) with KF as a flux, to be orthorhombic. They found that the crystal structures of the Ho and the In compounds (*34*) are significantly different, particularly the coordination sphere around the Cu^{2+}. Figure 13 shows the atom distribution of the unit cell of $Ho_2Cu_2O_5$. Unlike those of many other oxo–cuprates, the Cu^{2+} has been found to have four nearest oxygen neighbors arranged in a distorted tetrahedron configuration. Figure 13 further shows that two each of these polyhedra share a common edge and are connected via corners in a wavelike chain along [010]. The Ho^{3+} ions are surrounded by octahedra which form one-dimensional infinite chains connected via edges.

The structures and X-ray diffraction patterns of all seven $R_2Cu_2O_5$ compounds were later reexamined by E. Lambert in 1981 and 1982 (*36*). All materials were found to be isostructural and have the $Ho_2Cu_2O_5$-type structure with space group $Pna2_1$. Table V summarizes the crystallographic data and the PDF No. for eight binary $R_2Cu_2O_5$ phases, where R = lanthanide and yttrium. Figure 14 illustrates a plot of the cell volume V, of $R_2Cu_2O_5$ versus the ionic radii of Shannon. Similar to the corresponding plot of the R_2CuO_4 compounds, a monotonic decrease in crystallographic volumes is also observed as the ionic radius of the lanthanides decreases across the series.

II. Tie-Line Relationships

After the description of the crystal chemistry of individual phases and solid solution series in the CuO-rich region of the BaO–$\frac{1}{2}R_2O_3$–CuO systems, we are in a position to discuss the trend of the ternary diagrams

TABLE V

CRYSTALLOGRAPHIC DATA FOR $R_2Cu_2O_5$

Compound $R_2Cu_2O_5$[a]	Cell parameters a, b, c (nm)	Cell volume V (nm^3)	Density (g/cm^3)	Ionic radius R (nm)	PDF No.
$Tb_2Cu_2O_5$	1.0861 0.35455 1.2535	0.48269	7.223	0.1095	34-385
$Dy_2Cu_2O_5$	1.0837 0.35194 1.2485	0.47617	7.422	0.1083	33-455
$Y_2Cu_2O_5$	1.0799 0.34960 1.2456	0.47025	5.537	0.1075	33-511
$Ho_2Cu_2O_5$	1.0806 0.34950 1.2470	0.47095	7.573	0.1072	33-458
$Er_2Cu_2O_5$	1.0776 0.34714 1.2438	0.46528	7.732	0.1062	33-456
$Tm_2Cu_2O_5$	1.0742 0.34565 1.2382	0.45974	7.873	0.1052	34-386
$Yb_2Cu_2O_5$	1.0724 0.34329 1.2349	0.45462	8.082	0.1042	33-507
$Lu_2Cu_2O_5$	1.0698 0.34102 1.2358	0.45085	8.206	0.1032	34-387

[a] All isostructural, orthorhombic with space group $Pna2_1$.

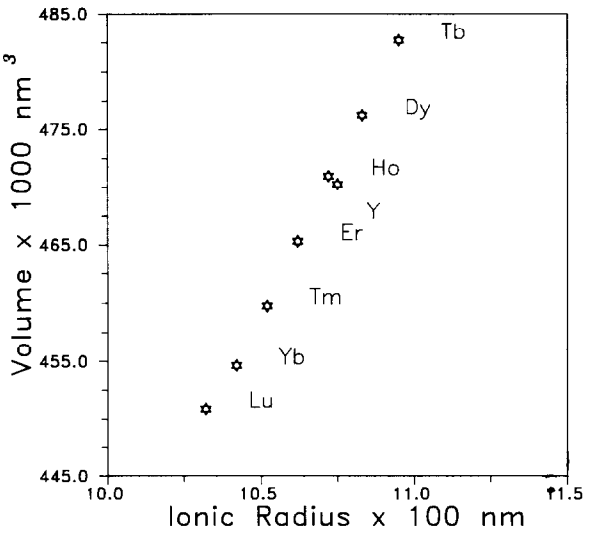

FIG. 14. Dependence of the unit cell volume of $R_2Cu_2O_5$ on the ionic radius of R for R = Tb, Dy, Y, Ho, Er, Tm, Yb, and Lu.

illustrated in Fig. 3. The La diagram appears to be the most complicated one. The presence of four solid solution series ($Ba_{2+2x}R_{4-2x}Cu_{2-x}O_{10-2x}$, $Ba_{2-z}R_{1+z}Cu_3O_{6+x}$, $Ba_{1+x}R_{2-x}Cu_2O_{6-x/2}$, and $R_{2-x}Ba_xCuO_4$) as well as the compound $BaR_4Cu_5O_{13+x}$ in the La system further makes the tie-line connection very different from the rest of the lanthanide series. The number of solid solution series changes into two in the Nd system ($Ba_{2+2x}R_{4-2x}Cu_{2-x}O_{10-2x}$, $Ba_{2-z}R_{1+z}Cu_3O_{6+x}$) and reduces into one at the Sm diagram ($Ba_{2-z}R_{1+z}Cu_3O_{6+x}$). The extent of the $Ba_{2-z}R_{1+z}Cu_3O_{6+x}$ solid solution decreases as the mismatch between Ba^{2+} and R^{3+} increases. This range of solid solution diminishes and ceases to exist beyond R = Gd. After the Gd system, only stoichiometric point compounds are found in the CuO-rich region.

Another feature of these diagrams is illustrated by the tie-line connection between the binary compound along the $\frac{1}{2}R_2O_3$–CuO edge to the 121 phase and the 213 series. As has been discussed previously, the R_2CuO_4 compound can only be prepared with the larger size of R, namely, from La to Gd, while the $R_2Cu_2O_5$ phase exists with the smaller size of R. The tie-line connection between this binary composition R_2CuO_4/$R_2Cu_2O_5$ to the 121 phase or the high T_c superconductor compositions appear to reflect the different extent of the $Ba_{2-z}R_{1+z}Cu_3O_{6+x}$ solid solution. When Rs are relatively large and the extent of the solid solution line is long, e.g., R = La, Nd, and Sm, a compatibility line is found to connect the R_2CuO_4 and the tetragonal end member of the $Ba_{2-x}R_{1+x}Cu_3O_{6+x}$ phase. In the systems with R = Eu and Gd, the tie-line connection switches to join the CuO phase and the $BaEu_2CuO_5$/$BaGd_2CuO_5$ phase, respectively. This trend remains hereafter in the systems with smaller Rs.

Conclusion

The size of the lanthanides, R^{3+}, has been found to have a profound effect on the trend of phase and solid solution formation

as well as phase compatibility relationships in the CuO-rich region of the BaO–$\frac{1}{2}R_2O_3$–CuO systems. The larger the size of R^{3+}, the greater the number of ternary compounds and solid solution series formed. In the series of $Ba_{2-z}R_{1+z}Cu_3O_{6+x}$, solid solution formation was identified to exist with the larger size rare-earth ions, namely, La, Pr, Nd, Sm, Eu, and Gd. The range of this solid solution formation decreases with increasing difference between the size of Ba^{2+} and R^{3+}. The trend of tie-line connection is also found to be dependent on the size of R^{3+}.

It is hoped that the relationships among compositions, structures, and the size of R^{3+} discussed in this report will enhance the understanding of the physical properties of high T_c superconductors and improve the strategy both for processing these materials with improved properties and for the search for new materials. Further work will continue in the phase equilibria studies of these lanthanide systems including the investigation of melting relationships and primary phase field determination of selective $Ba_2RCu_3O_{6+x}$ phases and of mixed lanthanide phases.

Acknowledgments

This project is partially supported by the Electric Power Research Institute. The valuable discussion with Drs. L. P. Cook and R. S. Roth and the critical review of the manuscript by Drs. H. F. McMurdie and S. Dapkunas are appreciated. Acknowledgment is also due to Ms. R. Drew for her performance of the ac magnetic susceptibility measurement.

References

1. Y. Le Page, T. Siegrist, S. A. Sunshine, L. F. Schneemeyer, D. W. Murphy, S. M. Zahurak, J. V. Waszczak, W. R. McKinnon, J. M. Tarascon, G. W. Hull, and L. H. Greene, *Phys. Rev. B* **36,** 3617 (1987).
2. W. Wong-Ng, L. P. Cook, C. K. Chiang, L. J. Swartzendruber, L. H. Bennett, J. E. Blendell, and D. Minor, *J. Mater. Res.* **3,** 5 (1988).
3. W. Wong-Ng, L. P. Cook, C. K. Chiang, L. J. Swartzendruber, and L. H. Bennett, *in* "Ceramic Superconductors II" (M. F. Yan, Ed.), pp. 27–42, Amer. Ceram. Soc. (1988).
4. W. Wong-Ng, M. A. Kuchinski, B. Paretzkin, J. Stalick, and E. R. Fuller, Jr., *J. Amer. Ceram. Soc.*, to be submitted for publication.
5. W. Wong-Ng, M. A. Kuchinski, H. F. McMurdie, and B. Paretzkin, *Powder Diffr.* **4**(1), 1 (1989).
6. W. Wong-Ng, and B. Paretzkin, *Powder Diffr.*, to be submitted for publication.
7. W. Wong-Ng, L. P. Cook, C. K. Chiang, M. D. Valdin, D. L. Kaiser, F. Beech, L. J. Swartzendruber, L. H. Bennett, and E. R. Fuller, Jr., submitted for publication.
8. W. Wong-Ng, B. Paretzkin, and E. R. Fuller, Jr., *Powder Diffr.*, in press.
9. J. E. Blendell, W. Wong-Ng, C. K. Chiang, R. D. Shull, and E. R. Fuller, Jr., *in* "Proceedings of the Annual Meetings of the Metallurgical Society, Las Vegas, Nevada, February 1989," in press.
10. W. I. F. David, W. T. A. Harrison, R. M. Ibberson, M. T. Weller, J. R. Grasmeder, and P. Lanchester, *Nature (London)* **328,** 328 (1987).
11. C. U. Segre, B. Dabrowski, D. G. Hinks, K. Zhang, J. D. Jorgensen, M. A. Beno, and I. K. Schuller, *Nature (London)* **329,** 227 (1987).
12. S. A. Sunshine, L. F. Schneemeyer, J. V. Waszczak, D. W. Murphy, S. Miraglia, A. Santoro, and F. Beech, *J. Cryst. Growth* **85**(4), 632 (1987).
13. D. Kilbanow, K. Sujata, and T. O. Mason, *J. Amer. Ceram. Soc.* **71**(5), C267 (1988).
14. R. S. Roth, C. J. Rawn, F. Beech, J. D. Whitler, and J. O. Anderson, *in* "Ceramic Superconductors II" (M. F. Yan, Ed.), pp. 13–26 Amer. Ceram. Soc. (1988).
15. D. M. de Leeuw, C. A. H. A. Mutsaers, C. Langereis, H. C. A. Smoorenburg, and P. J. Rommers, *Physica C,* **152,** 39 (1988).
16. C. Michel, L. Er-Rakho, and B. Raveau, *J. Solid State Chem.* **39,** 161 (1981).
17. C. Michel and B. Raveau, *J. Solid State Chem.* **43,** 73 (1982).
18. T. Provost, F. Struder, C. Michel, and B. Raven, *Synth. Met.* **4,** 147 (1981).
19. J. Stalick and W. Wong-Ng, in preparation.
20. W. Wong-Ng, M. A. Kuchinski, H. F. McMurdie, and B. Paretzkin, *Powder Diffr.* **4**(1), 46 (1989).
21. C. Michel, L. Er-Rakho, M. Hervieu, J. Pannetier, and B. Raveau, *J. Solid State Chem.* **68,** 143 (1987).
22. F. Herman, *Phys. Rev. B* **37,** 2309 (1988).

23. N. NGUYEN, L. ER-RAKHO, C. MICHEL, J. CHORSNET, AND B. RAVEAU, *Mater. Res. Bull.* **15,** 891 (1980).
24. B. GRANDE, HK. MULLER-BUSCHBAUM, AND M. SCHWEIZER, *Z. Anorg. Allg. Chem.* **428,** 120 (1977).
25. HK. MULLER-BUSCHBAUM AND W. WOLLSCHLAGER, *Z. Anorg. Allg. Chem.* **414,** 76 (1975).
26. A. SANTOROR, *in* "High Temperature Superconductivity" (J. W. Lynn, Ed.), Chap. 4, Vol. 84, Springer-Verlag, New York/Berlin, to be published.
27. J. D. JORGENSEN, H.-B. SCHUTTLER, D. G. HINKS, D. W. CAPONE II, K. ZHANG, AND M. B. BRODSKY, *Phys. Rev. Lett.* **58**(10), 1024 (1989).
28. J. G. BEDNORZ AND K. A. MÜLLER, *Z. Phys. B: Condens. Matter* **64,** 189 (1986).
29. Powder Diffraction File (PDF), JCPDS-International Center of Diffraction Data, Swarthmore, PA 19081.
30. T. J. KISTENMACHER, *Solid State Commun.* **65**(9), 981 (1988).
31. W. WONG-NG, H. F. MCMURDIE, B. PARETZKIN, M. A. KUCHINSKI, AND A. L. DRAGOO, *Powd. Diff.* **2**(3), 191 (1987); **2**(4), 257 (1987); **3**(1), 47 (1988); **3**(2), 113 (1988); **3**(3), 179 (1988); **3**(4), 246 (1988); **4**(1), 40 (1989); **4**(2), 106 (1989).
32. W. WONG-NG, H. F. MCMURDIE, B. PARETZKIN, M. A. KUCHINSKI, AND A. L. DRAGOO, *Powd. Diff.* **4**(2), 106 (1989).
33. O. SCHMITZ-DUMONT AND H. KASPER, *Monatsh. Chem.* **96,** 506 (1965).
34. G. BERGERHOFF AND H. KASPER, *Acta Crystallogr. B* **24,** 388 (1968).
35. H.-R. FREUND AND HK. MULLER-BUSCHBAUM, *Z. Naturforsch., B* **32,** 609 (1977).
36. E. LAMBERT, JCPDS Grant-in-Aid Report (1981) and (1982).